Quarkonium Scattering at High Energies

by

Gavin Phillip Salam

of King's College, Cambridge

A Dissertation submitted to the University of Cambridge
for the degree of Doctor of Philosophy
1996

Abstract

Quantum chromodynamics (QCD) is the theory governing the interactions of quarks and gluons. When a sufficiently hard scale is present, perturbative methods of study can be used. One result of such calculations is that in the light-cone wave function of a fast moving hadron (in particular in a quarkonium, also called onium for short), the number of low momentum gluons rises fast with the onium energy. As a result, the cross section for onium-onium scattering grows rapidly and eventually violates the unitarity bound. An approach, known as the dipole formulation, allows in principle the calculation, in a certain approximation of QCD, of both the rapid rise and of the corrections (the scattering of multiple gluons in each onium) which are expected to be dominant in the restoration of unitarity; however a full analytic treatment is not feasible. In this dissertation, a detailed study is presented of the characteristics of the onia which are important for understanding these corrections and a Monte Carlo simulation is developed for the high-energy onium evolution and for onium-onium scattering. This allows the determination of an elastic scattering amplitude which satisfies the unitarity bound. The results show that the modification of the total cross section is relatively slow, while the alteration of the elastic cross section is much stronger. Properties of the final state are also examined, and one finds that the multiple scatterings lead to a long tail in the distribution of final state multiplicity. At even higher energies, interactions between gluons in the same onium become likely — the problem of saturation, which is much less well understood than that of multiple scattering. Tools are developed which give an indication of the effects of taking saturation into account.

This dissertation is the result of my own work and includes nothing which is the outcome of work done in collaboration.

Gavin Salam

Acknowledgements

I should like to thank Bryan Webber, my supervisor, for initiating my interest in small-x physics and the dipole approach, as well as for his continuous encouragement and guidance and helpful discussions throughout my time here as a Ph.D. student. My gratitude goes also to Al Mueller, many of whose suggestions lie at the core of the work presented here and who has helped me to appreciate the subtleties of the dipole approach.

To others, I am indebted for comments and questions which set me thinking about problems which I might not otherwise have considered — these include Jochen Bartels, Keith Ellis, Francesco Hautmann, Peter Landshoff and especially Henri Navelet and Robi Peschanski with whom I have had a long series of stimulating and beneficial discussions. Bo Andersson, Stefano Catani, Yuri Dokshitzer, Boris Ermolaev and Pino Marchesini, among others, through lectures and conversations, have given me a number of insights into small-x physics and QCD more generally. I have also enjoyed and learnt from the numerous conversations with Ben Bullock, Mrinal Dasgupta, Markus Diehl, Jeff Forshaw, Mark Gibbs, Garth Leder, Stefano Moretti, Kosuke Odagiri, Christophe Royon, Mike Seymour, Wai-Keung Tang and Samuel Wallon.

I have been lucky to travel extensively over the past three years. This would not have been possible without funding from a variety of sources, including the Cavendish Laboratory, the European Union (EU Programme "Human Capital and Mobility", Network "Physics at High Energy Colliders", contract CHRX-CT93-0357 (DG 12 COMA)), King's College, the Italian INFN (Sezione di Milano), the Service de physique théorique de Saclay, and the UK Particle Physics and Astronomy Research Council (PPARC). The warm hospitality at CERN, Milan, St. Petersburg (at the 3rd PNPI Winter School) and Saclay greatly enhanced the pleasure of these trips. PPARC is also to be thanked for the Ph.D. studentship which enabled me to spend three years carrying out research — as is the INFN for the fellowship which will support me for the next two.

The Cavendish HEP group has provided a very relaxed and enjoyable environment in which to work, with Jan White always being ready to help and John Hill, Patrick Elcombe, Steve Wotton and Richard Dodsworth putting up with me, regardless of what I've tried to do to the computer systems!

Finally I would like to thank my family and friends for their invaluable support over the past three years.

Contents

List of Figures

CHAPTER 1

Introduction

A full understanding of high-energy hadron-hadron elastic scattering has long been elusive, despite the fact that its phenomenology is remarkably simple.

One can study the imaginary part of the forward elastic scattering amplitude by examining the total scattering cross section, because these two quantities are related by the optical theorem. To a first approximation, total cross sections are almost independent of the centre-of-mass energy, $\sqrt{s}$. This can be visualised as a geometrical phenomenon, where the cross section is simply a consequence of the finite size of the colliding objects. More accurately, there is a slow increase of the cross sections as energy increases, $\sigma_{\text{tot}} \sim s^{0.08}$, which seems to be independent of the particular hadrons which are involved, being for example the same for protons, pions and kaons.

The non-forward elastic amplitude $\mathcal{T}_{\text{el}}(t)$ is strongly peaked towards small momentum transfers $\sqrt{-t}$, dying off as $\mathcal{T}_{\text{el}} \sim \mathrm{e}^{bt}$. The parameter b increases linearly in the logarithm of the centre-of-mass energy — in other words elastic scattering becomes less central at high energies. These properties are neatly contained in the following equations

$$\mathcal{T}_{\text{el}}(s,t) \sim s^{\alpha_{\text{P}}(t)}, \quad \alpha_{\text{P}}(t) = 1 + \epsilon + b' t, \tag{1.1}$$

where $\epsilon \simeq 0.08$ and $b' \simeq 0.25$ GeV^{-2}. Such behaviour is characteristic of Regge theory [1] which relates the elastic amplitude to the exchange of families of particles (such as the ρ and ω mesons). In the high-energy limit, the exchange which dominates is referred to as the pomeron, named after Pomeranchuk, who suggested in the 1950's that hadronic total cross sections should tend to a constant at high energies [2].

Regge theory gives no explanation for the underlying processes which lead to the observed high-energy behaviour. For that, one should turn to quantum chromodynamics (QCD), which is the theory that governs the interactions of quarks and gluons — the constituents of hadrons. QCD has many similarities to quantum electrodynamics (QED), with the gluon being the

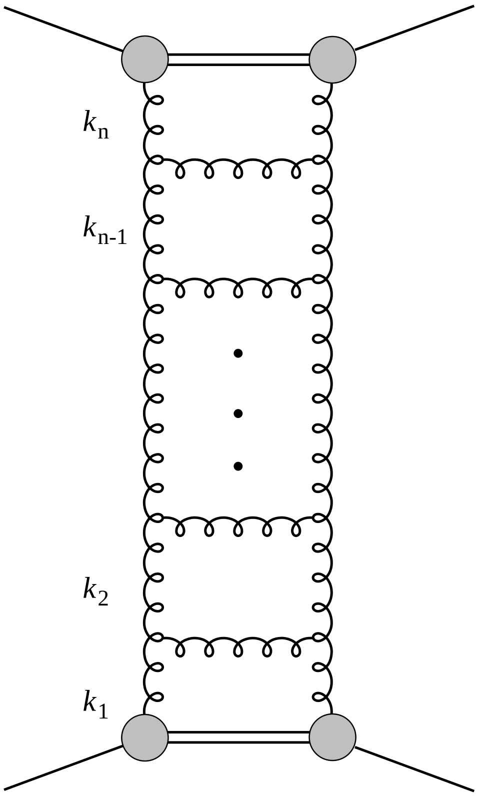

Figure 1.1: Schematic representation of the type of diagram which is resummed by the BFKL equation. Curly lines correspond to gluons and the straight lines at the top and bottom are the hadrons.

analogue of the photon. The crucial difference is that instead of a single kind of charge, QCD has three kinds of charges, referred to as different “colours”. Unlike the photon, the gluon is a charged object (roughly speaking, it carries a colour and a different anti-colour), so that gluons can interact with each other.

One of the properties of both QED and QCD is that if one takes any process and rescales all its momenta (and masses) by some factor, there is a modification of the effective coupling — the coupling depends on the typical momentum scale of the process. In QED, the coupling increases with higher momentum scales. But in QCD, because of the gluon self-interaction, the coupling decreases at larger scales. Conversely, at low scales the coupling becomes large and perturbation theory, the standard analytical technique used for QCD calculations, is not applicable. Since most of the hadrons are light, it is therefore very difficult to calculate their interactions.

Nevertheless, nearly twenty years ago, Balitsky, Fadin, Kuraev and Lipatov (BFKL) [3–5] set out to use perturbation theory to try to understand elastic scattering amplitudes in the high-energy limit. Schematically, the kinds of diagram which contribute correspond to ladders of gluons, as shown in figure 1.1. The various degrees of freedom separate into two parts: the longitudinal components of momenta (i.e. parallel to the direction of motion of the colliding hadrons) and the transverse ones. Along the ladder, as a consequence of the large centre-of-mass energy, the longitudinal components are strongly ordered, $k_{\|,1} \gg k_{\|,2} \gg \ldots$, while the transverse components are all of the same order, $k_{T,1} \sim k_{T,2} \sim \ldots$. This separation of the transverse and longitudinal components is natural given that relativistic effects will contract the hadrons in the longitudinal direction, but leave them unchanged in the transverse direction.

The result obtained by BFKL is that one should resum terms of the form $(\alpha_\mathrm{S} \ln s)^n$ (corresponding roughly to ladders with n rungs). These are known as leading-logarithmic (LL) terms. Summing them gives $\sigma_\mathrm{tot} \sim s^{(\alpha_{\mathrm{I\!P}}-1)}$, where $(\alpha_{\mathrm{I\!P}} - 1) = 4 \ln 2 \alpha_\mathrm{S} N_\mathrm{C}/\pi \simeq 0.5$, α_S is the strong coupling, and $N_\mathrm{C} = 3$ is the number of colours in QCD. The scale which sets the value of the coupling is the transverse scale, of the order of the size of the hadrons. The value that one obtains for the power is much larger than that observed, even more so given that the value of $\alpha_\mathrm{S} = 0.2$ used to obtain $(\alpha_{\mathrm{I\!P}} - 1) \simeq 0.5$ is unrealistically small for normal hadronic scales — the BFKL calculation clearly fails for normal high-energy hadron-hadron scattering.

So the interactions which govern high-energy scattering are often divided into two classes: the perturbative interaction of two hadrons via a gluon ladder is referred to as the exchange of a BFKL pomeron (also known as the hard pomeron because high momentum scales are described as being "hard") whereas the object relevant to the observed behaviour of the hadron-hadron total cross section is known as the soft pomeron (because low momentum scales are described as being "soft").

The BFKL type of behaviour is sufficiently striking that one might wonder whether there are any high-energy processes which are sufficiently perturbative that it can play a rôle. If one requires that there be one perturbative scale then there is a chance that for most of the ladder perturbation theory will apply. Relevant processes might be hadron-hadron scattering with an additional hard (i.e. large momentum) scale, such as high-energy transverse jets. Alternatively in deep inelastic scattering (DIS), the interaction of a highly virtual photon with a hadron ensures that there is at least one hard scale. These processes do have extra complications associated with them though: the fact that there are two transverse scales involved, for example in DIS those of the hadron and the virtual photon, means there are terms from the gluon ladder of the form $(\alpha_\mathrm{S} \ln s \, \ln Q^2)^n$, where Q is the ratio of the two transverse scales, because transverse momenta are now also strongly ordered along the ladder [6]. These are known as double-leading-logarithmic (DLL) contributions. Additionally, there is still the problem of one non-perturbative scale. There have been extensive phenomenological analyses to try and disentangle the various effects. Currently, there is no process in which the BFKL type of behaviour has definitely been seen yet, though there are data which are suggestive of its presence.

As well as being of phenomenological interest, the BFKL prediction has raised certain important theoretical questions. The rapid growth of the cross section becomes problematic at high energies, because one quickly ends up with a scattering amplitude which violates the condition of unitarity: for a given transverse separation (impact parameter) of the two hadrons, the probability for scattering should be always less than one. With the rapid rise of the amplitude, one reaches a situation where this condition is not satisfied by the BFKL prediction.

The solution to the problem is in the fact that at very high energies the exchange of a single pomeron is no longer the dominant contribution to the scattering amplitude. There are two relevant factors: the coupling of the ladder to the two hadrons, a factor of $O(\alpha_{\mathrm{S}}^2)$, and the enhancement due to the rungs along the gluon ladder, which gives a contribution of $O(\mathrm{e}^{(\alpha_{\mathbb{P}}-1)Y})$, where $Y = \ln s$ is known as the rapidity. For moderate values of Y, when

$$\alpha_{\mathrm{S}}^2 \mathrm{e}^{(\alpha_{\mathbb{P}}-1)Y} \ll 1, \tag{1.2}$$

the leading contribution is the exchange of a single ladder. But when

$$\alpha_{\mathrm{S}}^2 \mathrm{e}^{(\alpha_{\mathbb{P}}-1)Y} \sim 1, \tag{1.3}$$

multiple ladders are no longer disfavoured, and their contribution must be taken into account to restore unitarity. In fact the situation is quite complicated because an accurate calculation requires that one include the branching of one gluon ladder into two [7, 8] (and various other terms such as a 4-gluon ladder [9–11]) in all possible combinations, leading to some kind of effective field theory of gluon ladders [12–15].

There is a second way of viewing the BFKL growth of the cross section, which perhaps gives a more intuitive feel for the corrections that arise. One considers a particular frame, say the rest frame of one of the hadrons. Let x be the fraction of the fast-moving hadron's momentum which is carried by a given gluon inside the hadron. The stationary hadron will essentially be able to interact with any gluon which is moving towards it, i.e. any gluon with $x \gtrsim M^2/s$, where M is the mass of the hadron. Therefore the growth of the cross section can be understood by arguing that the fast-moving hadron contains of the order of $x^{-(\alpha_{\mathbb{P}}-1)}$ gluons with momentum fraction greater than x and that the cross section with a stationary hadron is proportional to the number of gluons present. In an arbitrary frame the cross section is proportional to the product of the number of gluons in the two hadrons. Since s is large, the typical values of $x \gtrsim M^2/s$ are small, and the scattering is controlled by the small-x properties of the hadron. The change in the gluon distribution as one decreases x is often referred to as the *evolution* in x of the gluon distribution.

In this way of viewing BFKL effects, the modifications at high energies appear to come about in a different manner — though they can of course be related to the multiple pomeron exchange picture. There are two kinds of corrections which play a role. Each gluon has associated with it a certain transverse momentum. In impact parameter, this corresponds to it occupying a finite area. If the density of gluons becomes too high, then in addition to the branching process which creates the rise in the number of small-x gluons, one expects that recombination of gluons will start to occur, which will dampen the rise. If one has evolved the hadron down to some value of $x = \mathrm{e}^{-y}$ then the probability of a given gluon interacting with another will be proportional to the density of nearby gluons, $\mathrm{e}^{(\alpha_{\mathbb{P}}-1)y}$, multiplied by the interaction between any two gluons, $O(\alpha_s^2)$. Therefore when

$$\alpha_s^2 \mathrm{e}^{(\alpha_{\mathbb{P}}-1)y} \sim 1 \tag{1.4}$$

one starts to get recombination of gluons. This effect is referred to as saturation, because it is expected to lead to the saturation of the density of gluons in the hadron.

A second effect comes about because, when the two hadrons collide, there may be more than one interaction. In a frame where one hadron is evolved to a rapidity y and the other to $Y - y$, the mean number of interactions will be proportional to

$$\alpha_s^2 \mathrm{e}^{(\alpha_{\mathbb{P}}-1)y} \mathrm{e}^{(\alpha_{\mathbb{P}}-1)(Y-y)} = \alpha_s^2 \mathrm{e}^{(\alpha_{\mathbb{P}}-1)Y}. \tag{1.5}$$

The (squared) scattering amplitude is proportional to the fraction of collisions in which an interaction occurs. When interactions are unlikely, this should be just the same as the mean number of interactions. But when multiple scatterings are common, the probability of there being an interaction reaches a ceiling (of one), while the mean number of interactions can be much larger than one. Therefore when

$$\alpha_s^2 \mathrm{e}^{(\alpha_{\mathbb{P}}-1)Y} \sim 1 \tag{1.6}$$

multiple-scattering corrections should be taken into account. This is the same condition as in the picture involving the exchange of gluon ladders.

A crucial observation, by Mueller [16], is that the relative importance of saturation and multiple-scattering corrections depends on the frame in which one examines the collision. In the lab frame (see figure 1.2a), where one of the hadrons is completely unevolved, the rapidity at which multiple-scattering corrections become important is defined by eq. (1.6). But this is also the point where saturation corrections start to matter since one has

$$\alpha_s^2 \mathrm{e}^{(\alpha_{\mathbb{P}}-1)y_1} = \alpha_s^2 \mathrm{e}^{(\alpha_{\mathbb{P}}-1)Y} \sim 1. \tag{1.7}$$

So in the lab frame, to understand the high-energy corrections one needs to take into account both multiple scattering and saturation.

In the centre-of-mass (CM) frame, depicted in figure 1.2b, multiple scattering becomes important at the same rapidity as in the lab frame, eq. (1.6), but saturation at that rapidity,

$$\alpha_s^2 \mathrm{e}^{(\alpha_{\mathbb{P}}-1)y_1} = \alpha_s^2 \mathrm{e}^{(\alpha_{\mathbb{P}}-1)Y/2} \ll 1 \tag{1.8}$$

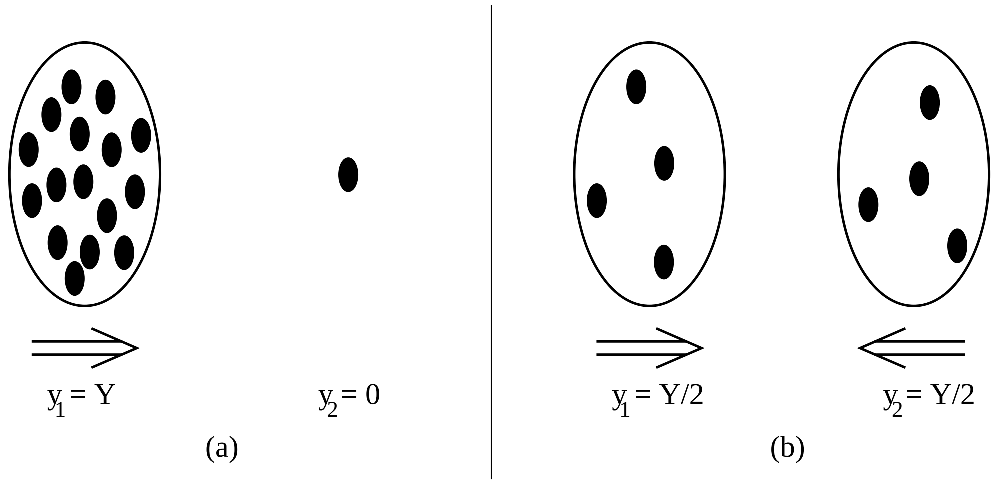

Figure 1.2: A schematic view of a hadron-hadron collision, (a) in the lab frame, where one hadron is evolved and contains many closely packed "gluons", while the other is stationary and contains only one "gluon", and (b) in the centre-of-mass frame where both hadrons contain a relatively dilute distribution of "gluons".

is much smaller, and it should be safe to neglect it. This is convenient, because there is a well defined procedure for calculating multiple-scattering corrections [16], whereas anything but a rough determination of the saturation corrections [7] is quite difficult.

The picture discussed so far illustrates the basic principles behind the high-energy corrections to BFKL behaviour. For an accurate calculation of the multiple-scattering corrections, there are a number of other relevant consideration which have not been brought out by the simple discussion above. Figure 1.2 shows the "gluons" as being restricted to a particular region of impact parameter, whereas in fact, in the purely perturbative case of BFKL evolution, there is no such restriction. It is important to know exactly how the gluons are distributed in impact parameter, because the same number of gluons will lead to different corrections depending on whether they are spread out over a large area or a small one and in fact the mean distribution of gluons will change smoothly across a range of impact parameters. In addition one will have gluons with a variety of different transverse momenta (or in impact parameter language, different effective sizes).

Secondly, it is not sufficient just to know the mean distribution of gluons: one can imagine a situation where gluons are always to be found in dense clumps, while the clumps themselves are dilutely distributed. If one averages over the positions of the clumps then one obtains a gluon distribution which appears dilute, but for any particular interaction, whenever two clumps interact there will be strong multiple scattering. So the property of a mean gluon distribution being dilute might be misleading when trying to calculate multiple-scattering corrections.

Such effects are difficult to estimate in the traditional approach to BFKL evolution, which is formulated in terms of transverse momenta. In particular, it would be difficult to extract the probabilities of individual gluon configurations inside the hadron.

In a recent series of papers, Mueller and collaborators [16–19] have developed an alternative, but equivalent, approach to BFKL evolution, which is explicitly in terms of impact parameters (a related approach has also been developed by Nikolaev, Zakharov and collaborators [20, 21]). To avoid the problems of the non-perturbative region of low mass scales, and of double-logarithmic contributions due to the presence of two different transverse scales, one considers the collisions of heavy quarkonia, bound $q\bar{q}$ states, also referred to simply as onia. These set a single perturbative scale. From the $q\bar{q}$ state, one can calculate, using light-cone perturbation theory [22–25], the probability of there being a state with an additional small-x gluon at some given impact parameter. The colour structure is such is that the extra gluon has the effect of converting the original colour dipole of the $q\bar{q}$ state into two colour dipoles, one formed from the quark and the gluon, the other from the gluon and the antiquark. In the approximation of QCD having a large number of colours, these two colour dipoles can then produce extra small-x gluons independently, in the same way as the original $q\bar{q}$ dipole. This branching of one dipole into two repeats itself many times, giving a cascade of small-x dipoles — the origin of the rise in the number of gluons at small x. Because one knows the probability distribution for the position of each extra gluon, it is possible to work out the probability of any given impact parameter configuration of dipoles. In addition, Mueller [16] provides a straightforward way of calculating the sum of all numbers of multiple scatterings (between dipoles, rather than between gluons) for a given pair of onium configurations, and shows that the procedure leads to a scattering amplitude which satisfies the unitarity bound.

Mueller's work lays the foundations for calculating multiple-scattering corrections. But because of the complexity of the dipole configurations that arise (there are very large numbers of dipoles, and one must know the rapidity and position of each), it is difficult to work out analytically anything other than the mean properties of the onium wave function. The intention of this dissertation is to go beyond the mean quantities, and obtain an accurate determination of the multiple-scattering corrections as well as a more approximate estimate of the saturation effects. This can only be done numerically. Simply writing a program to determine the corrections and plotting the resulting cross sections will give little understanding of the salient features of BFKL evolution which affect the multiple scatterings and saturation. Therefore in parallel to the determination of the cross sections, detailed analyses will be carried out (both analytically and numerically) to help understand the origins of the results.

As well as the unitarity bound on the amplitude, there is a second limit, known as the Froissart bound [26, 27], which states that asymptotically the cross section cannot grow faster than $(\ln s)^2$, as a consequence of the limited interaction range of the strong force (the relevant scale is the mass of the pion). Since Mueller's approach is purely perturbative, such effects are not included and the Froissart bound will not necessarily be satisfied. It will not be discussed any further.

The layout of the dissertation is the following. Chapter 2 consists of an introduction to QCD, concentrating on the features which are of particular relevance to the dipole formulation. It also discusses the bounds imposed by unitarity constraints. Chapter 3 gives a brief review of the field of small-x physics. It discusses other approaches to high-energy scattering — soft pomeron exchange and the double-leading-logarithmic approximation — as well as BFKL evolution, and addresses the status of the experimental evidence for the different kinds of behaviour. Chapter 4 describes the dipole formulation, in the approach by Mueller and collaborators. It considers the derivation of the evolution equation, and of the method used for calculating the multiple-scattering corrections, as well as including material on the nature of the approximations being used, the tools available for understanding the dipole distributions and scattering amplitudes and the relation between dipole and BFKL evolution. These three chapters consist entirely of a review of other people's work (except that chapter 4 occasionally gives more detail than is to be found elsewhere).

The remainder of this dissertation, chapters 5–8, and the appendices, consists entirely of original work (except for the introduction of section 7.5 and subsection 8.2.2). Chapter 5 describes the numerical tools that have been developed for studying onium evolution and interaction. Chapter 6 presents a variety of results on the properties of the dipole distribution in onium wave functions. Mean properties are shown for a variety of cases, for example where they help to illustrate the main features of the branching process. Results are also given for certain aspects of the fluctuations of the dipole distribution (i.e. the way in which the mean of the distributions is a poor indicator of the properties of the distributions).

Chapter 7 gives the principal results of the dissertation, the total and elastic onium-onium scattering cross sections, including the multiple-scattering corrections. There is an associated discussion of the main characteristics of the multiple scatterings, as well as an attempt to calculate the effect of multiple scatterings on the properties of the final state. Chapter 8 returns to the question of saturation and adopts a variety of techniques to try and determine firstly the effect of saturation in the regime where it should be small compared to multiple-scattering effects (i.e. trying to verify this approximation), and secondly some information on the behaviour of the onium wave function in the extremely high energy limit where saturation becomes important. Chapter 9 summarises the main conclusions of the work presented here.

CHAPTER 2

QCD

Quantum chromodynamics (QCD) is the theory of the strong force, which is responsible for the interactions between quarks and gluons. Like QED (see for example [28, 29]), it is a gauge theory. The main difference is that whereas in QED, there is only one variety of charge (the gauge group is $U(1)$), quarks can have three kinds of QCD or colour charge (the gauge group of QCD is $SU(3)$). Associated with this is the fact that the vector particles of the theory, the gluons, of which there are eight, also carry colour charge. As a result the gluons can interact with each other, which leads to very different behaviours from those found in QED. For a detailed account of QCD and its phenomenology, the reader is referred to books such as [30, 31].

This chapter will discuss the elements of QCD which are of relevance to the study of high-energy onium-onium collisions. First, we will review the form of the Lagrangian of QCD, and its property of gauge invariance. To make it feasible to do analytic calculations it is necessary to construct a perturbation theory. This requires that any interactions be only a small modification of the free theory. One of the most important results obtainable from perturbative calculations is the running of the coupling constant α_S. As in QED a modification of the momentum scale at which a process is taking place leads to a modification of the coupling. In QED, the coupling increases (slowly) as the scale increases. However in QCD, because of the triple-gluon coupling one finds the opposite: at large scales, the coupling becomes small. Conversely, at small momentum scales, the coupling becomes large, and perturbation theory is no longer valid — one enters into the non-perturbative regime of QCD. Therefore when carrying out perturbative calculations it is essential that one avoid problems related to low scales.

While it is covariant (or Feynman) perturbation theory which is the most commonly used, for much of the work in this dissertation, it will be more convenient to adopt light-cone perturbation theory [22–25] which is particularly suited to calculating light-cone wave functions of hadrons — the distribution of constituents that one sees inside a fast moving hadron. A second technique, which is vital for the work to follow, is the large N_C approximation, where instead of considering a theory such as $SU(3)$, one considers the limit of $SU(N_C)$ where N_C is large. One can perform an expansion in $1/N_{\rm C}$, and the leading term has the property that it corresponds only to planar graphs, greatly simplifying certain calculations.

Often when evaluating scattering amplitudes using the methods described above, one will choose a certain subset of graphs to evaluate, i.e. a certain subset of the full theory. It is important to check whether the quantities determined in this manner are self-consistent. One strong constraint will be related to properties of the S-matrix, which contains all the information about scattering in the theory. In particular, for conservation of probability the S-matrix must be unitary. This leads to limits on the maximum size of the interaction amplitude between two colliding objects.

2.1 Lagrangian

In QCD, one has fields for the quarks and gluons. The quarks are represented by spinors q_a, where the a is the colour index, running from 1 to 3 ($= N_{\rm C}$). (The spinor index is left out). The vector field (the gluons) is represented by $t^A_{ab}A^A_\mu = t.A_\mu$. The index μ is the usual Lorentz index. The index A, which runs from 1 to 8 ($= N_{\rm C}^2 - 1$) represents the presence of the 8 different kinds of gluons. The hermitian, traceless matrices t^A_{ab} encode the colour structure of these gluons, and of their interactions with themselves and the quarks.

The classical Lagrangian of chromodynamics is

$$\mathcal{L}_{\rm classical} = \sum_{\rm flavours} \bar{q}_a (i\gamma^\mu D_\mu - m)_{ab} q_b - \frac{1}{4} F^A_{\mu\nu} F^{\mu\nu}_A, \tag{2.1}$$

where, analogously to electrodynamics

$$(D_\mu)_{ab} = \partial_\mu \delta_{ab} + i g_{\rm S} (t^A A^A_\mu)_{ab}. \tag{2.2}$$

A straightforward extension has been made to include colour and the electromagnetic coupling e has been replaced with the strong coupling $g_{\rm S}$. The field tensor $F^A_{\mu\nu}$ is

$$F^A_{\mu\nu} = \partial_\mu A^A_\nu - \partial_\nu A^A_\mu - g_{\rm S} f^{ABC} A^B_\mu A^C_\nu. \tag{2.3}$$

The structure constants of QCD, the f^{ABC} (antisymmetric under interchange of indices), are defined by

$$[t^A, t^B] = i f^{ABC} t^C. \tag{2.4}$$

The part of the QCD field tensor which is absent from QED is the term $g_{\rm S} f^{ABC} A^B_\mu A^C_\nu$. In perturbative language, through the $F^A_{\mu\nu}F^{\mu\nu}_A$ term in the Lagrangian, this is what leads to three four gluon vertices. It can be seen to arise naturally if one uses the relation

$$igt.F_{\mu\nu} = [D_\mu, D_\nu], \tag{2.5}$$

so that $g_S f^{ABC} A_\mu^B A_\nu^C$ comes from the commutation relation eq. (2.4).

For reference, various properties of the colour matrices are summarised here:

$$\mathrm{Tr}\ t^A t^B = T_R \delta^{AB}, \qquad T_R = \frac{1}{2}, \tag{2.6}$$

$$\sum_A t^A_{ab} t^A_{bc} = C_F \delta_{ac}, \qquad C_F = \frac{N_C^2 - 1}{2N_C}. \tag{2.7}$$

In addition, matrices in the adjoint representation of $SU(3)$, T^A, will be needed, where

$$(T^A)_{BC} = -if^{ABC}, \qquad [T^A, T^B] = if^{ABC} T^C, \tag{2.8}$$

$$\mathrm{Tr} T^A T^B = \sum_{C,D} f^{ACD} f^{BCD} = C_A \delta^{AB}, \qquad C_A = N_C. \tag{2.9}$$

2.2 Gauge invariance

QCD is a gauge theory, which means that is invariant under transformations

$$q_a(x) \to q'_a(x) = \left[\mathrm{e}^{it^A \theta^A(x)}\right]_{ab} q_b(x) = U(x)_{ab} q_b(x), \tag{2.10}$$

where $\theta^A(x)$ is any set of functions depending on position and time. For the theory to be invariant under such transformations, the vector field must also be modified by the transformation, $A_\mu \to A'_\mu$, such that

$$D'_\mu q'(x) = (\partial_\mu + igt.A'_\mu) U(x) q(x) = U(x) D_\mu q(x), \tag{2.11}$$

from which one finds that

$$t.A'_\mu = U(x) t.A_\mu U^{-1}(x) + \frac{i}{g_S} [\partial_\mu U(x)] U^{-1}(x). \tag{2.12}$$

The field tensor, $F^A_{\mu\nu}$, therefore transforms as

$$t.F'_{\mu\nu} = U(x) t.F_{\mu\nu} U^{-1}(x). \tag{2.13}$$

One way of seeing that this is the correct form is by observing that the action of the gauge transformation on the covariant derivative is effectively $D'_\mu = U(x) D_\mu U^{-1}(x)$, where the derivative acts both on U^{-1} and whatever follows it. Then using eq. (2.5), eq. (2.13) follows straightforwardly. When carrying out the gauge transformation of the field tensor, the term $g_{\rm S} f^{ABC} A_\mu^B A_\nu^C$ is essential to obtain the result of eq. (2.13) which leads to the gauge invariance of the combination

$$\frac{1}{4} F_{\mu\nu}^A F_A^{\mu\nu} = \frac{1}{2} \mathrm{Tr}(t.F_{\mu\nu})(t.F^{\mu\nu}), \tag{2.14}$$

which appears in the Lagrangian (the trace is taken over the colour matrices).

One of the main calculational importances of gauge invariance is that the amplitude for any process should be independent of the gauge in which the calculation is performed, so that one can choose whichever gauge is most convenient. Various gauges will be discussed in the following sections.

2.3 Perturbation theory

When the coupling constant of the theory, $g_{\rm S}$, is sufficiently small, then it is possible to calculate interactions between particles using perturbation theory, on the basis of the interactions being small modifications of the free theory. Most commonly, Feynman perturbation theory is used, which will be described here. This consists of a structure for treating particles where one has vertices corresponding to the interactions between quarks and gluons, and propagators for quarks and gluons which are not final or initial particles. The vertices come from the parts of the Lagrangian which involve three or more fields, while the propagators are essentially the inverse of those parts involving just two fields.

To illustrate some of the difficulties which arise it is easiest, initially, to consider QED. One can write

$$-\frac{1}{4} F_{\mu\nu}^A F_A^{\mu\nu} = \frac{1}{2} A^\mu (g_{\mu\nu}\partial^2 - \partial_\mu \partial_\nu) A^\nu + \text{tot. deriv.}, \tag{2.15}$$

The propagator should be the inverse of this function. In momentum space, writing the propagator $iD^{\nu\lambda}(k) = i(Bg^{\nu\lambda}k^2 + Ck^\nu k^\lambda)$, one should have

$$(-g_{\mu\nu}k^2 + k_\mu k_\nu)(Bg^{\nu\lambda}k^2 + Ck^\nu k^\lambda) = \delta_\mu^\lambda \tag{2.16}$$

which has no solutions. The origin of the problem is the existence of redundant components in the vector potential due to the gauge invariance. The solution is to fix the gauge, by adding a gauge fixing term to the Lagrangian. One possibility is a covariant gauge fixing term, corresponding to the Lorentz gauge $\partial_\mu A^\mu = 0$:

$$\mathcal{L}_{\rm gauge-fixing} = -\frac{1}{2\lambda}(\partial_\mu A^{\mu A})^2, \tag{2.17}$$

where λ is termed the gauge parameter. This extra term can be understood as causing the gauge to become a conserved quantity of the Lagrangian. Modifying eq. (2.16) appropriately one now obtains a solution for the propagator

$$iD_{\mu\nu}(k) = -\frac{i}{k^2}\left[g_{\mu\nu} + (\lambda - 1)\frac{k_\mu k_\nu}{k^2}\right]. \tag{2.18}$$

The case with $\lambda = 1$ is referred to as the Feynman gauge.

When working with a non-abelian theory such as QCD, extra complications occur, and one finds that it is necessary to add a Faddeev-Popov 'ghost' term to the Lagrangian [32]. This can be seen using the path integral formalism [33]. For the covariant gauges introduced above, this is

$$\mathcal{L}_{\text{ghost}} = \partial_\mu \eta^{A\dagger}(D^\mu_{AB}\eta^B) \tag{2.19}$$

with

$$D_\mu^{AB} = \partial_\mu \delta^{AB} + ig(T^C A_\mu^C)_{AB}. \tag{2.20}$$

The η^A is a complex scalar field which obeys fermionic statistics. It does not correspond to a real particle, so it is present only as internal lines[1]. A physical interpretation of the role of the ghost fields is that they cancel unphysical degrees of freedom which would otherwise be present in covariant gauges. The form (and even presence) of the ghost term in the Lagrangian depends on the gauge condition.

Overall, the Lagrangian that will be used to give the Feynman rules is

$$\mathcal{L}_{\text{classical}} + \mathcal{L}_{\text{gauge-fixing}} + \mathcal{L}_{\text{ghost}}. \tag{2.21}$$

The resulting Feynman rules are given in figure 2.1. Each vertex must conserve four-momentum. The transition amplitude for a reaction is the sum of all diagrams. Spinors (defined as in [34]) are associated with initial and final state particles:

quark in initial state	$u^a(p)$,
quark in final state	$\bar{u}^a(p)$,
antiquark in initial state	$\bar{v}^a(p)$,
antiquark in final state	$v^a(p)$,

where the index a as usual refers to the colour state. As in QED, a fermion loop is associated with a factor of -1. In addition there are combinatoric factors, so that for example the gluon loop

[1] Note that the reason that it does not appear in QED is that the structure constants of QED, $iT^C_{AB} = f^{ABC}$ are effectively zero, so that the ghosts don't couple to real particles.

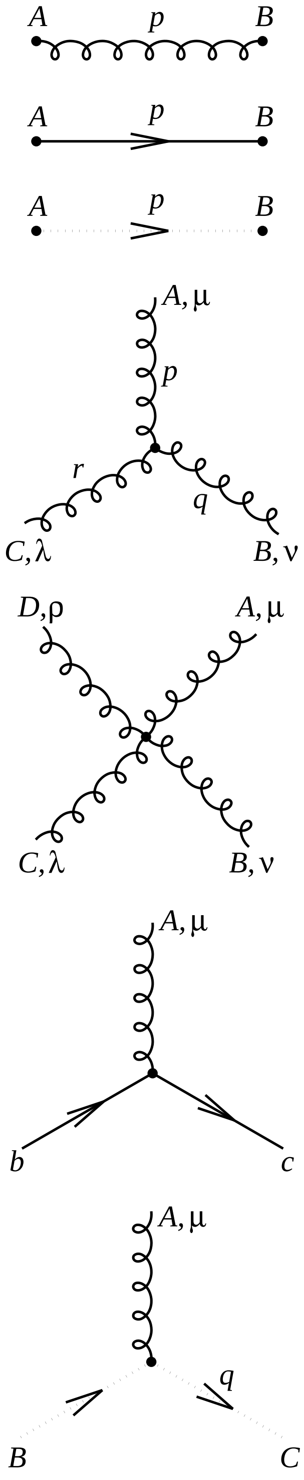

$$\delta^{AB}\left[-g^{\mu\nu}+(1-\lambda)\frac{p^\mu p^\nu}{p^2+i\epsilon}\right]\frac{i}{p^2+i\epsilon}$$

$$\delta^{ab}\frac{i}{\gamma.p-m+i\epsilon}$$

$$\delta^{AB}\frac{i}{p^2+i\epsilon}$$

$$-gf^{ABC}\left[(p-q)^\lambda g^{\mu\nu}+(q-r)^\mu g^{\nu\lambda}+(r-p)^\nu g^{\lambda\mu}\right]$$

all momenta incoming

$$-ig_s^2 f^{EAC}f^{EBD}[g^{\mu\nu}g^{\lambda\rho}-g^{\mu\rho}g^{\nu\lambda}]$$
$$-ig_s^2 f^{EAD}f^{EBC}[g^{\mu\nu}g^{\lambda\rho}-g^{\mu\lambda}g^{\nu\rho}]$$
$$-ig_s^2 f^{EAB}f^{ECD}[g^{\mu\lambda}g^{\nu\rho}-g^{\mu\rho}g^{\nu\lambda}]$$

$$-ig(t^A)_{cb}\gamma^\mu$$

$$gf^{ABC}q^\mu$$

Figure 2.1: Feynman rules for QCD in a covariant gauge. Gluons are curly lines, fermions are solid lines and ghosts are dotted lines

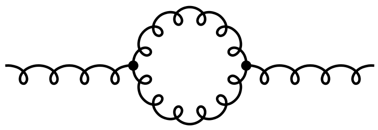

is associated with a factor of 1/2.

A second class of gauges which can be used is that of the axial gauges. The gauge fixing term is

$$\mathcal{L}_{\text{gauge-fixing}} = -\frac{1}{2\lambda}\left(n^\mu A_\mu^A\right)^2, \tag{2.22}$$

which depends on the vector n^μ, so that the gauge is not covariant. The propagator becomes

$$iD_{AB,\mu\nu}(p) = \delta_{AB}\frac{i}{p^2}\left[-g_{\mu\nu} + \frac{n_\mu . p_\nu + p_\mu . n_\nu}{n.p} - \frac{(n^2+\lambda p^2)p_\mu p_\nu}{(n.p)^2}\right]. \tag{2.23}$$

This is much more complicated than for the covariant gauges. The advantage of the axial gauge is that the ghost fields are not required. If one chooses $n^2 = 0$ and $\lambda = 0$, the propagator becomes

$$iD_{AB,\mu\nu}(p) = \delta_{AB}\frac{i}{p^2}d_{\mu\nu}(p,n) \tag{2.24}$$

with

$$d_{\mu\nu}(p,n) = -g_{\mu\nu} + \frac{n_\mu p_\nu + p_\mu n_\nu}{n.p}. \tag{2.25}$$

These are light cone gauges. They are sometimes referred to as being physical gauges because when $p^2 \to 0$ only two polarisations propagate:

$$n^\mu d_{\mu\nu}(n,p) = 0, \quad p^\mu d_{\mu\nu}(n,p) = 0. \tag{2.26}$$

One can then decompose $d_{\mu\nu}$ into the sum of the product of two polarisation vectors:

$$d_{\mu\nu} = \sum_{i=1}^{2} \epsilon_\mu^{(i)*}(p,n)\epsilon_\nu^{(i)}(p,n), \tag{2.27}$$

where $p.\epsilon^{(i)} = 0$ and $n.\epsilon^{(i)} = 0$.

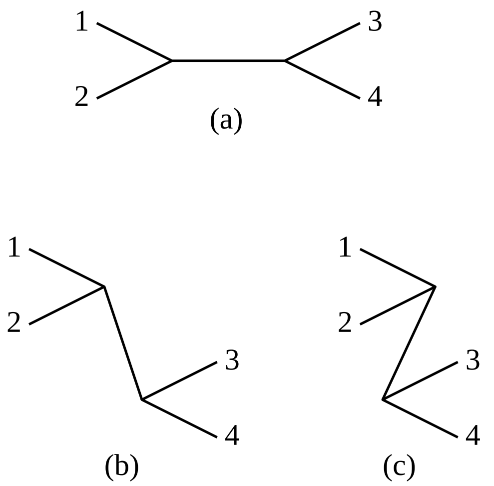

Figure 2.2: A simple ϕ^3 process in Feynman (a) and time-ordered (b), (c) perturbation theories: in (b) and (c), time flows from left to right

2.4 Light-cone perturbation theory

The Feynman graphs of the previous section can be decomposed into various time orderings: this gives time-ordered (or old-fashioned) perturbation theory (TOPTh). Taking as an example ϕ^3 theory, the Feynman diagram of figure 2.2a consists of the sum of two time-ordered diagrams shown in figure 2.2b and 2.2c. Instead of the four-momentum p being conserved at each vertex, only the three-momentum, $\mathbf{p}$ is conserved. The energy of a particle is then determined from

$$p_0 = \sqrt{\mathbf{p}^2 + m^2}, \tag{2.28}$$

where m is the mass of the particle, and to replace propagators, for each intermediate stage one includes a factor of the inverse of the difference between the energy of the incoming particles and the energy of all the particles in the intermediate state. Because of the square-root needed to determine the energies, the non-covariant nature of the calculations and the large number of diagrams that needs to be considered, this quickly becomes very complicated.

As a solution to some of the problems of TOPTh, it was suggested by Dirac [22] and Weinberg [23] that one examines problems in an infinite momentum (or light-cone) frame. One uses light-cone variables defined as

$$a_+ = a_0 + a_3, \tag{2.29}$$

$$a_- = a_0 - a_3, \tag{2.30}$$

$$\mathbf{a}_\perp = (a_1, a_2), \tag{2.31}$$

$$a.b = \frac{1}{2}(a_+b_- + a_-b_+) - \mathbf{a}_\perp.\mathbf{b}_\perp. \tag{2.32}$$

These variables have numerous advantages over the normal variables $a_{0...3}$. For example under a frame transformation in the longitudinal direction, light-cone momentum fractions, $z = p_+/P_+$ are invariant. One quantises at fixed light-cone time x_+ (rather than x_0), so that the equivalent of energy is its conjugate momentum, p_-

$$p_- = \frac{|\mathbf{p}_\perp^2| + m^2}{p_+}. \tag{2.33}$$

This is already considerably simpler than the TOPTh expression. One also has the condition that $p_+ > 0$, and since it is p_+ and $\mathbf{p}_\perp$ which are conserved at vertices, diagrams such as 2.2c can't contribute because at least one of the particles at the lower vertex would have to have a negative plus component of its momentum.

To see mathematically the features which arise when working with light-cone variables, consider the Klein-Gordon propagator:

$$\begin{aligned}\Delta(x) &= \int \frac{\mathrm{d}^4 p}{(2\pi)^4} \frac{\mathrm{e}^{-ip.x}}{p^2 - m^2 + i\epsilon} \\ &= \frac{1}{2(2\pi)^4} \int \mathrm{d}^2\mathbf{p}_\perp \int \mathrm{d}p_+ \mathrm{e}^{-i(p_+ x_-/2 - \mathbf{p}_\perp . \mathbf{x}_\perp)} \int \mathrm{d}p_- \frac{\mathrm{e}^{-ip_- x_+/2}}{p_+ p_- - p_\perp^2 - m^2 + i\epsilon}.\end{aligned} \tag{2.34}$$

The p_- integral can be evaluated by contour integration: the only non-zero contributions come from situations where either $x_+ > 0, p_+ > 0$ or $x_+ < 0, p_+ < 0$, allowing one to write

$$\Delta(x) = \frac{-i}{2(2\pi)^3} \int \mathrm{d}^2\mathbf{p}_\perp \int_0^\infty \frac{\mathrm{d}p_+}{p_+} \left[\theta(x_+)\mathrm{e}^{-ip.x} + \theta(-x_+)\mathrm{e}^{ip.x}\right], \tag{2.35}$$

where one has the on mass-shell condition

$$p_- = \frac{p_\perp^2 + m^2}{p_+}. \tag{2.36}$$

The condition $p_+ > 0$ has arisen through the redefinition of the momentum as always flowing from earlier to later times. If one examines the fermion propagator,

$$D(x) = (i\gamma^\mu \partial_\mu + m)\Delta(x), \tag{2.37}$$

one notices that the action of the derivative on the step functions, $\partial_- \theta(x_+) = \delta(x_+)$ is to introduce a component of the propagator with a delta function of x_+, i.e. an instantaneous part to the propagator.

With these ideas one can set up an alternative to TOPTh, which uses light-cone variables: light-cone perturbation theory (LCPTh). This was developed for QED by Kogut, Soper and Bjorken [24, 25] and the extension for QCD can be found for example in [35, 36]. The vertices of LCPTh are shown in figure 2.3. The rules for their use are the following:

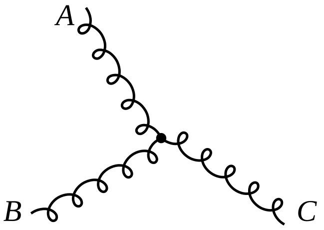

$$
\begin{aligned}
&ig_{\mathrm{s}} f^{ABC}[(p_A - p_B).\epsilon_C^*\epsilon_A.\epsilon_B \\
&+(p_B - p_C).\epsilon_A\epsilon_B.\epsilon_C^* + (p_C - p_A).\epsilon_B\epsilon_A.\epsilon_C^*]
\end{aligned}
$$

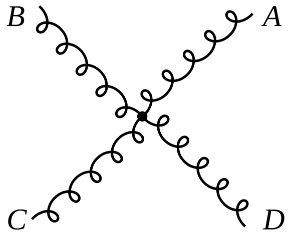

$$
\begin{aligned}
&+g_{\mathrm{s}}^2 f^{EAC} f^{EBD}[\epsilon_A^*.\epsilon_B\epsilon_C.\epsilon_D^* - \epsilon_A^*.\epsilon_D^*\epsilon_B.\epsilon_C] \\
&+g_{\mathrm{s}}^2 f^{EAD} f^{EBC}[\epsilon_A^*.\epsilon_B\epsilon_C.\epsilon_D^* - \epsilon_A^*.\epsilon_C\epsilon_B.\epsilon_D^*] \\
&+g_{\mathrm{s}}^2 f^{EAB} f^{ECD}[\epsilon_A^*.\epsilon_C\epsilon_B.\epsilon_D^* - \epsilon_A^*.\epsilon_D^*\epsilon_B.\epsilon_C]
\end{aligned}
$$

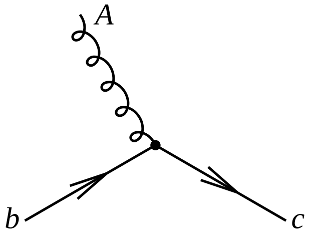

$$g_{\mathrm{s}}(t^A)_{cb}\bar{u}(c)\gamma.\epsilon_A u(b)$$

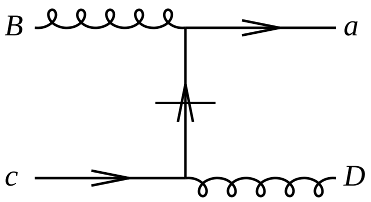

$$g_{\mathrm{s}}^2(t^B t^D)_{ca}\bar{u}(a)\gamma.\epsilon_B \frac{\gamma_+}{2(p_{c+} - p_{D+})}\gamma.\epsilon_D^* u(c)$$

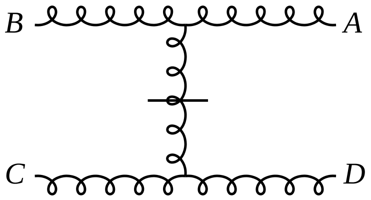

$$-g_{\mathrm{s}}^2 f^{EAB} f^{ECD}\epsilon_A^*.\epsilon_B \frac{(p_{A+} - p_{B+})(p_{C+} - p_{D+})}{(p_{C+} + p_{D+})^2}\epsilon_D^*.\epsilon_C$$

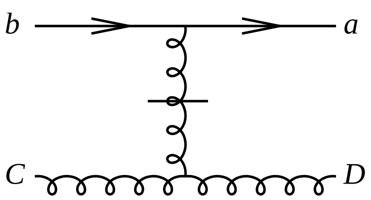

$$ig_{\mathrm{s}}^2 f^{CDE}(t^E)_{ab}\bar{u}(a)\gamma_+ u(b)\frac{(p_{C+} - p_{D+})}{(p_{C+} + p_{D+})^2}\epsilon_D^*.\epsilon_C$$

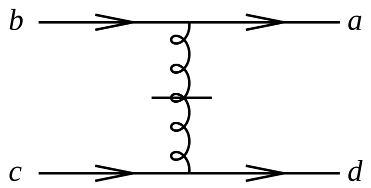

$$g_{\mathrm{s}}^2(t^E)_{ab}(t^E)_{dc}\frac{\bar{u}(a)\gamma_+ u(b)\bar{u}(d)\gamma_+ u(c)}{(p_{c+} - p_{d+})^2}$$

Figure 2.3: Rules for QCD vertices in light-cone perturbation theory. All gluon momenta are outgoing. Light-cone time flows from left to right. Lines with a cross bar represent instantaneous exchange.

1. One assigns a momentum k_μ to each line such that the total $k_+, k_\perp$ are conserved at each vertex, and that $k^2 = m^2$, or equivalently, $k_- = (k_\perp^2 + m^2)/k_+$. With each fermion one associates an on shell spinor, $u(k,\lambda)$ or $v(k,\lambda)$, normalised so that $\bar{u}(k,\lambda)\gamma_\mu u(k,\lambda') = 2k_\mu \delta_{\lambda\lambda'}$ where λ, λ' are spin indices. With each gluon line one associates a polarisation vector ϵ_μ, which satisfies $\epsilon_+ = 0$, $\epsilon(k).k = 0$ and $\epsilon(k)^2 = 1$.

2. A factor $\theta(k_+)/k_+$ is included for each internal line.

3. For each vertex there is a factor as illustrated in figure 2.3. To convert incoming into outgoing lines, and vice-versa, one replaces

$$u \longleftrightarrow v, \quad \bar{u} \longleftrightarrow -\bar{v}, \quad \epsilon \longleftrightarrow \epsilon^*, \tag{2.38}$$

4. For each intermediate state, there is a factor

$$\frac{1}{\sum_{\text{initial}} k_- - \sum_{\text{interm}} k_- + i\epsilon}, \tag{2.39}$$

   where the sums are over all particles in the initial and intermediate states respectively.

5. One integrates

$$\int \frac{\mathrm{d}^2\mathbf{k}_\perp}{16\pi^3} \int_0^\infty \mathrm{d}k_+ \tag{2.40}$$

   over each independent momentum and one sums over internal helicities and colours.

6. There is a factor of -1 for each closed fermion loop, and also for each fermion line both beginning and ending in the initial state and for each diagram in which fermion lines are interchanged in either the initial or final states and the usual combinatoric factors for example for gluon loops. Finally, to obtain the same normalisation as with the Feynman perturbation theory, there is an overall factor of $-i$ which should be associated with each graph.

2.5 Running of α_S

The coupling used in the perturbation theory in the two previous sections appears to be just a constant. However when one introduces higher order corrections to a given process, the procedure of renormalisation (see for example [29]) introduces an arbitrary scale μ into any given physical observable. Taking a dimensionless physical observable R, involving only one scale Q^2, then the fact that it should have no dependence on μ can be expressed as

$$\mu^2 \frac{\mathrm{d}}{\mathrm{d}\mu^2} R(Q^2/\mu^2, \alpha_\mathrm{S}) = \left[\mu^2 \frac{\partial}{\partial \mu^2} + \mu^2 \frac{\partial \alpha_\mathrm{S}}{\partial \mu^2} \frac{\partial}{\partial \alpha_\mathrm{S}}\right] R = 0. \tag{2.41}$$

Defining

$$t = \ln\left(\frac{Q^2}{\mu^2}\right) \qquad \beta(\alpha_\mathrm{S}) = \mu^2 \frac{\partial \alpha_\mathrm{S}}{\partial \mu^2}, \tag{2.42}$$

this can be rewritten as

$$\left[-\frac{\partial}{\partial t} + \beta(\alpha_\mathrm{S}) \frac{\partial}{\partial \alpha_\mathrm{S}}\right] R(e^t, \alpha_\mathrm{S}) = 0. \tag{2.43}$$

One can introduce an effective running coupling $\bar{\alpha}_\mathrm{S}$, as the solution of

$$\frac{\mathrm{d}\bar{\alpha}_\mathrm{S}(t, \alpha_\mathrm{S})}{\mathrm{d}t} = \beta \bar{\alpha}_\mathrm{S}, \tag{2.44}$$

with $\bar{\alpha}_\mathrm{S}(t = 0, \alpha_\mathrm{S}) = \alpha_\mathrm{S}$. Rewriting this as

$$t = \int_{\alpha_\mathrm{S}}^{\bar{\alpha}_\mathrm{S}(t,\alpha_\mathrm{S})} \frac{\mathrm{d}x}{\beta(x)} \tag{2.45}$$

and differentiating both sides with respect to α_S, one can see that

$$0 = \frac{1}{\beta(\bar{\alpha}_\mathrm{S})} \frac{\mathrm{d}\bar{\alpha}_\mathrm{S}}{\mathrm{d}\alpha_\mathrm{S}} - \frac{1}{\beta(\alpha_\mathrm{S})}, \tag{2.46}$$

or

$$\left[\frac{\partial}{\partial t} - \beta(\alpha_\mathrm{S}) \frac{\partial}{\partial \alpha_\mathrm{S}}\right] \bar{\alpha}_\mathrm{S}(t, \alpha_\mathrm{S}) = 0. \tag{2.47}$$

Therefore any function $R[1, \bar{\alpha}_\mathrm{S}(t, \alpha_\mathrm{S})]$ will be a solution of eq. (2.43): the scale dependence of R can be understood as entering through the running of an effective coupling, which from now will simply be denoted $\alpha_\mathrm{S}(Q^2) = \bar{\alpha}_\mathrm{S}(t, \alpha_\mathrm{S})$.

To understand how α_S runs, it is necessary to solve eq. (2.47) which requires a knowledge of β. The kinds of graphs which need to be computed to evaluate β are shown in figure 2.4, giving [37–40]

$$\beta(\alpha_\mathrm{S}) = -b\alpha_\mathrm{S}^2, \quad b = \frac{(11C_\mathrm{A} - 4n_f T_\mathrm{R})}{12\pi}, \tag{2.48}$$

where n_f is the number of light flavours and higher order contributions [41–43] have been neglected. Solving eq. (2.44) gives

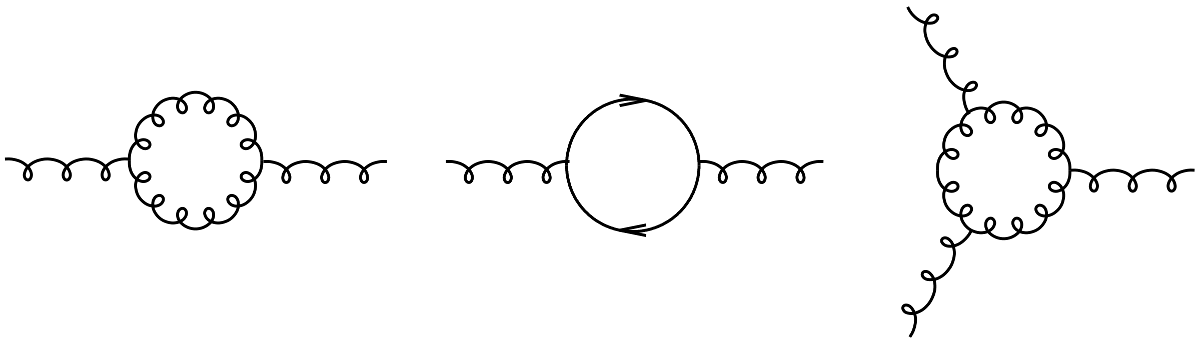

Figure 2.4: Some of the graphs which contribute to the 1-loop β-function.

$$\alpha_S(Q^2) = \frac{\alpha_S(\mu^2)}{1 + \alpha_S(\mu^2)bt}, \quad t = \ln\frac{Q^2}{\mu^2}. \tag{2.49}$$

This shows that as Q^2 increases to infinity, $\alpha_S(Q^2)$ decreases towards zero. This is a consequence of the negative β-function, and is known as the property of asymptotic freedom, namely that the theory approaches a free theory at large scales. The converse point is that as Q^2 is lowered the running coupling gets large and one can no longer apply perturbation theory (and the above perturbative equations break down). One can rewrite eq. (2.49) as

$$\alpha_S(Q^2) = \frac{1}{b\ln(Q^2/\Lambda^2)}, \tag{2.50}$$

so that instead of defining the coupling constant by its value for one particular value of Q^2, one defines it by a scale Λ at which it would diverge (if one extrapolates the running outside the perturbative region). The value of α_S is often quoted in terms of Λ, though care should be taken when defining it, for example because its relation to α_S depends on the number of flavours that one takes as "light". To be safely in the perturbative region one must have $Q^2 \gg \Lambda^2$.

2.6 Large N_C limit

The large N_C limit was introduced by 't Hooft [44] as an approximation to help understand the strong interaction. The idea is to consider the limit $N_C \to \infty$ with $\alpha_S N_C$ held fixed: the small parameter in the problem then becomes $1/N_C$. In this limit, 't Hooft found that a considerable simplification occurs in the set of graphs which contribute: one is left only with planar graphs. One might argue that $N_C = 3$ is hardly large enough. However the expansion will often turn out actually to be in $1/N_C^2$, which is already "respectably small". Further, as Witten pointed out in [45], if one examines the value of e in QED, with $e^2/4\pi \simeq 1/137$, one finds $e \simeq 0.302$, not much smaller than $1/N_C$.

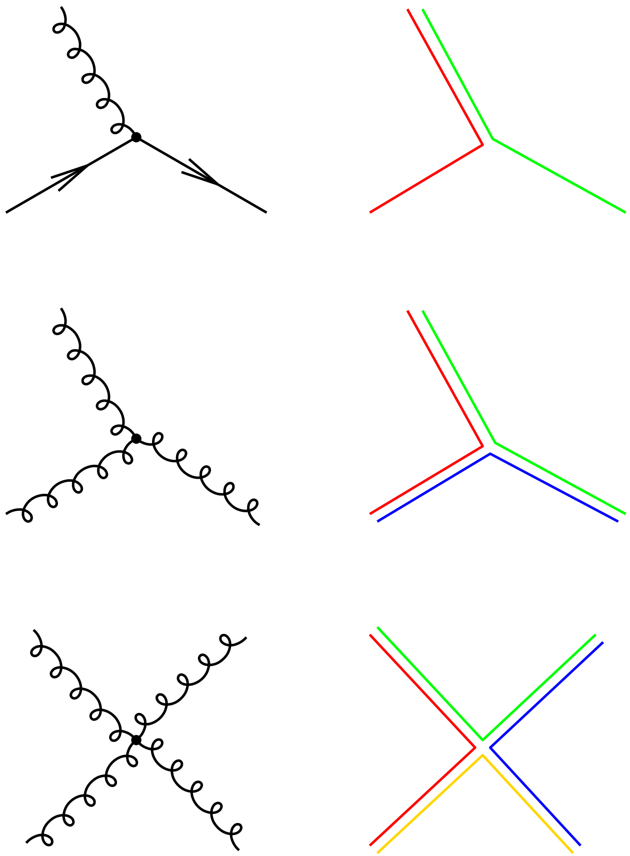

Figure 2.5: Representation of the colour flow of the various QCD vertices in the limit of large N_{C}.

The basis of the expansion is that when calculating the leading power of N_{C} in a given diagram, one can consider the colour structure of a gluon to be analogous to that of a quark and antiquark:

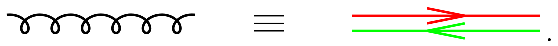

This is equivalent to saying that where the gluon field is represented by $(t^A A^A)_{ab}$, one has the component a for the quark part and the component b for the antiquark part. The effect of this on the vertices is shown in figure 2.5. To understand their structure, take for example the three gluon vertex, where one is dealing with terms such as $\mathrm{Tr} A_\mu A_\nu \partial_\mu A_\nu$: writing this with the colour indices explicit, one gets $(A_\mu)_{ab}(A_\nu)_{bc}\partial_\mu(A_\nu)_{ca}$, which has the structure shown in figure 2.5.

Having established this representation of the colour flow, one can can examine the leading-$1/N_{\mathrm{C}}$ behaviour of various diagrams. Take the graphs of figure 2.6, where overall the incoming quark-antiquark state is colour neutral, and where one averages over the colour of the quark. For diagram (a), with one colour loop, and a factor of $1/N_{\mathrm{C}}$ for the average over colours, one has a coefficient of order 1. Diagram (b) illustrates the addition of a single gluon: there is an

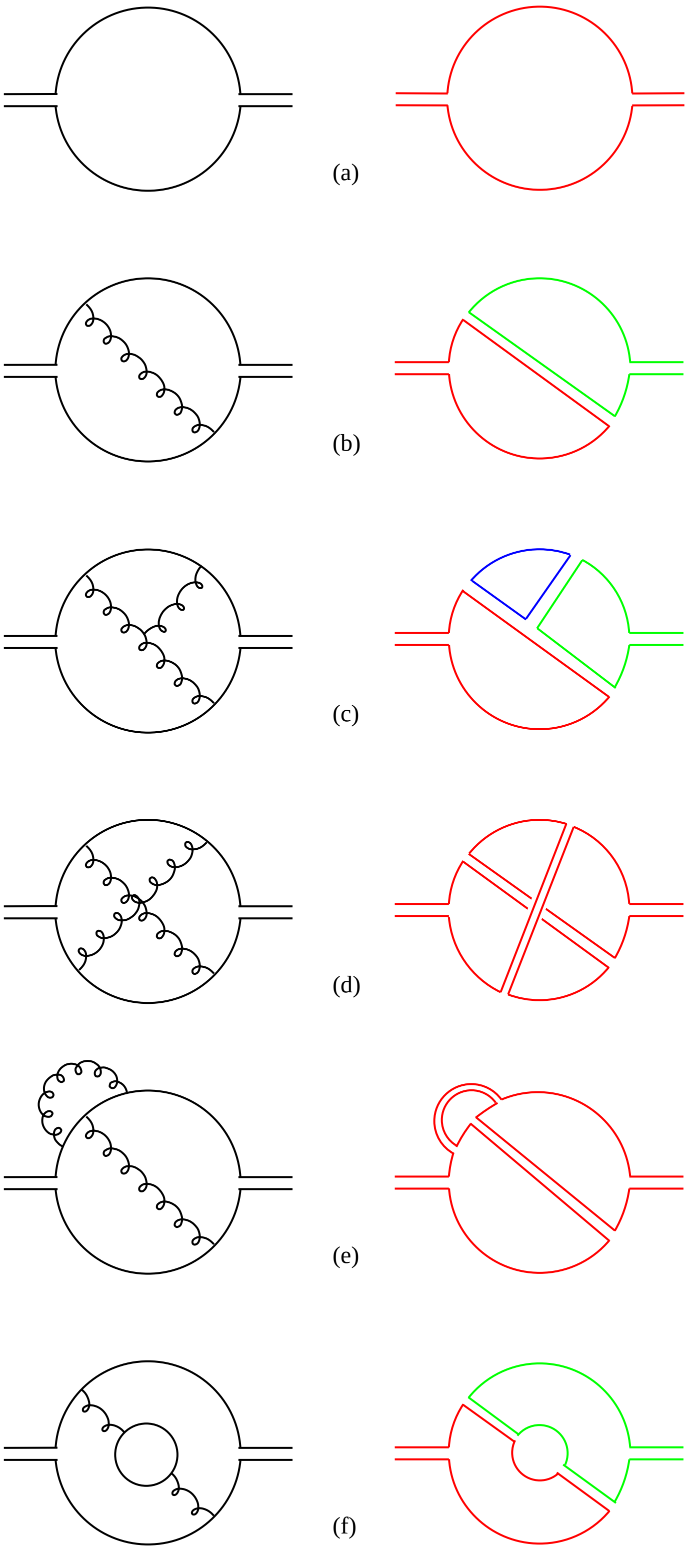

Figure 2.6: Various example graphs in the large-N_C limit (those on the right represent the colour flow).

additional colour loop, together with a factor of g_S^2, giving an overall factor for this diagram of $g_S^2 N_C$; (c) has three colour loops and four couplings, which gives $(g_S^2 N_C)^2$ — so far each factor of N_C is associated with a factor of g_S^2. Graph (d) on the other hand has only one colour loop, but still four couplings, so its contribution is $(g_S^2 N_C)^2/N_C^2$. When $g_S^2 N_C \sim 1$, it is suppressed by a factor N_C^2 relative to (a), (b) and (c). The difference between them is that (a), (b) and (c) are all planar, whereas (d) is non-planar and it can be shown that all non-planar graphs are suppressed by factors $1/N_C^2$ (to some integer power which depends on the degree of non-planarity) relative to planar ones. Graph (e) at first sight looks planar, but the presence of a gluon line on the "outside" of the diagram means that effectively it isn't, so that like (d), it will be suppressed by $1/N_C^2$. Finally quark loops also have an effect on the colour structure: figure (f) which has an internal quark loop has an overall factor of $n_f(g_S^2 N_C)^2/N_C$ associated with it, a suppression of n_f/N_C, which seems to be quite a weak suppression. On the other hand, in the running of α_S for example, quark loops do only make a small contribution. So the effect of quark loops is slightly unclear.

Summarising these results therefore, to examine the colour structure of a graph, one simply draws gluon lines as consisting of a quark and antiquark. The leading-$1/N_C$ graphs are those which are planar, where the outer lines of the graph are quarks and (to a lesser extent perhaps) where there are no internal quark loops.

2.7 The *S*-matrix and unitarity

All the information (calculated for example with the rules given above) on the scattering of particles can be encoded in an object called the S-matrix. This has certain general properties which are useful for checking that the calculations that one has performed are correct. For full details, the reader is referred to one of the standard textbooks, such as [29].

Starting with an initial state $|i\rangle$ (which will in general consist of several particles), for time $t \to -\infty$, normalised to be

$$\langle i|i\rangle = 1, \tag{2.51}$$

the evolution of that state to one at time $t \to +\infty$, $|t\rangle$ is given by

$$\lim_{t\to+\infty} |t\rangle = S|i\rangle. \tag{2.52}$$

Accordingly, the probability of producing a final state $|f\rangle$ as $t \to +\infty$, is given by

$$|\langle f|S|i\rangle|^2. \tag{2.53}$$

The probability of finding any of the possible final states must be equal to one, so

$$\begin{aligned}\sum_f |\langle f|S|i\rangle|^2 &= \sum_f \langle i|S^\dagger|f\rangle\langle f|S|i\rangle \\ &= \langle i|S^\dagger S|i\rangle \\ &= 1.\end{aligned} \tag{2.54}$$

Since this relation must be true for any normalised state $|i\rangle$, we have the condition that S must be a unitary matrix:

$$S^\dagger S = 1. \tag{2.55}$$

In general it is useful to write the S-matrix as a sum of two parts: the identity (which expresses the possibility of the particles in the initial state not interacting) and a part T which encodes the interaction:

$$S = I + iT. \tag{2.56}$$

The requirement of unitarity for S, leads to the following condition on T

$$(T - T^\dagger) = iT^\dagger T. \tag{2.57}$$

Including momentum conservation, one can define $\mathcal{T}_{fi}$

$$\langle f|T|i\rangle = (2\pi)^4\delta^4(P_f - P_i)\mathcal{T}_{fi}, \tag{2.58}$$

and one obtains the following relation

$$(\mathcal{T}_{fi} - \mathcal{T}^*_{if}) = i\sum_n (2\pi)^4\delta^4(P_n - P_i)\mathcal{T}^*_{nf}\mathcal{T}_{ni}, \tag{2.59}$$

where the sum has been introduced over all possible intermediate states $|n\rangle$ (the sum being understood to include integrations over the momenta of the final state particles). The perturbation rules given earlier calculate the quantity $i\mathcal{T}_{fi}$. It is useful to concentrate on two-body forward elastic scattering, choosing $|f\rangle = |i\rangle$, so that on the right hand side of eq. (2.59) one has the square of a matrix-element. Normalisation aside, the right hand side of eq. (2.59) corresponds to the total cross section, while the left hand side is proportional to the imaginary part of the forward elastic amplitude. Including the normalisations one obtains

$$\mathrm{Im}\,\mathcal{T}_{ii} = \lambda^{1/2}(s, m_a^2, m_b^2)\sigma_{\mathrm{tot}}(i), \tag{2.60}$$

where the factor $\lambda(s, m_a^2, m_b^2)$, relating to the scattering of two particles of masses m_a and m_b, with a centre-of-mass energy $\sqrt{s}$, is defined by

$$\lambda(x, y, z) = (x^2 + y^2 + z^2 - 2xy - 2xz - 2yz), \tag{2.61}$$

as can be found in any of the standard textbooks. Eq. (2.60) is known as the optical theorem. It places a self-consistency condition on the elastic scattering amplitude, since (to within normalisation factors) it constrains the imaginary part of the forward amplitude to be larger than the square of the amplitude integrated over momentum transfers (in other words, the total cross section must be larger than the elastic cross section).

If one examines non-forward elastic scattering, the constraints imposed by the unitarity of the S-matrix are much harder to interpret, because on the right-hand side of eq. (2.59), $|f\rangle \neq |i\rangle$ and one no longer has a squared matrix element. The solution is to find a basis in which the S-matrix is diagonal for elastic scattering. For high-energy scattering, when the squared momentum transfer $t \ll s$, it turns out that the appropriate basis is that of transverse position (also known as impact parameter), because transverse position becomes a conserved quantity during the course of the scattering [46–48], a consequence of the invariance of the S-matrix under rotations and Lorentz boosts. As a result it is possible to derive a condition on the amplitude which holds for every relative impact parameter of the colliding particles. The presentation of this which will be given here is a summary of that developed by Webber [48], to which the reader is referred for the full details.

We will use a state $|\mathbf{k}, p\rangle$ for a particle with longitudinal momentum p and transverse momentum $\mathbf{k}$ with normalisation

$$\langle \mathbf{k}' p' | \mathbf{k} p \rangle = (2\pi)^3 2E\delta^2(\mathbf{k} - \mathbf{k}')\delta(p - p'), \tag{2.62}$$

where $E = \sqrt{p^2 + |\mathbf{k}|^2}$. Working in the high-energy limit, $p \gg k$, the fourier transformed state is $|\mathbf{b}, p\rangle$,

$$|\mathbf{b}, p\rangle = \int \frac{\mathrm{d}^2\mathbf{k}}{(2\pi)^2} \mathrm{e}^{i\mathbf{k}.\mathbf{b}} |\mathbf{k}, p\rangle. \tag{2.63}$$

The normalisation condition becomes:

$$\langle \mathbf{b}' p' | \mathbf{b} p \rangle = (2\pi) 2E\delta^2(\mathbf{b} - \mathbf{b}')\delta(p - p'). \tag{2.64}$$

Note that if we hadn't used the high-energy limit, then the variation of E in the integral of eq. (2.63) would smear out the delta functions of eq. (2.64). The fourier transform of the elastic scattering amplitude $k_a, k_b \to k_1, k_2$ is calculated as follows

$$\langle \mathbf{b}_1 p_1 \mathbf{b}_2 p_2 | T | \mathbf{b}_a p_a \mathbf{b}_b p_b \rangle = \int \frac{\mathrm{d}^2\mathbf{k}_a}{(2\pi)^2}\frac{\mathrm{d}^2\mathbf{k}_b}{(2\pi)^2}\frac{\mathrm{d}^2\mathbf{k}_1}{(2\pi)^2}\frac{\mathrm{d}^2\mathbf{k}_2}{(2\pi)^2} \times \mathrm{e}^{i(\mathbf{k}_a.\mathbf{b}_a+\mathbf{k}_b.\mathbf{b}_b-\mathbf{k}_1.\mathbf{b}_1-\mathbf{k}_2.\mathbf{b}_2)}\langle \mathbf{k}_1 p_1 \mathbf{k}_2 p_2 | T | \mathbf{k}_a p_a \mathbf{k}_b p_b \rangle, \tag{2.65}$$

where in analogy with eq. (2.58), it is convenient to write

$$\langle \mathbf{k}_1 p_1 \mathbf{k}_2 p_2 | T | \mathbf{k}_a p_a \mathbf{k}_b p_b \rangle = \mathcal{T}_{22}(\mathbf{k}_a p_a \mathbf{k}_b p_b \mathbf{k}_1 p_1 \mathbf{k}_2 p_2) \times (2\pi)^4 \delta^2(\mathbf{k}_a + \mathbf{k}_b - \mathbf{k}_1 - \mathbf{k}_2)\delta(p_a + p_b - p_1 - p_2)\delta(E_a + E_b - E_1 - E_2). \tag{2.66}$$

The subscript 22 on $\mathcal{T}_{22}$ indicates it the amplitude for a $2 \to 2$ process. When performing the fourier transform above one exploits the invariance of $\mathcal{T}$ under Lorentz boosts and rotations. In the centre-of-mass frame, where $p_a = -p_b$ are large compared to the transverse momenta, a Lorentz boost with the (small) velocity

$$\mathbf{v} = \frac{\mathbf{k}_a + \mathbf{k}_b}{E_a + E_b} \tag{2.67}$$

has the effect of transforming

$$\mathbf{k}_i \to \mathbf{k}_i - \mathbf{v}E_i = \mathbf{k}_i - \frac{E_i}{2E_a}(\mathbf{k}_a + \mathbf{k}_b), \tag{2.68}$$

while an appropriate small rotation gives

$$\mathbf{k}_i \to \mathbf{k}_i - \frac{p_i}{2p_a}(\mathbf{k}_a - \mathbf{k}_b). \tag{2.69}$$

Since the velocity and angle are small the longitudinal components of the momentum are essentially unchanged. Combined together, these two transformations have the effect of taking $\mathbf{k}_i$ to $\mathbf{k}_i{}'$ where

$$\mathbf{k}_i{}' = \mathbf{k}_i - \frac{1}{2}\left(\frac{E_i}{E_a} + \frac{p_i}{p_a}\right)\mathbf{k}_a - \frac{1}{2}\left(\frac{E_i}{E_a} - \frac{p_i}{p_a}\right)\mathbf{k}_b. \tag{2.70}$$

In particular,

$$\mathbf{k}'_a = 0, \tag{2.71}$$

$$\mathbf{k}'_b = 0, \tag{2.72}$$

$$\mathbf{k}'_1 = \mathbf{k}_1 - \mathbf{k}_a, \tag{2.73}$$

$$\mathbf{k}'_2 = \mathbf{k}_2 - \mathbf{k}_b. \tag{2.74}$$

Exploiting the invariance of the transition matrix under these transformations, one obtains

$$
\begin{aligned}
\langle \mathbf{b}_1 p_1 \mathbf{b}_2 p_2 | T | \mathbf{b}_a p_a \mathbf{b}_b p_b \rangle &= (2\pi)^2 \delta(p_1 + p_2) \delta(E_a + E_b - E_1 - E_2) \\
&\quad \times \int \frac{\mathrm{d}^2 \mathbf{k}_a}{(2\pi)^2} \frac{\mathrm{d}^2 \mathbf{k}_b}{(2\pi)^2} \frac{\mathrm{d}^2 \mathbf{k}_1'}{(2\pi)^2} \frac{\mathrm{d}^2 \mathbf{k}_2'}{(2\pi)^2} \mathrm{e}^{+i(\mathbf{k}_a.(\mathbf{b}_a - \mathbf{b}_1) + \mathbf{k}_b.(\mathbf{b}_b - \mathbf{b}_2)) - i(\mathbf{k}_1'.\mathbf{b}_1 + \mathbf{k}_2'.\mathbf{b}_2)} \\
&\qquad \times \mathcal{T}_{22}(\mathbf{0} p_a \mathbf{0} p_b, \mathbf{k}_1' p_1 \mathbf{k}_2' p_2) (2\pi)^2 \delta^2(\mathbf{k}_1' + \mathbf{k}_2') \\
&= (2\pi)^2 \delta(p_1 + p_2) \delta(E_a + E_b - E_1 - E_2) \delta^2(\mathbf{b}_a - \mathbf{b}_1) \delta^2(\mathbf{b}_b - \mathbf{b}_2) \widetilde{\mathcal{T}}_{22}(p_a, \mathbf{b}_1 p_1 \mathbf{b}_2 p_2),
\end{aligned} \tag{2.75}
$$

where

$$
\widetilde{\mathcal{T}}_{22}(p_a, \mathbf{b}_1 p_1 \mathbf{b}_2 p_2) = \int \frac{\mathrm{d}^2 \mathbf{k}_1}{(2\pi)^2} \frac{\mathrm{d}^2 \mathbf{k}_2}{(2\pi)^2} \mathrm{e}^{-i(\mathbf{k}_1.\mathbf{b}_1 + \mathbf{k}_2.\mathbf{b}_2)} \mathcal{T}_{22}(\mathbf{0} p_a \mathbf{0} - p_a, \mathbf{k}_1 p_1 \mathbf{k}_2 p_2) (2\pi)^2 \delta^2(\mathbf{k}_1 + \mathbf{k}_2). \tag{2.76}
$$

The main result from this is the pair of delta functions which indicate that impact parameter is conserved separately for the left and right-moving particles. In a more general case, where one produces many particles in the final state, $i = 1 \ldots n$ then one obtains the conservation law

$$
\mathbf{b}_a = \sum_{z_i > 0} z_i \mathbf{b}_i \tag{2.77}
$$

for the right movers, where $z_i = p_i / p_a$, with a similar law for the left-movers. This can be interpreted as a form of angular momentum conservation which holds separately for the left and right movers.

The expressions above look fairly complex, partly because they have been written in a form which allows straightforward extension to the case of many particle production. For the case of elastic scattering they can be rewritten fairly simply as

$$
\widetilde{\mathcal{T}}_{22}(s, \mathbf{r}) = \int \frac{\mathrm{d}^2 \mathbf{q}}{(2\pi)^2} \mathrm{e}^{-i\mathbf{q}.\mathbf{r}} \mathcal{T}_{22}(s, \mathbf{q}), \tag{2.78}
$$

where $\sqrt{s}$ is the centre-of-mass energy, $\mathbf{r} = \mathbf{b}_b - \mathbf{b}_a$ is the separation between the colliding particles and the momentum transfer $\mathbf{q}$ is from a to b.

It is now possible to write an impact parameter form for the unitarity equation, eq. (2.57):

$$
\begin{aligned}
\mathrm{Im}\, \widetilde{\mathcal{T}}_{22}(s, \mathbf{r}) &= \frac{1}{2} \sum_n \int \prod_{i=1}^{n} \frac{\mathrm{d}^2 \mathbf{b}_i \mathrm{d} p_i}{4\pi E_i} |\widetilde{\mathcal{T}}_{2n}(s, \mathbf{b}_1 p_1 \ldots \mathbf{b}_n p_n)|^2 \\
&\quad \times (2\pi)^2 \delta\left(\sum p_i\right) \delta\left(\sqrt{s} - \sum E_i\right) \delta^2\left(\mathbf{b}_a - \sum_{z_i > 0} |z_i| \mathbf{b}_i\right) \delta^2\left(\mathbf{b}_b - \sum_{z_i < 0} |z_i| \mathbf{b}_i\right).
\end{aligned} \tag{2.79}
$$

This is the impact parameter unitarity equation. The transition matrix for $2 \to n$ is defined in analogy with the $2 \to 2$ matrix. If the particles labelled i are identical then one should include a $1/n!$ factor for combinatoric purposes. It should be noted that the details of the δ-functions and integrations on the right hand side of eq. (2.79) are not essential: the important aspects are that one obtains the square of the matrix element and that one sums over all allowable intermediate states. To study the implications of eq. (2.79), one can write

$$A(s,\mathbf{r}) = \frac{1}{2s}\widetilde{\mathcal{T}}_{22}(s,\mathbf{r}), \quad F(s,\mathbf{r}) = \mathrm{Im}\, A. \tag{2.80}$$

Using

$$\mathcal{T}_{22}(s,t=0) = \int \mathrm{d}^2\mathbf{r}\widetilde{\mathcal{T}}_{22}(s,\mathbf{r}) \tag{2.81}$$

in conjunction with eq. (2.60), it is then clear that

$$\sigma_{\mathrm{tot}}(s) = \int \mathrm{d}^2\mathbf{r}\, 2F(s,\mathbf{r}). \tag{2.82}$$

The elastic cross section is obtained from

$$\sigma_{\mathrm{el}} = \int \mathrm{d}^2\mathbf{r}\, |A^2|. \tag{2.83}$$

Therefore we can identify $2F(\mathbf{r})$ with a "differential total cross section" in impact parameter, and $|A^2|$ with a "differential elastic cross section" in impact parameter:

$$\frac{\mathrm{d}^2\sigma_{\mathrm{tot}}}{\mathrm{d}^2\mathbf{r}} = 2F, \quad \frac{\mathrm{d}^2\sigma_{\mathrm{el}}}{\mathrm{d}^2\mathbf{r}} = |A^2|. \tag{2.84}$$

This is the impact parameter equivalent of the optical theorem, and it allows one to write the following constraint on the impact parameter amplitudes:

$$2F(\mathbf{r}) = F^2(\mathbf{r}) + \frac{\mathrm{d}^2\sigma_{\mathrm{inel}}}{\mathrm{d}^2\mathbf{r}}, \tag{2.85}$$

where A has been taken as purely imaginary. This will be seen to be justified in subsequent chapters, and is in any case thought to be true to a good approximation for high-energy scattering [48]. The inelastic part, coming from the $n \geq 3$ contributions on the right hand side of eq. (2.79), is positive definite. Therefore eq. (2.85) forces the amplitude to satisfy $F(\mathbf{r}) \leq 2$. A further expectation in the high-energy case, is that the amplitude will be driven by the inelastic contribution, i.e. $F(\mathbf{r}) \to 0$ as $\mathrm{d}^2\sigma_{\mathrm{inel}}/\mathrm{d}^2\mathbf{r} \to 0$. One can accordingly write

$$F(\mathbf{r}) = 1 - \sqrt{1 - \frac{\mathrm{d}^2\sigma_{\mathrm{inel}}}{\mathrm{d}^2\mathbf{r}}}, \tag{2.86}$$

from which one has

$$F(\mathbf{r}) \leq 1. \tag{2.87}$$

In an optical analogy, the $F = 1$ limit corresponds to complete absorption, or equivalently scattering from a black object.

CHAPTER 3

A review of small-x physics

The purpose of this chapter is to briefly review the current knowledge about elastic amplitudes (or equivalently total cross sections) for high-energy hadronic collisions.

In such processes, it is generally convenient to consider the longitudinal and transverse directions separately. Qualitatively this can be understood as being a consequence of the relativistic compression of the fast moving hadrons in the longitudinal direction. The scale which determines the relevant value of α_{S} for the hadron will be the transverse scale, i.e. the size of the hadron. Accordingly, one can classify hadronic collisions according to whether both, one or neither of the hadronic scales is non-perturbative.

When both scales are soft one has little hope of using perturbative QCD and the only tool available for understanding the total cross section is Regge theory [1] which will be discussed in section 3.1. When one scale is soft and the other sufficiently hard (also when the ratio of the two scales is large), then one can establish some non-perturbative starting conditions, which are dependent only on the properties of the soft object and then calculate perturbatively the dependence of the cross section on the properties of the hard object. This is the basis of Dokshitzer, Gribov, Lipatov, Altarelli, Parisi (DGLAP) evolution [49–51], which will be discussed in section 3.2. Finally, there is the situation where both scales are hard and of the same order as each other, in which case the total cross section should be calculable entirely perturbatively. This limit, which was first studied by Balitsky, Fadin, Kuraev and Lipatov (BFKL) [3–5], is the main subject of this dissertation and will be considered in section 3.3.

Experimentally, there are two main processes which are used to study (and search for) the above regimes. For subsequent reference, they are briefly introduced here. Proton-(anti)proton scattering provides two soft scales, of the order of the proton mass, m_p. The variables which are of relevance are (see figure 3.1)

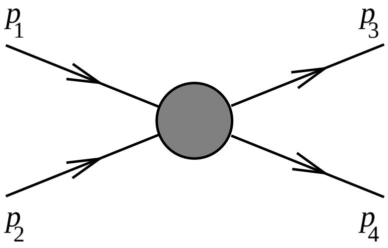

Figure 3.1: Labelling of the momenta for proton-(anti)proton elastic scattering

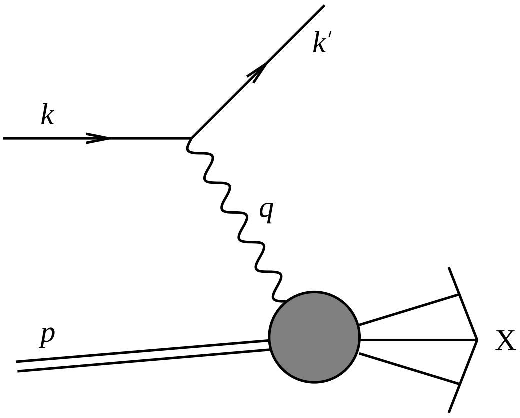

Figure 3.2: Labelling of the momenta for electron-proton elastic scattering (the double line corresponds to the proton).

$$s = (p_1 + p_2)^2, \tag{3.1}$$

$$t = (p_3 - p_1)^2, \tag{3.2}$$

$$u = (p_3 - p_2)^2. \tag{3.3}$$

The centre-of-mass energy is therefore $\sqrt{s}$ while the square of the exchanged four-momentum is t (or u for the crossed scattering). It will also be useful to define the rapidity, $Y = \ln(s/m_p^2)$. The optical theorem allows one to relate the forward ($t = 0$) elastic scattering amplitude to the total cross section (where the only variable is s).

The second process of interest is electron-proton scattering (figure 3.2), where the interaction between the electron and the proton is mediated by the photon. The variables which are commonly defined are

$$
\begin{aligned}
q &= k - k', & (3.4)\\
Q^2 &= -q^2, & (3.5)\\
m_p^2 &= p^2, & (3.6)\\
x &= \frac{Q^2}{2p.q}, & (3.7)\\
W^2 &= (q+p)^2 = M_X^2, & (3.8)\\
\zeta &= \frac{p.q}{p.k}. & (3.9)
\end{aligned}
$$

W is the centre-of-mass energy of the photon-proton system; ζ is the fractional energy transfer in the proton rest frame (it is normally referred to as y, but ζ was chosen here, in view of the use of y for rapidity).

In the limit of the photon being on-shell, $Q^2 = 0$, one has photo-production. If one considers the photon as behaving hadronically (which will later be seen to be justified), this process can be understood as involving two soft hadronic scales, similar to pp scattering. When the virtuality of the photon is high, $Q^2 \gg m_p^2$ then this is referred to as deep inelastic scattering (DIS). The photon effectively provides a hard hadronic scale, while the proton provides once again a soft scale. In the parton model, x (only relevant to DIS) is the fraction of the proton's light-cone momentum carried by the struck parton. When $W^2 \gg Q^2$, we have $1/x \simeq W^2/Q^2$, so that small values of x are equivalent to large centre-of-mass energies.

3.1 Regge theory

Regge theory [1] is a formalism which was developed to describe exchanges of families of particles, as in figure 3.3. This section will give a brief summary of some important results. In the channel where t is the centre-of-mass energy (i.e. $1 + \bar{3} \to \bar{2} + 4$), writing the amplitude as a function of the orbital angular momentum ℓ and the centre-of-mass energy, one expects poles where an intermediate particle with the appropriate angular momentum is on shell. For a family of particles, for example the ρ and its spin 3 (ρ_3) and spin 5 (ρ_5) excitations, one can

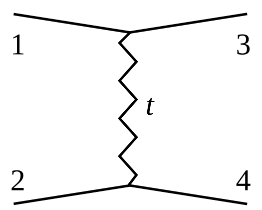

Figure 3.3: Scattering of $1 + 2 \to 3 + 4$ via the t-channel exchange of a family of particles (denoted by the "spring").

define a trajectory $\alpha(t)$ (the spin associated with squared energy t) such that

$$\alpha(m_\rho^2) = 1, \quad \alpha(m_{\rho_3}^2) = 3, \quad \alpha(m_{\rho_5}^2) = 5. \tag{3.10}$$

The partial-wave amplitude, $\mathcal{T}_\ell(t)$, defined such that

$$\mathcal{T}(s,t) = \sum_{\ell=0}^{\infty}(2\ell+1)\mathcal{T}_\ell(t)P_\ell\left(z_t = \cos\theta_t = 1 + \frac{2s}{t-4m^2}\right), \tag{3.11}$$

where m is the mass of the particles being scattered (a more complicated expression arises where the 4 particles have different masses) and the P_ℓ are Legendre polynomials of the first kind, will then have a pole in the complex ℓ-plane:

$$\mathcal{T}_\ell(t) \sim \frac{1}{\ell - \alpha(t)}. \tag{3.12}$$

By expressing the sum over partial waves, eq. (3.11), as an integral transform, continuing to the region where $\sqrt{s} = (p_1+p_2)^2$ is now the centre-of-mass energy, and using the approximation $P_\ell(z_t) \sim z_t^\ell$, one finds that that the high-energy behaviour of the amplitude should be

$$\mathcal{T}(s,t) \sim s^{\alpha(t)}, \tag{3.13}$$

and therefore that the total cross section satisfies

$$\sigma_{\text{tot}} \sim s^{\alpha(0)-1}. \tag{3.14}$$

For ρ, ω, f_2, a_2, ..., from figure 3.4, there should therefore be a contribution to the total cross section which behaves roughly as $s^{-0.5}$. Experimentally, the total cross section is found to rise slowly at large energies (figure 3.5). One simple way of accounting for this is by arguing that there is a second trajectory [53], the pomeron trajectory (named after Pomeranchuk, who predicted that high-energy cross sections should tend to a fixed limit [2]), which corresponds to a pole in the complex angular momentum plane which would give a cross section only weakly dependent on s, i.e. $\alpha_{\rm P} = 1 + \epsilon_0$, where ϵ_0 is small and positive.

Accordingly, Donnachie and Landshoff [54] have performed fits to total cross section data, of the form

$$\sigma_{\text{tot}} = As^{(\alpha_{\rm R}(0)-1)} + Bs^{(\alpha_{\rm P}(0)-1)}, \tag{3.15}$$

where they obtain $\alpha_{\rm R}(0) = 0.5475$ and $\alpha_{\rm P}(0) = 1.0808$. The match with the $\bar{p}p$ data is shown in the left hand plot of figure 3.5, and is good over the whole range of energies. The same powers

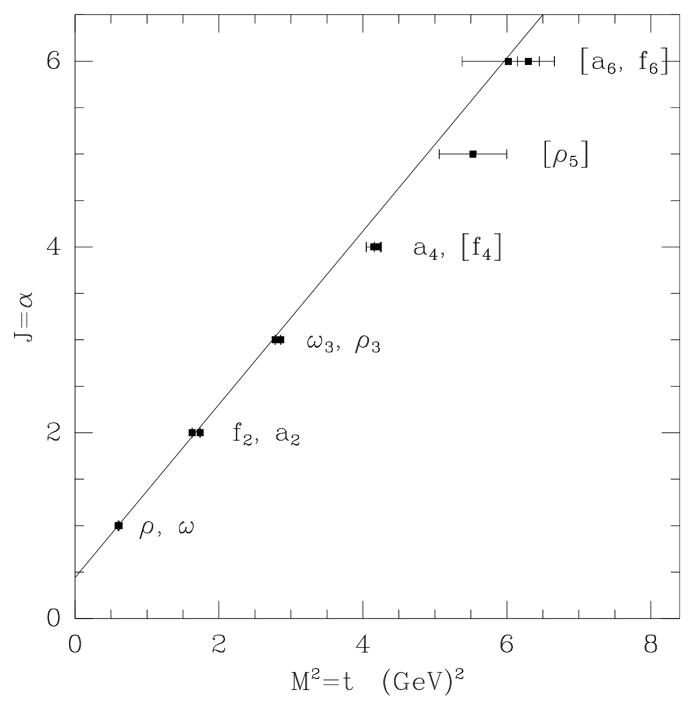

Figure 3.4: Trajectories for the ρ, ω, f and a. Figure taken from [52].

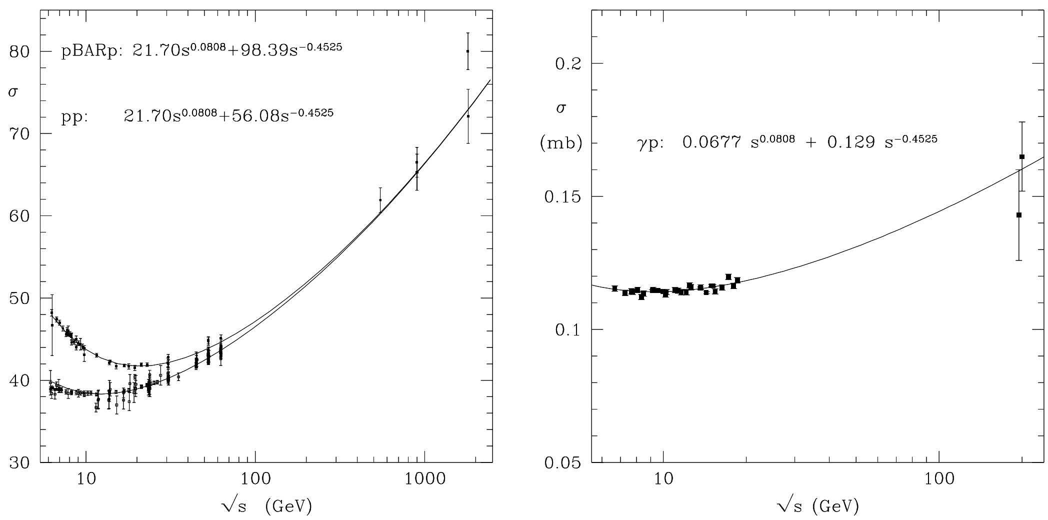

Figure 3.5: Total cross sections with power fits as in eq. (3.15), using values from [54]. Figure taken from [52].

(with different coefficients) can be used to to fit a wide variety of processes, such as πp or γp, providing evidence for the universality of the exchanged objects. The γp results are shown in the right-hand plot of figure 3.5. The highest energy points had not been measured when the fits were originally made, illustrating the predictive power of the fits.

In addition to results for total cross sections, a successful phenomenology based on the soft pomeron has been developed by Donnachie and Landshoff [55] for elastic scattering, which gives a linear trajectory

$$\alpha_{\mathrm{P}}(t) = 1 + \epsilon_0 + 0.25t. \tag{3.16}$$

The "pomeron" discussed so far is found to be involved in purely soft reactions. It is therefore often referred to as the "soft pomeron". While it gives a good description of soft data, there is only limited understanding of its behaviour from the point of view of QCD: a model of Landshoff and Nachtmann [56] reproduces many of its qualitative features, but not the weak power dependence of the cross section on s. Attempts to understand the pomeron (defined as the object which governs the high-energy behaviour of hadron-hadron scattering) from perturbative QCD are only well defined if the both hadrons are of a scale where perturbation theory applies; this leads to a different behaviour, as will be seen in section 3.3.

3.2 DGLAP evolution

In deep inelastic scattering (shown in figure 3.2), where there is one hard scale and one soft one, the cross section can be written as

$$\frac{\mathrm{d}^2\sigma}{\mathrm{d}x\mathrm{d}Q^2} = \frac{4\pi\alpha_{\mathrm{em}}^2}{xQ^4}\left\{\frac{1}{2}\zeta^2(2xF_1 - F_2) + \frac{1}{2}\left[1 + (1-\zeta)^2\right]F_2\right\}, \tag{3.17}$$

where $F_1(x,Q^2)$ and $F_2(x,Q^2)$ are the structure functions of the proton. In the parton model, one finds

$$F_2 = 2xF_1 = \sum_q e_q^2 x f_q(x), \tag{3.18}$$

with $f_q(x)$ being the probability of finding a quark of type q with momentum fraction x inside the proton. The absence of any Q^2 dependence in F_i is the property of Bjorken scaling characteristic of point particles.

QCD corrections cause the simple parton picture to break down. Qualitatively this is because as one increases Q^2, one is probing the partons at higher resolution, where for example a quark might be resolved as consisting of a quark and a gluon. The parton distributions at some initial Q^2 can be viewed as non-perturbative characteristics of the proton. Perturbative QCD allows one to predict the manner in which the parton distributions vary as one increases the virtuality of the probe.

Formally, any measurable quantity associated with a virtuality Q^2 can be written as a function of the parton distributions at that virtuality. For example F_2 can be written as

$$\frac{F_2(x,Q^2)}{x} = \sum_{i=q,\bar{q},g} \int_x^1 \frac{\mathrm{d}z}{z} f_i(z,Q^2) C_{i2}\left(\frac{x}{z}, \alpha_\mathrm{S}(Q^2)\right), \tag{3.19}$$

where the C_{i2} are known as the coefficient functions. For the quarks one has

$$C_{q2}(z) = e_q^2 \delta(1-z) + O(\alpha_\mathrm{S}), \tag{3.20}$$

while the contribution from the gluon arises only at order α_S. To relate the parton distributions at different values of Q^2, one uses the DGLAP evolution equation [49–51],

$$\frac{\partial f_i(x,Q^2)}{\partial \ln Q^2} = \frac{\alpha_\mathrm{S}(Q^2)}{2\pi} \sum_j \int_x^1 \frac{\mathrm{d}z}{z} f_j(z,Q^2) P_{ij}\left(\frac{x}{z}\right). \tag{3.21}$$

The P_{ij} are the splitting functions and correspond in some sense to the rate of production of of parton i from parton j as one evolves in $\ln Q^2$. Their values, at leading order, are

$$P_{qq}(z) = C_\mathrm{F}\left[\frac{1+z^2}{(1-z)_+} + \frac{3}{2}\delta(1-z)\right], \tag{3.22}$$

$$P_{qg}(z) = T_\mathrm{R}\left[z^2 + (1-z)^2\right], \tag{3.23}$$

$$P_{gq}(z) = C_\mathrm{F}\frac{1+(1-z)^2}{z}, \tag{3.24}$$

$$P_{gg}(z) = 2C_\mathrm{A}\left[\frac{z}{(1-z)_+} + \frac{1-z}{z} + z(1-z)\right] + \left(\frac{11C_\mathrm{A} - 4n_f T_\mathrm{R}}{6}\right)\delta(1-z). \tag{3.25}$$

where A_+ is defined such that

$$\int_0^1 \mathrm{d}z\ A_+(z) f(z) = \int_0^1 \mathrm{d}z\ A(z)[f(z) - f(1)], \tag{3.26}$$

and where $f(z)$ is an arbitrary function. The splitting function which will be of most relevance to the discussion of small-x behaviour is P_{gg}, because of its divergence as $z \to 0$. To see what will happen as one evolves to small x and large Q^2 [6], one can visualise the evolution as a ladder diagram, figure 3.6. With just one rung, one has

$$xg(x,Q^2) \sim \frac{\alpha_\mathrm{S} N_\mathrm{C}}{\pi} \int_{Q_0^2}^{Q^2} \frac{\mathrm{d}k^2}{k^2} \int_x^1 \frac{\mathrm{d}z}{z} zg(z,Q_0^2). \tag{3.27}$$

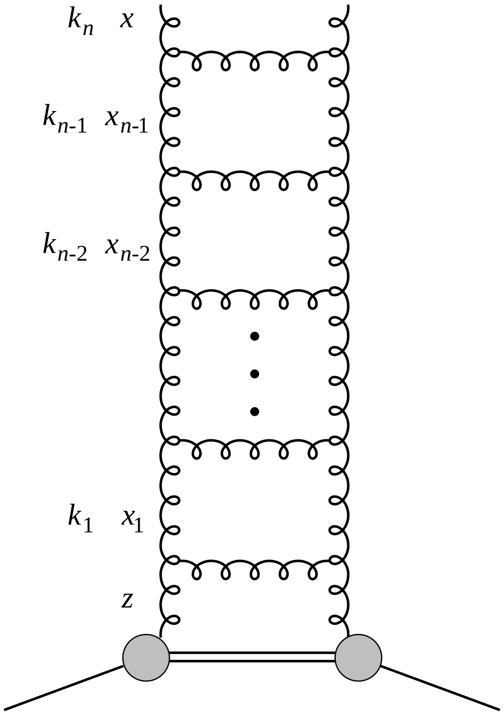

Figure 3.6: Gluon ladder diagram.

With n rungs, the dominant contribution comes from the region of strongly ordered transverse momenta, $Q^2 \gg k_n^2 \gg \cdots \gg k_1^2 \gg Q_0^2$:

$$\left(\frac{\alpha_S N_C}{\pi}\right)^n \int^{Q^2} \frac{\mathrm{d}k_n^2}{k_n^2} \int^{k_n^2} \frac{\mathrm{d}k_{n-1}^2}{k_{n-1}^2} \cdots \int^{k_2^2} \frac{\mathrm{d}k_1^2}{k_1^2} = \frac{1}{n!}\left(\frac{\alpha_S N_C}{\pi} \ln \frac{Q^2}{Q_0^2}\right)^n, \tag{3.28}$$

and the region of strongly ordered longitudinal momenta, $x \ll x_{n-1} \ll \cdots \ll z$, which gives

$$\int_x^1 \frac{\mathrm{d}x_{n-1}}{x_{n-1}} \cdots \int_{x_2}^1 \frac{\mathrm{d}x_1}{x_1} \int_{x_1}^1 \frac{\mathrm{d}z}{z}\, zg(z) = \frac{1}{n!}\left(\ln \frac{1}{x}\right)^n G_0, \tag{3.29}$$

with $G_0 = zg(z, Q_0^2)$ being assumed to be roughly independent of z (this is referred to as a flat input distribution). Putting the two integrals together and summing over the number of rungs gives

$$\begin{aligned} xg(x, Q^2) &\sim \sum_n \left(\frac{1}{n!}\right)^2 \left(\frac{\alpha_S N_C}{\pi} \ln \frac{Q^2}{Q_0^2} \ln \frac{1}{x}\right)^n G_0 & (3.30) \\ &\sim G_0 \exp\left[2\sqrt{\frac{\alpha_S N_C}{\pi} \ln \frac{Q^2}{Q_0^2} \ln \frac{1}{x}}\right], & (3.31) \end{aligned}$$

where the approximation which has been used to perform the sum is

$$\sum_n \left(\frac{1}{n!}\right)^2 \left(\frac{y^2}{4}\right)^n = I_0(y) \sim \frac{e^y}{\sqrt{2\pi y}}. \tag{3.32}$$

Eq. (3.31) is the asymptotic behaviour of the gluon distribution in the double-leading-logarithmic approximation (DLLA). Its main feature is that it predicts a rapid rise of the gluon distribution at small x. Note that though the rise is always weaker than a power of $1/x$, over a small region of x it can mimic such a power rise. Because the photon must split into a $q\bar{q}$ state to interact with the gluons, the photon is referred to as behaving hadronically.

If one includes the running of $\alpha_{\rm S}$eq. (3.31), the result of the k^2 integrations, is modified and one finds

$$xg(x,Q^2) \sim G_0 \exp\left[2\sqrt{\xi(Q^2,Q_0^2)\ln\frac{1}{x}}\right], \tag{3.33}$$

where

$$\begin{aligned}\xi(Q^2,Q_0^2) &= \int_{Q_0^2}^{Q^2} \frac{\mathrm{d}k^2}{k^2}\frac{\alpha_{\rm S}(k^2)N_{\rm C}}{\pi} \\ &= \frac{N_{\rm C}}{\pi b}\frac{\ln Q^2/\Lambda^2}{\ln Q_0^2/\Lambda^2},\end{aligned} \tag{3.34}$$

where b is as defined in eq. (2.48). This shows that the effect of running $\alpha_{\rm S}$ is to reduce the scaling violations, which is not unexpected: since $\alpha_{\rm S}$ decreases at larger scales, the evolution in Q^2 is slowed down.

3.3 BFKL evolution

In situations where the ratio Q^2/Q_0^2 is much smaller than $1/x$, logarithms of Q^2 should no longer dominate compared to logarithms of $1/x$. Therefore instead of an evolution in $\ln k^2$, one should consider an evolution in $\ln 1/x$. One can visualise this as a set of ladder graphs, as in figure 3.6, with the x_i strongly ordered ($x \ll x_{n-1} \ll \cdots \ll z$) and with the k_i totally unordered, though the correspondence between the Feynman diagrams and the ladder is fairly complicated.

This evolution in $\ln 1/x$ was first derived by Balitsky, Fadin, Kuraev and Lipatov [3–5]. Since it relies on perturbation theory, it is valid only for sufficiently large transverse momenta. Because there is no longer any strong ordering over transverse momenta, it is necessary to leave the final transverse momentum integration undone, and work in terms of the unintegrated gluon distribution $f(x,k^2)$:

$$xg(x,Q^2) = \int^{Q^2} \frac{\mathrm{d}k^2}{k^2} f(x,k^2). \tag{3.35}$$

The differential form for the BFKL evolution equation is then

$$-x\frac{\partial f(x,k^2)}{\partial x} = \frac{\alpha_{\rm S} N_{\rm C}}{\pi^2}\int \frac{{\rm d}^2\mathbf{k}'}{k'^2}\left[\frac{k^2}{|\mathbf{k}+\mathbf{k}'|^2} f(x,|\mathbf{k}+\mathbf{k}'|^2) - f(x,k^2)\theta(k^2-k'^2)\right]$$
$$= K\otimes f. \tag{3.36}$$

Treating this as an eigenvalue equation, it will be the highest eigenvalue of the kernel K which will dominate, giving

$$\frac{\partial f}{\partial \ln(1/x)} = \lambda f, \tag{3.37}$$

which results in the power law $f \sim x^{-\lambda}$. More precisely, the leading small-x behaviour of the solution to eq. (3.36) has the form

$$f(x,k^2) \sim (k^2)^{1/2}\frac{x^{-(\alpha_{\rm I\!P}-1)}}{\sqrt{\ln(1/x)}}\exp\left(-\frac{\pi\ln^2(k^2/\bar{k}^2)}{56\alpha_{\rm S}N_{\rm C}\zeta(3)\ln(1/x)}\right), \tag{3.38}$$

where the Riemann zeta function $\zeta(3)\simeq 1.202$ and $(\alpha_{\rm I\!P}-1)$ is

$$(\alpha_{\rm I\!P}-1) = \frac{\alpha_{\rm S}N_{\rm C}}{\pi}4\ln 2. \tag{3.39}$$

With $\alpha_{\rm S}\simeq 0.2$, i.e. a scale of about 10 GeV, the power should be $(\alpha_{\rm I\!P}-1)\simeq 0.5$. This is much faster than the rise for the soft pomeron, and is the reason for the extensive interest in BFKL evolution. Because of the analogy with the soft case, and the fact that all momentum scales should be perturbative (and therefore hard), this rapid rise is often referred to as being due to the BFKL or hard pomeron (hence the use of a symbol for the power, $\alpha_{\rm I\!P}$, which is similar to that adopted for the soft pomeron, $\alpha_{\rm P}$). Unlike the soft pomeron (which is a pole in the complex angular momentum plane), the hard pomeron corresponds to a branch cut.

When solving eq. (3.36) a typical transverse momentum scale $\bar{k}^2$ was introduced as an initial condition (i.e. for $f(x\sim 1)$). The effect of the evolution is to cause a “diffusion” (a random walk) in $\ln(k^2)$, so that the low-x gluons are spread over a much wider range of transverse momenta. This leads us to the first of many problems with the BFKL equation, namely that the solution tends to enter into the infra-red (low k^2) region where perturbation theory is no longer valid. Various attempts have been made to model the infra-red effects, for example by running $\alpha_{\rm S}$ according to some (slightly arbitrary) prescription and then usually introducing an infra-red cutoff [20, 57–59]. This leads to a modification of the power and a large change in the normalisation of the solution. In fact a full understanding of how to include the running of $\alpha_{\rm S}$ into the BFKL equation requires knowledge of the next-to-leading-order kernel which is currently in the process of being evaluated (see below).

A second problem is that the BFKL equation doesn't take into account the recoil of the gluon from which the small-x gluon is emitted: the first (x) moment of the gluon distribution (which should be constant in a theory with only gluons, because of momentum conservation) changes as a result of the evolution [60]. Related to this is the observation that energy is not conserved by the evolution [61]. Attempts to include such effects indicate that they may slow down the evolution quite considerably [62, 63].

These problems are connected with the fact that only the leading-logarithmic part of the BFKL kernel is known, and they should to some extent be resolved by knowledge of the next-to-leading-logarithmic (NLL) part (i.e. which includes contributions of the form ${\alpha_s}^n (\ln 1/x)^{n-1}$ as well as ${\alpha_s}^n (\ln 1/x)^n$). The quark-gluon contribution to the NLL kernel has already been calculated by Catani and Hautmann [64,65], and there is a vigorous effort in progress to determine the full NLL contributions [66–74].

The BFKL and DGLAP equations describe evolution in different variables, and are valid in different regions of x and Q^2. There are cases (in particular for the structure functions which are discussed in the next section) where one wants information continuously across the whole range of x and Q^2 — i.e. one needs somehow to put the BFKL and DGLAP evolutions together. One method is to view the BFKL terms as contributions to the DGLAP evolution, which while formally non-leading, actually contribute significantly to the Q^2 evolution because of the large range in x [60, 75–77]. In a separate approach, Ciafaloni, Catani, Fiorani and Marchesini (CCFM) [78, 79] have produced an equation based on the angular ordering of gluon emissions which is valid over the whole (perturbative) range of Q^2 and x, and which, in the appropriate limits, can be shown to reduce to the BFKL or DGLAP equations, and which, when studied in an approximate numerical form allows one to see the transition between DGLAP and BFKL regimes [80].

The limit which will be of interest in much of this dissertation is that of very small x, where the (heavy) hadron-hadron scattering amplitude becomes so large that it violates the unitarity bound. An associated problem is that the number of gluons becomes so high that that one expects that they might start recombining. This recombination has been calculated by Gribov, Levin and Ryskin [7] (GLR) and later also by Mueller and Qiu [81, 82] and is proportional to the square of the density (in transverse position) of gluons, as one might expect. Including the recombination, the BFKL equation is modified to give the GLR equation [7, 81, 82]

$$-x\frac{\partial f(x,k^2)}{\partial x} = K \otimes f - \frac{81}{16k^2R^2}\alpha_s^2[xg(s,k^2)]^2, \tag{3.40}$$

where R is the radius of the transverse area in which the gluons are concentrated. There have been a number of studies based on the GLR equation (and variations of it) — see for example [58, 59, 83, 84]. One of the main problems is that one isn't sure what value should be used for R, and changing its value has a drastic effect on the gluon density and recombination. In fact, as will be seen later, in the purely perturbative case, there isn't any mean scale R that one can use, because of the diffusion in the logarithm of the transverse scale. Additionally, the use of a mean distribution of gluons, as in eq. (3.40) is problematic.

Essentially, recombination effects (also referred to as unitarity or shadowing corrections) consist of the inclusion of diagrams where one gluon ladder (2 gluons) splits into two ladders (4 gluons), and then later rejoins back into one, together with more complicated graphs (multiple pomeron exchange). The $2 \to 4$ gluon branching has been determined in detail in [8] and there are hopes that a system including all such branchings might in principle be exactly soluble [12–15]. However that is formal mathematical statement, and doesn't mean that the solution would be easy to find. The following chapters will present, and find solutions for, a different approach, by Mueller and collaborators [16–19], which includes the subset of these corrections which are expected to be dominant over the range of rapidities where the corrections set in.

3.4 The experimental situation

One of the main activities at the HERA collider is to see whether there is any evidence for the BFKL type of behaviour. The phenomenology on this topic is vast — this section can give only the briefest of reviews of the current situation, and is not in any way intended to be complete.

Considerable effort has been put into the measurement of the F_2 structure function of the proton, as a function of x and Q^2 [85–87]. Since there is still one perturbative scale, there might be the possibility, at moderate Q^2, of seeing some kind of rise which is due to BFKL evolution, for example a structure function which increases as $x^{-0.5}$. Because of the leading $\sqrt{k^2}$ factor and the k^2 dependence in the exponential in eq. (3.38) one would also expect strong scaling violations (though they would probably be reduced once one took into account the running of α_S as happens in the DLLA case). The problem is that over the range of x and Q^2 available at HERA it is difficult to distinguish between the BFKL and DLLA behaviours, especially given the poor understanding of a variety of important (but formally non-leading) effects for BFKL evolution, and the relative freedom in choosing starting distributions when carrying out DGLAP evolution.

The experimental results [85–87] are shown in figures 3.7 and 3.8. There is a clear rise at small x, the steepness of which increases at higher values of Q^2, and there are strong scaling violations[1]. There have been a variety of attempts to analyse and understand the data. At the simplest level, one can parameterise it, verify its consistency with (next-to-leading order) DGLAP evolution, and obtain some estimate of the gluon from the scaling violations. This has been done by the MRS [95] and the CTEQ [96] collaborations. The main result is that the data are consistent with DGLAP evolution and that at moderate and high values of Q^2 the gluon rises significantly at small x, but the details of the rise depend to some extent on the fitting procedure.

[1] At low Q^2 (< 1 GeV^2) the small x behaviour starts to become quite flat, which is expected because eventually one must tend to the photo-production limit.

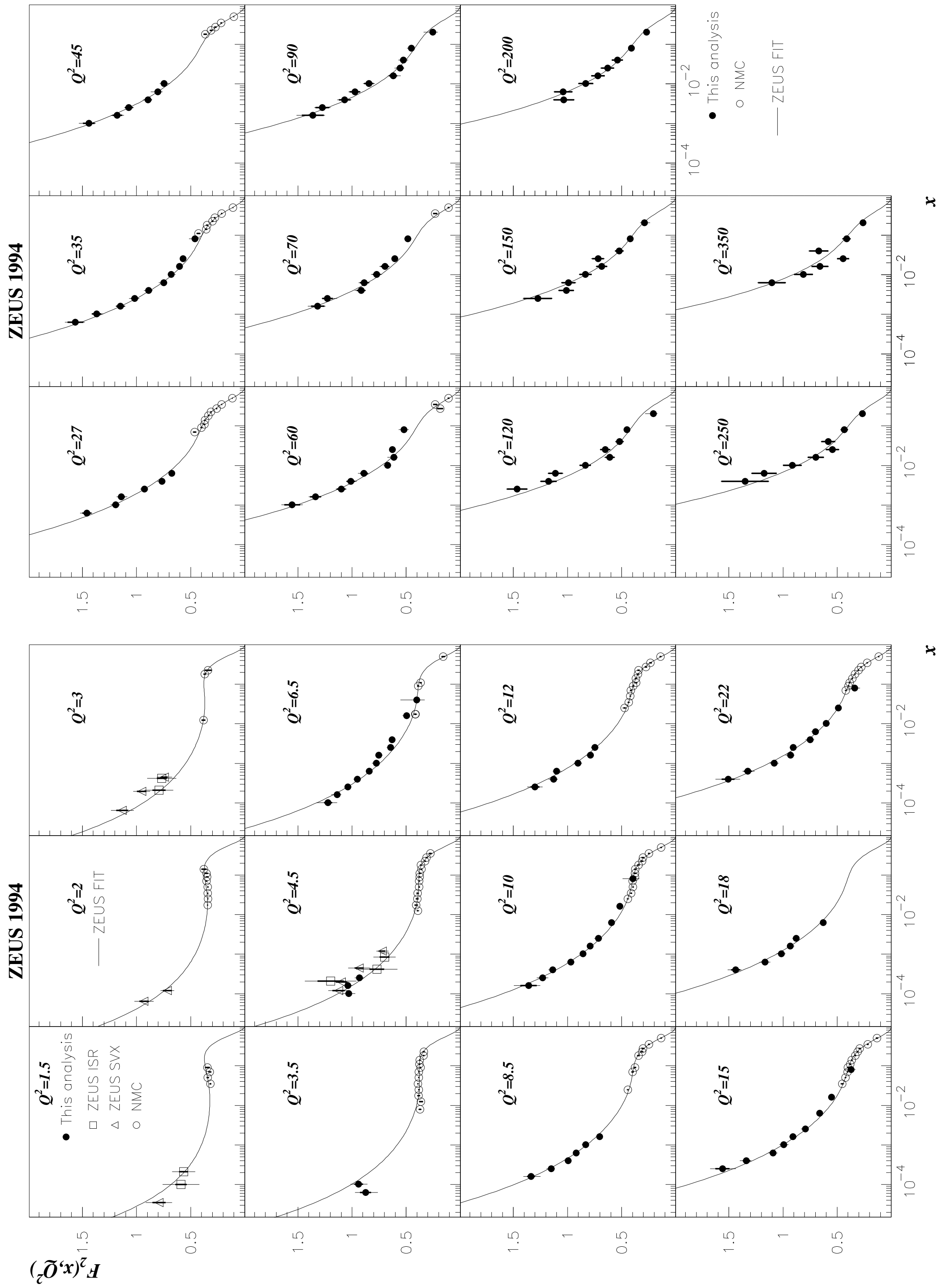

Figure 3.7: F_2 as measured by the ZEUS collaboration [86, 87]. Also shown are data from the NMC collaboration [88]. The values of Q^2 are in units of GeV^2. Figure taken from [87].

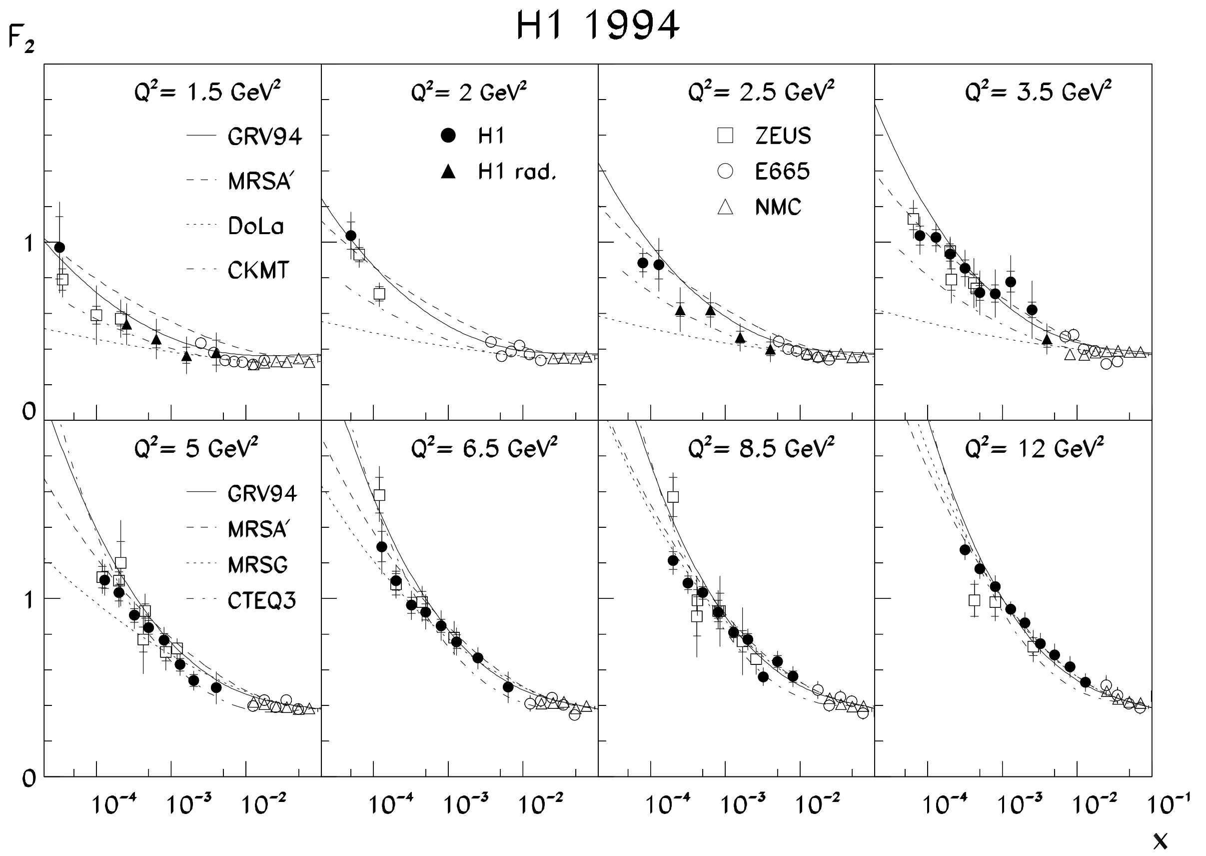

Figure 3.8: F_2 at low Q^2 as measured by H1 [85], ZEUS [86], E665 [89] and NMC [88]. Various fits are shown: Donnachie and Landshoff [90], CKMT [91] (also based on a soft pomeron, but one which includes shadowing corrections), MRS [92] and CTEQ [93, 94].

Another approach, that of Glück, Reya and Vogt (GRV) [97], is to assume that at some low scale, of the order of 0.4 GeV^2, one has flat input distributions and that the steep rise at larger Q^2 is generated entirely by DGLAP evolution. This successfully reproduces the HERA data over nearly the whole range of Q^2 and x, with only a moderate amount of arbitrariness in terms of the starting scale for the evolution and some details of the initial distributions. Work by Ball and Forte [98] has shown that there is a reasonably good agreement with the DLLA approximation.

On the other hand, using a BFKL type of formula (i.e. similar to eq. (3.38)) one can also fit the data well over most of the range of Q^2, with only 3 parameters, with the proviso that the effective value of α_s that one ends up using is roughly half of what one would expect over the central range of Q^2 (i.e. instead of a power of about 0.5, one finds a power of 0.3) [99, 100]. But there are also claims that for consistency with other data [101] and also from estimates of the various corrections that should be applied to the BFKL pomeron [102], the contribution from the BFKL pomeron to HERA processes should be much too small to be detectable, and separately that a BFKL contribution is disfavoured by the current HERA data [103].

There are various other observables which are more directly sensitive to the gluon distribution and which in principle could serve to discriminate between different models for the origin of the small-x rise, though they generally all have problems associated with them. The charm quark component of the structure function, F_2^c, is particularly sensitive to the gluon distribution, because at leading order heavy quarks are produced only via the process $\gamma^* g \to q\bar{q}$ [104–106]. Including the next-to-leading order contributions [107], one finds that F_2^c remains a sensitive and well-understood probe for the gluon distribution [108, 109]. From the experimental point of view, it suffers from the disadvantage that the efficiency for tagging charm mesons is relatively low [110], though preliminary results have been reported [111]. The longitudinal structure function, $F_L = F_2 - 2xF_1$, is also theoretically well-defined and sensitive to the gluon distribution [104, 106], but it is even more difficult to measure accurately, requiring that one combine results from runs at two different energies (see for example [110, 112]) or make use of events where there has been hard photon emission collinear to the beam (effectively reducing the electron energy) [113]. Diffractive vector meson photo- and electro-production, in particular J/ψ production [114–118], which has already been measured, showing a steep rise at small x [119–121], looks particularly attractive, because it should be proportional to the square of the gluon distribution. But there are significant theoretical uncertainties associated with a lack of knowledge about the wave functions of the vector mesons.

Another topic which has excited much interest is the observation that about 10% of all DIS events have a large rapidity gap (i.e. a large empty region between the proton and the jet(s) associated with the photon) [122, 123]. Such measurements are indicative of multiple (two) pomeron exchange (i.e. unitarity or shadowing corrections). There is considerable debate as to whether the diffraction that is being seen is really a hard process or a soft one.

Various other properties of the final state have also been examined, such as transverse energy

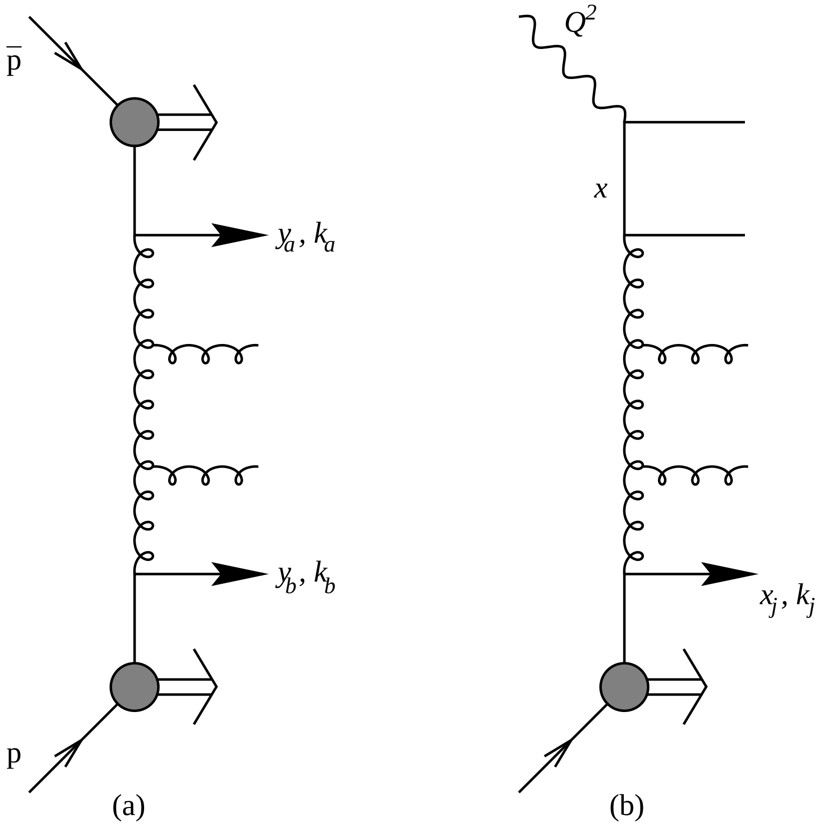

Figure 3.9: The types of process suggested by Mueller and Navelet, designed to show up BFKL behaviour.

flows [124–126] and the distribution of jet multiplicities [127,128] (see also [129]), and generally one might expect larger transverse energy flows or multiplicities from BFKL evolution because of the lack of ordering of the transverse momenta. However there are many problems relating these parton-level calculations to experimental observations because of the uncertainties which arise due to hadronisation effects.

In any case, if one wants to observe BFKL behaviour, the presence of two different transverse scales, and the fact that even one of them is soft are bound to create problems. In the subsequent chapters, the theoretical tool of onium-onium collisions [18] will be used to understand the details of BFKL behaviour without the complications of the soft scale and without the confusing element of being in the double-logarithmic region. As a more experimentally accessible possibility, it has been suggested by Mueller and Navelet [130] that one can use jets to ensure the presence of a perturbative scale. So for $\bar{p}p$ scattering, as in figure 3.9a, one requires two jets separated by a large rapidity. Since the jets have moderately large and similar transverse energies, there should be perturbative evolution between them which is dominantly in $\ln 1/x$. Accordingly one expects the cross section to be proportional to $\mathrm{e}^{(\alpha_{\mathbb{P}}-1)|y_a-y_b|}$, where y, the rapidity of a jet with momentum k, is defined to be

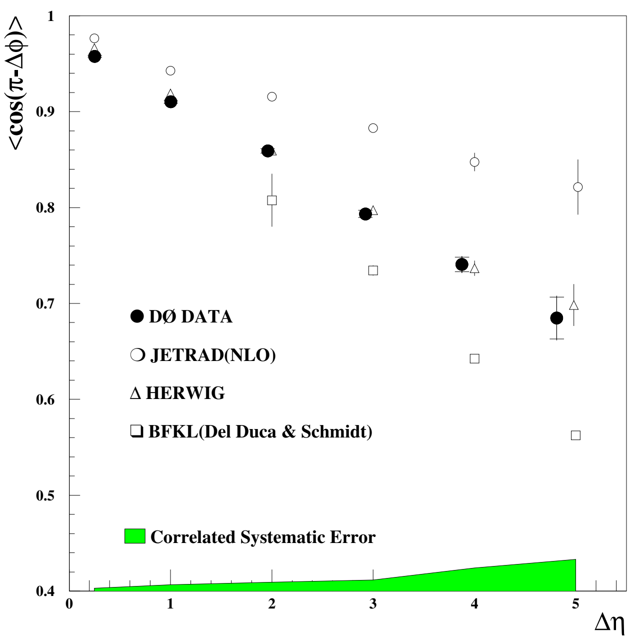

Figure 3.10: D0 results for angular decorrelation between jets (figure taken from [133]). $\Delta\phi$ is the azimuthal angle between the jets and $\Delta\eta$ is the rapidity interval between them.

$$y = \frac{1}{2}\ln\frac{k_0 + k_3}{k_0 - k_3}. \tag{3.41}$$

Unfortunately, for a fixed centre-of-mass energy this rapid rise can't be seen experimentally because there is also a rapidity dependence arising from the structure functions of the protons which causes the cross sections to decrease as the rapidity interval between the jets increases. The task of disentangling these two effects seems quite difficult [131, 132]. Another possible observable, which avoids some of these difficulties, is the angular correlation between the two jets most widely separated in rapidity. If there is no radiation between the jets, then azimuthally they should be back-to-back. Since BFKL evolution is associated with emission of gluons with (non-ordered) transverse momenta of the same order of size as those of the jets, one expects that with increasing rapidity, there should be increasing decorrelation between the orientations of the jets [131, 132].

Experimental results from the D0 collaboration [133], shown in figure 3.10, are halfway between the next-to-leading order (the first order at which decorrelation appears) calculation using JETRAD [134, 135] and that of Del Duca and Schmidt [136], which takes into account BFKL dynamics while attempting to correct for the error induced by the large rapidity approximation. The event generator HERWIG [137] agrees well with the data, but is is not clear that the underlying physics is correctly treated by HERWIG in this situation [138].

The equivalent process for DIS is shown in figure 3.9b. A hard forward jet with transverse momentum $k_T^2 \sim Q^2$ is demanded at $x_j \gg x$. Again one expects the cross section to increase roughly as $(x_j/x)^{(\alpha_{\mathbb{P}}-1)}$. In principle the extraction of this behaviour is more straightforward than for the $\bar{p}p$ case because the convolution with partons occurs only at the bottom end, and one can always keep x_j fixed and just vary x (equivalent in the $\bar{p}p$ case to keeping y_a and y_b fixed and changing the centre-of-mass energy). Unfortunately, because of the need to tag the forward jet, the measurement is experimentally quite difficult. Results so far indicate that there is a rise in the cross section, considerably larger than that suggested by a leading-order calculation [126, 139]. However there is still considerably more experimental work to be done, and on the theoretical level the next-to-leading order contribution turns out to be very important, so that it is really with the NLO [140, 141] calculation that one should compare the BFKL based predictions [142].

To summarise, there are various experimental observables in which a hint of the BFKL type of behaviour may have been seen, but there is as yet no strong evidence for the presence of BFKL effects.

C H A P T E R 4

The dipole formulation

This chapter will review the dipole formulation of BFKL evolution, following the approach taken by Mueller and collaborators [16–19]. A related approach has also been developed by Nikolaev, Zakharov and collaborators [20, 21]. So as to ensure that the calculation can be done perturbatively, one examines the small-x structure and scattering of heavy quarkonia (where the mass of the heavy quark and antiquark can be taken as large as one wants to avoid the region of large α_{S}). The evolution of the onia is formulated in terms of colour dipoles, rather than gluons, which leads to a simple colour structure (in the large-N_{C} limit), with dipoles all evolving independently of one another. Further, instead of considering the transverse momentum distribution of dipoles, one uses their transverse positions, which is important when determining the unitarity corrections to the scattering amplitude.

4.1 Derivation of the dipole formulation

The object of this section is to understand how to construct the small-x, infinite momentum wave function of an heavy quarkonium, using the approach of [17]. Consider the onium wave function containing no soft gluons (in this context, "soft" means carrying a small proportion of the onium's longitudinal momentum). The light-cone wave function is $\psi^{(0)}_{\alpha\beta}(\mathbf{k}_1, z_1)$ where α and β are quark and antiquark spinor indices and $z_1 = k_{1+}/p_+$, p is the momentum of the onium and k is the momentum of the quark (figure 4.1).

It will be convenient to use transverse position variables

$$\psi^{(0)}_{\alpha\beta}(\mathbf{b}_{01}, z_1) = \int \frac{\mathrm{d}^2\mathbf{k}_1}{(2\pi)^2} \mathrm{e}^{i\mathbf{k}_1 . \mathbf{b}_{01}} \psi^{(0)}_{\alpha\beta}(\mathbf{k}_1, z_1), \tag{4.1}$$

where the antiquark has transverse position $\mathbf{b}_0$, the quark is at $\mathbf{b}_1$ and $\mathbf{b}_{ij} = \mathbf{b}_j - \mathbf{b}_i$. The normalisation is

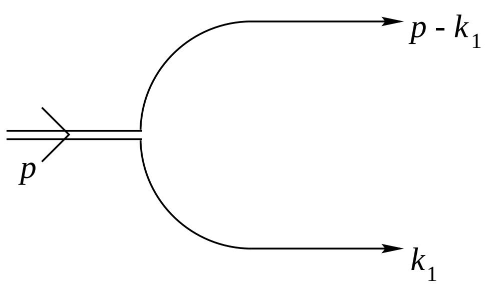

Figure 4.1: Onium wave function without any soft gluons.

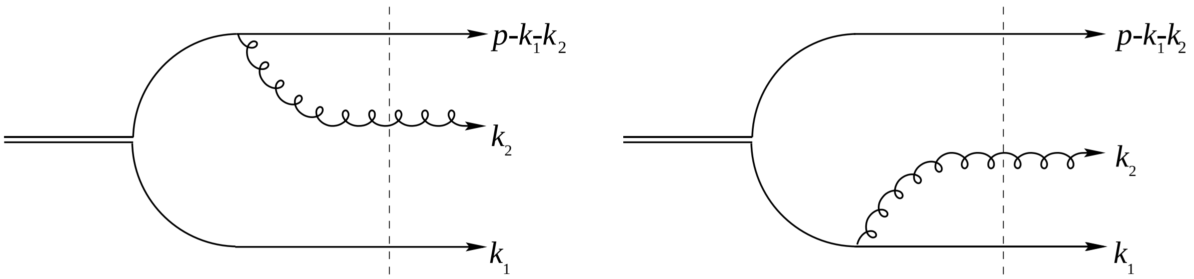

Figure 4.2: Onium wave function with one soft gluon. The dashed line indicates the point where the light-cone perturbation theory energy denominator needs to be evaluated.

$$\int \frac{\mathrm{d}^2\mathbf{k}_1}{(2\pi)^2} \int_0^1 \mathrm{d}z_1 \Phi^{(0)}(\mathbf{k}_1, z_1) = \int \mathrm{d}^2\mathbf{b}_{01} \int_0^1 \mathrm{d}z_1 \Phi^{(0)}(\mathbf{b}_{01}, z_1) = 1, \tag{4.2}$$

where

$$\Phi^{(0)}(\mathbf{k}_1, z_1) = \sum_{\alpha,\beta} \left|\psi^{(0)}_{\alpha\beta}(\mathbf{k}_1, z_1)\right|^2 \tag{4.3}$$

and

$$\Phi^{(0)}(\mathbf{b}_1, z_1) = \sum_{\alpha,\beta} \left|\psi^{(0)}_{\alpha\beta}(\mathbf{b}_1, z_1)\right|^2. \tag{4.4}$$

For simplicity, from here onwards, the spinor indices α and β will be usually be neglected.

4.1.1 Addition of one soft gluon

The order α_s correction to the wave function from the addition of a gluon with momentum k_2 has the two contributions shown in figure 4.2. Since we are interested in the large energy, or small-x (actually small-z in the notation being used in this chapter) properties of the wave function, we can make the approximation that the gluon is soft, $z_2 = k_{2+}/p_+ \ll z_1, (1-z_1)$. There are certain properties of soft gluon emission which will make evaluation of this (and subsequent) amplitudes relatively simple. Using the light-cone perturbation theory rules of section 2.4, the vertex for the emission of the gluon with momentum k_2, colour index A and polarisation vector ϵ_2^λ (with λ being the polarisation index) from the quark line (with momentum $k_1 + k_2$) is

$$g_s t^A \, \bar{u}(k_1) \, \gamma.\epsilon_2^\lambda \, u(k_1 + k_2). \tag{4.5}$$

We will use a real polarisation vector, so that the vector and its complex conjugate are the same. Because the + components of the momenta are the dominant ones, and because $k_{1+} \gg k_{2+}$, $u(k_1 + k_2)$ can be approximated as $u(k_1)$ and the vertex becomes $2 g_s t^A k_1.\epsilon_2$. The polarisation vector in the light-cone gauge is

$$\epsilon_2^\lambda = \left(0, \frac{2\mathbf{k}_2.\boldsymbol{\epsilon}_2^\lambda}{k_{2+}}; \boldsymbol{\epsilon}_2^\lambda\right), \tag{4.6}$$

so that the vertex is

$$2 g_s t^A \frac{k_{1+}}{k_{2+}} \mathbf{k}_2.\boldsymbol{\epsilon}_2^\lambda. \tag{4.7}$$

In addition to the vertex factor, one needs a contribution $\theta[(k_1 + k_2)_+]/(k_1 + k_2)_+$ for the extra internal line which has been added, and an energy denominator, evaluated at the position of the dashed line on figure 4.2:

$$\frac{1}{p_- - [(p - k_1 - k_2)_- + k_{1-} + k_{2-}]}. \tag{4.8}$$

As long as k_{2-} is the largest of the terms in the denominator (i.e. $|\mathbf{k}_1|^2/|\mathbf{k}_2|^2 \ll z_1/z_2$), then the factor associated with the emission of the gluon is

$$-2 g_s t^A \frac{\mathbf{k}_2.\boldsymbol{\epsilon}_2^\lambda}{k_2^2}, \tag{4.9}$$

where from now on k^2 will be used to denote $|\mathbf{k}|^2$. Putting this together with the emission from the antiquark, one obtains the 1-gluon contribution to the wave function:

$$\psi^{(1)A}(\mathbf{k}_1, \mathbf{k}_2; z_1, z_2) = 2 g_s t^A \left[\psi^{(0)}(\mathbf{k}_1, z_1) - \psi^{(0)}(\mathbf{k}_1 + \mathbf{k}_2, z_1)\right] \frac{\mathbf{k}_2.\boldsymbol{\epsilon}_2^\lambda}{|\mathbf{k}_2|^2}. \tag{4.10}$$

At this one gluon level, the square of the wave function takes the form:

$$\Phi^{(1)}(\mathbf{k}_1, z_1) = \frac{1}{(2\pi)^3} \int \mathrm{d}^2\mathbf{k}_2 \int_{z_0}^{z_1} \frac{\mathrm{d}z_2}{2z_2} \sum_{A\lambda\alpha\beta} \left| \psi_{\alpha\beta}^{(1)A}(\mathbf{k}_1, \mathbf{k}_2; z_1, z_2) \right|^2. \tag{4.11}$$

The $\mathbf{k}_2$ integration includes an ultra-violet divergence, but this will be cancelled by virtual corrections to be discussed presently. The lowest value of z down to which the wave function is being evaluated is defined to be z_0, but note that the z_2 integration will also be altered by the inclusion of virtual corrections.

While the form with one soft gluon is relatively straightforward in momentum space, as soon as one introduces extra soft gluons, it becomes substantially more complex, because the wave function with with a particular set of gluon and quark momenta is created from different configurations of the no-gluon wave function depending on where the various gluons are emitted from (this is already visible in the 1-gluon wave function, which depends on two configurations of the no-gluon wave function, where the gluon has been emitted from the quark and antiquark respectively). In transverse position, the situation is much clearer, because the transverse position of all harder particles is effectively frozen during the lifetime of the softest gluon. Defining the gluon position to be $\mathbf{b}_2$, the fourier transformed wave function with one soft gluon becomes:

$$\psi^{(1)A}(\mathbf{b}_{01}, \mathbf{b}_2; z_1, z_2) = \int \frac{\mathrm{d}^2\mathbf{k}_1 \mathrm{d}^2\mathbf{k}_2}{(2\pi)^4} \mathrm{e}^{i\mathbf{k}_1.\mathbf{b}_{01} + i\mathbf{k}_2.\mathbf{b}_{02}} \psi^{(1)A}(\mathbf{k}_1, \mathbf{k}_2; z_1, z_2), \tag{4.12}$$

which gives

$$\psi^{(1)A}(\mathbf{b}_{01}, \mathbf{b}_2; z_1, z_2) = \frac{ig_{\mathrm{S}} t^A}{\pi} \psi^{(0)}(\mathbf{b}_{01}, z_1) \left(\frac{\mathbf{b}_{02}}{b_{02}^2} - \frac{\mathbf{b}_{12}}{b_{12}^2} \right) .\boldsymbol{\epsilon}_2^{\lambda}. \tag{4.13}$$

where use has been made of

$$\int \frac{\mathrm{d}^2\mathbf{k}}{(2\pi)^2} \frac{\boldsymbol{\epsilon}.\mathbf{k}}{|\mathbf{k}|^2} \mathrm{e}^{i\mathbf{k}.\mathbf{b}} = \frac{i}{2\pi} \frac{\boldsymbol{\epsilon}.\mathbf{b}}{b^2}. \tag{4.14}$$

Note the resemblance of the factor in eq. (4.13) to the classical field from an electric dipole in $2+1$ dimensions. In transverse position, the square of the wave function becomes

$$\Phi^{(1)}(\mathbf{b}_{01}, z_1) = \frac{1}{2\pi} \int \mathrm{d}^2\mathbf{b}_2 \int_{z_0}^{z_1} \frac{\mathrm{d}z_2}{2z_2} \sum_{A\lambda\alpha\beta} \left| \psi_{\alpha\beta}^{(1)A}(\mathbf{k}_1, \mathbf{k}_2; z_1, z_2) \right|^2, \tag{4.15}$$

which evaluates to

$$\Phi^{(1)}(\mathbf{b}_{01}, z_1) = \int \mathrm{d}^2\mathbf{b}_2 \int_{z_0}^{z_1} \frac{\mathrm{d}z_2}{z_2} \frac{\alpha_{\mathrm{S}} N_{\mathrm{C}}}{2\pi^2} \frac{b_{01}^2}{b_{02}^2 b_{12}^2} \Phi^{(0)}(\mathbf{b}_{01}, z_1). \tag{4.16}$$

This form has the advantage that addition of an extra gluon factorises from the onium wave function (i.e. any given 1-gluon configuration depends only on a single no-gluon configuration). In anticipation of the large N_{C} limit to be taken shortly, C_{F} has been replaced with $N_{\mathrm{C}}/2$.

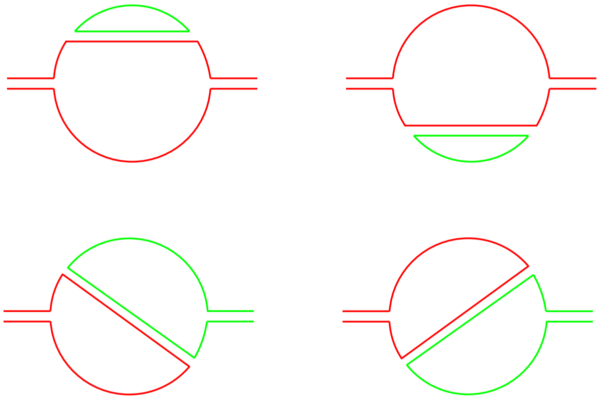

Figure 4.3: Colour structure of an onium wave function with one soft gluon — lines represent colour flow. Gluons correspond to a pair of lines.

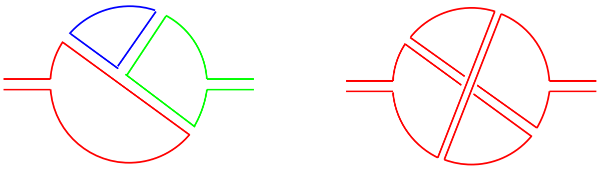

A B

Figure 4.4: Colour structure of two possible two gluon contributions to the onium wave function.

4.1.2 Wave function with several soft gluons

To understand what happens when one adds a second soft gluon, it is necessary first to examine the colour structure. The integrand on the right hand side of eq. (4.16) can be rewritten as:

$$\frac{\alpha_{\mathrm{S}} N_{\mathrm{C}}}{2\pi^2} \frac{b_{01}^2}{b_{02}^2 b_{12}^2} = \frac{\alpha_{\mathrm{S}} N_{\mathrm{C}}}{2\pi^2} \left(\frac{1}{b_{02}^2} + \frac{1}{b_{12}^2} - \frac{2\mathbf{b}_{02}.\mathbf{b}_{12}}{b_{02}^2 b_{12}^2} \right), \tag{4.17}$$

where the first two terms correspond to the top two diagrams of figure 4.3, while the third, an interference term, corresponds to the lower two diagrams. As in section 2.6, the lines represent colour flow in the large N_{C} limit, with a pair of lines being used to represent a gluon. In each of the diagrams the colour factor is the same (there are the same number of colour loops, each of which is associated with a factor of $N_{\mathrm{C}}/2$). When adding a second gluon, in the large N_{C} limit, there are now two classes of diagrams that can be considered, illustrated in figure 4.4. There are those similar to A, which are planar and have a colour factor $O(N_{\mathrm{C}}^2)$. Those like B which are non-planar, have only one colour loop, and are associated with a colour factor of $O(1)$: they are suppressed by a factor N_{C}^2, as discussed in section 2.6. Graph B corresponds to coherent emission from the original $(q\bar{q})$ dipole. Therefore once a dipole has emitted a gluon, it effectively no longer emits any more. Non-planar graphs also arise if one wants to perform an explicit calculation of saturation corrections.

For most of what follows, these non-planar graphs will be neglected. As a result, the number of diagrams to be calculated is vastly reduced: the emission of the first gluon converts a single colour dipole into two colour dipoles. The "quark part" of the gluon line forms a colour dipole with the antiquark, and the "antiquark part" of the gluon forms a second colour dipole with the quark.

A second element which is important when adding extra gluons is that (colour factors aside) the vertex for the emission of a soft gluon from a gluon is the same as that for the emission of a soft gluon from a quark. This can shown by examining the triple-gluon vertex, figure 2.3, and noting that in the soft limit only one of the three terms survives, the one that conserves the helicity of the fast gluon, giving a factor $2g_S k_2.\epsilon_3$ for the emission of a soft gluon 3 from a gluon 2, similar to that for the emission of gluon 2 from the quark. Contributions from instantaneous terms and from the 4-gluon vertex are suppressed by factors of the form k_{3+}/k_{2+}.

Finally if two dipoles are to behave independently, one must check that the emission of a soft gluon from one does not affect the emission of a soft gluon from the other, even if the two soft gluons have similar + momenta. The two vertex factors will not affect each other, but the energy denominators do appear to depend on the two gluons in combination. If gluon 3 is emitted from dipole 02 and subsequently gluon 4 is emitted from dipole 12, then one will have a product of two energy denominators (only the most dominant terms are retained):

$$\frac{1}{p_{3-}(p_{3-}+p_{4-})} \tag{4.18}$$

.

If the emission is in the opposite order, i.e. gluon 4 first (remembering that in light-cone perturbation theory the ordering of the diagrams matters) then the contribution is

$$\frac{1}{p_{4-}(p_{3-}+p_{4-})}. \tag{4.19}$$

Adding these two terms gives

$$\frac{1}{p_{3-}(p_{3-}+p_{4-})} + \frac{1}{p_{4-}(p_{3-}+p_{4-})} = \frac{1}{p_{3-}p_{4-}}, \tag{4.20}$$

so that the emission of the two gluons factorises, and it is safe to consider the emission from the two dipoles independently. Similar arguments can be developed when there are many gluons present. Note that if $p_{3-} \ll p_{4-}$ (equivalent to $p_{3+} \gg p_{4+}$), then the only term which contributes is that where gluon 4 is emitted after 3: the softest gluons are emitted latest. Intuitively this corresponds to the idea that since soft gluons have short lifetimes, $1/k_- \propto k_+$, for them to be present when the wave function is probed, they must have been created only shortly before the time of probing (i.e. late in the evolution).

As a result of this factorisation of the emission from different dipoles, all the content of the evolution in rapidity $y = \ln 1/z$, of the square of the wave function can be expressed in the branching of a single dipole: the rate (in rapidity) of conversion of a dipole $\mathbf{b}_{ij}$ into two, by production of a gluon at $\mathbf{b}_k$ is

$$\frac{\alpha_{\rm S} N_{\rm C}}{2\pi^2} \frac{b_{ij}^2}{b_{ik}^2 b_{jk}^2}, \tag{4.21}$$

and the original dipole is destroyed at a rate

$$\int \frac{\alpha_{\rm S} N_{\rm C}}{2\pi^2} \frac{b_{ij}^2 \mathrm{d}^2\mathbf{b}_k}{b_{ik}^2 b_{jk}^2} \tag{4.22}$$

(the virtual correction to the wave function evolution). In any physical quantity, the divergences in these two equations will cancel because they relate to the production of a very small dipole (while the original one is almost unchanged) and small dipoles have small interactions with any probe.

The fact that the evolution in rapidity is essentially like a sequence of decays of dipoles into pairs of dipoles, and that different dipoles "decay" independently of one another means that it will be relatively straightforward to implement the evolution through a Monte Carlo program. This will be discussed in detail in chapter 5.

4.2 Analytical solution

A general way of expressing the dipole branching is using a generating functional $Z(b, y, u)$, defined such that the probability of finding n dipoles of transverse size c with rapidity less than y, generated from a parent of size b is:

$$P_n(c, b, y) = \frac{1}{n!} \frac{\delta^n Z(b, y, u)}{\delta u(c)^n}\bigg|_{u=0}. \tag{4.23}$$

The equation for the branching can then be written in two forms. As an integro-differential equation:

$$\frac{\mathrm{d}Z(b_{01}, y, u)}{\mathrm{d}y} = \frac{\alpha_{\rm S} N_{\rm C}}{2\pi^2} \int \frac{b_{01}^2 \mathrm{d}^2\mathbf{b}_2}{b_{02}^2 b_{12}^2} [Z(b_{02}, y, u) Z(b_{12}, y, u) - Z(b_{01}, y, u)], \tag{4.24}$$

with the initial condition $Z(b, y = 0, u) = u(b)$, or as an integral equation (represented graphically in figure 4.5)

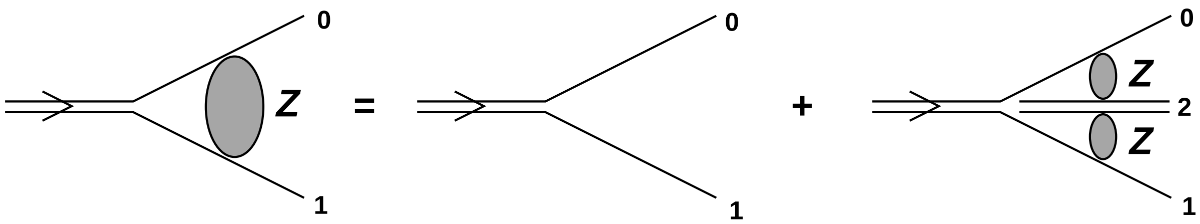

Figure 4.5: Graphical representation of eq. (4.25).

$$
\begin{aligned}
Z(b_{01},y,u) &= \mathrm{e}^{-\frac{2\alpha_S N_C y}{\pi}\ln(b_{01}/\rho)} u(b_{01}) \\
&+ \int_0^y \mathrm{d}y' \int_{b_{02},b_{12}>\rho} \frac{b_{01}^2 \mathrm{d}^2\mathbf{b}_2}{b_{02}^2 b_{12}^2} \mathrm{e}^{-\frac{2\alpha_S N_C y'}{\pi}\ln(b_{01}/\rho)} Z(b_{02},y-y',u) Z(b_{12},y-y',u). \quad (4.25)
\end{aligned}
$$

The main difference between these two forms is in the way the virtual corrections are put in. In eq. (4.24) the virtual corrections are in the subtraction term and the divergences for small b_{02} and b_{12} (which cancel between the real and virtual terms) can be dealt with in whichever way one wishes. In eq. (4.25), the virtual term is separated out, and gives a lifetime $1/V(b_{01}/\rho)$ to the dipole of size b_{01}, where

$$
V = \frac{\alpha_S N_C}{2\pi^2} \int_{b_{02},b_{12}>\rho} \frac{b_{01}^2 \mathrm{d}^2\mathbf{b}_2}{b_{02}^2 b_{12}^2}. \quad (4.26)
$$

It is because this integral diverges that one needs to specify an explicit regularisation (in this case an ultra-violet cutoff ρ) in eq. (4.25). V is evaluated by writing $b_{01}^2 = \mathbf{b}_{01}.(\mathbf{b}_{02} - \mathbf{b}_{12})$ and noting that both terms will give the same contribution. If one evaluates V using the second term, and the change of variables $b_{02} = ub_{01}$, with an angle θ between $\mathbf{b}_{02}$ and $\mathbf{b}_{01}$, one has

$$
V = \frac{\alpha_S N_C}{\pi^2} \int_{u>\rho/b_{01}} \mathrm{d}u\mathrm{d}\theta \frac{1 - u\cos\theta}{u(1 - 2u\cos\theta + u^2)}. \quad (4.27)
$$

In this term, the divergence at $u = 1$, $\theta = 0$ is integrable and not affected by the cutoff (except for a correction of $O(\rho/b_{01})$). After the θ integration, for $u > 1$ one obtains 0, leaving

$$
V = \frac{2\alpha_S N_C}{\pi} \int_{\rho/b_{01}}^1 \frac{\mathrm{d}u}{u} = \frac{2\alpha_S N_C}{\pi} \ln\frac{b_{01}}{\rho}, \quad (4.28)
$$

as used in eq. (4.25).

Since the mean number of dipoles of size c from an onium of size b is easily obtained from the generating functional:

$$
n(c,b,y) = \left.\frac{\delta Z(b,y,u)}{\delta u(c)}\right|_{u=1}, \quad (4.29)
$$

it is straightforward to write down an equation for the evolution of n with y:

$$\frac{\mathrm{d}n(c, b_{01}, y)}{\mathrm{d}y} = \frac{\alpha_{\mathrm{S}} N_{\mathrm{C}}}{2\pi^2} \int \frac{b_{01}^2 \mathrm{d}^2\mathbf{b}_2}{b_{02}^2 b_{12}^2} [n(c, b_{02}, y) + n(c, b_{12}, y) - n(c, b_{01}, y)]. \tag{4.30}$$

To solve this, one defines

$$n(c, b, y) = \int_{1-i\infty}^{1+i\infty} \frac{\mathrm{d}\lambda}{2\pi i} \left(\frac{b}{c}\right)^{\lambda} n_{\lambda}(y) \tag{4.31}$$

and

$$\chi(\lambda) = \frac{1}{4\pi} \int \frac{b_{01}^2 \mathrm{d}^2\mathbf{b}_2}{b_{02}^2 b_{12}^2} \left[\left(\frac{b_{02}}{b_{01}}\right)^{\lambda} + \left(\frac{b_{12}}{b_{01}}\right)^{\lambda} - 1 \right]. \tag{4.32}$$

Eq. (4.24) then becomes

$$\frac{\mathrm{d}n_{\lambda}}{\mathrm{d}y} = \frac{2\alpha_{\mathrm{S}} N_{\mathrm{C}}}{\pi} \chi(\lambda) n_{\lambda}. \tag{4.33}$$

Since to start with there is only one dipole, of size $c = b_{01}$ at $y = 0$, the initial conditions are $n_{\lambda}(0) = 1$, giving

$$n_{\lambda}(y) = \mathrm{e}^{\frac{2\alpha_{\mathrm{S}} N_{\mathrm{C}}}{\pi} \chi(\lambda) y}. \tag{4.34}$$

It now just remains to determine $\chi(\lambda)$. The second term of eq. (4.32) will give a result identical to the first one. For the third term, one can (again) write $b_{01}^2 = \mathbf{b}_{01}.(\mathbf{b}_{02} - \mathbf{b}_{12})$ both parts of which will give the same result. Here it is useful to use the first term. Using, as before, $b_{02} = u b_{01}$ and letting the angle between b_{02} and b_{01} be θ, one obtains

$$\chi(\lambda) = \frac{1}{2\pi} \int \frac{\mathrm{d}u \mathrm{d}\theta}{1 - 2u\cos\theta + u^2} \left(u^{\lambda-1} - \cos\theta\right). \tag{4.35}$$

The θ integration gives different answers depending on whether $u > 1$ or $u < 1$. It is convenient to rewrite the $u > 1$ answer with the substitution $u \to 1/u$, giving

$$\begin{aligned} \chi(\lambda) &= \int_0^1 \mathrm{d}u \frac{u^{\lambda-1} + u^{1-\lambda} - 2u}{1 - u^2} \\ &= \psi(1) - \frac{1}{2}\psi(1 - \lambda/2) - \frac{1}{2}\psi(\lambda/2), \end{aligned} \tag{4.36}$$

where $\psi(x) = \mathrm{d}\ln\Gamma(x)/\mathrm{d}x$ is the digamma function. The main features of $\chi(\lambda)$ are that it has a minimum at $\lambda = 1$ and a divergence at $\lambda = 0$ (and also at $\lambda = 2$). The shapes around these two points are

$$\chi(\lambda) = 2\ln 2 + \frac{7}{4}\zeta(3)(\lambda-1)^2 + O(\lambda-1)^4, \tag{4.37}$$

$$\chi(\lambda) = \frac{1}{\lambda} + \frac{1}{4}\zeta(3)\lambda^2 + O(\lambda^4). \tag{4.38}$$

To obtain the distribution of dipoles as a function of c, it is necessary to evaluate the inverse Mellin transform, eq. (4.31). When c/b is close to 1, the leading-$\ln 1/x$ limit, one can use a saddle point approximation around a point close to $\lambda = 1$, using the expansion eq. (4.37), to give

$$n(c,b,y) \simeq \frac{b}{c\sqrt{\pi k y}} \exp\left[(\alpha_{\mathrm{IP}}-1)y - \frac{1}{ky}\ln^2\left(\frac{c}{b}\right)\right], \tag{4.39}$$

with $k = 14\alpha_{\mathrm{S}}N_{\mathrm{C}}\zeta(3)/\pi$ and $(\alpha_{\mathrm{IP}}-1) = 4\ln 2\alpha_{\mathrm{S}}N_{\mathrm{C}}/\pi$. This is valid in the limit $|\ln(c/b)| \ll ky$ and has the usual BFKL form. In the opposite limit, $\ln(b/c) \gg ky$ it is necessary to take the saddle point close to $\lambda = 0$, using eq. (4.38), with the result

$$n(c,b,y) \simeq \left(\frac{\tilde{\alpha}y}{16\pi^2\ln^3 b/c}\right)^{1/4} \exp\left[2\sqrt{\tilde{\alpha}y\ln\frac{b}{c}}\right], \tag{4.40}$$

where $\tilde{\alpha} = 2\alpha_{\mathrm{S}}N_{\mathrm{C}}/\pi$. This is just the usual double-leading-logarithmic expression (for constant α_{S}).

4.3 Operator formalism

To go further than this, and in particular to obtain information about the spatial distribution of dipoles within the onium, Mueller in [16] developed an operator formalism to describe the evolution of an onium. Define an operator $a^\dagger(\mathbf{r},\mathbf{b})$ which creates a dipole consisting of sources at $\mathbf{r}+\mathbf{b}/2$ and $\mathbf{r}-\mathbf{b}/2$ (i.e. with position $\mathbf{r}$ and size $\mathbf{b}$), as well as an analogous annihilation operator, $a(\mathbf{r},\mathbf{b})$, which have the commutation relation:

$$\left[a(\mathbf{r},\mathbf{b}), a^\dagger(\mathbf{r}',\mathbf{b}')\right] = \delta^2(\mathbf{r}-\mathbf{r}')\delta^2(\mathbf{b}-\mathbf{b}'). \tag{4.41}$$

The basic vertex of the dipole picture, V_1,

$$V_1 = \frac{\alpha_{\mathrm{S}}N_{\mathrm{C}}}{2\pi^2}\int \frac{c_{01}^2}{c_{02}^2c_{12}^2}\mathrm{d}^2\mathbf{c}_{01}\mathrm{d}^2\mathbf{c}_2\mathrm{d}^2\mathbf{r}\, a^\dagger\left(\mathbf{r}+\frac{\mathbf{c}_{12}}{2},\mathbf{c}_{02}\right) a^\dagger\left(\mathbf{r}+\frac{\mathbf{c}_{02}}{2},\mathbf{c}_{12}\right) a(\mathbf{r},\mathbf{c}_{01}), \tag{4.42}$$

destroys the dipole $\mathbf{b}_{01}$ and creates the two new ones formed with the gluon at $\mathbf{b}_2$. The virtual corrections, V_2, must also be included, and are given by

$$V_2 = -\frac{\alpha_S N_C}{2\pi^2}\int \frac{c_{01}^2}{c_{02}^2 c_{12}^2} \mathrm{d}^2\mathbf{c}_{01}\mathrm{d}^2\mathbf{c}_2\mathrm{d}^2\mathbf{r}\, a(\mathbf{r},\mathbf{c}_{01})a^\dagger(\mathbf{r},\mathbf{c}_{01}), \tag{4.43}$$

and $V = V_1 + V_2$. Since we now have the extra degree of freedom given by positions of dipoles, the generating functional must be generalised so that the probability P_n of finding n dipoles of size $\mathbf{c}$ at position $\mathbf{r}$, after evolution through y of an onium of size $\mathbf{b}_{01}$ and position $\mathbf{r}_0$ is

$$P_n = \frac{1}{n!}\frac{\delta^n Z(\mathbf{r}_0,\mathbf{b}_{01},y,u)}{\delta u(\mathbf{r},\mathbf{c})^n}\bigg|_{u=0}. \tag{4.44}$$

The generating functional can then be expressed as

$$Z(\mathbf{r}_0,\mathbf{b}_{01},y,u) = \left\langle 0 \left| \mathrm{e}^{a_u}\mathrm{e}^{yV}a^\dagger(\mathbf{r}_0,\mathbf{b}_{01})\right| 0\right\rangle, \tag{4.45}$$

where

$$a_u = \int \mathrm{d}^2\mathbf{r}\mathrm{d}^2\mathbf{c}\, u(\mathbf{r},\mathbf{c})a(\mathbf{r},\mathbf{c}), \tag{4.46}$$

and the state $|0\rangle$ is such that $a(\mathbf{r},\mathbf{b})|0\rangle = 0$. To see that eq. (4.45) is the correct expression for Z, one can read it from right to left as follows: starting with the vacuum, one creates the initial onium dipole at $\mathbf{r}_0$. Then one evolves it with the operator V, incrementing the rapidity in $y/\delta y$ infinitesimally small steps δy, giving $(1 + V\delta y)^{y/\delta y}$. Finally it is necessary to replace each $a^\dagger$ with a u and return to the vacuum state in the process. That the e^{a_u} term has this effect can be seen by noting that

$$\mathrm{e}^{a_u}a^\dagger(\mathbf{r},\mathbf{b}) = [a^\dagger(\mathbf{r},\mathbf{b}) + u(\mathbf{r},\mathbf{b})]\mathrm{e}^{a_u}. \tag{4.47}$$

4.3.1 The spatial distribution of dipoles

Having understood how the generating functional is built up in the operator formalism, one can go on to work out the spatial distribution of dipoles, by taking the functional derivative with respect to $u(\mathbf{r},\mathbf{c})$:

$$\frac{\delta Z(\mathbf{r}_0,\mathbf{b}_{01},y,u)}{\delta u(\mathbf{r},\mathbf{c})}\bigg|_{u=1} = \frac{1}{2\pi c^2}n(c,b_{01},|\mathbf{r}-\mathbf{r}_0|,y); \tag{4.48}$$

$n(c,b_{01},|\mathbf{r}-\mathbf{r}_0|,y)$ is the density of dipoles of size $\mathbf{c}$, at position $\mathbf{r}$, produced by evolution through y of an onium of size $\mathbf{b}_{01}$ situated at $\mathbf{r}_0$. The factor of $[2\pi c_{01}]^{-2}$ is to convert from the measure of $\mathrm{d}^2\mathbf{c}$ associated with the functional derivative of Z, to the measure $\mathrm{d}c/c$ used for n. Using eqs. (4.45) and (4.47) one can (with some algebra) obtain

$$\left.\frac{\delta Z(\mathbf{r}_0, \mathbf{b}_{01}, y, u)}{\delta u(\mathbf{r}, \mathbf{c})}\right|_{u=1} = \left\langle 0 \left| a(\mathbf{r}, \mathbf{c}) \mathrm{e}^{y a^\dagger K a} a^\dagger(\mathbf{r}_0, \mathbf{b}_{01}) \right| 0 \right\rangle, \tag{4.49}$$

where

$$a^\dagger K a = \int \mathrm{d}^2\mathbf{r}\, \mathrm{d}^2\mathbf{b}\, \mathrm{d}^2\mathbf{b}'\, \mathrm{d}^2\boldsymbol{\zeta}\; a^\dagger(\mathbf{r}+\boldsymbol{\zeta}, \mathbf{b}') K(\boldsymbol{\zeta}, \mathbf{b}', \mathbf{b}) a(\mathbf{r}, \mathbf{b}), \tag{4.50}$$

with

$$K(\zeta, \mathbf{b}', \mathbf{b}) = \frac{\alpha_{\mathrm{S}} N_{\mathrm{C}}}{2\pi^2} \frac{b^2}{b'^2 |\mathbf{b}-\mathbf{b}'|^2} \left[\delta^2\left(\boldsymbol{\zeta} - \frac{\mathbf{b}-\mathbf{b}'}{2}\right) + \delta^2\left(\boldsymbol{\zeta} + \frac{\mathbf{b}-\mathbf{b}'}{2}\right)\right] - \frac{2\alpha_{\mathrm{S}} N_{\mathrm{C}}}{\pi} \ln(b/\rho) \delta^2(\boldsymbol{\zeta}) \delta^2(\mathbf{b}-\mathbf{b}'). \tag{4.51}$$

One can see that eq. (4.49) is of the correct form by applying the same kind of analysis that was used to explain eq. (4.45). The aim is to integrate over all paths which start with a dipole $(\mathbf{r}_0, \mathbf{b}_{01})$ and at the end include a dipole $(\mathbf{r}, \mathbf{c})$. The first step is to create the initial dipole. One then acts on it with a kernel whose function is to *replace* one dipole with that into which it will have evolved after an infinitesimally small rapidity (summing over the two dipoles which are produced and taking into account the removal of the original one). This is the action of $a^\dagger K a$. By exponentiating it one covers all possible sequences of branching — but this differs from eq. (4.45) in that the states which are produced are only single dipole (inclusive) states. Finally one selects out dipoles with a particular size and position using $a(\mathbf{r}, \mathbf{c})$.

To obtain an actual expression for n from eq. (4.49) one rewrites the operators a and $a^\dagger$ in terms of eigenfunctions $E^{n\nu}$ of the kernel, which are given by Lipatov in [5]:

$$a(\mathbf{r}, \mathbf{b}) = \sum_{n=-\infty}^{+\infty} \int_{-\infty}^{+\infty} \frac{\mathrm{d}\nu}{(\pi)^2} \left(\frac{n}{2} + i\nu\right) \int \frac{\mathrm{d}^2\mathbf{w}}{b^4} E^{n\nu}(\mathbf{r}+\mathbf{b}/2-\mathbf{w}, \mathbf{r}-\mathbf{b}/2-\mathbf{w}) a_{n\nu}(\mathbf{w}) \tag{4.52}$$

and

$$a^\dagger(\mathbf{r}, \mathbf{b}) = \sum_{n=-\infty}^{+\infty} \int_{-\infty}^{+\infty} \frac{\mathrm{d}\nu}{(\pi)^2} \left(\frac{n}{2} - i\nu\right) \int \mathrm{d}^2\mathbf{w} E^{n\nu *}(\mathbf{r}+\mathbf{b}/2-\mathbf{w}, \mathbf{r}-\mathbf{b}/2-\mathbf{w}) a^\dagger_{n\nu}(\mathbf{w}). \tag{4.53}$$

From the completeness of the $E^{n\nu}$ [5]

$$\sum_{n=-\infty}^{\infty} \int_{-\infty}^{+\infty} \mathrm{d}\nu \left(\frac{n^2}{4} + \nu^2\right) \int \frac{16\, \mathrm{d}^2\boldsymbol{\rho}_0}{\rho_{12}^2\, \rho_{1'2'}^2} E^{n\nu *}(\boldsymbol{\rho}_{01'}, \boldsymbol{\rho}_{02'}) E^{n\nu}(\boldsymbol{\rho}_{01}, \boldsymbol{\rho}_{02}) = (2\pi)^4 \delta^2(\boldsymbol{\rho}_{11'}) \delta^2(\boldsymbol{\rho}_{22'}), \tag{4.54}$$

one can see that the commutation relation

$$\left[a_{n\nu}(\mathbf{w}), a^{\dagger}_{n'\nu'}(\mathbf{w}')\right] = \delta_{nn'}\delta(\nu - \nu')\delta^2(\mathbf{w} - \mathbf{w}') \tag{4.55}$$

is the equivalent for the $a_{n\nu}(\mathbf{w})$ of eq. (4.41) for the $a(\mathbf{r}, \mathbf{b})$. The action of the dipole kernel, K, on the $E^{n\nu}$ is[1]

$$\begin{aligned}\int \mathrm{d}^2\mathbf{r}\mathrm{d}^2\mathbf{b}K(\mathbf{r}' - \mathbf{r}, \mathbf{b}', \mathbf{b})&\frac{E^{n\nu}(\mathbf{r} + \mathbf{b}/2 - \mathbf{w}, \mathbf{r} - \mathbf{b}/2 - \mathbf{w})}{b^4} \\ &= \frac{2\alpha_{\mathrm{S}}N_{\mathrm{C}}}{\pi}\chi(n,\nu)\frac{E^{n\nu}(\mathbf{r}' + \mathbf{b}'/2 - \mathbf{w}, \mathbf{r}' - \mathbf{b}'/2 - \mathbf{w})}{b'^4},\end{aligned} \tag{4.56}$$

where[2]

$$\chi(n,\nu) = \psi(1) - \frac{1}{2}\psi\left(\frac{|n|+1}{2} + i\nu\right) - \frac{1}{2}\psi\left(\frac{|n|+1}{2} - i\nu\right). \tag{4.57}$$

With the aid of eqs. (23) and (A.16) of [5], eq. (4.56) allows one to write

$$a^{\dagger}Ka = \frac{2\alpha_{\mathrm{S}}N_{\mathrm{C}}}{\pi}\sum_{n=-\infty}^{+\infty}\int \mathrm{d}\nu\mathrm{d}^2\mathbf{w}\chi(n,\nu)a^{\dagger}_{n\nu}(\mathbf{w})a_{n\nu}(\mathbf{w}). \tag{4.58}$$

Combining these various equations together one obtains

$$\begin{aligned}n(c,b,r,y) = \sum_{n=-\infty}^{+\infty} 16\int_{-\infty}^{+\infty}\frac{\mathrm{d}\nu}{(2\pi)^3}\left(\frac{n^2}{4} + \nu^2\right)\mathrm{e}^{\frac{2\alpha_{\mathrm{S}}N_{\mathrm{C}}}{\pi}\chi(n,\nu)y} \\ .\int\frac{\mathrm{d}^2\mathbf{w}}{c^2}E^{n\nu}(\mathbf{r} + \mathbf{c}/2 - \mathbf{w}, \mathbf{r} - \mathbf{c}/2 - \mathbf{w})E^{n\nu}(\mathbf{b}/2 - \mathbf{w}, -\mathbf{b}/2 - \mathbf{w}).\end{aligned} \tag{4.59}$$

The leading term in energy is that for $n = 0$ (since for higher values of n, $\chi(n,\nu)$ decreases). The functions $E^{0\nu}$ are

$$E^{0\nu}(\mathbf{r}, \mathbf{r}') = \left[\frac{|\mathbf{r} - \mathbf{r}'|}{rr'}\right]^{1+2i\nu}. \tag{4.60}$$

The result obtained in [16] for the evaluation of eq. (4.59) is

$$n(c,b,r,y) \simeq \frac{2b}{cr^2}\ln\left(\frac{r^2}{bc}\right)\frac{\exp[(\alpha_{\mathrm{I\!P}} - 1)y - \ln^2(r^2/bc)/ky]}{(\pi ky)^{3/2}}, \tag{4.61}$$

valid for $r \gg b, c$ and $\ln r^2/bc \ll ky$. This result will be discussed in more detail in chapter 6. The main feature to note at this stage is that if one integrates with respect to $\mathbf{r}$ one obtains the total number of dipoles of size c, eq. (4.39).

[1] Note that in [16], it was E/b^2, not E/b^4, which was quoted as being the eigenfunction. This was wrong (it causes the integration with the kernel to be divergent), but a number of other errors led to the final answer, eq. (30) of [16], being correct.

[2] $\chi(0,\nu)$, as defined here, is the same as $\chi(\lambda = 1 + 2i\nu)$ in eq. (4.36).

4.4 Onium-onium interaction

In much of the work which will follow, we will be discussing the onium-onium elastic scattering amplitude. The lowest order interaction between two onia is by exchange of a colour neutral pair of gluons between a dipole in one onium and a dipole in the other onium. One requires at least two gluons, so that the exchange can be colour neutral, and they must couple to the same dipole in an onium otherwise that dipoles they connected to would be destroyed. The amplitude for the elastic scattering can be written

$$A(\mathbf{r}, Y) = i \int \mathrm{d}^2\mathbf{b}\mathrm{d}^2\mathbf{b}' \int \mathrm{d}z\mathrm{d}z' \Phi(\mathbf{b}, z)\Phi(\mathbf{b}', z')F(\mathbf{b}, \mathbf{b}', \mathbf{r}, Y). \tag{4.62}$$

The rapidity Y is approximately $\ln s/M^2$, with M being the onium mass and $\sqrt{s}$ the centre-of-mass energy. The amplitude is determined for a fixed relative impact parameter $\mathbf{r}$ between the onia and as in section 4.1, $\Phi(\mathbf{b}, z)$ is the square of the heavy quark-antiquark part of the onium wave functions with $\mathbf{b}$ the transverse separation between the quark and antiquark and z the longitudinal momentum fraction of the antiquark. For two gluon exchange (equivalent to 1-pomeron exchange) $F = F^{(1)}$, with

$$F^{(1)}(\mathbf{b}, \mathbf{b}', \mathbf{r}, Y) = \int \frac{\mathrm{d}^2\mathbf{c}}{2\pi c^2}\frac{\mathrm{d}^2\mathbf{c}'}{2\pi c'^2}\mathrm{d}^2\mathbf{R}\mathrm{d}^2\mathbf{R}' f(\mathbf{R}-\mathbf{R}', \mathbf{c}, \mathbf{c}')n(\mathbf{c}, \mathbf{b}, \mathbf{R}, y)n(\mathbf{c}', \mathbf{b}', \mathbf{R}'-\mathbf{r}, Y-y). \tag{4.63}$$

The terms $n(c, b, R, y)$ are the density of dipoles of size c at a distance R from a parent onium of size b after evolution through a rapidity y as defined in the previous section. The factors $1/2\pi c^2$ are just to compensate for the normalisation of each wave function (which from now on refers to the dipole distribution of an onium of fixed size). Note that for two gluon exchange the division of rapidity between the two onia (the choice of y) is arbitrary. The amplitude (divided by i) for interaction between a dipole of size $\mathbf{c}$ and one of size $\mathbf{c}'$ whose centres are separated by $\mathbf{r}$, $f(\mathbf{r}, \mathbf{c}, \mathbf{c}')$, is

$$f(\mathbf{r}, \mathbf{c}, \mathbf{c}') = \int \frac{\mathrm{d}^2\mathbf{q}}{(2\pi)^2}\mathrm{e}^{-i\mathbf{r}.\mathbf{q}} f(\mathbf{q}, \mathbf{c}, \mathbf{c}'), \tag{4.64}$$

where

$$f(\mathbf{q}, \mathbf{c}, \mathbf{c}') = \frac{\alpha_s^2}{2}\int \frac{\mathrm{d}^2\boldsymbol{\ell}}{|\boldsymbol{\ell}|^2|\mathbf{q}-\boldsymbol{\ell}|^2}\left[\mathrm{e}^{i\boldsymbol{\ell}.\mathbf{c}/2} - \mathrm{e}^{-i\boldsymbol{\ell}.\mathbf{c}/2}\right]\left[\mathrm{e}^{-i\boldsymbol{\ell}.\mathbf{c}'/2} - \mathrm{e}^{i\boldsymbol{\ell}.\mathbf{c}'/2}\right]$$
$$\cdot \left[\mathrm{e}^{i(\mathbf{q}-\boldsymbol{\ell}).\mathbf{c}/2} - \mathrm{e}^{-i(\mathbf{q}-\boldsymbol{\ell}).\mathbf{c}/2}\right]\left[\mathrm{e}^{-i(\mathbf{q}-\boldsymbol{\ell}).\mathbf{c}'/2} - \mathrm{e}^{i(\mathbf{q}-\boldsymbol{\ell}).\mathbf{c}'/2}\right], \tag{4.65}$$

and $f(\mathbf{q}, \mathbf{c}, \mathbf{c}')$ just corresponds to the amplitude (to within a normalisation factor of i) for the kinds of diagrams shown in figure 4.6. The ℓ_+ and ℓ_- components of the loop momentum are constrained to be small, as are the q_+ and q_- components of the exchanged 4-momentum q.

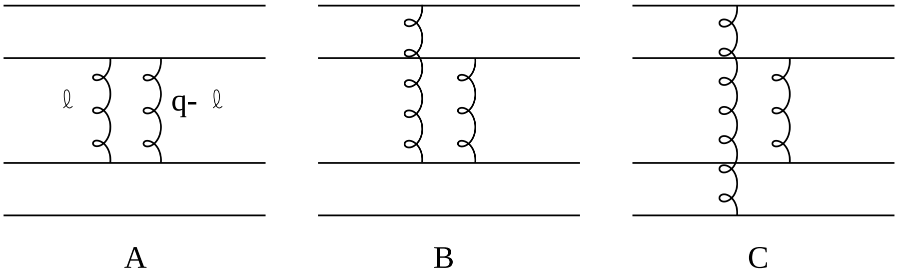

Figure 4.6: The three types of diagrams that contribute to dipole-dipole scattering.

The evaluation of the fourier transform, eq. (4.64), can be done straightforwardly by noting that eq. (4.65) is the convolution of two identical terms, each of which is the single gluon potential between a pair of dipoles in two dimensions. The result for $f(\mathbf{r},\mathbf{c},\mathbf{c}')$ is then

$$f(\mathbf{r},\mathbf{c},\mathbf{c}') = \frac{\alpha_s^2}{2}\left[\ln\frac{|\mathbf{r}+\mathbf{c}/2-\mathbf{c}'/2||\mathbf{r}-\mathbf{c}/2+\mathbf{c}'/2|}{|\mathbf{r}+\mathbf{c}/2+\mathbf{c}'/2||\mathbf{r}-\mathbf{c}/2-\mathbf{c}'/2|}\right]^2, \tag{4.66}$$

which is simply the square of the two-dimensional dipole-dipole potential.

The normalisations have been chosen such that the elastic cross section σ_{el} is

$$\frac{\mathrm{d}\sigma_{\mathrm{el}}}{\mathrm{d}t} = \frac{1}{4\pi}|A(q,Y)|^2, \tag{4.67}$$

with $t=-q^2$ and

$$A(q,Y) = \int \mathrm{d}^2\mathbf{r}\mathrm{e}^{i\mathbf{q}.\mathbf{r}}A(\mathbf{r},Y). \tag{4.68}$$

The total cross section is then twice the imaginary part of the forward elastic amplitude:

$$\sigma_{\mathrm{tot}}(Y) = 2\mathrm{Im}A(\mathbf{q}=0,Y) = 2\int \mathrm{d}^2\mathbf{r}\;\mathrm{Im}A(\mathbf{r},Y), \tag{4.69}$$

as in section 2.7. In all the calculations which will be presented here, the integral over the wave functions Φ of the initial, unevolved onia will be left undone. Accordingly the integral of $F(b,b',r,Y)$ with respect to $\mathbf{r}$,

$$F(b,b',Y) = \int \mathrm{d}^2\mathbf{r}\;F(b,b',r,Y), \tag{4.70}$$

will be referred to as the total amplitude and is equal to half the total cross section for the scattering of a pair of onia with fixed $q\bar{q}$ separations.

4.4.1 The total amplitude

In most of the work of Mueller and collaborators, the dipole-dipole amplitude has been averaged over the angles of the interacting dipoles. Since one must in general take an average over the orientations of the two onia, this is correct at the level of two gluon exchange. A second approximation that is made is that the interaction is local and can be approximated as a δ-function. This is reasonable because from eq. (4.66) on can show that the interaction dies off as $1/r^4$. In any case, for the determination of the total cross section, all that is needed is that the integral of the interaction over $\mathbf{r}$, $f(c,c')$, be correct. One obtains

$$f(c,c') = 4\pi\alpha_{\mathrm{S}}^2 \int \frac{\mathrm{d}\ell}{\ell^3}\,[1 - J_0(\ell c)]\,[1 - J_0(\ell c')] \tag{4.71}$$

$$= \pi\alpha_{\mathrm{S}}^2 c_<^2 \left(1 + \ln\frac{c_>}{c_<}\right), \tag{4.72}$$

with $c_<$ being the smaller of c and c', and $c_>$, the larger. The scale which comes into the interaction is therefore the smaller of the two dipoles, with the effect of the larger one being only logarithmic. When determining the onium-onium total interaction one need only convolute $f(c,c')$ with the distribution of dipoles in the two onia, ignoring the spatial distribution of the dipoles. This is most easily done using the Mellin transforms of the dipole distributions (an approach suggested by Navelet, Peschanski and Royon in [99]). The forward elastic amplitude for the scattering of onia of sizes b and b' is then

$$F(b,b',Y) = \int \frac{\mathrm{d}\lambda}{2\pi i}\frac{\mathrm{d}\lambda'}{2\pi i}\frac{\mathrm{d}c}{c}\frac{\mathrm{d}c'}{c'}\left(\frac{b}{c}\right)^{\lambda}\left(\frac{b'}{c'}\right)^{\lambda'} e^{\frac{2\alpha_{\mathrm{S}}N_{\mathrm{C}}}{\pi}[y\chi(\lambda)+(Y-y)\chi(\lambda')]}\pi\alpha_{\mathrm{S}}^2 c_<^2\left(1 + \ln\frac{c_>}{c_<}\right). \tag{4.73}$$

One uses

$$\pi\alpha_{\mathrm{S}}^2 \int \frac{\mathrm{d}c'}{c'}\left(\frac{1}{c'}\right)^{\lambda} c_<^2\left(1 + \ln\frac{c_>}{c_<}\right) = \pi\alpha_{\mathrm{S}}^2 c^2 \left(\frac{1}{c}\right)^{\lambda}\left(\frac{1}{\lambda} + \frac{1}{2-\lambda} + \frac{1}{(\lambda)^2} + \frac{1}{(2-\lambda)^2}\right)$$

$$= 4\pi\alpha_{\mathrm{S}}^2 c^2 \left(\frac{1}{c}\right)^{\lambda}[1 + O((\lambda-1)^2)]. \tag{4.74}$$

The expansion around $\lambda = 1$ is taken because the saddle point which arises shortly will be taken close to $\lambda = 1$ (and it will be possible to neglect the $O((\lambda-1)^2)$ terms. Using also

$$\int \frac{\mathrm{d}c}{c} c^{2-\lambda-\lambda'} = 2\pi i\delta(2 - \lambda - \lambda'), \tag{4.75}$$

and the fact that $\chi(\lambda) = \chi(2-\lambda)$, one obtains

$$F(b,b',Y) = 4\pi\alpha_{\mathrm{S}}^2 bb' \int \frac{\mathrm{d}\lambda}{2\pi i}\left(\frac{b}{b'}\right)^{\lambda-1} \mathrm{e}^{\frac{2\alpha_{\mathrm{S}}N_{\mathrm{C}}Y}{\pi}\chi(\lambda)} \tag{4.76}$$

$$\simeq \frac{4\pi\alpha_{\mathrm{S}}^2 bb'}{\sqrt{\pi k Y}} \exp[(\alpha_{\mathrm{IP}} - 1)Y - \ln^2(b'/b)/kY], \tag{4.77}$$

where the dλ integral is straightforwardly evaluated by noting that it is just $4\pi\alpha_S^2 b^2 n(b, b', Y)$. The validity of the saddle point integration is, as usual, $|\ln b/b'| \ll ky$.

Eq. (4.75) is what leads to the independence of the amplitude on the division of the rapidity between the onia. Accordingly, using eq. (4.74) one could have written eq. (4.77) straight away by performing the calculation in the lab frame: one need only take the dipole density eq. (4.39), integrated over $\mathbf{r}$, and write

$$F(b, b', Y) = 4\pi\alpha_S^2 b^2 n(b, b', Y). \tag{4.78}$$

Note that this trick is not quite so simple to use in the DLLA limit, where the λ dependence of eq. (4.74) can no longer be neglected.

Using the assumption that the dipole-dipole interaction is local one can use the same trick to easily determine onium-onium amplitude $F(b, b', r, Y)$, as a function of the separation r, between the two onia. It should just be

$$\begin{aligned} F(b, b', r, Y) &\simeq 4\pi\alpha_S^2 b^2 n(b, b', r, Y) \\ &\simeq \frac{8\pi\alpha_S^2 bb'}{r^2} \ln\left(\frac{r^2}{bb'}\right) \frac{\exp[(\alpha_{\mathbb{P}} - 1)Y - \ln^2(r^2/bb')/kY]}{(\pi kY)^{3/2}}, \end{aligned} \tag{4.79}$$

where eq. (4.61) has the been used for the spatial distribution of dipoles (and one has the same limits for the validity of the equation). If one determines the spatial distribution of the amplitude in an arbitrary frame, one obtains the same answer.

From the nature of the Y growth, it is clear that for sufficiently high energy, unitarity is violated. A second feature of eq. (4.79) is that the logarithmic prefactor causes the dominant part of the interaction to come from impact parameters of the order

$$\ln\left(\frac{r^2}{bb'}\right) \sim \sqrt{kY}, \tag{4.80}$$

much larger than the onium radius, and where the amplitude is much smaller than at central impact parameters. This will delay the onset of unitarity corrections to the total amplitude. Note that the integral of eq. (4.79) with respect to $\mathbf{r}$ (using appropriate limits) gives eq. (4.77), as it should.

4.5 Unitarity corrections

One of the reasons why unitarity is violated is that multiple interactions between the onia become important at higher energies. So far, these were neglected as being higher order in $1/N_C$: the interaction of a pair of dipoles gives a factor α_S^2 (see eq. (4.72)). But when the energy is high, there is a large number of dipoles in each onium, and the total number of possible interactions is of order $\mathrm{e}^{(\alpha_{\mathbb{P}}-1)(y+(Y-y))}$ (the product of the number of dipoles in each onium). So when $\alpha_S^2\mathrm{e}^{(\alpha_{\mathbb{P}}-1)Y}\sim 1$, one should take into account multiple-scattering corrections — multiple pomeron exchange — despite the fact that they are suppressed by $1/N_C^2$. There are also other $1/N_C^2$ suppressed terms, which correspond to interactions of dipoles within the same wave function (which will be referred to as saturation corrections). The effect that these have on a given dipole is proportional to the number of other dipoles in the same onium, and therefore of order $\alpha_S^2\mathrm{e}^{(\alpha_{\mathbb{P}}-1)y}$ or $\alpha_S^2\mathrm{e}^{(\alpha_{\mathbb{P}}-1)(Y-y)}$. In general this will be of the same order as the multiple-scattering corrections, but if one chooses $y=Y/2$, i.e. one performs the scattering in the centre-of-mass frame, dividing the rapidity equally between the two onia, then the saturation corrections are of order $\alpha_S^2\mathrm{e}^{(\alpha_{\mathbb{P}}-1)Y/2}$ and don't become important until roughly twice the rapidity at which multiple-scattering corrections start to matter. This is fortunate, because saturation corrections are difficult to calculate, while multiple-scattering corrections will, at least in principle, be straightforward. These arguments are of course hand-waving, and will be the subject of more detailed study in chapter 8. For the time being, though, they will be taken to be reasonable.

The principle behind the calculation of multiple-scattering corrections is as follows. First one takes a particular configuration of each onium (i.e. a particular arrangement of the dipoles in each one). Let these be referred to as γ and γ' for the two onia. The number of dipoles in the first onium is n_γ and individual dipoles are referred to by unprimed indices such as $i=1\dots n_\gamma$. The second onium has $n'_{\gamma'}$ dipoles, and they are referred to by primed indices, $i'=1\dots n'_{\gamma'}$. The interaction between a pair of dipoles i and i' is $f_{ii'}$, where

$$f_{ii'}=f(\mathbf{r}_i-\mathbf{r}'_{i'},\mathbf{c}_i,\mathbf{c}'_{i'}), \tag{4.81}$$

using the definition of eq. (4.66) and with $\mathbf{r}_i$ and $\mathbf{c}_i$ being the position and size of dipole i. With this notation, for a particular pair of configurations the single interaction can be written as $F^{(1)}_{\gamma,\gamma'}$, or $f_{\gamma,\gamma'}$ where

$$F^{(1)}_{\gamma,\gamma'}=f_{\gamma,\gamma'}=\sum_{i=1}^{n_\gamma}\sum_{i'=1}^{n'_{\gamma'}}f_{ii'}. \tag{4.82}$$

This is just the statement that one is taking into account the interaction of every dipole in the first onium with every dipole in the second onium. To obtain the actual scattering amplitude one must remember to sum over all possible onium configurations, with the correct weights. Defining $P_\gamma(\mathbf{r}_0,\mathbf{b},y)$ as the probability of producing a configuration γ from an onium of size $\mathbf{b}$ at position $\mathbf{r}_0$ after evolution through a rapidity y, the single interaction (or equivalently one-pomeron) amplitude between two onia separated by $\mathbf{r}$ is

$$F^{(1)}(\mathbf{r},\mathbf{b},\mathbf{b}',Y)=\sum_{\gamma,\gamma'}P_\gamma(\mathbf{r}_0,\mathbf{b},y)P_{\gamma'}(\mathbf{r}_0+\mathbf{r},\mathbf{b}',Y-y)f_{\gamma,\gamma'}, \tag{4.83}$$

which can be shown to be independent of y (see appendix B). The double interaction (or, equivalently, two pomeron component) involves looking at the product of the interaction of two pairs of dipoles (each pair consists one dipole in the first onium, and one in the second):

$$F^{(2)}_{\gamma,\gamma'} = -\frac{1}{2!}\sum_{i,j=1}^{n_\gamma}\sum_{i',j'=1}^{n'_{\gamma'}} f_{ii'}f_{jj'}, \tag{4.84}$$

with the conditions $i \neq j$ and $i' \neq j'$ in the sum. The factor of $1/2$ in front is to compensate for the double-counting. Note that the double interaction has the opposite sign from the single interaction, so that its effect is to reduce the amplitude. Similarly one can have three dipoles interacting, which gives

$$F^{(3)}_{\gamma,\gamma'} = \frac{1}{3!}\sum_{i,j,k=1}^{n_\gamma}\sum_{i',j',k'=1}^{n'_{\gamma'}} f_{ii'}f_{jj'}f_{kk'}, \tag{4.85}$$

with the conditions $i \neq j$, $i \neq k$, etc... Again the factor in front is to compensate for multiple counting. It is straightforward to extend these equations to larger numbers of interactions. From the point of view evaluating them, one quickly runs into problems, since if there are $N = n_\gamma n'_{\gamma'}$ terms to evaluate for a single interaction, there are of order N^k for k interactions, and when N is large this quickly becomes prohibitive. But when n and n' are large, to a good approximation[3], one can write

$$F^{(k)}_{\gamma,\gamma'} \simeq (-1)^{k+1}\frac{\left[f_{\gamma,\gamma'}\right]^k}{k!}, \tag{4.86}$$

which is a great simplification. Accordingly one can write the k-interaction (or k-pomeron) contribution to the amplitude as

$$F^{(k)}(\mathbf{r},\mathbf{b},\mathbf{b}',Y) \simeq (-1)^{k+1}\sum_{\gamma,\gamma'} P_\gamma(\mathbf{r}_0,\mathbf{b},Y/2)P_{\gamma'}(\mathbf{r}_0+\mathbf{r},\mathbf{b}',Y/2)\frac{\left[f_{\gamma,\gamma'}\right]^k}{k!} \tag{4.87}$$

(where the symmetric division of the rapidity interval has been explicitly included). Note now that if we sum over all numbers of interactions, we obtain a result which explicitly satisfies the unitarity bound,

$$F(\mathbf{r},\mathbf{b},\mathbf{b}',Y) \simeq \sum_{\gamma,\gamma'} P_\gamma(\mathbf{r}_0,\mathbf{b},Y/2)P_{\gamma'}(\mathbf{r}_0+\mathbf{r},\mathbf{b}',Y/2)\left[1-\mathrm{e}^{-f_{\gamma,\gamma'}}\right], \tag{4.88}$$

since $F \leq 1$. Equivalently one can write the S-matrix for the collision, $S = 1 - F$

[3]If there are n interacting dipoles in each onium, then the error in eq. (4.86) is of order $1/n$.

$$S(\mathbf{r},\mathbf{b},\mathbf{b}',Y) = \sum_{\gamma,\gamma'} P_\gamma(\mathbf{r}_0,\mathbf{b},Y/2) P_{\gamma'}(\mathbf{r}_0+\mathbf{r},\mathbf{b}',Y/2) \mathrm{e}^{-f_{\gamma,\gamma'}}. \tag{4.89}$$

One can also write the multiple-scattering corrections in terms of the operator formalism (as reviewed in section 4.3). This is how they were presented by Mueller in [19] and for reference that approach is also included here (though it should be pointed out that these are just two equivalent ways of writing the same quantity). It is necessary to introduce operators d and $d^\dagger$ for the right moving onium (a and $a^\dagger$ were for the left moving one) and one needs two distinct evolution operators to replace V: V_L for the left moving onium and V_R for the right-moving one. The operator f gives the sum of all dipole-dipole interactions for any given set of dipoles in the left and right-moving onia:

$$f = \int \mathrm{d}^2\mathbf{R}\mathrm{d}^2\mathbf{R}'\mathrm{d}^2\mathbf{c}\mathrm{d}^2\mathbf{c}' f(\mathbf{R}-\mathbf{R}',\mathbf{c},\mathbf{c}') d^\dagger(\mathbf{R},\mathbf{c}) d(\mathbf{R},\mathbf{c}) a^\dagger(\mathbf{R}',\mathbf{c}') a(\mathbf{R}',\mathbf{c}'), \tag{4.90}$$

so that the k-pomeron amplitude is

$$F^{(k)}(\mathbf{r},Y) = -\left\langle 0 \left| \mathrm{e}^{a_1+d_1} \frac{(-f)^k}{k!} \mathrm{e}^{(V_L+V_R)Y/2} d^\dagger(\mathbf{r}+\mathbf{r}_0,\mathbf{b}') a^\dagger(\mathbf{r}_0,\mathbf{b}') \right| 0 \right\rangle. \tag{4.91}$$

Reading from right to left, one creates the initial onia, then produces all possible configurations resulting from evolution through $Y/2$, determines the amplitude for k interactions for each configuration and finally gets rid of all dipoles before contracting with the vacuum state. Similarly one can write down an expression for the sum of all numbers of interactions.

4.5.1 Two pomeron exchange

The question of two-pomeron exchange is somewhat simpler than that of all including all multiple-scattering terms and accordingly there has been some analytic work on it. Mueller and Patel [18] have calculated that the total two-pomeron amplitude should be $F^{(2)}(Y)$,

$$F^{(2)}(Y) \simeq -\Lambda \left(\frac{[F^{(1)}(Y)]}{\pi k Y} \right)^2 \sim -\frac{e^{2(\alpha_{\mathbb{P}}-1)Y}}{(kY)^3} \tag{4.92}$$

where the constant Λ was given in the form of an unevaluated integral. This form for $F^{(2)}$ can be understood as follows: the 1-pomeron interaction, as a function of impact parameter, eq. (4.79), has a rapidity behaviour $e^{(\alpha_{\mathbb{P}}-1)Y}/Y^{3/2}$. When performing the integration over impact parameter, the leading-$1/r^2$ behaviour is balanced by the $\mathrm{d}^2\mathbf{r}$ integration measure and a wide region of impact parameter contributes. This effectively gives a factor Y, which leads to the total 1-pomeron interaction, eq. (4.77), having a $1/\sqrt{Y}$ factor. The 2-pomeron contribution, in impact parameter will be of the same order as the square of the 1-pomeron interaction (at least at small r). Accordingly the rapidity dependence is $e^{2(\alpha_{\mathbb{P}}-1)Y}/Y^3$. When doing the integration in impact parameter, the leading behaviour is $1/r^4$, which is no longer balanced by the $\mathrm{d}^2\mathbf{r}$ measure, so the integral is dominated by a much more central region and one does not gain an extra factor of Y, leaving the dependence of eq. (4.92).

Work has also been carried out by Białas and Peschanski [143–145] on evaluating the 1-pomeron to 2-pomeron vertex. This has been used for example for the calculation of diffraction. They also find the characteristic $1/Y^3$ factor throughout their calculations and make the point that phenomenologically this could significantly reduce the power observed in a process such as diffraction. They have said that they could also work out the magnitude of the coefficient Λ [146].

4.6 Toy model

The formalism for multiple interactions, while conceptually simple, turns out to be complex from the calculational point of view: there is an infinite number of possible configurations that should be taken into account, and one has to determine the interactions between all the dipoles in each onium. The main purpose of this thesis is to carry out these calculations.

Many of the complications arise from the presence of the transverse dimensions (which give 4 degrees of freedom per dipole). One approach developed by Mueller to gain a qualitative understanding of some of the important aspects of multiple-scattering corrections is a 'toy model', where the transverse dimensions have been left out. Starting with a 'toy onium' consisting of one 'toy dipole', one has a system where the branching rate (in rapidity, for the square of the 'onium wave function') of one dipole into two is $(\alpha_{\mathbb{P}}-1)$. One can define a generating function $Z(y,u)$, such that the probability of there being n dipoles at rapidity y is

$$P_n(y) = \frac{1}{n!}\frac{\mathrm{d}^n Z(y,u)}{\mathrm{d}u^n}. \tag{4.93}$$

The equation satisfied by Z is

$$\frac{\mathrm{d}Z}{\mathrm{d}y} = (\alpha_{\mathbb{P}}-1)(Z^2 - Z). \tag{4.94}$$

This can be compared with eq. (4.24) for the real case. Using the initial condition

$$Z(y=0,u) = u, \tag{4.95}$$

one finds the solution to be

$$Z(y,u) = \frac{u}{u + (1-u)\mathrm{e}^{(\alpha_{\mathbb{P}}-1)y}}. \tag{4.96}$$

Using eq. (4.93) this gives

$$P_n = \mathrm{e}^{-(\alpha_{\mathbb{P}}-1)y}\left(1-\mathrm{e}^{-(\alpha_{\mathbb{P}}-1)y}\right)^{n-1}, \tag{4.97}$$

so that the mean number of dipoles is

$$\mu = \sum_{n=1}^{\infty} nP_n = \mathrm{e}^{(\alpha_{\mathbb{P}}-1)y}, \tag{4.98}$$

in analogy with the real case. Eq. (4.97) can therefore be written

$$\mu P_n = \left(1-\frac{1}{\mu}\right)^{n-1} \simeq \mathrm{e}^{-n/\mu}, \tag{4.99}$$

where the approximation is valid for large μ. Note that this obeys KNO scaling [147]. The amplitude $F^{(k)}$ for the exchange of k pomerons is then

$$F^{(k)}(Y) \simeq -\sum_{m,n} P_m(Y/2)P_n(Y/2)\frac{(-f\alpha_\mathrm{S}^2 mn)^k}{k!}, \tag{4.100}$$

where f sets the strength of the interaction. Using the approximation of eq. (4.99) for P_n, this is straightforward to evaluate and gives

$$F^{(k)}(Y) \simeq -\left(-f\alpha_\mathrm{S}^2\mathrm{e}^{(\alpha_{\mathbb{P}}-1)Y}\right)^k k!. \tag{4.101}$$

Note the $k!$ divergence, which would render impossible a sum over k to produce an amplitude including all numbers of pomeron exchange. The origin of the divergence is that because of the exponential tail of the probability distribution there are always configurations whose large number of dipoles overcomes the rareness of the configuration and lead to a significant k-pomeron exchange (which is enhanced by n^k). To obtain a non-divergent amplitude including all numbers of pomeron exchange, one must first perform the sum over the number of pomerons, and then average over onium configurations:

$$\begin{aligned} S(Y) &= 1 - F(Y) \\ &= \sum_{m,n} P_m(Y/2)P_n(Y/2)\mathrm{e}^{-f\alpha_\mathrm{S}^2 nm}. \end{aligned} \tag{4.102}$$

Since the exponential term is always bound to be less than 1, the sum is now well behaved. If one carries out an approximate evaluation of the S-matrix using this form and eq. (4.97), one obtains

$$S(Y) \sim \frac{-1}{f\alpha_s^2 e^{(\alpha_{I\!P}-1)Y}} \ln\left[f\alpha_s^2\left(1+\frac{1}{f\alpha_s^2 e^{(\alpha_{I\!P}-1)Y/2}}\right)^2\right], \tag{4.103}$$

valid for $f\alpha_s^2 e^{(\alpha_{I\!P}-1)Y} \gg 1$. The leading energy behaviour of the S-matrix is therefore $S \sim e^{-(\alpha_{I\!P}-1)Y}$. This is different from the eikonal approximation [1] (advocated for example in [148–150]), where one has

$$S(Y) = e^{-F^{(1)}(Y)} = \exp\left[-f\alpha_s^2 e^{(\alpha_{I\!P}-1)Y}\right]. \tag{4.104}$$

One notes also that if the S-matrix is evaluated in the lab frame, one obtains a different answer from that in the centre-of-mass frame:

$$\begin{aligned} S_{Lab}(Y) &\simeq \sum_{m,n} P_m(0)P_n(Y)e^{-f\alpha_s^2 nm} \\ &\simeq \frac{1}{f\alpha_s^2 e^{(\alpha_{I\!P}-1)Y}}, \end{aligned} \tag{4.105}$$

also valid for $f\alpha_s^2 e^{(\alpha_{I\!P}-1)Y} \gg 1$. This relates to the argument of section 4.5 that the centre-of-mass frame is the optimum frame to use to calculate unitarity corrections, because saturation corrections can be neglected, whereas in the lab frame, they must be taken into account.

So the main points to take from the toy model, which need to be kept in mind for the subsequent work, are that (i) the determination of multiple-scattering corrections has to be done carefully otherwise one obtains a divergent answer (i.e. the sum over numbers of interactions must be performed before the sum over possible configurations); (ii) the eikonal approximation fails badly; (iii) it is important that the calculation be done in the centre of mass frame.

4.7 Equivalence to BFKL

There are a number of questions that can be raised concerning the derivation of the dipole formulation as summarised in sections 4.1 and 4.4. The main ones are the following:

- The relation between the BFKL and dipole kernels: though from the Mellin transforms one can see that kernels are the same [17], the separation into real and virtual parts is different.

- The wave function for one onium appears to be calculated in one light-cone gauge, while the second wave function seems to be calculated in the opposite light cone gauge (i.e. because the second onium is moving in the opposite direction).

- When calculating the total cross section, final state interactions don't seem to have been taken into account.

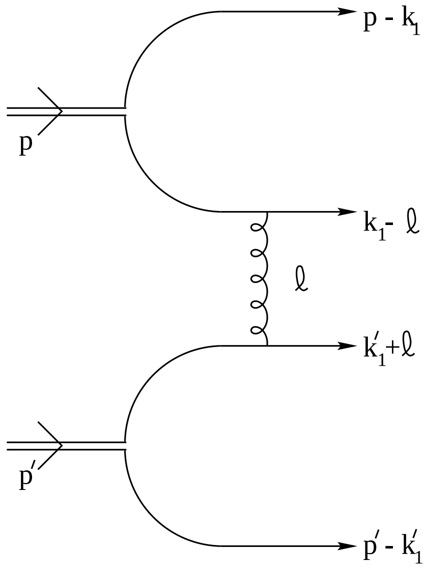

Figure 4.7: Lowest order diagram for onium-onium total cross section.

These issues were addressed in a more detailed derivation of the dipole formulation by Chen and Mueller [19], where the whole calculation, including final state corrections, was performed in a single gauge. The connection between the BFKL and dipole forms of the kernel turns out to be closely related to the question of final state interaction: if these are explicitly included then one obtains the BFKL equation. But they can be shown to cancel between real and virtual parts, leaving the dipole form.

In this approach, when calculating the total cross section, one must consider the interaction between the onia at the same time as doing the evolution. At lowest order, the onium-onium scattering cross section is

$$\sigma = \frac{\alpha_{\mathrm{S}}^2}{(2\pi)^4} \int \mathrm{d}^2\boldsymbol{\ell}\mathrm{d}^2\mathbf{k}\mathrm{d}^2\mathbf{k}' \int \mathrm{d}z_1\mathrm{d}z_1'|T|^2 \tag{4.106}$$

where the amplitude T, one of whose terms is given in figure 4.7, is

$$T = [\psi(\mathbf{k}_1, z_1) - \psi(\mathbf{k}_1 - \boldsymbol{\ell}, z_1)] \frac{-i}{\ell^2} [\psi(\mathbf{k}_1', z_1') - \psi(\mathbf{k}_1' + \boldsymbol{\ell}, z_1')] \,. \tag{4.107}$$

The wave functions are as defined in section 4.1. The large components of the momenta are p_+ and p'_-. Colour factors are taken in the large N_{C} limit. The calculation is performed in the Coulomb gauge: for a right moving gluon (k_+ large) this becomes equivalent to the light cone gauge with gauge vector $\eta_- = 1, \eta_+ = \eta_\perp = 0$ (and for left movers, it becomes the opposite light-cone gauge).

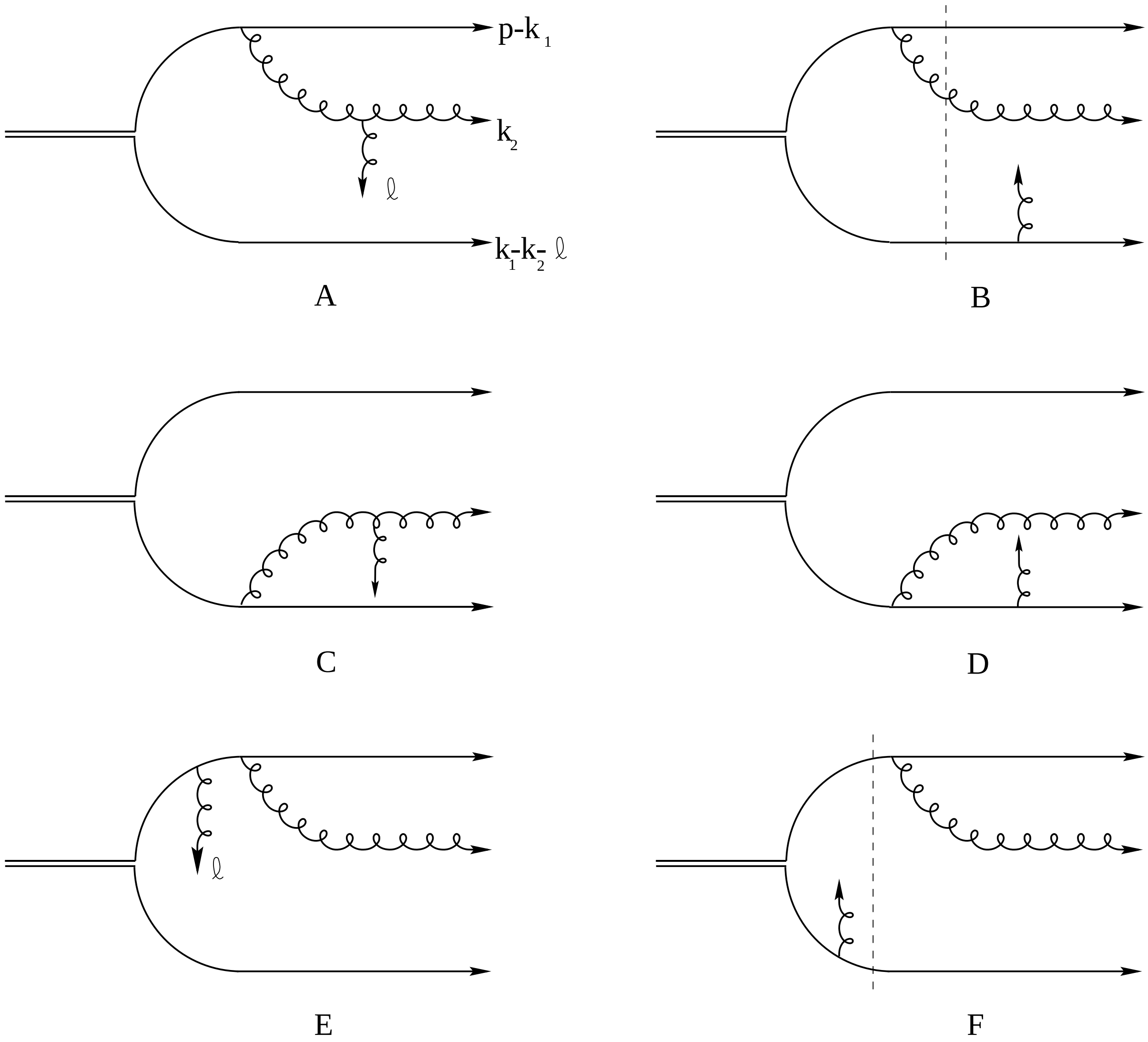

Figure 4.8: The real diagrams which include one soft gluon in the onium for onium-onium scattering. The dashed line (where shown) indicates the point where the energy denominator is needed.

4.7.1 Real corrections

The amplitude including the emission of one soft gluon corresponds to the set of light cone perturbation theory graphs shown in figure 4.8 (which replace the upper part of figure 4.7). Only shown are the graphs where the exchanged gluon is emitted from the lower dipole of the onium. A similar set of graphs contributes where the gluon is emitted from the upper dipole. Because different time-orderings correspond to different diagrams, it is necessary to distinguish graphs B and F (the sum of which would correspond to a single Feynman diagram). The contributions of the various graphs are

$$\psi_A = \frac{2g_S\boldsymbol{\epsilon}^\lambda.(\mathbf{k}_2+\boldsymbol{\ell})}{(\mathbf{k}_2+\boldsymbol{\ell})^2}\psi(\mathbf{k}_1-\mathbf{k}_2-\boldsymbol{\ell}), \tag{4.108}$$

$$\psi_B = -\psi_F = \frac{-2g_S\boldsymbol{\epsilon}^\lambda.\mathbf{k}_2}{k_2^2}\psi(\mathbf{k}_1-\mathbf{k}_2), \tag{4.109}$$

$$\psi_C = \frac{-2g_S\boldsymbol{\epsilon}^\lambda.(\mathbf{k}_2+\boldsymbol{\ell})}{(\mathbf{k}_2+\boldsymbol{\ell})^2}\psi(\mathbf{k}_1), \tag{4.110}$$

$$\psi_D = \frac{2g_S\boldsymbol{\epsilon}^\lambda.\mathbf{k}_2}{k_2^2}\psi(\mathbf{k}_1), \tag{4.111}$$

$$\psi_E = \frac{-2g_S\boldsymbol{\epsilon}^\lambda.\mathbf{k}_2}{k_2^2}\psi(\mathbf{k}_1-\mathbf{k}_2-\boldsymbol{\ell}). \tag{4.112}$$

The evaluation of the graphs A–F, is similar to the calculation for the soft gluon emission in section 4.1. There are a couple of points to note though: in graph A, the exchanged gluon ($\boldsymbol{\ell}$) is no longer emitted off the antiquark line, therefore one must take into account the different factor (coming from the different + components of the antiquark and gluon momenta) which arises from it being emitted from the gluon ($\mathbf{k}_2$).

The second important point is in the evaluation of the energy denominators: one needs to determine the difference between the energy at an intermediate point and the initial (or final) energy. The complication is that in the diagrams of figure 4.8 the second onium is still present (albeit not drawn) and it should be included in the calculation of the energy denominators. The solution to this problem is to calculate the difference in energies between two states where the second onium has not changed. In the leading-logarithmic approximation, $\boldsymbol{\ell}$ is the softest gluon and relative to all other time scales is exchanged instantaneously (i.e. it is not favourable for ℓ_- it to appear in more than one energy denominator). Therefore the second onium is modified only at the time of the exchange of gluon $\boldsymbol{\ell}$, and can be taken as constant on either side of that exchange. So only if both terms in the energy denominator are worked out on the same side of the gluon exchange, can one neglect the second onium (because it cancels between the two terms). This explains why diagrams B and F are identical except for a sign. All factors for vertices and internal lines are identical, but the energy denominators differ. In B, one should compare the intermediate energy with the initial state, giving a factor

$$\frac{1}{p_- - [(p-k_1)_- + k_{2\_} + (k_1-k_2)_-]}, \tag{4.113}$$

which reduces to $-1/k_{2-}$, once orderings of + momenta are taken into account. For graph F, the intermediate energy must be compared with the final state energy and the corresponding factor is

$$\frac{1}{[(p-k_1)_- + k_{2-} + (k_1-k_2-\ell)_-] - [(p-k_1+k_2)_- + (k_1-k_2-\ell)_-]}, \tag{4.114}$$

which reduces to $1/k_{2-}$, i.e. the same as for graph B, except for the different sign.

If we take into account all the diagrams A–F, we will obtain the real part of the BFKL kernel: adding them together gives

$$\begin{aligned}\psi^{(1)} =& \psi_A + \psi_B + \cdots + \psi_F \\ =& 2g_{\mathrm{S}}\boldsymbol{\epsilon}^{\lambda}.\left(\frac{\mathbf{k}_2+\boldsymbol{\ell}}{(\mathbf{k}_2+\boldsymbol{\ell})^2} - \frac{\mathbf{k}_2}{k_2^2}\right)(\psi(\mathbf{k}_1-\mathbf{k}_2-\boldsymbol{\ell}) - \psi(\mathbf{k}_1)).\end{aligned} \tag{4.115}$$

To see the evolution of the cross section, one writes the cross section with no emitted gluons, $\sigma^{(0)}$, as

$$\sigma^{(0)} = \alpha_{\mathrm{S}}^2 \int \frac{\mathrm{d}^2\boldsymbol{\ell}}{|\boldsymbol{\ell}|^4} f_0(\boldsymbol{\ell}) f_0'(\boldsymbol{\ell}), \tag{4.116}$$

with

$$f_0(\boldsymbol{\ell}) = \int \frac{\mathrm{d}^2\mathbf{k}_1}{(2\pi)^2} \int \mathrm{d}z_1 |\psi(\mathbf{k}_1, z_1) - \psi(\mathbf{k}_1-\boldsymbol{\ell}, z_1)|^2, \tag{4.117}$$

and an analogous formula for f_0'. The cross section, $\sigma^{(1)}$ with one emitted gluon is then

$$\sigma^{(1)} = \alpha_{\mathrm{S}}^2 \int \frac{\mathrm{d}^2\boldsymbol{\ell}}{|\boldsymbol{\ell}|^4} \left[f_1(\boldsymbol{\ell}) f_0'(\boldsymbol{\ell}) + f_0(\boldsymbol{\ell}) f_1'(\boldsymbol{\ell})\right], \tag{4.118}$$

with f_1 given as

$$f_1 = 2\frac{N_{\mathrm{C}}}{2} \int \frac{\mathrm{d}^2\mathbf{k}_1}{(2\pi)^2} \int \mathrm{d}z_1 \frac{\mathrm{d}^2\mathbf{k}_2 \mathrm{d}k_{2+}}{(2\pi)^3 2k_{2+}} |\psi^{(1)}|^2. \tag{4.119}$$

The factor of 2 accounts for the set of graphs where the exchanged gluon is exchanged from the upper dipole. The factor $N_{\mathrm{C}}/2$ is the colour factor associated with the graphs shown. There is a cutoff on the k_{2+} integration since the evaluation of the graphs in figure (4.8) assumes $k_{2+} > k_{2-} = \mathbf{k}_2^2/2k_{2+}$ (otherwise the gluon would be emitted from the lower onium). Substituting eq. (4.115) into eq. (4.118) gives

$$f_1(\boldsymbol{\ell}, Y/2) = \frac{\alpha_{\mathrm{S}} N_{\mathrm{C}}}{\pi^2} \int_0^{Y/2} \mathrm{d}y \int \frac{\mathrm{d}^2\mathbf{k}_2 \ell^2}{k_2^2(\mathbf{k}_2+\boldsymbol{\ell})^2} f_0(\mathbf{k}_2+\boldsymbol{\ell}). \tag{4.120}$$

This is simply the real emission part of the BFKL kernel. In the large-N_{C} limit the argument can be extended at leading-logarithmic level to give

$$\sigma = \alpha_{\mathrm{S}}^2 \int \frac{\mathrm{d}^2\boldsymbol{\ell}}{|\boldsymbol{\ell}|^4} f(\boldsymbol{\ell}, Y/2) f'(\boldsymbol{\ell}, Y/2), \tag{4.121}$$

where

$$f(\boldsymbol{\ell}, Y/2) = f_0(\boldsymbol{\ell}) + \frac{\alpha_{\mathrm{S}} N_{\mathrm{C}}}{\pi^2} \int_0^{Y/2} \mathrm{d}y \int \frac{\mathrm{d}^2\mathbf{k} \ell^2}{k^2(\mathbf{k}+\boldsymbol{\ell})^2} f(\mathbf{k}+\boldsymbol{\ell}, y). \tag{4.122}$$

There are still of course the virtual terms to evaluate.

If one keeps only the diagrams A–D in figure (4.8), one obtains the dipole kernel. Defining, as in section 4.1,

$$\psi(\mathbf{k}_1, z_1) = \int \mathrm{d}^2\mathbf{b}_{01} \mathrm{e}^{-i\mathbf{k}_1.\mathbf{b}_{01}} \psi(\mathbf{b}_{01}, z_1), \tag{4.123}$$

one finds

$$f_0(\boldsymbol{\ell}) = \int \mathrm{d}^2\mathbf{b}_{01} \int \mathrm{d}z_1 |\psi(\mathbf{b}_{01}, z_1)|^2 \left(2 - \mathrm{e}^{-i\boldsymbol{\ell}.\mathbf{b}_{01}} - \mathrm{e}^{i\boldsymbol{\ell}.\mathbf{b}_{01}}\right). \tag{4.124}$$

Similarly, one can express the diagrams in figure (4.8) in transverse coordinate space using

$$\psi_\alpha(\mathbf{k}_1, \mathbf{k}_2, \boldsymbol{\ell}) = \int \mathrm{d}^2\mathbf{b}_{02} \mathrm{d}^2\mathbf{b}_{01} \mathrm{e}^{-i\mathbf{k}_2.\mathbf{b}_{12} - i\mathbf{k}_1.\mathbf{b}_{01} + i\boldsymbol{\ell}.\mathbf{b}_1} \psi_\alpha(\mathbf{b}_0, \mathbf{b}_1, \mathbf{b}_2, \boldsymbol{\ell}) \tag{4.125}$$

where $\alpha = A \cdots D$, to give

$$\psi_A(\mathbf{b}_0, \mathbf{b}_1, \mathbf{b}_2, \boldsymbol{\ell}) = \frac{ig_{\mathrm{S}}}{\pi} \frac{\boldsymbol{\epsilon}^\lambda.\mathbf{b}_{02}}{b_{02}^2} \psi(\mathbf{b}_{01}) \mathrm{e}^{-i\boldsymbol{\ell}.\mathbf{b}_2}, \tag{4.126}$$

$$\psi_B(\mathbf{b}_0, \mathbf{b}_1, \mathbf{b}_2, \boldsymbol{\ell}) = \frac{-ig_{\mathrm{S}}}{\pi} \frac{\boldsymbol{\epsilon}^\lambda.\mathbf{b}_{02}}{b_{02}^2} \psi(\mathbf{b}_{01}) \mathrm{e}^{-i\boldsymbol{\ell}.\mathbf{b}_1}, \tag{4.127}$$

$$\psi_C(\mathbf{b}_0, \mathbf{b}_1, \mathbf{b}_2, \boldsymbol{\ell}) = \frac{-ig_{\mathrm{S}}}{\pi} \frac{\boldsymbol{\epsilon}^\lambda.\mathbf{b}_{12}}{b_{12}^2} \psi(\mathbf{b}_{01}) \mathrm{e}^{-i\boldsymbol{\ell}.\mathbf{b}_2}, \tag{4.128}$$

$$\psi_D(\mathbf{b}_0, \mathbf{b}_1, \mathbf{b}_2, \boldsymbol{\ell}) = \frac{ig_{\mathrm{S}}}{\pi} \frac{\boldsymbol{\epsilon}^\lambda.\mathbf{b}_{12}}{b_{12}^2} \psi(\mathbf{b}_{01}) \mathrm{e}^{-i\boldsymbol{\ell}.\mathbf{b}_1}. \tag{4.129}$$

The sum of the contributions is

$$\psi^{(1)}(\mathbf{b}_0, \mathbf{b}_1, \mathbf{b}_2) = \frac{ig_{\mathrm{S}}}{\pi}\boldsymbol{\epsilon}^{\lambda}.\left(\frac{\mathbf{b}_{12}}{b_{12}^2} - \frac{\mathbf{b}_{02}}{b_{02}^2}\right)\left(\mathrm{e}^{-i\boldsymbol{\ell}.\mathbf{b}_1} - \mathrm{e}^{-i\boldsymbol{\ell}.\mathbf{b}_2}\right)\psi(\mathbf{b}_{01}). \tag{4.130}$$

Apart from the factor $(\mathrm{e}^{-i\boldsymbol{\ell}.\mathbf{b}_1} - \mathrm{e}^{-i\boldsymbol{\ell}.\mathbf{b}_2})$, which relates to the coupling to the second onium, and the colour factors which here are left out, this is the same as eq. (4.13). Accordingly one can write (for the contribution with one soft gluon)

$$f_1(\boldsymbol{\ell}, Y/2) = \int \mathrm{d}^2\mathbf{b}_{01}\int \mathrm{d}z_1|\psi(\mathbf{b}_{01}, z_1)|^2\frac{\alpha_{\mathrm{S}}N_{\mathrm{C}}}{\pi^2}\int \mathrm{d}y\int\frac{b_{01}^2\mathrm{d}^2\mathbf{b}_2}{b_{02}^2 b_{12}^2}\left(2 - \mathrm{e}^{-i\boldsymbol{\ell}.\mathbf{b}_{12}} - \mathrm{e}^{i\boldsymbol{\ell}.\mathbf{b}_{12}}\right), \tag{4.131}$$

or at the resummed level,

$$f(\boldsymbol{\ell}, Y/2) = \int \mathrm{d}^2\mathbf{b}_{01}\int \mathrm{d}z_1|\psi(\mathbf{b}_{01}, z_1)|^2\int \mathrm{d}^2\mathbf{c}\; n(\mathbf{c}, \mathbf{b}_{01}, Y/2)\left(2 - \mathrm{e}^{-i\boldsymbol{\ell}.\mathbf{c}} - \mathrm{e}^{i\boldsymbol{\ell}.\mathbf{c}}\right), \tag{4.132}$$

where n satisfies

$$n(\mathbf{c}, \mathbf{b}_{01}, Y/2) = n_0(\mathbf{c}, \mathbf{b}_{01}) + \frac{\alpha_{\mathrm{S}}N_{\mathrm{C}}}{\pi^2}\int_0^{Y/2}\mathrm{d}y\int\frac{b_{01}^2\mathrm{d}^2\mathbf{b}_2}{b_{02}^2 b_{12}^2}n(\mathbf{c}, \mathbf{b}_{12}, y), \tag{4.133}$$

and

$$n_0(\mathbf{c}, \mathbf{b}_{01}) = \delta(\mathbf{b}_{01} - \mathbf{c}). \tag{4.134}$$

This is the real emission part of the dipole kernel, which has been obtained by ignoring graphs E and F of figure 4.8. Physically, the justification for dropping them is that they correspond to gluons produced after the onium-onium scattering has taken place, and thus will only correspond to a unitary rearrangement of the final state, and cannot affect the total cross section. The inclusion of different sets of graphs also allows one to understand why the dipole kernel has an ultra-violet divergence, whereas the BFKL kernel has an infra-red divergence. In graphs A–D, the gluon $\mathbf{k}_2$ is emitted from the onium, whose size provides a natural infra-red regulator. However in graphs E–F, since the interaction has already taken place when gluon $\mathbf{k}_2$ is emitted, the onium may have already broken up, so that there is no longer an infra-red scale in the problem, and the emission can be infra-red divergent. Since the onium is being probed with a gluon with transverse momentum $\boldsymbol{\ell}$, it isn't possible for the gluon to "resolve" an emitted gluon with $\mathbf{k}_2 \gg \boldsymbol{\ell}$, which leads to the finiteness of the BFKL kernel in the ultra-violet. The dipole kernel does not include all the graphs, which is why it need not obey this constraint.

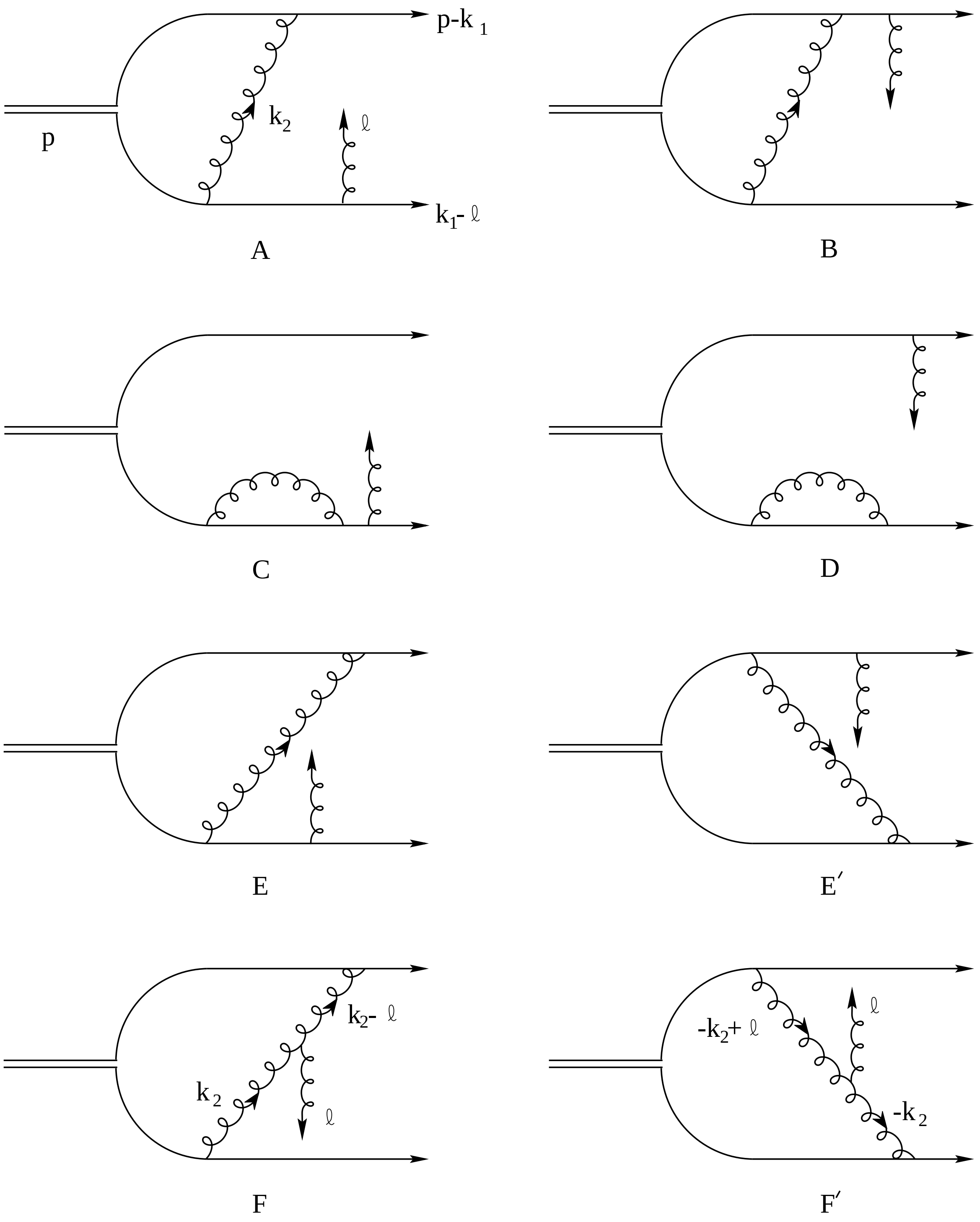

Figure 4.9: Virtual corrections to the wave function evolution.

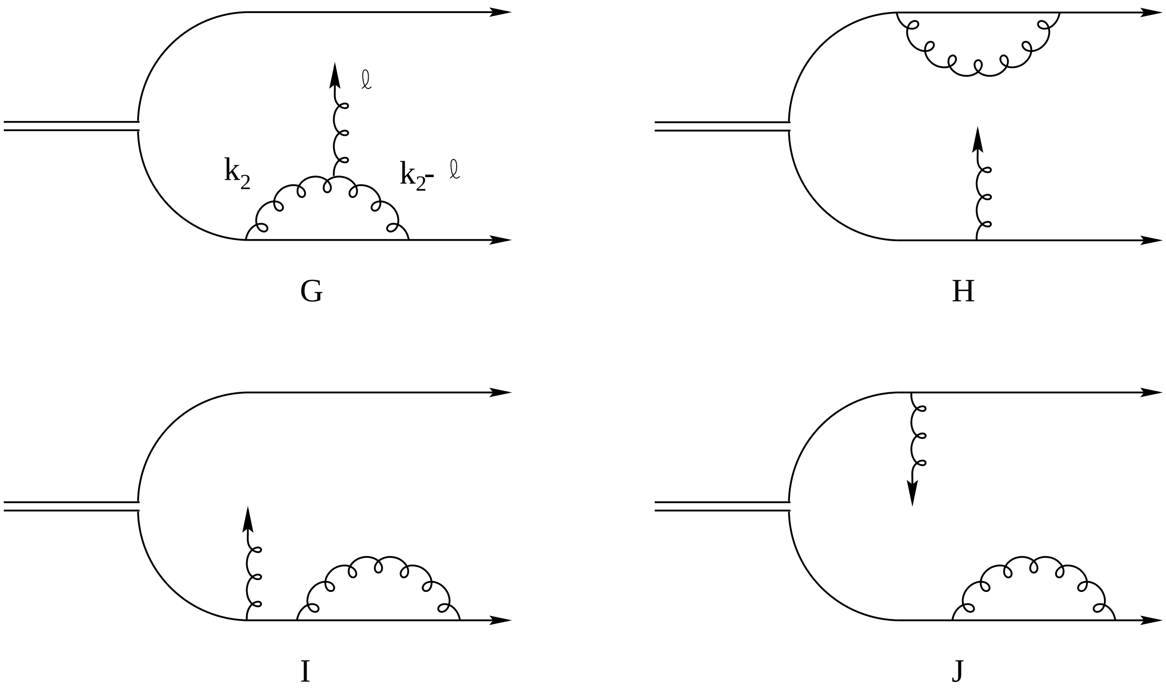

Figure 4.10: More virtual corrections to the wave function evolution.

4.7.2 Virtual corrections

The graphs contributing to the virtual corrections are shown in figures 4.9 and 4.10. Graphs which are identical except for a mirror reflection through a horizontal line have been left out in most cases (they are labelled $A', B', \dots$). The relation to light-cone perturbation theory is considerably more complicated than in the case of the real emissions, and only the basic results will be summarised here. For full details, the reader is referred to the paper by Chen and Mueller [19]. The calculations of the individual graphs yield

$$\psi_\alpha = \frac{N_\mathrm{C}}{2} \int \frac{\mathrm{d}^2\mathbf{k}_2 \mathrm{d}k_{2+}}{(2\pi)^3 2k_{2+}} \chi_\alpha, \tag{4.135}$$

where

$$\chi_A + \chi_{A'} = \chi_B + \chi_{B'} = \frac{2g_\mathrm{S}^2}{k_2^2} \left[\psi(\mathbf{k}_1 + \mathbf{k}_2) - \psi(\mathbf{k}_1 + \mathbf{k}_2 - \boldsymbol{\ell})\right], \tag{4.136}$$

$$\chi_C + \chi_{C'} = \chi_D + \chi_{D'} = \frac{-2g_\mathrm{S}^2}{k_2^2} \left[\psi(\mathbf{k}_1) - \psi(\mathbf{k}_1 - \boldsymbol{\ell})\right], \tag{4.137}$$

$$\chi_E + \chi_{E'} = -2(\chi_A + \chi_{A'}), \tag{4.138}$$

$$\chi_F + \chi_{F'} = 0, \tag{4.139}$$

$$\chi_G + \chi_{G'} = \frac{4g_\mathrm{S}^2 \mathbf{k}_2.(\mathbf{k}_2 - \boldsymbol{\ell})}{k_2^2 (\mathbf{k}_2 - \boldsymbol{\ell})^2} \left[\psi(\mathbf{k}_1) - \psi(\mathbf{k}_1 - \boldsymbol{\ell})\right], \tag{4.140}$$

$$\chi_H + \chi_{H'} = -2(\chi_C + \chi_{C'}), \tag{4.141}$$

$$\chi_I + \chi_{I'} = \chi_J + \chi_{J'} = \chi_C + \chi_{C'}. \tag{4.142}$$

Summing up all these contributions and using the result to work out the virtual contributions to $f_1(\boldsymbol{\ell})$ gives

$$f_1(\boldsymbol{\ell}, Y/2) = -\frac{\alpha_{\rm S} N_{\rm C}}{2\pi^2}\int_0^{Y/2} {\rm d}y \int \frac{{\rm d}^2\mathbf{k}_2 \ell^2}{k_2^2(\mathbf{k}_2 - \boldsymbol{\ell})^2} f_0(\boldsymbol{\ell}) \tag{4.143}$$

which is just the virtual correction term in the BFKL kernel (to relate this to the virtual corrections as they appear in eq. (3.36), it is useful to make use of eqs. (4.26) and (4.28)).

If one takes just the graphs A–D and A'–D', then after some manipulation, one can obtain for the contribution with one virtual gluon

$$f_1(\boldsymbol{\ell}, Y/2) = -\int {\rm d}^2\mathbf{b}_{01} \int {\rm d}z_1 |\psi(\mathbf{b}_{01}, z_1)|^2 \times \left(2 - {\rm e}^{-i\boldsymbol{\ell}.\mathbf{b}_{01}} - {\rm e}^{i\boldsymbol{\ell}.\mathbf{b}_{01}}\right) \frac{\alpha_{\rm S} N_{\rm C}}{2\pi^2}\int_0^{Y/2} {\rm d}y \int \frac{b_{01}^2 {\rm d}^2\mathbf{b}_2}{b_{02}^2 b_{12}^2} \tag{4.144}$$

which is just the virtual correction to the dipole kernel. As for the real part, this has been obtained by neglecting the final state interactions. The justification for this, is that the final state interactions can be shown to cancel between the real and virtual terms. If first one takes those graphs which correspond to interaction completely in the final state, for the real part, one has diagrams E and F of figure 4.8, whose contribution to f_1 is

$$N_{\rm C}\int \frac{{\rm d}^2\mathbf{k}_1}{(2\pi)^2}\int {\rm d}z_1 \int \frac{{\rm d}^2\mathbf{k}_2 {\rm d}k_{2+}}{(2\pi)^3 2k_{2+}} \frac{4g_{\rm S}^2}{k_2^2} |\psi(\mathbf{k}_1 - \mathbf{k}_2, z_1) - \psi(\mathbf{k}_1 - \mathbf{k}_2 - \boldsymbol{\ell}, z_1)|^2. \tag{4.145}$$

The virtual part comes from graphs I, I', J and J', which give a contribution

$$-N_{\rm C}\int \frac{{\rm d}^2\mathbf{k}_1}{(2\pi)^2}\int {\rm d}z_1 \int \frac{{\rm d}^2\mathbf{k}_2 {\rm d}k_{2+}}{(2\pi)^3 2k_{2+}} \frac{4g_{\rm S}^2}{k_2^2} |\psi(\mathbf{k}_1, z_1) - \psi(\mathbf{k}_1 - \boldsymbol{\ell}, z_1)|^2. \tag{4.146}$$

Integrating over $\mathbf{k}_1$, one sees that eqs. (4.145) and (4.146) cancel. There still remain the cases where only one of the interactions of the $\mathbf{k}_2$ line is a final state interaction. For the real terms, these are $A + B + C + D$ multiplied by the complex conjugate of $E + F$ which give

$$N_{\rm C}\int \frac{{\rm d}^2\mathbf{k}_1}{(2\pi)^2}\int {\rm d}z_1 \int \frac{{\rm d}^2\mathbf{k}_2 {\rm d}k_{2+}}{(2\pi)^3 2k_{2+}} 4g_{\rm S}^2 \left[\frac{\mathbf{k}_2 + \boldsymbol{\ell}}{(\mathbf{k}_2 + \boldsymbol{\ell})^2}\psi(\mathbf{k}_1 - \mathbf{k}_2 - \boldsymbol{\ell}, z_1) - \frac{\mathbf{k}_2}{k_2^2}\psi(\mathbf{k}_1 - \mathbf{k}_2, z_1) - \frac{\mathbf{k}_2 + \boldsymbol{\ell}}{(\mathbf{k}_2 + \boldsymbol{\ell})^2}\psi(\mathbf{k}_1, z_1) + \frac{\mathbf{k}_2}{k_2^2}\psi(\mathbf{k}_1, z_1)\right] . \frac{\mathbf{k}_2}{k_2^2}\Big[\psi(\mathbf{k}_1 - \mathbf{k}_2, z_1) - \psi(\mathbf{k}_1 - \mathbf{k}_2 - \boldsymbol{\ell}, z_1)\Big]^*. \tag{4.147}$$

The virtual contributions with one final state interaction come from the graphs $E + E' + F + F' + G + G' + H + H'$ of figures 4.9 and 4.10 which overall give

$$\frac{N_C}{2}\frac{\mathrm{d}^2\mathbf{k}_1}{(2\pi)^2}\int \mathrm{d}z_1 \int \frac{\mathrm{d}^2\mathbf{k}_2 \mathrm{d}k_{2+}}{(2\pi)^3 2k_{2+}}(-4g_S^2)\left[\frac{1}{k_2^2}\Big(\psi(\mathbf{k}_1+\mathbf{k}_2,z_1) - \psi(\mathbf{k}_1+\mathbf{k}_2-\boldsymbol{\ell},z_1) - \psi(\mathbf{k}_1,z_1)\right.$$
$$\left. + \psi(\mathbf{k}_1-\boldsymbol{\ell},z_1)\Big) - \frac{(\mathbf{k}_2-\boldsymbol{\ell}).\mathbf{k}_2}{(\mathbf{k}_2-\boldsymbol{\ell})^2 k_2^2}\Big(\psi(\mathbf{k}_1,z_1) - \psi(\mathbf{k}_1-\boldsymbol{\ell},z_1)\Big)\right]\Big[\psi(\mathbf{k}_1,z_1) - \psi(\mathbf{k}_1-\boldsymbol{\ell},z_1)\Big]^*. \tag{4.148}$$

To see that eqs. (4.147) and (4.148) add to give zero, one replaces $\mathbf{k}_1$ with $\mathbf{k}_1+\mathbf{k}_2$ in eq. (4.147). The third term in the first square bracket of (4.147) can then be shown to integrate to zero and the remaining terms to cancel with eq. (4.148).

4.8 Treatment of α_S

In the formulation of Mueller, α_S is kept fixed on the grounds that one does not know how to include its running. One might worry that the various results on multiple-scattering corrections may be invalid if running α_S effects become important before multiple scattering. However, it was shown in [16] that if one chooses a sufficiently small onium size, then this will not be the case. The largest impact parameter, R which will contribute to the scattering of onia of size b will satisfy $\ln R^2/b^2 \ll kY$. Accordingly (see eq. (2.49)),

$$\frac{\alpha_S(R)-\alpha_S(b)}{\alpha_S(R)} \ll \alpha_S N_C kY. \tag{4.149}$$

Multiple-scattering effects become important when $\alpha_S^2(Q_0)\mathrm{e}^{(\alpha_{\mathbb{P}}-1)Y} \sim 1$, or equivalently when $Y \sim (-\ln\alpha_S^2)/(\alpha_{\mathbb{P}}-1)$. Combining these together, ignoring factors other than α_S and N_C gives

$$\frac{\alpha_S(R)-\alpha_S(b)}{\alpha_S(R)} \ll \alpha_S N_C \ln\left(\frac{1}{\alpha_S^2}\right), \tag{4.150}$$

which means that for $\alpha_S N_C$ small the coupling can be considered to be fixed over the region of rapidity and transverse size being considered.

For phenomenology involving moderate scales (those being investigated at HERA), the running of α_S is likely to have a significant effect. There are two main sources of ambiguity when this is included: the first is simply a question of which scale to use for α_S in the kernel. The second arises from the fact that BFKL diffusion will always take one into the non-perturbative, low Q^2 region, where some procedure must be adopted to deal with the divergence of α_S. In the approach to the dipole formulation by Nikolaev and Zakharov [20, 21], running α_S is included with the following rationale: whenever there is some ambiguity about which of two scales should be used for α_S, they take the higher (Q^2) scale. To deal with infra-red problems, they freeze the running at $\alpha_{\mathrm{S}} = 0.8$. Thirdly, They modify the long distance behaviour of the kernel, essentially replacing the $|\mathbf{k}_2|^2$ denominator in eq. (4.10) with $|\mathbf{k}_2|^2 + \mu^2$, where, in their words, "μ is some kind of effective mass of gluons introduced so that colour forces do not propagate beyond the confinement radius." Their expression for the square of the wave function containing one gluon at $\mathbf{b}_2$ with momentum fraction z_2 is

$$\Phi^{(1)}(\mathbf{b}_{01}, \mathbf{b}_2; z_1, z_2) = \int_{z_0} z_1 \frac{\mathrm{d}z_2}{z_2} \int \mathrm{d}^2\mathbf{b}_2 \frac{N_{\mathrm{C}}}{8\pi^3}\mu^2 \left| g_{\mathrm{S}}\left(b_{02}^{(\mathrm{min})}\right) K_1(\mu b_{02}) \frac{\mathbf{b}_{02}}{b_{02}} - g_{\mathrm{S}}\left(b_{12}^{(\mathrm{min})}\right) K_1(\mu b_{02}) \frac{\mathbf{b}_{12}}{b_{12}} \right|^2 \Phi^{(0)}(\mathbf{b}_{01}, z_1). \tag{4.151}$$

The definition of $b_{i2}^{(\mathrm{min})}$ is $\min(b_{i2}, b_{01})$, while the effective gluon mass enters through the modified Bessel function K_1. The transverse position running coupling relates to the normal momentum coupling through

$$\frac{g_{\mathrm{S}}^2(b)}{4\pi} = \alpha_{\mathrm{S}}(Q^2 = C^2/b^2) \tag{4.152}$$

where $\alpha_{\mathrm{S}}(Q^2)$ is taken as in eq. (2.50) and C is quoted as being $C \simeq 1.5$. When all the transverse sizes are sufficiently small that one can neglect the running of α_{S}, eq. (4.151) reduces to the fixed coupling kernel (eq. (4.21)). Using this form for the inclusion of the running of α_{S}, Nikolaev, Zakharov and collaborators have produced an extensive phenomenology relating to HERA physics (see for example [118] and references therein).

In an alternative approach to the introduction of running α_{S}, Anderson, Ross and Sotiropoulos [151] start with a form of eq. (4.10) which includes a running coupling whose scale is the transverse momentum of the emitted gluon (as for a time-like cascade [31]), and with the aid of Borel transform (which effectively puts the divergences into a manageable form during the intermediate stages of the calculation, avoiding the need for somewhat arbitrary infra-red cut-offs), arrive at the following form for the component of the squared wave function with one gluon:

$$\Phi^{(1)}(\mathbf{b}_{01}, \mathbf{b}_2; z_1, z_2) = \frac{N_{\mathrm{C}}}{2\pi^3} \int_{z_0}^{z_1} \frac{\mathrm{d}z_2}{z_2} \int \frac{\mathrm{d}^2\mathbf{b}_2}{b_{02}^2 b_{12}^2} \int_0^\infty \mathrm{d}\tau \mathrm{d}\tau' \, J_1(\tau) J_1(\tau') \int_0^1 \frac{\mathrm{d}\omega}{\sqrt{\omega(1-\omega)}}$$
$$\times \left\{ \alpha_{\mathrm{S}}(\lambda^2/d^2) b_{01}^2 + \left[\alpha_{\mathrm{S}}(\lambda^2/b_{02}^2) - \alpha_{\mathrm{S}}(\lambda^2/d^2)\right] b_{12}^2 + \left[\alpha_{\mathrm{S}}(\lambda^2/b_{12}^2) - \alpha_{\mathrm{S}}(\lambda^2/d^2)\right] b_{02}^2 \right\} \Phi^{(0)}(\mathbf{b}_{01}, z_1), \tag{4.153}$$

where

$$d^2(\omega) = |\mathbf{b}_{02}|^{2\omega} |\mathbf{b}_{12}|^{2(1-\omega)}, \tag{4.154}$$

$$\lambda^2(\tau, \tau', \omega) = \tau^{2\omega} \tau'^{2(1-\omega)}, \tag{4.155}$$

so that the argument of the running coupling in the different terms is a complicated function of b_{02} and b_{12}. Unlike the form used by Nikolaev and Zakharov, one does not have the product of couplings with different arguments. As one would expect, if one takes α_S to be fixed, then eq. (4.153) reduces to eq. (4.21). It is also possible to leave the kernel in a Borel transformed form and for example write the corresponding eigenvalue equation, to try and understand the details of its infra-red behaviour, but results on this have not yet appeared.

Because of the many complexities (and associated arbitrariness) which would arise with the use of a running coupling, it has been decided, in the work of the following chapters, to use a fixed α_S. The value which will be used is $\alpha_S = 0.177$, corresponding to a scale of the order of 10 GeV, which is a compromise between phenomenological relevance (i.e. scales which are appropriate to HERA, the Tevatron or the LHC) and being in a region where the running and infra-red effects are not too important. Most of the results can be easily extrapolated to larger (momentum) scales.

CHAPTER 5

A Monte Carlo approach to the dipole formulation

This chapter will discuss the two main numerical tools which have been developed to study onium evolution and interaction. The first is a program which performs numerical solution of the integro-differential equation for evolution (in rapidity) of the mean dipole distribution as a function of dipole size. This is a quick method of obtaining inclusive information (including the single-pomeron onium-onium scattering cross section) which can then be used to check the results from the second method, a Monte Carlo simulation of the evolution. The numerical evolution also offers a simple way of examining the effects on the evolution of cutoffs on dipole size. This is important because in the Monte Carlo simulation one is forced to have an ultra-violet cutoff which is a finite fraction of the initial onium size and one needs to know how important this is.

The Monte Carlo method gives the complete distribution of dipoles, i.e. the probability of obtaining any given configuration of dipoles. This is essential when calculating multiple-scattering corrections. The Monte Carlo approach is divided into two stages: the simulation of the dipole branching, to produce dipole configurations, and the determination of the interaction between dipole configurations.

5.1 Numerical evolution of the dipole distribution

The rate (in rapidity) of emission of a gluon from a dipole of size b_{01} ($=b$), where the gluon is at distances c_0 and c_1 (which it is sometimes more convenient to refer to as b_{02} and b_{12} respectively) from the two sources of the dipole, is

$$\frac{\alpha_{\mathrm{S}} N_{\mathrm{C}}}{2\pi^2} \frac{b^2}{c_0^2 c_1^2}. \tag{5.1}$$

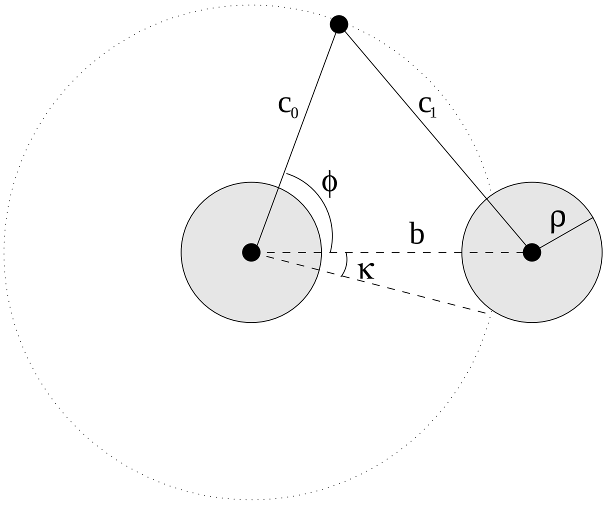

Figure 5.1: The geometrical arrangement of the source dipole and the emitted gluon — the emission rate is integrated over the circle

In the large N_{C} limit this is equivalent to the production of two new dipoles, c_0 and c_1 and the removal of the initial one.

This branching can be cast as a differential equation for the evolution in rapidity of the dipole distribution. It can then be solved using standard numerical techniques. This is considerably easier if the distribution depends only on dipole sizes and not on their orientation or position. Defining $n(c, y)$ to be the number density of dipoles of size c (the measure of the distribution is $\mathrm{d}\ln c$ rather than $\mathrm{d}c$) with rapidity less than y, one can see that the evolution will be of the following form:

$$\frac{\mathrm{d}n(c,y)}{\mathrm{d}y} = K \otimes n = \int_{\rho}^{R} K_E(c,b)n(b,y)\mathrm{d}b - V(c,\rho,R)n(c,y). \tag{5.2}$$

The full kernel K comprises two parts: $K_E(c, b)$ is the rate of production of dipoles of size c from one of size b by gluon emission; V is the rate of loss of dipoles of size c as a result of their having emitted a gluon, which is the virtual correction. A lower cutoff ρ is introduced to regulate the divergence of the integral for small size dipoles, while the upper cutoff R is needed for the numerical treatment later so that one has a finite number of bins.

The emission part of the kernel, $K_E(c_0, b)$, is the rate of production of a dipole of size c_0, regardless of the size of the other produced dipole, c_1. Therefore K_E can be evaluated by integrating out c_1 from the emission rate. This is achieved by using using polar coordinates (c_0, ϕ), to give:

$$K_E(c_0,b) = \frac{\alpha_{\mathrm{S}} N_{\mathrm{C}}}{\pi^2} \int_{\kappa}^{2\pi-\kappa} \frac{b^2 \mathrm{d}\phi}{c_0(b^2 + c_0^2 - 2bc_0\cos\phi)}. \tag{5.3}$$

The lower limits, κ and $2\pi - \kappa$, arise from the cutoffs on dipole size: if $(b-\rho) \leq c_0 \leq (b+\rho)$ then there are values of ϕ where c_1 would be smaller than the cutoff ρ and κ is chosen so as to exclude these (see figure 5.1). Otherwise κ is 0. An analogous method is used to implement the upper cutoff (which is defined such that neither of the produced dipoles may be larger than R). A factor of two is included in K_E to allow for a similar integration keeping c_1 constant and eliminating c_0 — this gives the production of two dipoles per emitted gluon.

When neither cutoff is relevant the integral gives

$$K_E(c,b) = \frac{2\alpha_{\mathrm{S}} N_{\mathrm{C}}}{\pi} \frac{b^2}{c|c^2-b^2|}. \tag{5.4}$$

When either of the cutoffs is relevant, then the necessary calculations can be performed using:

$$\int \frac{d\phi}{b^2+c_0^2-2bc_0\cos\phi} = \frac{2}{|b^2-c_0^2|}\tan^{-1}\left(\frac{|b+c_0|}{|b-c_0|}\tan\phi/2\right). \tag{5.5}$$

The limits κ on ϕ are chosen to satisfy: $(b^2+c_0^2-2bc_0\cos\kappa) = \rho^2$ (or R^2 as applicable).

The virtual corrections correspond to the removal of the source dipole when it produces a pair of child dipoles by gluon emission. Therefore for each dipole produced, half a dipole of the source size is removed and accordingly, V is:

$$V(c,\rho,R) = \frac{1}{2}\int_\rho^R K_E(c',c)dc'. \tag{5.6}$$

5.1.1 Tricks for Numerical Solution

From analytical approximations, one expects the solution of the BFKL equation to extend over a wide range of scales: its width in $\ln c$ is should behave as $\ln(c_{\max}/c_{\min}) \sim \sqrt{y}$, since for large y, and an initial source of size b

$$n(c,b,y)\mathrm{d}\ln c \simeq \frac{b}{c\sqrt{\pi k y}} \exp\left((\alpha_{\mathrm{IP}}-1)y - \frac{\ln^2(c/b)}{ky}\right)\mathrm{d}\ln c. \tag{5.7}$$

Therefore it is logical to bin the distribution uniformly in $\ln c$ rather than in c. This will have other advantages as well, as we shall see shortly.

Since the distribution is binned, the kernel must be discretised into a two dimensional array, connecting child and parent bins. Furthermore every element of this array needs to be accessed at each step of the rapidity evolution. Given that the evaluation of many of the kernel elements will involve a numerical integration, generating these elements each time they are needed is effectively ruled out. An alternative possibility would be to generate all the kernel elements once, and then to store them for subsequent use. If one wishes to use a large number of bins, then considerable amounts of memory would be needed (1000 distribution bins, with double precision storage of the kernel elements, would require 8MB): this would constrain the maximum number of allowed bins (though probably not too severely) and lead to a long startup time for the program. However, a large proportion of the kernel elements are independent of the cutoffs, with $K(c, b) = K(c/b)$, or for the discretised kernel $K_d(i, j) = K_d(i - j)$. Here one sees the other advantage of a uniform spacing in $\ln c$, namely that a given ratio of scales always corresponds to the same difference in bin number (this would not apply with a uniform spacing in c).

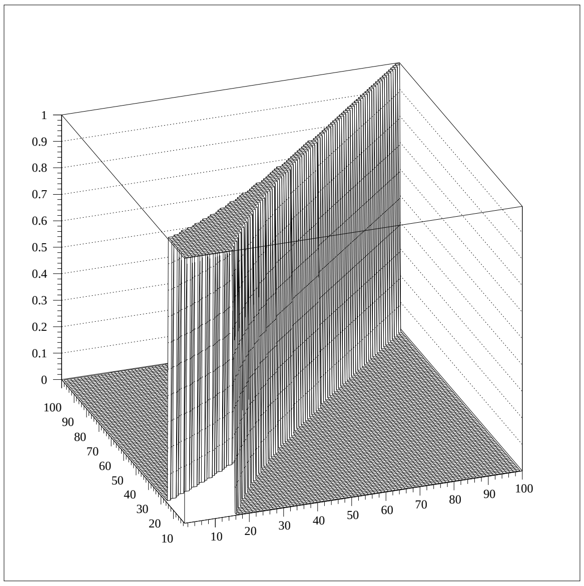

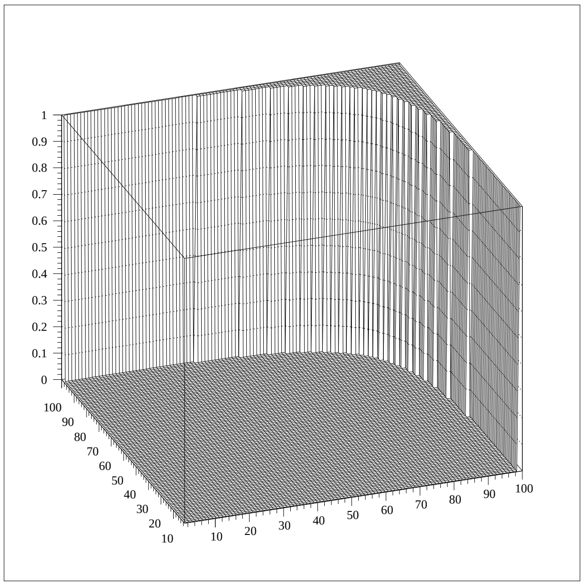

Figure 5.2: Raised points correspond to kernel elements which depend on the lower (left-hand plot) and upper (right-hand plot) cutoffs, using 100 bins of logarithmic size 0.05. The horizontal axes correspond to parent and child bin numbers.

Figure 5.2 shows the regions of the discretised kernel which depend on the two cutoffs — one can see that for a distribution with M bins, the number of kernel elements to be stored will be proportional to M, and not M^2 as would be the case if one were storing each element of the kernel. This is because the regions dependent on the cutoffs are strips whose width depends only on the bin size, while their lengths depend on the number of bins. When evaluating the kernel, first one calculates only the real component. Then, since the virtual corrections are just minus half the integral over all child sizes of the rate of production of new dipoles, in the discretised case, $V_d(i) = -\sum_j K_d(j, i)/2$.

To further improve speed, information is stored about the distribution of cutoff dependence such that no floating point operations are needed to obtain the value of a particular bin of the full kernel. To achieve sufficient accuracy, especially in the region where the lower cutoffs are relevant, it was not sufficient when obtaining kernel elements simply to sample the kernel at one point — instead it was necessary to integrate at least either over the range of child or of parent

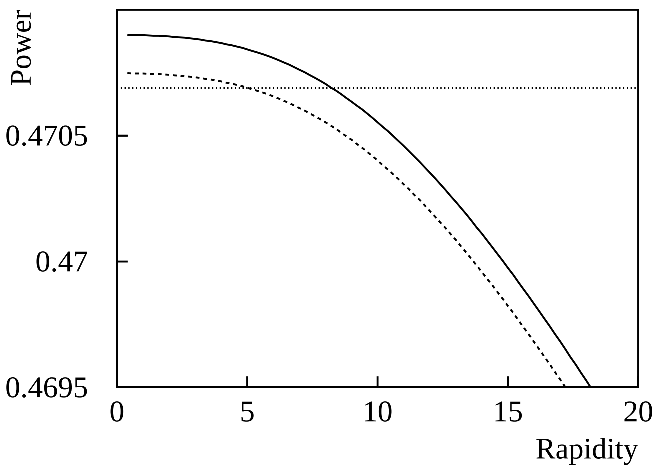

Figure 5.3: Test of the numerical evolution of the dipole distribution: starting with a $1/c$ distribution the power associated with the growth of the integrated (weighted with c) distribution is plotted as a function of rapidity. The solid curve corresponds to 600 bins of logarithmic size 0.05; the dashed curve, 1200 bins of size 0.025; and the dotted line is the analytically predicted power of $(\alpha_{\mathbb{P}} - 1)$.

dipole sizes. The integration was performed over the child sizes, at several values of the parent size. Some transformations were needed at the edge of the region where the cutoff came into play in order to be able to perform the numerical integration with sufficient accuracy. Though the integral could have been performed analytically outside the lower cutoff region when the higher cutoff was not relevant, the special approach would in any case have been necessary when the upper and lower cutoffs set in close to one another.

5.1.2 Testing

Various test have been performed, essentially ensuring that the dipole distribution does tend to the analytically predicted one at high rapidities. One test which clearly indicates both effect of bin size and of the cutoffs is shown in figure 5.3. This starts with a $1/c$ distribution. The figure shows the power growth associated with the moment $\int \mathrm{d}(\ln c)\, cn(c)$, which analytically would be a constant: $(\alpha_{\mathbb{P}} - 1)$ (shown by the flat line). In fact one sees that at small rapidities, the power is constant but very slightly different from the $(\alpha_{\mathbb{P}} - 1)$. This is a consequence of the discretisation in dipole size, and one finds that the discrepancy is roughly proportional to the square of the bin size. As rapidity increases, the growth of this moment becomes sensitive to the cutoffs (which are in the same positions for the two bin sizes), because the evolution close to the cutoffs is reduced. Nevertheless, for the ranges of variables and parameters used (which are typical of those which will be used in later calculations), these numerical artefacts are too small to be of importance.

5.2 Monte Carlo simulation of dipole branching

To perform a Monte Carlo simulation of dipole branching, one needs to to write the evolution equations in terms of the probability of a dipole (with sources at positions $\mathbf{b}_0$ and $\mathbf{b}_1$) emitting a gluon at a position $\mathbf{b}_2$ and with a fraction e^{-y} of the light-cone momentum of the slower component of the dipole:

$$\frac{\mathrm{d}P}{\mathrm{d}y\mathrm{d}^2\mathbf{b}_2} = e^{-y/\lambda}\frac{\alpha_{\mathrm{S}}N_{\mathrm{C}}}{2\pi^2}\frac{b_{01}^2}{b_{02}^2 b_{12}^2}. \tag{5.8}$$

The effective lifetime in rapidity (y), λ, of the dipole, is related to the virtual corrections (or more intuitively, conservation of probability):

$$\lambda^{-1} = \frac{\alpha_{\mathrm{S}}N_{\mathrm{C}}}{2\pi^2}\int\frac{b_{01}^2\mathrm{d}^2\mathbf{b}_2}{b_{02}^2 b_{12}^2}. \tag{5.9}$$

In the limit of large N_{C}, the colour structure means that the two new dipoles which arise ($\mathbf{b}_{02}$ and $\mathbf{b}_{12}$) can themselves independently emit gluons, while the original colour dipole is effectively destroyed. This branching of dipoles repeats itself until the rapidity of any new gluons which would be produced exceeds the maximum rapidity available. Through this branching process, one can establish the probability of any given configuration of dipoles, or equivalently generate a set of random dipole configurations with the appropriate weights.

As discussed in chapter 4, one of the aspects of eq. (5.8) is that it has non-integrable divergences at $b_{02} = 0$ and $b_{12} = 0$. This leads to the integral for λ^{-1} being infinite. A solution to this problem is to introduce a cutoff on the dipole size, eliminating any region of $\mathbf{b}_2$ where $b_{02} < \rho$ or $b_{12} < \rho$. This has to be used in both eq. (5.8) and eq. (5.9). It is also useful to have the facility of an upper cutoff, for the purpose of being able to accurately compare results from the Monte Carlo simulation of branching with those from the differential equation solution discussed in the previous section (which is forced to have an upper cutoff).

5.2.1 Generation of $\mathbf{b_2}$

Considering eq. 5.8, one can see that there are two regimes where the generation of the transverse should be relatively easy: for large b_{02} and b_{12} there is effectively a $\mathrm{d}b_2/b_2^3$ distribution which is nearly circularly symmetric: this can be integrated and inverted, for use in a Monte Carlo simulation, without difficulty. For b small, then again there is a simple radial distribution, this time around each of the sources: $\mathrm{d}b_2/b_2$ with a nearly circularly symmetric distribution.

The difficulty comes in linking together the two regimes: for $b_{02} \sim b_{01}$ there is a region where b_{12} is small, leading to a divergence (regulated by a cutoff); so to go from small b_2 to

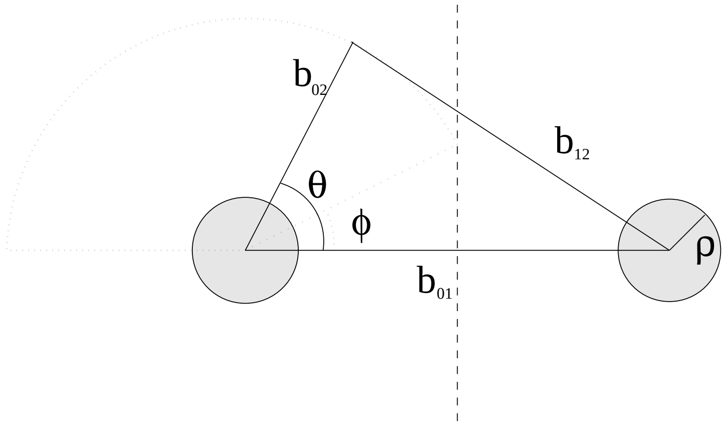

Figure 5.4: Generation of gluon transverse position: points are only produced in the upper left hand quadrant. For a given b, this places restrictions on the angle θ, in particular a lower limit ϕ. The lower cutoff is easy to implement, because there is never any danger of $b)_{12} < \rho$.

large b_2 would be difficult without dividing the range of b_2 into three regions. Normally this might not be a problem, however the probabilities of being in the different regions of b_{02} are a non trivial function of b_{01} and the cutoffs: while the cutoffs stay fixed in a particular run, the value of b_{01} is different for each emission and one would have to parameterise the probabilities of being in the different regions as function of b_{01} – while possible, this would add complexity to the program and slow it down.

An alternative solution is to use the four-fold symmetry about the centre of the parent dipole: one generates the correct distribution in one quadrant and then randomly rotates each generated position to one of the four quadrants. To generate the position in the quadrant, first one chooses a value for b_{02}. To obtain the correct asymptotic distribution one generates the following distribution:

$$P_{\text{approx}}(b) \propto \frac{1}{b_{02}(b_{01}^2 + k^2 b_{02}^2)}. \tag{5.10}$$

The constant k can be tuned to give the best fit to the actual distribution:

$$P(b_{02}) \propto \int_{\phi}^{\pi} \mathrm{d}\theta \frac{1}{b_{02}(b_{01}^2 + b_{02}^2 - 2b_{01}b_{02}\cos\theta)}. \tag{5.11}$$

The angle ϕ is shown in fig. 5.4 and depends on b in such a way as to ensure that all points are generated within the quadrant. The actual distribution is obtained from the approximate one by accepting only a certain fraction of the generated points:

$$P_{\text{acceptance}}(b_{02}) = \frac{P(b_{02})/P_{\text{approx}}(b_{02})}{[P/P_{\text{approx}}]_{\max}}. \tag{5.12}$$

With $k = 1$ the efficiency of generation is about $1/2$, so one requires on average about 4 random numbers to generate a value of b_{02}.

Generation of the angle is relatively simple since the angular distribution is easily integrated and inverted. If an upper cutoff is being implemented, then the angle is generated regardless of the cutoff and then the point rejected if it falls outside the allowed region.

5.2.2 Generation of the rapidity

The lifetime of the dipole is given by eq. (5.9) with the condition that the integration region excludes the areas $b_{02} < \rho$ and $b_{12} < \rho$ (and if an upper cutoff is implemented, then also the areas $b_{02} > R$ and $b_{12} > R$). In principle this could be evaluated each time a dipole decays, but the time taken to accurately evaluate the integral would probably become the limiting factor in determining the speed of the Monte Carlo. But since the cutoffs remain fixed during a single run, the decay rate is effectively a function only of the parent dipole size, and it is possible to use a combination of lookup tables and analytic approximations to allow quick access to the rate of decay for any particular parent size. To do this the range of parent sizes is broken up into several regions:

- A region of small dipole sizes, affected by the lower cutoff: use a lookup table.
- Intermediate dipole sizes, not significantly affected by either cutoff: analytic approximation is suitable.
- Large dipole sizes, affected by the upper cutoff: use a lookup table
- Dipole sizes very close to the upper cutoff: use a lookup table

The tabulation is uniform in the logarithm of the dipole size. The reason for having two regions for large dipoles is that very close to the upper cutoff, the rate drops sharply and the easiest way to model this accurately is to divide the region into two. The intermediate region where the integral is approximated analytically is necessary if the ratio of the cutoffs is large, to avoid sparse sampling of the regions near the cutoffs, and is in any case necessary if no upper cutoff is used. In this case the value of the integral is taken to be $2\alpha_{\mathrm{S}} N_{\mathrm{C}}/\pi \ln(b_{01}/\rho)$. Once the rate is obtained, it is straightforward to generate the appropriate exponential distribution for the lifetime. If the resulting total rapidity is larger than the maximum rapidity to which one is evolving the onium then that dipole is not branched.

5.2.3 Storage of the dipole distribution

It is often necessary to store the results of the evolution so that it can subsequently be analysed — information that is needed is a complete list of the dipoles that have been produced, knowledge about whether or not they have branched (and if so, some form of link to the relevant child dipoles) as well as the positions and rapidities of the gluons or quarks of which they are comprised. The branching process can result in a fairly complex tree of dipoles and its structure is most easily held with the use of pointers indicating the immediate children of each dipole (in principle, one could also have pointers back to the parents as well). When generating a tree there are at least two obvious approaches: one can evolve each dipole at a particular level of the tree and then move on to the next level, repeating until one reaches a level where none of the dipoles branch (because by doing so they would exceed the rapidity limit). An alternative is to use recursion: the basic routine branches a dipole, calls itself to perform the branching of the two child dipoles and then returns. If the branching is not allowed (due to the rapidity limit) then it simply returns. This causes it to go down one branch of the tree until it can't go any further and then to take one step back and try the other branch, evolving it if it can or taking more steps back until nothing remains to be evolved. There is probably relatively little difference between the two methods — recursion was used because it was simpler to code.

The Monte Carlo program was written in Fortran 90: this allowed the use of data types for a dipole and for a gluon. For example the data type for a dipole contains the size of the dipole, pointers to data types for the gluons or quarks that make up the dipole and pointers to the child dipoles. It also made possible the use of the recursive evolution. C would also have been suitable. Details of the code and instructions on its use are given in appendix C.

5.2.4 Testing

A variety of tests were carried out during the development of the Monte Carlo simulation (for example testing that the various random variables that are generated, such as b_{02}, do have the correct distributions). Once these have been shown to work, the main test is that the final distribution of dipoles is correct.

Figure 5.5 shows a comparison of the Monte Carlo and differential equation solutions for the distribution of dipole sizes. A large lower cutoff is used to allow large statistics to be obtained (the smaller the value of the cutoff, the larger the number of dipoles in each configuration, so it takes longer to generate the configurations), and a small upper cutoff is used because large dipoles are rare so to get good results for large dipole sizes, one needs very high statistics. The distribution that is shown is weighted with c (so that the asymptotic distribution would be flat). One should therefore bear in mind that the distribution for larger dipole sizes is based on far fewer events than for small dipole sizes. Because of this it was necessary to generate a large number of onium configurations (over 20 million!) to get the observed agreement. Since the two approaches are essentially solving the same equation one expects perfect agreement to within the errors of the Monte Carlo. This very good agreement between the two approaches is in fact seen in the test run shown here.

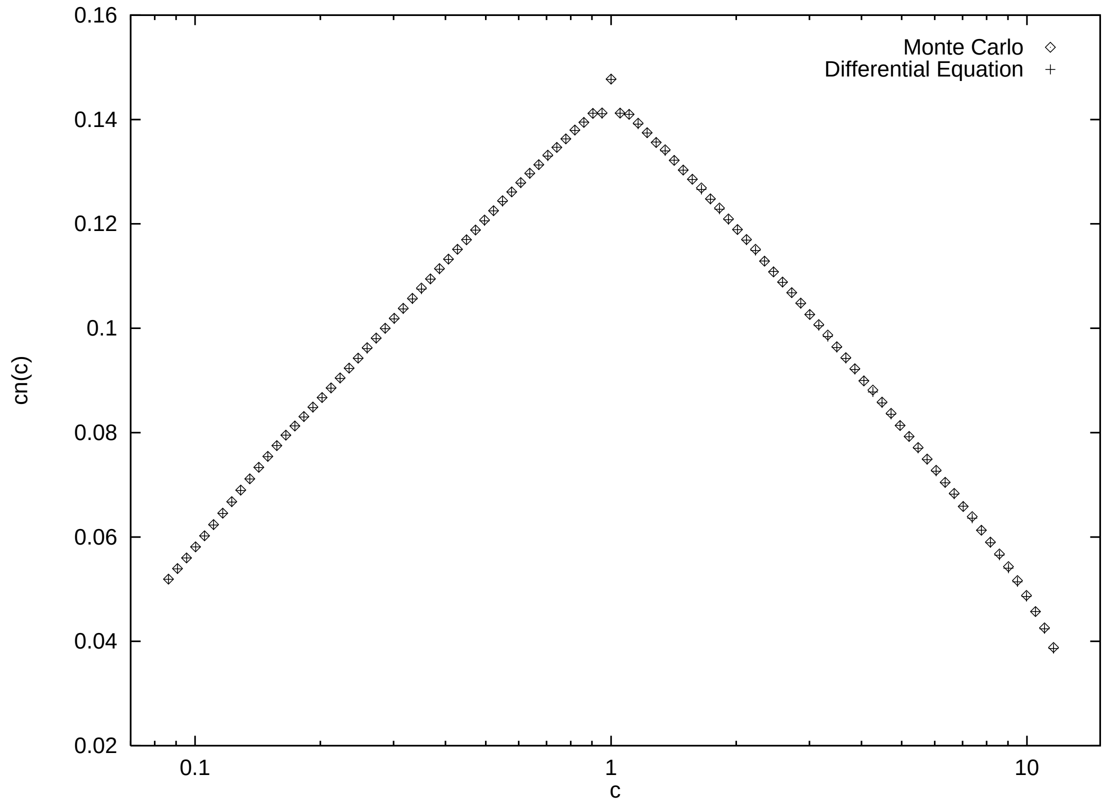

Figure 5.5: Comparison of Monte Carlo results and differential equation solution for dipole distribution: $y = 6$, $\alpha_S \simeq 0.18$, parent size = 1.0, 99 bins of logarithmic size 0.05. The initial dipole is in the centre of the middle bin.

5.3 Interactions between onia

Interactions between the onia can be determined for the differential equation solution of the number of dipoles and also from the Monte Carlo simulation of onium wave function branching. The calculation of the scattering amplitude was discussed in detail in chapter 4 — the results relevant to the numerical evaluations are summarised here.

If one just has the number of dipoles as a function of size, $n(c, y)$ then for a total rapidity Y, the two-gluon exchange (one-pomeron) forward scattering amplitude, $F(Y)$, is

$$F(b, b', Y) = \int \frac{\mathrm{d}c}{c}\frac{\mathrm{d}c'}{c'}\pi\alpha_S^2 c_<^2 \left(1 + \ln\frac{c_>}{c_<}\right) n(c, b, y) n(c', b', Y - y), \tag{5.13}$$

which, using the dipole distribution as determined in section 5.1, can be evaluated by discretising the integral. The result should be (and is) independent of the value of y, the division of the rapidity between the two onia (at least when cutoffs are unimportant), since the cross section must be independent of frame. Using the dipole distributions obtained by differential equation evolution, the integrations of eq. (5.13) are straightforward to carry out numerically (simply a sum over all bins of a pair of dipole distributions).

If one wishes to obtain more detailed information about onium-onium scattering, such as the distribution of the amplitude in impact parameter, or an understanding of the multi-pomeron contributions one needs to use results from the Monte Carlo simulation of the evolution. One wishes to obtain the amplitude $F(\mathbf{b}, \mathbf{b}', \mathbf{r}, Y)$, for elastic scattering between two onia of sizes (and orientations) $\mathbf{b}$ and $\mathbf{b}'$, whose centres are separated by a transverse distance $\mathbf{r}$, with a total rapidity between them of Y.

As discussed in chapter 4, let γ be a particular dipole configuration for an onium, which contains dipoles of position and size $(\mathbf{r}_1, \mathbf{c}_1) \ldots (\mathbf{r}_{n_\gamma}, \mathbf{c}_{n_\gamma})$. The interaction between two such onia, moving in opposite directions is:

$$f_{\gamma,\gamma'} = \sum_{i=1}^{n_\gamma} \sum_{i'=1}^{n'_{\gamma'}} f(\mathbf{r}_i - \mathbf{r}'_{i'}, \mathbf{c}_i, \mathbf{c}'_{i'}), \tag{5.14}$$

where $f(\mathbf{r}, \mathbf{c}, \mathbf{c}')$, the interaction between dipoles of size $\mathbf{c}$ and $\mathbf{c}'$, whose centres are separated by $\mathbf{r}$ is:

$$f(\mathbf{r}, \mathbf{c}, \mathbf{c}') = \frac{\alpha_{\mathrm{S}}^2}{2} \left[\ln \frac{|\mathbf{r} + \mathbf{c}/2 - \mathbf{c}'/2||\mathbf{r} - \mathbf{c}/2 + \mathbf{c}'/2|}{|\mathbf{r} + \mathbf{c}/2 + \mathbf{c}'/2||\mathbf{r} - \mathbf{c}/2 - \mathbf{c}'/2|} \right]^2 . \tag{5.15}$$

One has to average $f_{\gamma,\gamma'}$ over dipole configurations γ, γ' of the two onia. Therefore at the level of one pomeron exchange, the elastic amplitude is:

$$F^{(1)}(\mathbf{b}, \mathbf{b}', \mathbf{r}, Y) = \sum_{\gamma,\gamma'} P_\gamma(\mathbf{r}_0, \mathbf{b}, y) P_{\gamma'}(\mathbf{r}_0 + \mathbf{r}, \mathbf{b}', Y - y) f_{\gamma,\gamma'}, \tag{5.16}$$

where $P_\gamma(\mathbf{r}_0, \mathbf{b}, y)$ is the probability of obtaining a dipole configuration γ after evolution through y of an onium of size $\mathbf{b}$ centred at $\mathbf{r}_0$. The result should not depend on y (see appendix B).

For the contributions to the amplitude involving the exchange of k pomerons, one evaluates

$$F^{(k)}(\mathbf{b}, \mathbf{b}', \mathbf{r}, Y) = -\frac{1}{k!} \sum_{\gamma,\gamma'} P_\gamma(\mathbf{r}_0, \mathbf{b}, y) P_{\gamma'}(\mathbf{r}_0 + \mathbf{r}, \mathbf{b}', Y - y)(-f_{\gamma,\gamma'})^k, \tag{5.17}$$

and summing all numbers of pomeron exchange one gets an amplitude F which explicitly satisfies the unitarity bound:

$$F(\mathbf{b}, \mathbf{b}', \mathbf{r}, Y) = \sum_{\gamma,\gamma'} P_\gamma(\mathbf{r}_0, \mathbf{b}, y) P_{\gamma'}(\mathbf{r}_0 + \mathbf{r}, \mathbf{b}', Y - y)(1 - \mathrm{e}^{-f_{\gamma,\gamma'}}). \tag{5.18}$$

These last two equations are approximations based on there being a large number of dipoles interacting. Because one is not taking into account saturation in the wave function, the multi-pomeron contributions do depend on the frame in which the calculation is performed, and one should take $y = Y/2$, where these saturation corrections should be smallest.

5.3.1 Implementation considerations

One of the main difficulties in calculating onium-onium scattering amplitudes is the large numbers of interactions which have to be worked out: in principle the product of the numbers of dipoles in each onium, multiplied by the number of points at which one needs to know the interaction.

The first way to ease the problem is to note that the dipole-dipole interaction, eq. (5.15), is relatively local: at large distances it dies off as $1/r^4$ where r is the separation between the centres of the dipoles (in two dimensions, the field at a distance r from a dipole is proportional to $1/r^2$, and therefore so is the potential of a second dipole in that field; since the interaction is proportional to the square of the dipole-dipole potential, the interaction must die off as $1/r^4$). Therefore it should be safe to neglect the interaction between dipoles if their separation is sufficiently large, say greater than twice the sum of their sizes. This is found to reproduce the total dipole-dipole interaction to better than one percent[1].

One will generally want to know the amplitude at many different impact parameters (i.e. onium-onium separations), for example to work out the total cross section. One way to do this is to work out the interaction on a grid. Since there can be large fluctuations in the spatial extent of the dipole configurations, the grid size has to be variable — it should completely cover the area where dipole-dipole interactions are significant. By summing the interactions at each point of the grid one obtains an approximation to the total amplitude for that configuration pair (the finer the grid, the better the approximation).

This approach is necessary if one wants to find a good approximation to the total amplitude for each configuration pair, however it is slow and does not offer any easy way to store the results so that they can be retrieved for later analysis (for example if one only wanted to look at 1 and 2 pomeron exchange, but after the run, decided that 3 pomeron exchange would also be interesting) — if one uses a grid with 100×100 squares, then one requires 40 kilobytes per pair of configurations, for a single value of rapidity. To gain adequate accuracy one needs several tens of thousands of events; with, say, 5 values of rapidity this gives several gigabytes of data. A second point to note with this approach is that when the grid is too large, dipoles interactions at small impact parameters, which can still contribute significantly are liable to "fall through the grid". Though after summing over many configurations this should average out, if one wants accurate estimates of the interactions from single configuration pairs when these are large, one might need to refine the grid (which would drastically increase the time for evaluation of the interaction).

One reason why it is important to sample a large number of configuration pairs, is that rare, large configurations contribute significantly to the total cross section (as will be discussed in chapters 6 and 7). Also, multiple-pomeron contributions are dominated by rare, dense

[1]Note that this may not correctly reproduce the profile of the interaction at large onium-onium separations, where the density of dipoles is also dying off also as $1/r^4$ (though enhanced by double-leading-logarithmic factors). However this region is not important for the total interaction.

configurations, because they are enhanced by the $f^k_{\gamma,\gamma'}$ factor of eq. (5.17). For a given pair of dipole configurations, however, the variation of the amplitude (at those points where it is significant) with impact parameter is not so large. So it can be advantageous to evaluate fewer points in impact parameter (i.e. making a worse approximation to the amplitudes of individual configuration pairs) in exchange for a larger sample of configurations. The limit of this is to evaluate the onium-onium interaction, not on a grid, but along a radial line. In addition, because there are fewer points in impact parameter it becomes feasible to store the results. In fact the individual amplitudes are not stored event by event, rather a probability distribution for obtaining a particular interaction amplitude, as a function of impact parameter, $P(f,r,Y)$ is stored at consecutive bins in radial position. This information can then be retrieved and used to determine whichever quantity one is interested in. For example, the amplitude including multiple-scattering corrections, integrated over impact parameter is

$$F(Y) = \int 2\pi r \mathrm{d}r \, \mathrm{d}f \, P(f,r,Y) \left(1 - \mathrm{e}^{-f}\right). \tag{5.19}$$

Various checks have been made to ensure that one is obtaining the correct answer, and in particular that one is not neglecting certain dipole-dipole interactions as unimportant when they in fact contribute significantly to the final interaction. One possible verification is just to make sure that the total, one-pomeron onium-onium interaction from the Monte Carlo evaluation agrees with that from the differential equation evolution method (and this will be shown later). However this has the problem that one expects large fluctuations in the onium-onium amplitude from the wide range of onium configurations that contribute. A more sophisticated test is to use the grid evaluation of the amplitude, together with an evaluation which uses the same set of onium configurations but approximates the onium-onium interaction as

$$f(\mathbf{r},\mathbf{c},\mathbf{c}') = \pi \alpha_{\mathrm{s}}^2 c_<^2 \left(1 + \ln \frac{c_>}{c_<}\right) \delta^2(\mathbf{r}), \tag{5.20}$$

which gives the correct dipole-dipole interaction when averaged over the dipole angles and integrated over their relative positions. These two methods give almost identical evaluations of the total amplitude (to within the 1% which is the target discussed above, connected with neglecting dipole-dipole interactions if they are separated by too large a distance).

Details of the code and instructions on its use are once again given in appendix C.

5.3.2 Choice of the lower cutoff

As discussed in section 5.2, to regulate the ultra-violet divergence of the dipole kernel, it is necessary to place a lower cutoff, ρ, on the dipole size. When this lower cutoff is taken to zero one obtains the correct result. However there is the problem that as the lower cutoff is reduced, the number of dipoles in the wave function increases rapidly (see for example eq. (5.7)), roughly as $1/\rho$. This is a problem because the time taken to generate an onium configuration is proportional to the number of dipoles, while the time taken to determine an onium-onium interaction is roughly proportional to the product of the number of dipoles in each of the onia (so proportional roughly to $1/\rho^2$). In fact the problem is slightly less severe than this, because if dipoles are small then they will interact in a smaller region and there will be fewer impact parameters at which one has to calculate their interaction with other dipoles. If the determination of onium-onium interactions takes too long then one is limited in the number of onium-onium configuration pairs that one can consider, and one will lose accuracy through lack of statistics (especially as a significant fraction of the interaction is coming from rare configurations). However if the cutoff is too large, then one will be neglecting evolution paths which include small dipoles, which will modify the distribution of dipoles even well above the cutoff (essentially, to within the range accessible through diffusion), as well as simply causing one to neglect the interaction of dipoles below the cutoff size. The compromise which will be used, will be to set the cutoff at a value ($\rho = 0.01b$) such that for the worst case being considered (i.e. determination of the onium-onium total cross section at $Y \simeq 20$), the errors due to a finite cutoff size should be similar to those due to the lack of available statistics.

CHAPTER 6

Properties of onium wave functions

Before being able to understand the characteristics of onium-onium interactions it is necessary to understand in detail the properties of onium wave functions. These can be divided up into several aspects: there are mean quantities, integrated over all impact parameters, or as a function of impact parameter, and then there are fluctuations in these quantities from configuration to configuration.

6.1 Mean total numbers of dipoles

The simplest quantity which one can examine is the mean number of dipoles as a function of dipole size. Starting with a single dipole of size b, as shown in chapter 4, after an evolution through a rapidity y, one expect the mean number of dipoles of size c to be

$$n^{(1)}(c,b,y) \simeq \frac{b}{c\sqrt{\pi k y}} \exp((\alpha_{\mathbb{P}}-1)y - \ln(c/b)^2/ky), \tag{6.1}$$

valid for $|\ln(c/b)| \ll ky$. This is the saddle point approximation. One can see how it compares with the numerical solution in figure 6.1. As expected, at large rapidity there is good agreement between the saddle point and numerical solution. At lower rapidity (and correspondingly, at large and small c) the numerical solution is significantly different. One reason is that the initial dipole leaves the remainder of a delta-function peak at $c = b$. More significant, is that at large and small c, logarithms of size become as important as those of energy and the double-leading-logarithmic approximation (DLLA) solution should be used:

$$n^{(1)}_{DLLA}(c,b,y) \simeq \left(\frac{\widetilde{\alpha} y}{16\pi^2 \ln^3 b/c}\right)^{1/4} \exp\left[2\sqrt{\widetilde{\alpha} y \ln\frac{b}{c}}\right], \tag{6.2}$$

with $\widetilde{\alpha} = 2\alpha_{\mathrm{S}} N_{\mathrm{C}}/\pi$. The solution for large sizes is analogous, but with a leading factor of b^2/c^2. For $|\ln c/b| \gg y$ the DLLA solution deviates only slowly from a power, and is much larger than

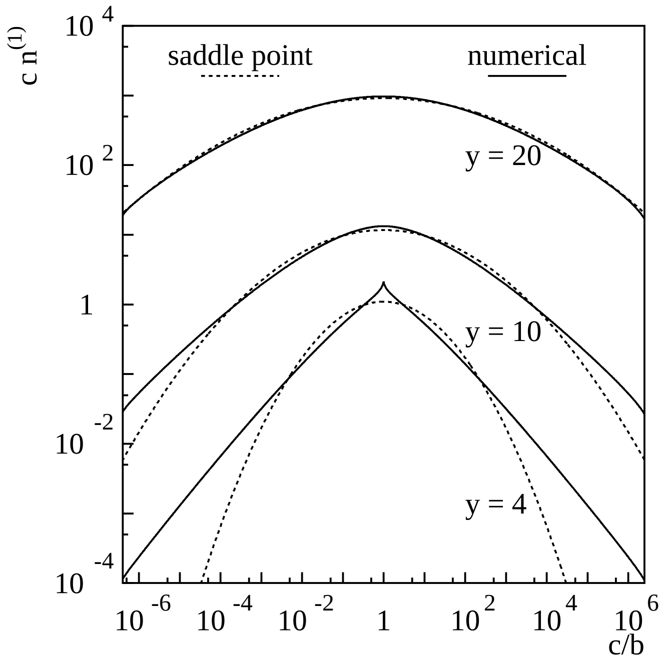

Figure 6.1: Numerical and saddle point solutions for $cn^{(1)}(c, b, y)$ for three different values of y.

the saddle-point solution. This is most clearly seen for the $y = 4$ curve of figure 6.1, where the numerical solution gives a relatively straight line, while the saddle point solution drops off rapidly.

Figure 6.2 shows a comparison between the numerically evolved dipole distribution and the DLLA result, eq. (6.2), for very small dipole sizes. For low values of y there is good agreement. As y increases, the approach to asymptotia becomes much slower, i.e. if one doubles y, then it is not sufficient to double $\ln(c/b)$ for the DLLA solution to be as good as at the lower y. Nevertheless all the solutions do seem to be tending towards the asymptotic limit.

6.2 Effect of cutoffs

Aside from considering the solution to the full dipole evolution equation, one can examine the effect of introducing infra-red and ultra-violet cutoffs on transverse size. This relates to work which has studied cutoffs in the momentum form of the BFKL equation [59, 61, 152, 153]. An infra-red cutoff is useful to help gauge the effect of eliminating from consideration the non-perturbative region. The justification used for introducing an ultra-violet cutoff is that it gives a crude measure of the effect of energy conservation which places a limit on the largest accessible transverse momentum. Inclusion of running α_s would also provide an effective ultra-violet cutoff [59].

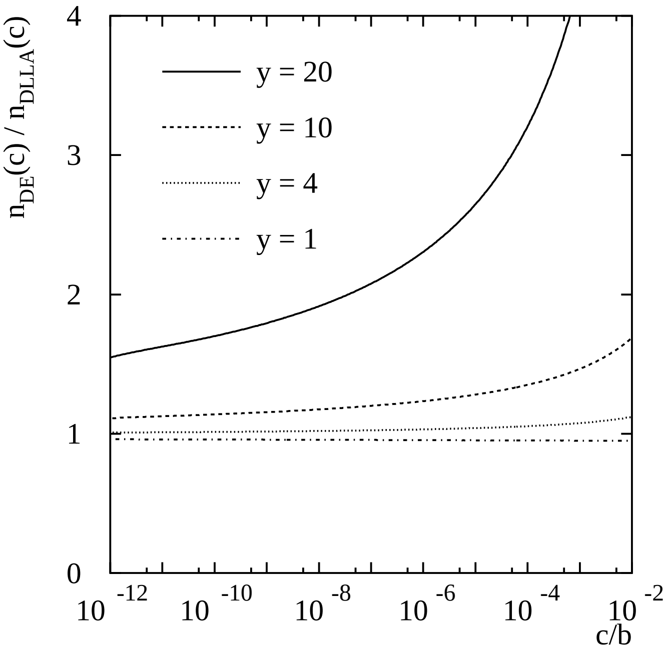

Figure 6.2: Ratio of numerical (n_{DE}) and DLLA (n_{DLLA}) solutions for the dipole distribution at various values of y.

Figure 6.3 shows the dependence on the ratio of the cutoffs, of the power growth of $n^{(1)}$ with respect to y. It also shows the prediction for the leading power from ref. [153]:

$$(\alpha_{\mathbb{P}} - 1)\left(\frac{1}{1 + 4\bar{\omega}^2}\right), \tag{6.3}$$

where $\bar{\omega}$ is the lowest positive solution of $2\bar{\omega} = \cot[\bar{\omega}\ln(c_{\max}/c_{\min})]$. The shapes of the two solutions appear to be fairly similar, but shifted in $c_{\max}/c_{\min}$. One could argue that this discrepancy is a consequence of going from cutoffs in position space to ones in momentum space. However any such effect should cancel out when taking the ratio of the cutoffs. Instead, it is probably due to their scope being different: in ref. [153], they were placed only on the real emission terms of the BFKL kernel, whereas in the numerical solution, they apply to the whole kernel. Note that the virtual terms in the BFKL kernel and in the dipole picture are not equivalent, and that in the dipole picture, it is not possible to put a cutoff on the real terms and not the virtual ones, because it would lead to a divergence.

When considering the relevance of these calculations to observations at HERA, it should be kept in mind that the power being discussed here is the asymptotic one. The initial power (ignoring logarithmic corrections) will be the full BFKL power, and the power will be affected only when the width of the solution is of the same order as the separation of the cutoffs.

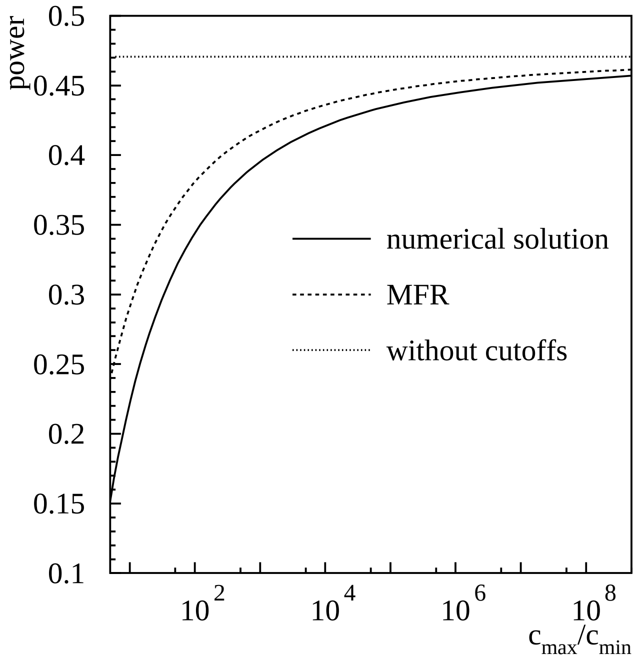

Figure 6.3: Asymptotic (large y) power for the growth of $n^{(1)}$, as a function of the ratio of the upper and lower cutoffs on dipole size. For the curve labelled MFR, which corresponds to eq. (6.3), derived by McDermott, Forshaw and Ross [153], $c_{\max}/c_{\min}$ should be taken to mean $k_{\perp,\max}/k_{\perp,\min}$.

6.3 The second moment of the number of dipoles

The easiest way to obtain higher moments of distributions of dipoles is to start from the equation for the generating functional, as described in chapter 4.

$$\frac{\mathrm{d}Z(b_{01},y,u)}{\mathrm{d}y} = \frac{\alpha_{\mathrm{S}} N_{\mathrm{C}}}{2\pi^2} \int \frac{b_{01}^2 \mathrm{d}^2\mathbf{b}_2}{b_{02}^2 b_{12}^2} [Z(b_{02},y,u)Z(b_{12},y,u) - Z(b_{01},y,u)]. \tag{6.4}$$

Defining the q^{th} multiplicity moment to be $n^{(q)} = \langle n(n-1)\dots(n-q+1)\rangle$, one can see that

$$n^{(q)}(c,b,y) = \frac{\delta^q Z(b,y,u)}{\delta u(c)^q}|_{u=1}. \tag{6.5}$$

Therefore, functionally differentiating eq. (6.4) q times with respect to $u(c)$, one obtains an equation for $n^{(q)}$ based on $n^{(0)}$ to $n^{(q-1)}$. With the knowledge that $n^{(0)}$ is 1, this leads to:

$$\frac{\mathrm{d}n^{(q)}(c,b_{01},y)}{\mathrm{d}y} = I^{(q)} + \frac{\alpha_{\mathrm{S}} N_{\mathrm{C}}}{2\pi^2} \int \frac{b_{01}^2 \mathrm{d}^2\mathbf{b}_2}{b_{02}^2 b_{12}^2} [n^{(q)}(c,b_{02},y) + n^{(q)}(c,b_{12},y) - n^{(q)}(c,b_{01},y)], \tag{6.6}$$

with the inhomogeneous term, $I^{(q)}$, defined to be

$$I^{(q)} = \frac{\alpha_{\mathrm{S}} N_{\mathrm{C}}}{2\pi^2} \int \frac{b_{01}^2 \mathrm{d}^2\mathbf{b}_2}{b_{02}^2 b_{12}^2} \sum_{i=1}^{q-1} C_i^q n^{(i)}(c, b_{02}, y) n^{(q-i)}(c, b_{12}, y). \tag{6.7}$$

With these equations one can then solve iteratively for successively higher multiplicity moments. Given that $n^{(1)}$ is known, it can be used to calculate the inhomogeneous term for eq. (6.6) with $q = 2$.

In many other situations where one is solving for higher moments it is possible to use a KNO ansatz, namely that the shape of the probability distribution is independent of the mean,

$$P_n(c, b, y) = \frac{1}{\langle n \rangle} f\left(\frac{n}{\langle n \rangle}\right), \tag{6.8}$$

and only the mean $\langle n \rangle$ depends on c, b and y. In terms of multiplicity moments, this is equivalent to saying that:

$$n^{(q)}(c, b, y) \simeq \beta_q [n^{(1)}(c, b, y)]^q, \tag{6.9}$$

where the β_q are independent of c, b, and y. However, when investigating the inhomogeneous term of eq. (6.6) for the second moment, one finds that the symmetry between large and small scales, which is characteristic of the first moment, is substantially altered, so that a KNO ansatz is not appropriate. This means that the form of the integral for the inhomogeneous term is different for each higher moment.

The evaluation of these integrals is unfortunately quite complicated, and analytical approximations have been found only for a limited ranges of child dipole sizes. It is nonetheless instructive to look at these analytical approximations, because they point to some of the main features of the fluctuations and to the nature of the violations of KNO scaling. Consider $I^{(2)}$, the inhomogeneous term for the second moment.

$$I^{(2)} = \frac{\alpha_{\mathrm{S}} N_{\mathrm{C}}}{2\pi^2} \int \frac{b_{01}^2 \mathrm{d}^2\mathbf{b}_2}{b_{02}^2 b_{12}^2} n^{(1)}(c, b_{02}, y) n^{(1)}(c, b_{12}, y). \tag{6.10}$$

For large values of c/b_{01} one can make the approximation that $b_{02} \simeq b_{12}$ in the dominant region of the integration ($c \sim b_{02}$). The two exponents in the integrand are then the same and easily integrated over:

$$I^{(2)} \simeq \frac{\alpha_{\mathrm{S}} N_{\mathrm{C}}}{\pi} \left(\frac{b_{01}}{c}\right)^2 \int \frac{\mathrm{d}b_{02}}{b_{02}} \frac{\mathrm{e}^{2(\alpha_{\mathrm{I\!P}}-1)y - 2\ln(b_{02}/c)^2/ky}}{\pi k y} = \frac{\alpha_{\mathrm{S}} N_{\mathrm{C}}}{\pi} \frac{\mathrm{e}^{2(\alpha_{\mathrm{I\!P}}-1)y}}{\sqrt{2\pi k y}} \left(\frac{b_{01}}{c}\right)^2, \quad (c \gg b_{01}). \tag{6.11}$$

This is valid for $\ln(c/b_{01}) \gg \sqrt{ky}$, though it remains a reasonable approximation down to values of c close to b_{01} and remains true even outside the saddle point approximation for $n^{(1)}$.

The only other region where the inhomogeneous term can be estimated is for small c. In this case, most of the contribution to the integral comes from the regions of small b_{02} and small b_{12}, where one of the exponentials decouples, leaving only the other to integrate over. The main difference is that the leading powers of c/b shift the position of the maximum of the integrand, and in the process introduce an extra exponential dependence on the rapidity. This leaves $I^{(2)}$ with the following dependence for small c:

$$\begin{aligned} I^{(2)} &\simeq \frac{2\alpha_{\mathrm{S}} N_{\mathrm{C}}}{\pi} \frac{b_{01}}{\pi k y c} \mathrm{e}^{2(\alpha_{\mathrm{IP}}-1)y - \ln(b_{01}/c)^2/ky} \int \frac{\mathrm{d}b_{02}}{b_{02}} \frac{b_{02}}{c} \mathrm{e}^{-\ln(b_{02}/c)^2/ky} \\ &\simeq \frac{b_{01}\mathrm{e}^{2(\alpha_{\mathrm{IP}}-1)y}}{c\sqrt{\pi k y}} \mathrm{e}^{ky/4 - \ln(b_{01}/c)^2/ky}, \qquad (c \ll b_{01}). \end{aligned} \tag{6.12}$$

More precisely, this is valid for $-ky \ll \ln(c/b_{01}) \ll -ky/2 - \sqrt{ky}$ (the requirements that the saddle-point solution be valid and that $b_{02} \ll b_{01}$ for the relevant range of integration). Violation of KNO scaling in b (at least for $I^{(2)}$) is clearly visible in both of the limits considered here, since in neither case is the is the b/c dependence correct; since the b dependence for $n^{(1)}$ also involves y, one expects violation of KNO scaling in y as well.

Having discussed the form of $I^{(2)}$, one can examine $n^{(2)}$ which is related to $I^{(2)}$ by eq. (6.6). Figure 6.4 was obtained by numerical solution of eq. (6.6) for $q = 2$. There are various stages to the numerical determination of $n^{(2)}$. The first is to calculate $I^{(2)}$ which requires an integration which depends on $n^{(1)}$. Unfortunately the solution from the differential equation evolution of $n^{(1)}$ is not suitable for direct use in the integration, partly because it is not smooth enough (being binned), and partly because the range of c for which it is valid is not large enough. Therefore a fit is used which by default has the correct DLLA and power behaviour for large and small c/b, and where the parameters are adjusted to give the normalisation and to fit the shape of the curve for intermediate c/b. The function used is

$$A \frac{b}{c} \frac{1}{[\ln^2 c/b + B]^{3/8}} \exp\left[2\sqrt{\tilde{\alpha} y (\sqrt{\ln^2 c/b + C} - \sqrt{C})}\right] [\cosh(D \ln c/b)]^{-1/D}, \tag{6.13}$$

where A, B, C and D are the parameters to adjust. The fit needs to be performed at two neighbouring values of y so that one can calculate the derivative of $n^{(2)}$. Once $I^{(2)}$ is known, it is used (divided by $2(\alpha_{\mathrm{IP}} - 1)$) as a trial solution for $n^{(2)}$. This is fed into eq. (6.6) which is solved iteratively until a stable solution is reached.[1] The fact that one has to obtain a derivative from

[1] One must actually make certain assumptions about how to deduce $n^{(2)}$ given its derivative (as calculated from eq. (6.6)) — the technique used was to use the values of $n^{(2)}$ at two different values of y for one iteration, to calculate a ratio between $n^{(2)}$ and its derivative, and to use that ratio in going from the derivative to $n^{(2)}$ in the next iteration

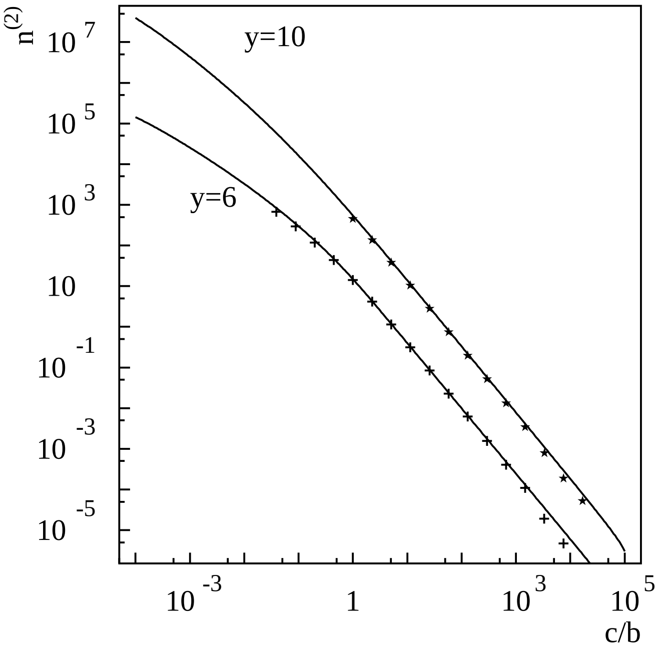

Figure 6.4: The second multiplicity moment as a function of dipole size. The curves are generated by numerical solution of eq. (6.6) for $n^{(2)}$. The points correspond to Monte Carlo results where the bin includes sizes up to a factor of 1.5 either side of the central value. For $y = 6$ a lower cutoff of $0.01b_0$ is used, while for $y = 10$ the lower cutoff is $0.1b_0$.

the function fitted at two neighbouring values of y is probably the main source of inaccuracy in this calculation.

The main features of $I^{(2)}$ can be seen to be also present in $n^{(2)}$ (figure 6.4): the c^{-2} behaviour at large c is reflected in the steep descent in $n^{(2)}$. The power dependence though is actually slightly different from c^{-2}: it is actually $c^{-2+\lambda}$ where $\lambda \simeq 0.366$ is the solution to $\chi(2-\lambda) = 2\chi(1)$, with χ defined as in eq. (4.36). At smaller dipole sizes there is a tailing off of $n^{(2)}$, as expected, and this tailing off occurs at larger c for $y = 6$ than for $y = 10$.

Figure 6.4 also shows $n^{(2)}$ as determined from the Monte Carlo simulation of the branching. The accessible range of c is limited, at small c because of the need for a lower cutoff on dipoles size, and at large c because large size events are rare, so one needs high statistics. However, in the region that the Monte Carlo determination can be used, there is good agreement with the numerical techniques already discussed, giving extra confidence in their validity outside that region.

When trying to understand the shape (scaled by the mean) of the probability distribution $P_n(c, b, y)$, it is the normalised moments $\beta_q = n^{(q)}/[n^{(1)}]^q$ which are of relevance[2]. If one

[2]Strictly speaking, one should use $\langle n^q \rangle$ and opposed to $n^{(q)} = \langle n(n-1)\ldots(n-q+1)\rangle$, however this will only

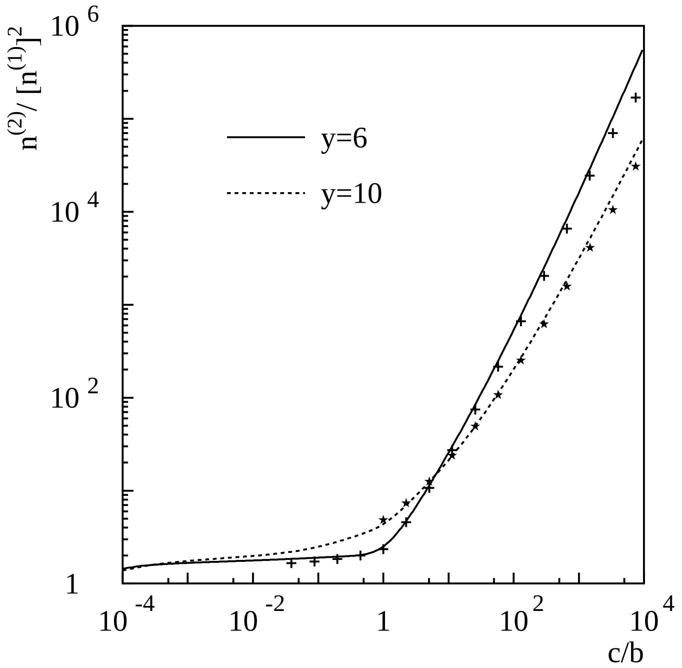

Figure 6.5: The curves correspond to $n^{(2)}/[n^{(1)}]^2$ as obtained by solving eq. (6.6) numerically. The points are results from Monte Carlo simulations of the branching process.

considers β_2 for large c, assuming that $n^{(2)}(c) \propto I^{(2)}(c)$, one finds that:

$$\beta_2 \sim \mathrm{e}^{2\ln(c/b)^2/ky}. \tag{6.14}$$

This corresponds to the probability distribution $P_n(c, b, y)$ being much broader relative to its mean for large sizes of dipoles than for intermediate sizes, which is to be expected: though the probability of producing a single large dipole is relatively small, once this has occurred, many more are quite likely to follow, increasing the values of all the higher moments.

Figure 6.5 shows the dependence of $\beta_2 = n^{(2)}/[n^{(1)}]^2$ on dipole size. It is clear that at large sizes there is a rapid increase in β_2. As y increases, the steepness of the curve for β_2 is reduced, in accordance with expectations from eq. (6.14). Deviation from eq. (6.14) arises for a variety of reasons, including the facts that the power dependence of $n^{(2)}$ is not quite that of $I^{(2)}$, and that at large c one should use the DLLA form for $n^{(1)}$. At small sizes, β_2 is almost independent of both rapidity and size. This is a signature of KNO scaling and certainly not consistent with one's expectations from eq. (6.12). The reason for this is that the validity of eq. (6.12) is limited by the range of applicability of the LL($1/x$) saddle point solution. Instead one should

have an effect where $n^{(q)}$ is small, i.e. for large values of $\ln(c/b)$. Then, using $n^{(q)}$ instead of $\langle n^q \rangle$ will cause one to underestimate the width of the distribution.

use the DLLA solution. This is known to give KNO scaling with the following relations for the coefficients β_q [154]:

$$\beta_q = \frac{q^2}{2(q^2-1)} \sum_{i=1}^{q-i} C_i^q \frac{\beta_i \beta_{q-i}}{i(q-i)}. \tag{6.15}$$

This is only valid in the region of asymptotically small size. One can see that the curves in figure 6.5 are approaching the value of $\beta_2 = 4/3$ from eq. (6.15).

So far we have considered in detail only the first and second multiplicity moments. It would be of interest to obtain more information about higher moments, to help understand the tail of the distribution. In principle, eq. (6.6) could be solved numerically for successively higher moments, using the previously determined lower moments to construct the inhomogeneous terms. However, one would need also to fit $n^{(2)}$ at two different values of y and the procedure would be very tedious. An alternative approach is presented in the next section.

6.4 Higher moments of the number of dipoles

The tail of the distribution can be analysed with the assumption that the occasional high-multiplicity event results from the initial production of a large 'source' dipole which produces a cascade of smaller dipoles. The probability of producing a large dipole of size a is proportional to $1/a^2$. On average it will then produce $n^{(1)}_{DLLA}(c,a,y)$ dipoles. From eq. (6.2) therefore, the size a associated with a multiplicity n is $a \sim c\exp[(\ln^2 n)/4\tilde{\alpha}y]$, giving a probability $P_n \sim \exp[-(\ln^2 n)/2\tilde{\alpha}y]/c^2$. This argument suggests a distribution with a long tail which is independent of dipole size except that its normalisation scales as $1/c^2$.

The distribution can be calculated in more detail using the moments for the DLLA distribution produced by the large dipole:

$$n^{(q)}_{DLLA} = \beta_q [n^{(1)}_{DLLA}]^q. \tag{6.16}$$

For large q, one has

$$\beta_q \simeq 2\gamma^q q q!, \tag{6.17}$$

where γ is 0.39 [154]. To obtain the moment of the actual multiplicity distribution, the DLLA moment for a given source size a is multiplied by the probability of producing a dipole of that size, and the result is integrated over a:

$$n^{(q)}(c,y) \sim \int_c^\infty \frac{\mathrm{d}\ln a}{a^2} n^{(q)}_{DLLA}(c,a,y). \tag{6.18}$$

It would be more accurate to include the DLLA correction to the probability for producing the initial large dipole. But this is a correction suppressed by a power of q, so it will have little effect on the shape of the tail, though it will modify the normalisation, which is not being determined here. To obtain $n^{(q)}$, eq. (6.18) is evaluated with the saddle point approximation. The logarithmic prefactor in eq. (6.2) is held constant when determining the position of the saddle point, which is again equivalent to taking the limit of large q. The result is then integrated with respect to the rapidity of the initially produced dipole. This gives

$$n^{(q)} \sim \frac{1}{c^2}\left(\frac{\phi}{q}\right)^{q/2} q^{1/2} \mathrm{e}^{q^2\widetilde{\alpha}y/2}, \tag{6.19}$$

with ϕ being

$$\phi = \frac{2\gamma^2 w^2}{\pi\widetilde{\alpha}y\mathrm{e}^2}, \tag{6.20}$$

where w is the logarithmic width of the bin for c. The normalisation of the moments has been left out because it would in any case be altered by inclusion of the DLLA corrections to the probability of producing the initial dipole. The probability distribution for large n is obtained from the moments, by taking the inverse Mellin transform of $n^{(q)}$, using the saddle point approximation to give

$$\begin{aligned} P_n(c,y) \sim \frac{1}{c^2}\exp\Bigg[&-\frac{\ln^2 n}{2\widetilde{\alpha}y} - \ln n\left(1 + \frac{1}{2\widetilde{\alpha}y}\ln\left(\frac{\ln n}{\widetilde{\alpha}y\phi}\right)\right) \\ &- \frac{1}{8\widetilde{\alpha}y}\left(\ln\left(\frac{\ln n}{\widetilde{\alpha}y\phi}\right)\right)^2 + \frac{1}{2}\ln\left(\frac{\ln n}{\widetilde{\alpha}y}\right)\Bigg]. \end{aligned} \tag{6.21}$$

This is similar to the expression derived earlier, but also includes corrections relevant to moderate multiplicities.

6.4.1 Monte Carlo calculation of the multiplicity distribution

One way of testing these ideas is to use results from the Monte Carlo simulation of the branching process, from which one can directly determine the multiplicity distribution.

Figure 6.6 shows the Monte Carlo results (curve (a)), together with the asymptotic prediction from eq. (6.21), for two ranges of dipole size. When plotting the theoretically predicted distribution it is necessary to fix the normalisation. This is done so as to give agreement with the Monte Carlo results for larger sizes. The shape of the predicted distribution agrees surprisingly well with that of the Monte Carlo results, even down to a multiplicity as low as 5. For the smaller sizes, the prediction is high, particularly at lower multiplicities. The reason for this is that the probability of producing the initial 'large' dipole of size c falls below the $1/c^2$ approximation, especially at the smaller values of c which are relevant to low multiplicities

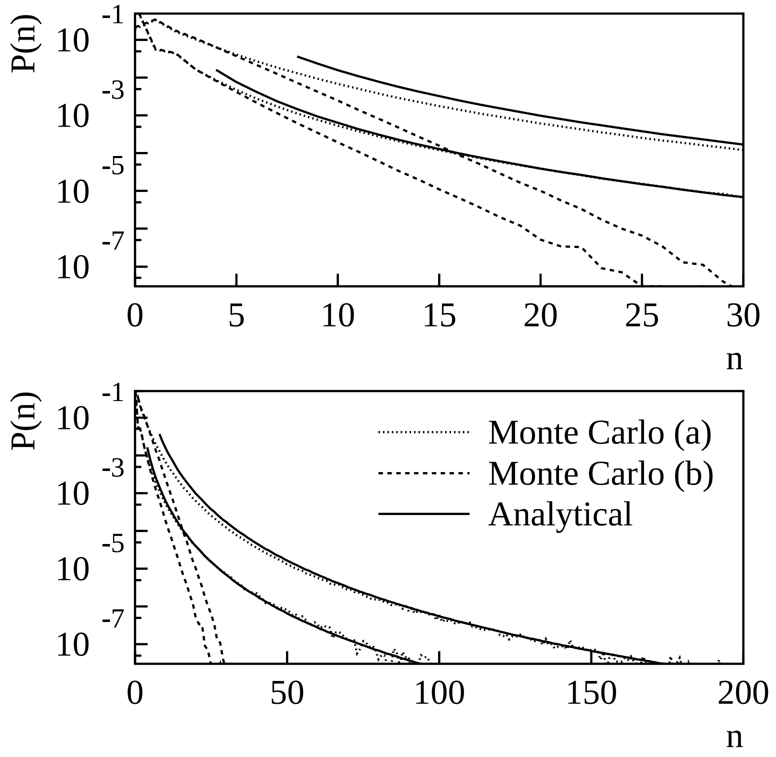

Figure 6.6: The Monte Carlo curves (a) are the probability distribution for the total multiplicity of dipoles of size $c \simeq c_0$. The curves (b) are for the multiplicity in a central disc of radius $2c_0$. The curves labelled analytical correspond to eq. (6.21). In each plot, the upper set of curves corresponds to $c_0 = b$, the lower to $c_0 = 5b$. Apart from the scale for n, the upper and lower plots are identical. The rapidity is $y = 6$.

(to see this, take the limit of $c \lesssim b$, where the probability is close to 1, independent of c, and therefore bound to be smaller than a $1/c^2$ distribution).

One consequence of the atypical configurations with high multiplicities is purely technical: namely that when running a Monte Carlo simulation, one has to be prepared to allow configurations that have numbers of dipoles which are orders of magnitude larger than the mean. This can cause problems for storage (to the extent that for some applications it is necessary to use techniques which never store the whole set of dipoles).

The main physical consequences of this long tail to the multiplicity distribution can be seen if one considers it in terms of the fluctuations in the onium-onium cross section between one pair of configurations and another. If there is a large number of dipoles then the cross section will be much larger. Because the probability of obtaining a large number of dipoles dies off so slowly one can have a situation where moderately rare configurations, because individually they give such a large contribution to the cross section, overall account for a significant proportion of the cross section. When an amplitude is dominated by atypical configurations, then average quantities tend to be misleading (for example as a gauge of when multiple-scattering corrections should be important). This will be discussed in some detail in chapter 7.

6.5 Fluctuations in dipole density

When considering multi-pomeron contributions to scattering amplitudes, as will be done in the next chapter, it will not be the total number of dipoles which is relevant, but the dipole density: to obtain a large interaction between a pair of wave functions, it is necessary for many dipoles to be interacting at the same time, and if the dipoles are spread out in each of the onia then there will never be more than a fraction of the possible interactions for any given impact parameter. It is therefore necessary to limit the region over which one counts dipoles: the curves (b) of figure 6.6 show the distribution of the number of dipoles in a restricted region of transverse position space: for a dipole to contribute, its centre must be less than $2c_0$ from the centre of the source dipole (where c_0 is roughly the mean of the dipole sizes being considered). The distribution of densities shows an exponential decrease, very distinct from the $\exp(-\ln^2 n)$ behaviour of the total multiplicity. This difference arises because the density of dipoles from a large initial source is controlled by two factors: the total number of dipoles $\sim \exp(2\sqrt{\bar{\alpha} y \ln a})$, divided by the total area which scales as $a^{-2} = \exp(-2\ln a)$, which means that the occasional large source will not contribute to high densities.

For a region of size r, the largest numbers of dipoles within the region will therefore be produced by an initial source no larger than r. Because r is not much bigger than c_0 it is not really legitimate to apply the DLLA approximation to determine the fluctuations. If one nevertheless tries, one obtains a multiplicity distribution proportional to $n \exp(-n/\mu_{\mathrm{DLLA}})$, with

$$\mu_{\mathrm{DLLA}} \simeq \gamma n^{(1)}_{\mathrm{DLLA}}(r, c, y). \tag{6.22}$$

Fitting such a distribution to the Monte Carlo curves (b) one can obtain a value μ_{MC} and compare the two, as in the following table:

y	μ_{DLLA}	μ_{MC}
6	1.52	1.65
10	3.45	4.3

For $y = 6$ there is a reasonable agreement, but for $y = 10$ there is already a significant deviation, which arises because the DLLA solution is not appropriate for such a large rapidity with such a small range of size. It is therefore necessary to include the full LL$(1/x)$ fluctuations.

A detailed derivation of the exponential nature of the LL$(1/x)$ density fluctuations is presented in appendix A. The basis of the derivation is that at large Y, the c and b dependences factorise, as can be seen from eq. (6.28). The q^{th} moment of the distribution of dipoles of size

c inside a region of size ρ, from a parent of size b which is also in the same region, can then be expressed in the form:

$$n_\rho^{(q)}(c,b,y) = e_q q! A^q(c/\rho) \left(\frac{b}{\rho}\right)^{\lambda_q} \mathrm{e}^{q(\alpha_{\mathbb{P}}-1)y}, \tag{6.23}$$

where, for the purposes of the analysis, A can be any function, though it will actually be proportional to ρ/c. All the moments are defined by the coefficients e_q and the exponents λ_q which are approximately independent of b. Note that this form explicitly exhibits KNO scaling [147] in c and y. One then obtains the following relations, valid for large q:

$$\lambda_q \simeq 2 - \frac{1}{2q\ln 2}, \tag{6.24}$$

and

$$e_q \simeq \frac{1}{4\ln 2}\frac{1}{q}\sum_i^{q-i} e_i e_{q-i}\frac{1}{\lambda_i + \lambda_{q-i} - 2}. \tag{6.25}$$

Therefore for large q, one has $e_q \propto C^q$, where the exact value of C depends strongly on the behaviour of e_q for low q. This gives for the probability of finding n dipoles of size c within a region of size ρ (in the limit of large n):

$$P_n(c,b,\rho,y) \sim \exp\left[-\frac{n}{A(c/\rho)C\mathrm{e}^{(\alpha_{\mathbb{P}}-1)y}}\right]. \tag{6.26}$$

This agrees with the Monte Carlo results to within the uncertainties, which are due to the accessible values of y being non-asymptotic and also because the above formulas are valid only for large q, while the value of C retains a dependence on the behaviour of e_q at smaller q.

Note that the shape of the distribution for large n is independent of the size b of the initial dipole, or equivalently of the size of the dipoles whose distribution is being studied (as long as the scale of the region in which they should be found is proportional to their size): i.e. the shape of the tail of the distribution is independent of the starting conditions of the evolution. For example it is possible to produce high-density fluctuations anywhere in impact parameter, as long as a dipole of size $\simeq \rho$ is produced at that point in impact parameter, early on in the evolution, so that it has a long range in y to produce many child dipoles. The only aspect of the tail of the distribution which does depend on the starting conditions is the normalisation: in the above example, the probability of producing a dipole of the appropriate size, at the correct impact parameter, depends on the position and size of the parent dipole. This is illustrated in figure 6.6, where the distributions for the two sizes of dipole (in regions whose scale is proportional to the dipole size), curves (b), have almost identical slopes.

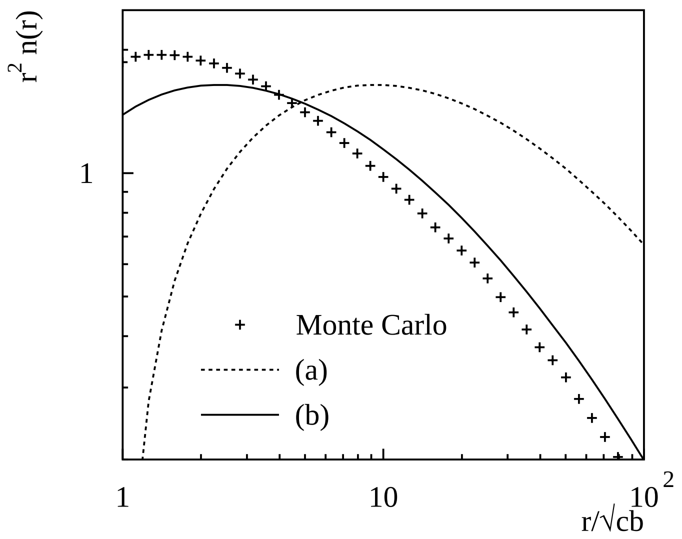

Figure 6.7: The mean spatial distribution of dipoles in an onium, for $y = 14$ with $c = b$. The curve labelled (a) corresponds to eq. (6.27) and the curve (b) to eq. (6.28).

6.6 Mean spatial distribution of dipoles

An approximate form for the average dipole distribution has been given in chapter 4, as taken from [16]:

$$n(c, b, r, y) \simeq \frac{2b}{cr^2} \ln\left(\frac{r^2}{bc}\right) \frac{\exp[(\alpha_{\mathbb{P}} - 1)y - \ln^2(r^2/bc)/ky]}{(\pi k y)^{3/2}}. \tag{6.27}$$

This is the number density of dipoles of size c, at a distance r from the parent dipole of size b, after evolution through a rapidity y. The equation is valid for $r \gg b, c$ and $\ln r^2/bc \ll ky$. One of its main characteristics is that the maximum of the dipole distribution is at large r (see the dashed line of figure 6.7). This would imply that scattering is taking place at values of r where the average dipole distribution would be quite dilute (though fluctuations would still have to be taken into account). It would also have the consequence that one might reach the dangerous infra-red region, where non-perturbative effects come into play, somewhat sooner than expected. The Monte Carlo results (the + symbols on figure 6.7), however, show that the distribution is far more central.

The source of this discrepancy is a missing portion of one of the integrals used in the derivation of eq. (6.27). The details are discussed in appendix A.2, where it is shown that a better approximation has an extra factor in the logarithms:

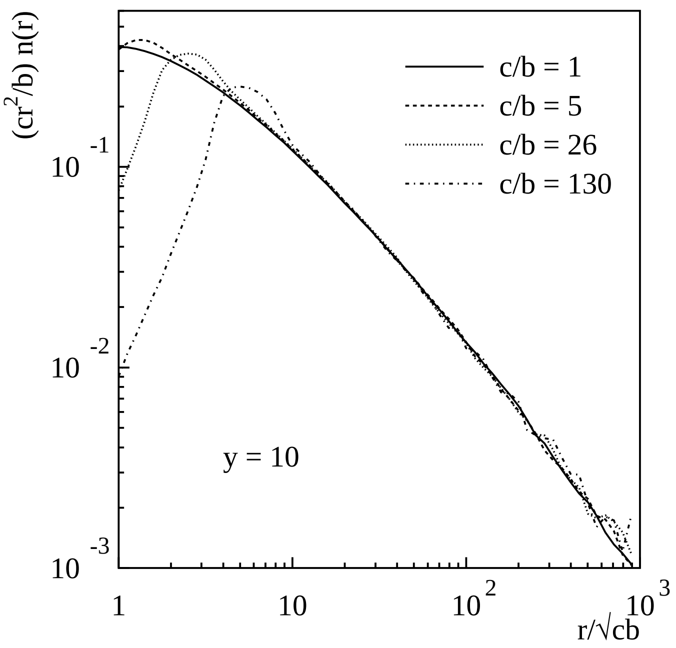

Figure 6.8: The impact parameter distribution of dipoles for different dipole sizes. A lower cutoff of 0.1b is used during evolution to allow increased statistics.

$$n(c,b,r,y) \simeq \frac{2b}{cr^2} \ln\left(\frac{16r^2}{bc}\right) \frac{\exp[(\alpha_{\mathrm{I\!P}}-1)y - \ln^2(16r^2/bc)/ky]}{(\pi k y)^{3/2}}. \tag{6.28}$$

The extra factor effectively arises from taking into better account contributions from intermediate paths which involve gluon production close to either the initial dipole or the final dipole.

One characteristic of eq. (6.28) as well as eq. (6.27) is that, except for a leading factor of b/cr^2, the spatial distribution of dipoles is a function only of r^2/bc, (in the limit $r \gg b, c$). If this really is the case then a plot of $(cr^2/b)n(r)$ against r^2/bc should be independent of b/c — that this is true is shown clearly in figure 6.8. The origins of the dependence only on r^2/bc lie in the property of conformal invariance of the dipole kernel: the number of medium sized dipoles a long way from the parent centred at $r = 0$, is related to the number of small dipoles positioned close to $r = 0$. The number of small dipoles close to the centre can depend only on their size, not on their position, and correspondingly, the density of medium sized dipoles a long way from the origin can only depend on one quantity, which turns out to be r^2/bc. The argument is presented in detail in appendix B.2 (for the related case of the onium-onium scattering amplitude). For $r \sim b \ll c$, a different argument applies, and in fact it can be shown that for $c \gg b$ the dipole density at $r = 0$ is the same as that at $r = c$.

6.7 Origins of the mean spatial distribution

When first investigating the apparent discrepancy in the dipole distribution, various other techniques were examined for obtaining the spatial distribution. The reason for discussing them here is that they give information on the mechanisms responsible for the spatial distribution.

The basic argument that will be used in this section is that it is large dipoles in an evolution sequence which are responsible creating the spatial distribution. Take a random walk which includes a variety of dipoles sizes. Generally the number of steps of size b in the random walk will be of order $(\alpha_{\mathbb{P}}-1)y$ (and not $\mathrm{e}^{(\alpha_{\mathbb{P}}-1)y}$, since different dipoles in the configuration will have taken different evolution paths), which will give a mean diffusion distance of $\mu \sim b\sqrt{(\alpha_{\mathbb{P}}-1)y}$. The distribution of distances (assuming the rapidity to be reasonably large) will then be a Gaussian:

$$P(\mathbf{r}) \sim \mathrm{e}^{-2r^2/\mu^2}. \tag{6.29}$$

In contrast, the probability of making a large step via a dipole of size r, is proportional roughly to $\mathrm{e}^{(\alpha_{\mathbb{P}}-1)y} b^2/r^4$ (taking into account that any of the small dipoles can make the step), which, while small, still gives a much larger distribution than that from a random walk of small dipoles.

6.7.1 The DLLA spatial distribution

The basis of this section is therefore, that if a dipole of size c is found at a large distance r from the initial dipole (of size b), then at some stage in the evolution process a large dipole of size of order r was created which subsequently emitted gluons in that region of space. More formally, for a dipole to be created at position r, the evolution process must have passed via a dipole of size a, such that $a > \mu r$, with μ a constant still to be determined. The dipoles from the large dipole of size a are taken (on average) to be spread uniformally over a disc of radius a/μ. Therefore to obtain the density of dipoles at a certain radius r, one must integrate over all the possible large sizes which could contribute and all the rapidities at which the large dipole can be produced:

$$n(c,b,r,Y) = \int_0^Y \mathrm{d}y \int_{a=\mu r}^{\infty} \mathrm{d}\ln a \frac{\mu^2}{\pi a^2} \frac{\mathrm{d}n^{\uparrow}(a,b,y)}{\mathrm{d}y} n^{\downarrow}(c,a,Y-y), \tag{6.30}$$

where $n^{\uparrow}(a,b,y)$ is the DLLA number of dipoles of size a produced from one of size b, with $a \gg b$:

$$n^{\uparrow}(a,b,y) \simeq \frac{b^2}{2a^2} \left(\frac{\tilde{\alpha} y}{\pi^2 \ln^3 a/b} \right)^{1/4} \exp\left[2\sqrt{\tilde{\alpha} y \ln \frac{a}{b}} \right], \tag{6.31}$$

with $\tilde{\alpha} = 2\alpha_{\mathrm{S}} N_{\mathrm{C}}/\pi$. In eq. (6.30), the derivative is used so that one gets the number of dipoles produced at that particular rapidity rather than the total number up to that rapidity.

When taking the derivative one ignores the contribution from the logarithmic factors since their variation is non-leading. Going down in size from the large dipole, one uses $n^{\downarrow}$ instead, which is the same as $n^{\uparrow}$ except that there is no leading power dependence on the ratio of the dipole sizes (i.e. there is no a^2/c^2 factor).

First the a integral is evaluated. It is simplest to ignore the logarithmic a dependence in the exponentials and prefactors of $n^{\uparrow}$ and $n^{\downarrow}$, since it is much weaker than the power dependence which is present. This gives

$$n(c,b,r,Y) = \frac{b^2}{4\pi r^4 \mu^2} \int \mathrm{d}y \frac{\mathrm{d}n^{\uparrow}(\mu r, b, y)}{\mathrm{d}y} n^{\downarrow}(c, \mu r, Y-y). \tag{6.32}$$

Then one performs the y integration. This cannot be done exactly, however it is possible to use the saddle point approximation (again ignoring the slow variation of the logarithmic prefactors) with the saddle point at

$$y = \frac{Y \ln(\mu r/b)}{\ln(\mu^2 r^2/bc)}. \tag{6.33}$$

The result is

$$n(c,b,r,Y) = \frac{b^2}{8\pi r^4 \mu^2} \left(\frac{\tilde{\alpha}^3 Y^3}{\pi^2 \ln^5(\mu^2 r^2/cb)} \right)^{1/4} \exp\left[2\sqrt{\tilde{\alpha} Y \ln \frac{\mu^2 r^2}{cb}} \right]. \tag{6.34}$$

Note that if one examines $(cr^2/b)n(r)$ one obtains a quantity which depends only on r^2/bc, as in the previous section. All that remains to be determined is the value of μ. Generally one edge of a large dipole will be close to the position of the initial dipole, and subsequently produced smaller dipoles are unlikely to be far beyond the outer gluon of the large dipole. Therefore the dipoles produced by a dipole of size a are likely to be situated within a disc of radius $r = a$ centred on the initial dipole. Therefore $\mu \simeq 1$. As rapidity increases (for fixed a/c) the size interval will decrease between successive branchings in the cascade down, meaning that there will be more diffusion due to a random walk sort of process and so one expects μ to decrease slowly; however this will probably be less important than the onset of LL$(1/x)$ type corrections. Results for $y = 14$ are shown in figure 6.9. The DLLA curves have a similar shape to the Monte Carlo curves, though they are a bit low at small values of r (indicating that one needs some element of LL$(1/x)$ type evolution to fully account for the results). At smaller values of y, the agreement is almost perfect.

One might wonder why it is that at such large rapidities one can still use the DLL approximation and get reasonable results (the agreement is no worse than with the LL$(1/x)$ formula, eq. (6.28)). To some extent, it is because the relevant rapidity to consider is not y, but $y/2$, since one first has to go up in size (for half the rapidity) and then down in size (for the other half of the rapidity). And for the values of r^2/bc being studied this quickly brings one into the range of validity of the DLL approximation.

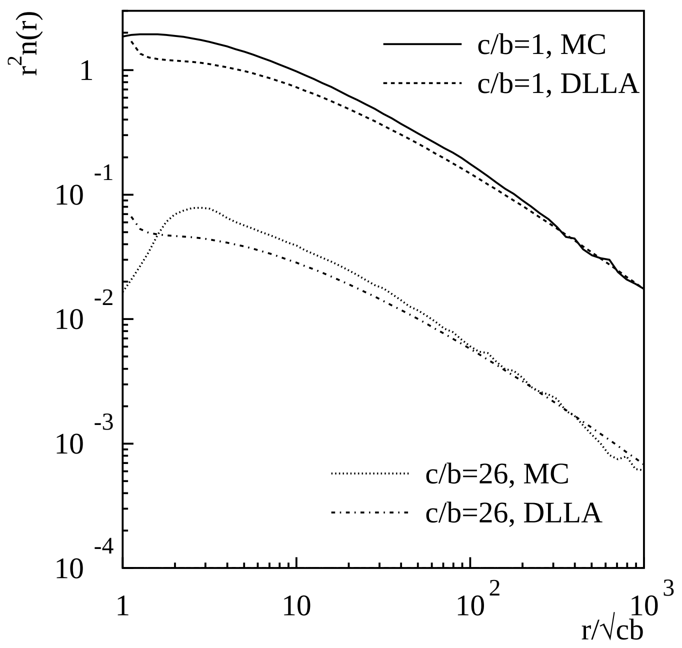

Figure 6.9: The DLLA approximation to the spatial distribution of dipoles in the onium wave function, for $y = 14$, compared with Monte Carlo results.

6.7.2 LL($1/x$) spatial distribution

Despite the relatively good agreement between the DLLA and the Monte Carlo results, it would be useful to have a LL($1/x$) understanding of the spatial distribution – one which should legitimately apply at relatively small radii. One cannot simply convert the above approach by substituting the LL($1/x$) dipole distribution instead of the DLLA one. In the DLLA formula the evolution is ordered in sizes, so that one can specify that first one goes directly up in size and then directly down. The LL($1/x$) evolution does not include this ordering. As a result, for example, one evolution path could go up to size a at a rapidity y_1, down in size a bit, then back up to size a at a second rapidity y_2, before going down to size c. Integrating the rate of production of dipoles of size a times the number of smaller dipoles that they end up producing, would cause such a contribution to be double-counted.

An alternative approach involves the use of an upper cutoff. One retains the argument, that for dipole to be found at a position r, it must have passed via a dipole of size $a > \mu r$. With an upper cutoff this is easy to require: take $n^a(c, b, y)$, the number of dipoles produced when the cutoff is a, subtract it from $n^{a'}(c, b, y)$, and one has the number of dipoles whose production involved a sequence which passed via at least one dipole of size in the range a to a'. As a result, the spatial distribution becomes:

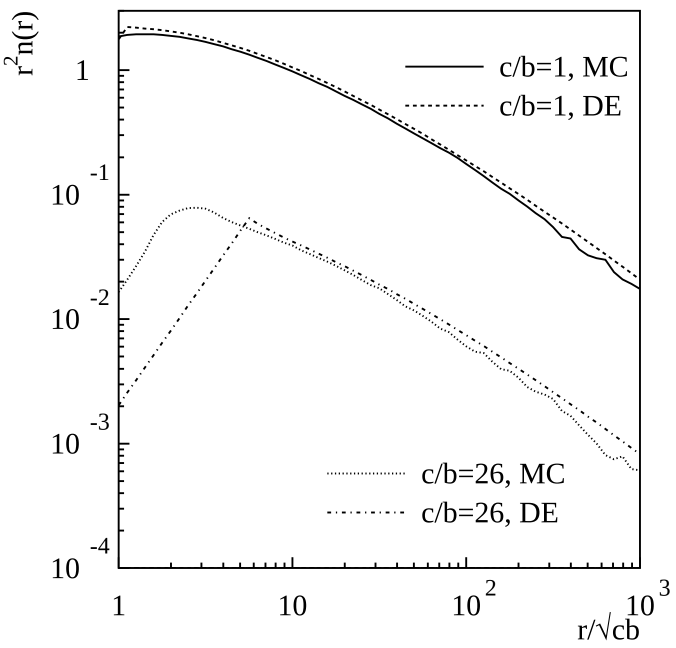

Figure 6.10: Determination of spatial distribution of dipoles in the onium wave function, for $y = 14$, using eq. (6.35) (curves labelled DE), compared to Monte Carlo results (curves labelled MC).

$$n(c, b, r, y) \simeq \int_{\mu r}^{\infty} \mathrm{d}a \frac{\mu^2}{\pi a^2} \frac{\mathrm{d}n^a(c, b, y)}{\mathrm{d}a}. \tag{6.35}$$

Because of the presence of the cutoff this cannot be evaluated analytically, but it is be amenable to numerical calculation, using the differential equation evolution of the dipole distribution discussed in section 5.1, though the process is slow (because the dipole distribution has to be evolved for each value of the cutoff). Results are shown in figure 6.10 and they indicate close agreement between this approach and the true (Monte Carlo) distribution for the range of applicability of eq. (6.35) ($r \gg c, b$). For values of $r < c$, the results from eq. (6.35) are just a straight line proportional to r^2 — since one is plotting $r^2 n(r)$, this is just a manifestation of the property that the density becomes roughly constant below a certain impact parameter. The Monte Carlo curve has a similar behaviour but starting at roughly $r \simeq c/2$. This difference arises because $\mathbf{r}$ is the mean of the positions of the two sources of the dipole, and so if one is producing dipoles of size c from smaller (central) ones then the position of those will be $r = c/2$ rather than $r = c$.

The results from this section therefore confirm the idea that the main mechanism for producing dipoles at a large distance r from the onium is through a branching path which includes a large dipole of size of the order of r.

6.8 Summary

This chapter has investigated a variety of the properties of onium wave functions.

As an introduction to the quantities which are being dealt with, and to gain some feeling for the ranges of validity of different analytic approximations, numerical results for the mean number of dipoles as a function of size were compared with saddle point solutions to the dipole equation, in the single-leading-logarithmic limit (logarithms of $1/x$), and in the double-leading-logarithmic limit.

The next stage was to investigate fluctuations in the total number of dipoles of any given size. For dipoles much smaller than the original onium, these are well described by pre-existing results for the DLL approximation: the dominant branching sequence is strongly ordered in transverse size and the probability distribution for n dipoles has an exponential tail $\sim \mathrm{e}^{-n}$. For dipoles of the same size as, or larger than the original onium, the most important branching sequence for producing many dipoles is the early production of a large dipole, which then cascades into many smaller ones.

It is also this kind of process which is responsible for the moderate to large r spatial distribution of dipoles: the only way for a dipole of size c to be produced at an impact parameter $r \gg c, b$ is if the branching sequence includes a dipoles of size r or larger. A variety of calculations based on this idea, together with the Monte Carlo results indicate that the distribution of dipoles is considerably more central than found in [16]. The discrepancy is explained in appendix A in terms of the approximations that were used in [16].

Important for the understanding of multiple-scattering corrections, in the next chapter, is the probability distribution of the density of dipoles, or equivalently of the number in a restricted region. Branching sequences involving dipoles larger than that region don't contribute, because the child dipoles are dilutely spread over too large an area. The Monte Carlo results and the calculations of appendix A show that the distribution has an exponential tail.

CHAPTER 7

Onium-onium interactions

As a brief reminder of the ideas of the previous chapters we will start by examining a couple of Monte Carlo "events". Figure 7.1 shows the dipole-dipole interaction as a function of the separation of the two dipoles. The main feature to note is that the interaction dies off quickly as the separation increases, justifying approximations that the dipole-dipole interaction is local. The other point to observe is that when two colour charges are close to each other, the interaction diverges (logarithmically) leading to the spikes in the amplitude.

The Monte Carlo procedure, as described in chapter 5 is to generate a pair of onium configurations, determine the interaction between them at a number of points in impact parameter, and then repeat the procedure until one has sampled a sufficient number of configurations. Figure 7.2 illustrates this process. At the top of the figure, a couple of onium configurations are shown (each for $y = 10$), each consisting of a chain of dipoles tracing out a random path in impact parameter. The lower part shows the interaction between these two configurations (corresponding to a total rapidity $Y = 20$). Calculating the one-pomeron amplitude, one finds the largest interaction in the region where the largest numbers of dipoles overlap from the two onia. In this region, the amplitude is much larger than 1, violating the unitarity bound. Again spikes are visible because because of the logarithmic divergences in the dipole-dipole amplitudes. When one takes into account all the multiple-pomeron (or multiple-scattering) terms, one obtains an amplitude which has an extended plateau in impact parameter, where the interaction is just below the unitarity limit of 1 — strongly reduced compared to the 1-pomeron amplitude.

As discussed previously, when carrying out most of the calculations presented here it will actually be more efficient to sample the interaction along a radial line, rather than on a grid.

7.1 One and two pomeron amplitudes

Before drawing any conclusions from the Monte Carlo calculations, it is necessary to check that the answers obtained are in good accord with expectations. All the results which will be given

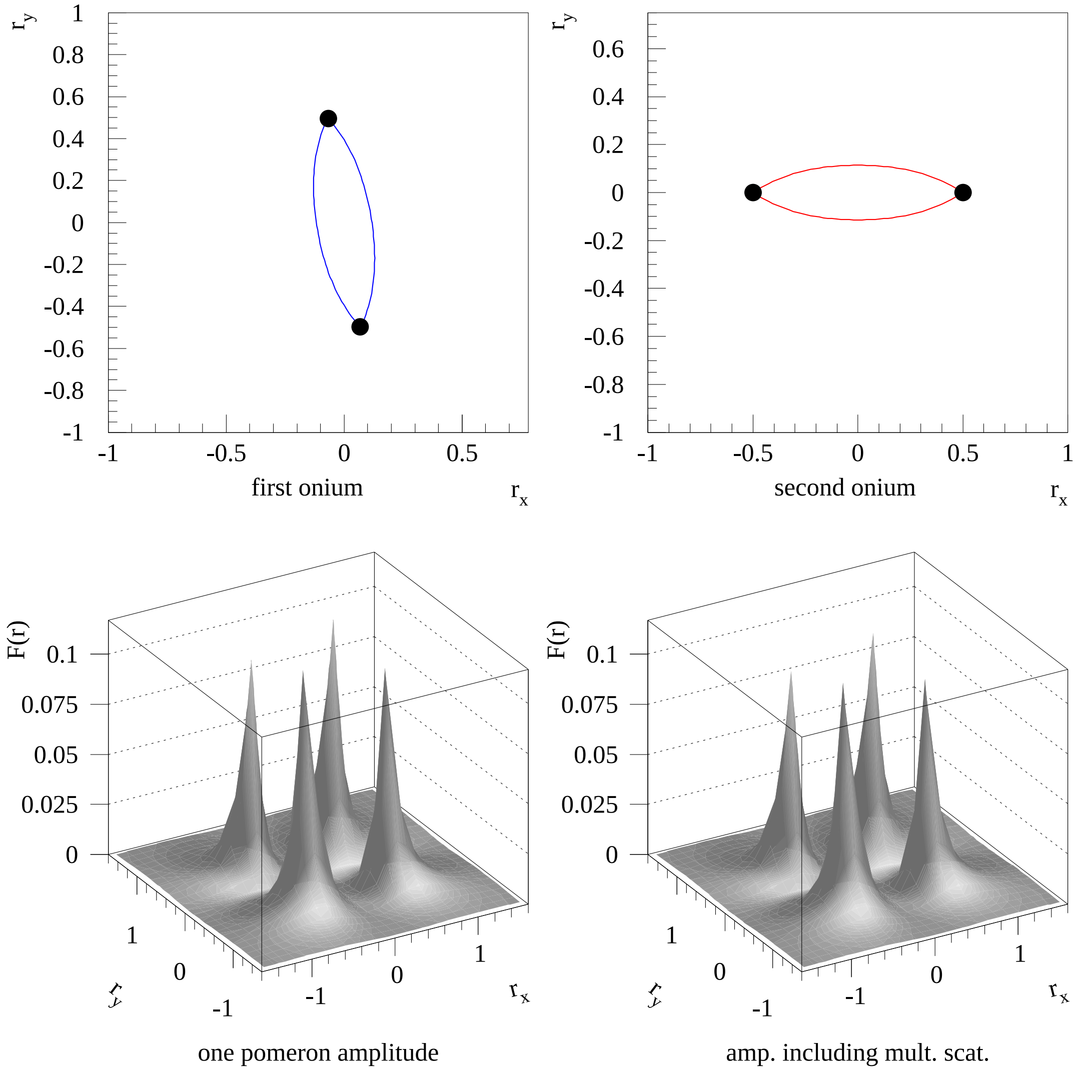

Figure 7.1: The dipole-dipole interaction as a function of the distance from the first dipole to the second. The black discs correspond to the colour sources, while the cigar shaped pairs of lines represent colour dipoles. The plot labelled 'mult. scat.' is not valid in this situation because the accurate evaluation of multiple-scattering corrections requires that there be many dipoles present.

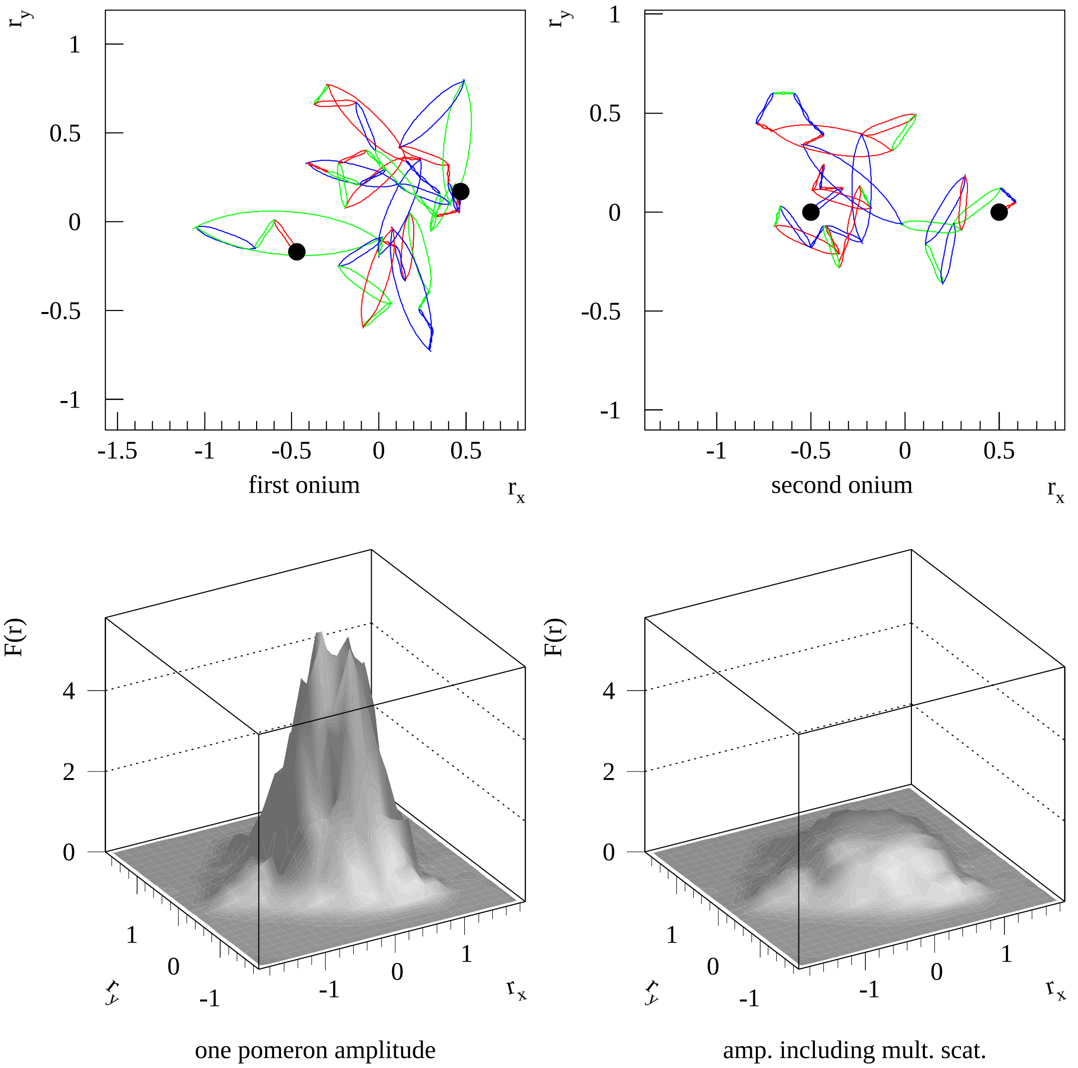

Figure 7.2: A pair of example onium configurations, and their interaction amplitudes with and without multiple-scattering corrections. The black discs represent the positions of the quark-antiquark pair for each onium. Cigar shapes represent colour dipoles (the colours used are purely for decorative purposes!). Each onium is evolved to a rapidity of $y = 10$.

here will be for the collision of onia of the same size, b.

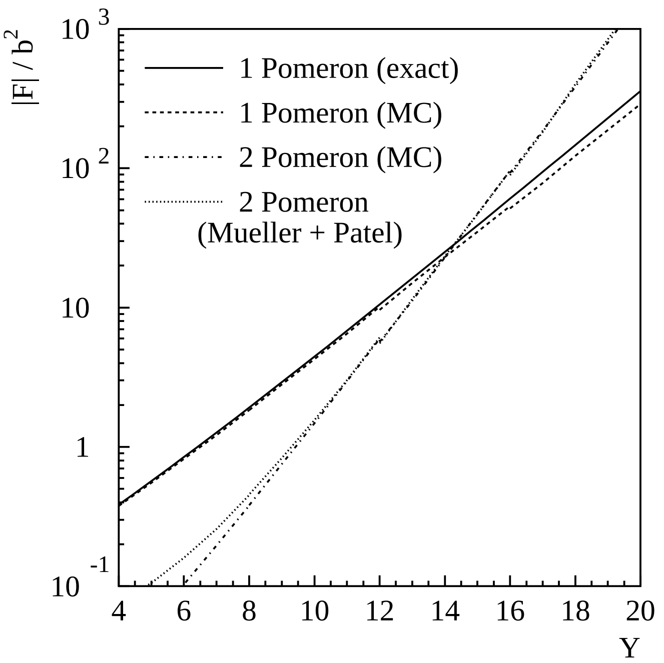

Figure 7.3: The total amplitude for onium-onium scattering as a function of rapidity. See text for details.

Figure 7.3 shows Monte Carlo results for 1 pomeron exchange, compared with the result from the numerical solution of the differential equation governing the evolution (which is essentially exact). Slight mismatches between Monte Carlo line segments are visible at $Y = 12$ and $Y = 16$: the points between $Y = 12$ and 16 all share the same evolution up to $Y = 12$, so that the errors due to fluctuations in the onium wave function are correlated, making it easier to see the trends in the evolution. The points from $Y = 16$ to 20 share their evolutions up to $Y = 16$, but they use a different set of evolutions from the points $Y = 12 - 16$, hence the mismatch at $Y = 16$ (and analogously at $Y = 12$), which is a measure of the statistical error. Note that the fluctuations in the wave functions increase at larger Y, while the accessible statistics go down (because of the larger number of dipoles in the onia), so that the statistical error increases at large Y. This is translated into a downwards shift of the amplitude, because one usually misses out on fluctuations with large amplitudes which would tend to increase the average amplitude. In addition, at higher rapidities a suppression of the same order sets in due to the lower cutoff on dipole size. These small factors aside, the Monte Carlo simulation gives a good estimate of the amplitude.

The main point of figure 7.3 is to show the relation between the two-pomeron and the one-pomeron amplitudes. This is of interest because the rapidity at which the two amplitudes are the same should be related to the rapidity at which unitarity corrections become important. The cross over occurs at $Y \simeq 14$, corresponding to an energy which is well beyond the reach of current accelerators.

In [18], Mueller and Patel derived the following relation for the total two pomeron amplitude:

$$F^{(2)}(Y) = -\Lambda \left(\frac{[F^{(1)}(Y)]}{\pi k Y} \right)^2 . \tag{7.1}$$

The expression which was given for Λ was left unevaluated. Eq. (7.1) is plotted in figure 7.3, using the Monte Carlo value for $F^{(1)}$, with a fitted value of $\Lambda = 6.9 \times 10^2$ (including uncertainties due to the cutoff, there is an error on this of about 5%). The agreement is good, except at low rapidities where non-asymptotic contributions are important.

7.2 Multi-pomeron amplitudes

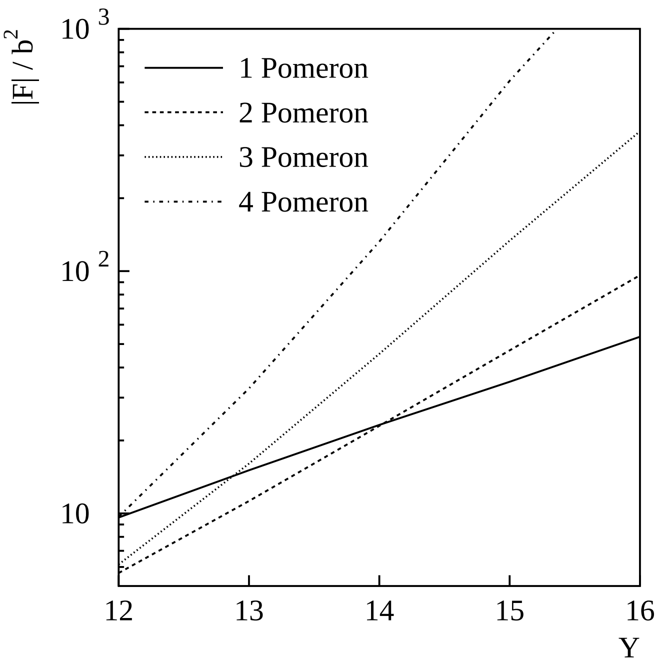

Figure 7.4: Total k-pomeron amplitude for onium-onium scattering as a function of rapidity, as obtained from the Monte Carlo simulation.

In section 4.6, it was shown for the toy model (without transverse dimensions) that because of the exponential fluctuations in the probability distribution for the number of dipoles, the multiple-pomeron series diverges. In section 6.5 it was shown that the probability of obtaining high dipole densities in the real situation (i.e. with transverse dimensions) was also exponential, suggesting that in the real case as well, there could be a divergence of the multiple-pomeron series. This is expected to set in once the one and two-pomeron amplitudes are of the same magnitude, from which point the multiple-pomeron series will be of no use in determining unitarity corrections. This is clearly visible in figure 7.4 which shows 1 to 4-pomeron exchange for $Y = 12$–16. Above $Y = 14$ the series looks divergent, while at lower rapidities, it looks asymptotic, with 2 and 3 pomeron exchange crossing over before 1 and 2 pomeron exchange, and so on and so forth for higher k.

One can test the ideas of section 4.6 in more detail by plotting $F^{(k)}(r=0)/F^{(k-1)}(r=0)$. In the toy model discussed there, this would be equal to $k(\alpha_S\mu)^2$, giving a straight line when plotted against k (μ was the mean number of dipoles in the onium without transverse dimensions). The same should apply for the case with 2 transverse dimensions, except that $(\alpha_S\mu)^2$ will be replaced by some factor which should be proportional to $F^{(1)}(r=0)$. The complications due to the transverse dimensions mean that it is not possible to make any prediction about the constant of proportionality.

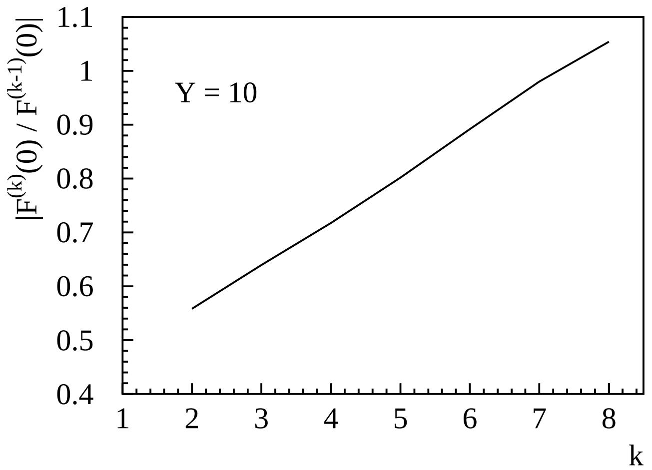

Figure 7.5: Ratio of k to $(k-1)$-pomeron exchange amplitude for impact parameter $\mathbf{r} = 0$.

Figure 7.5 shows the ratio $F^{(k)}(r=0)/F^{(k-1)}(r=0)$ for $Y = 10$. A low value of Y is chosen to allow the greater statistics which are needed to sample the tails of the probability distributions, which are relevant for large k. As one can see, the ratio has a clear linear dependence on k. The intercept with the k axis is at non-zero k, indicating that the k pomeron amplitude behaves as $(k+n)!$, rather than $k!$, where $-n \simeq -3$ is the value of the intercept. This difference means that, after taking into account the effects of the transverse dimensions, the fluctuations of the wave functions effectively deviate from exponential at low multiplicities, which is not unreasonable (the calculation showing the fluctuations to be exponential was valid only for the tails of the fluctuations). If one examines plots of the same ratio for other values of Y (in the range $Y = 8$ to 12) one finds that the slope of the straight line is approximately equal to $\beta F^{(1)}(r)$, where $\beta \simeq 0.2$. From the linear dependence of the ratio on k, and the behaviour of its slope with Y, one concludes therefore that the k-pomeron exchange amplitude at $r = 0$ is roughly proportional to $(k+n)![\beta F^{(1)}(0)]^k$, confirming that when multiple-pomeron contributions become important, the multiple-pomeron series diverges.

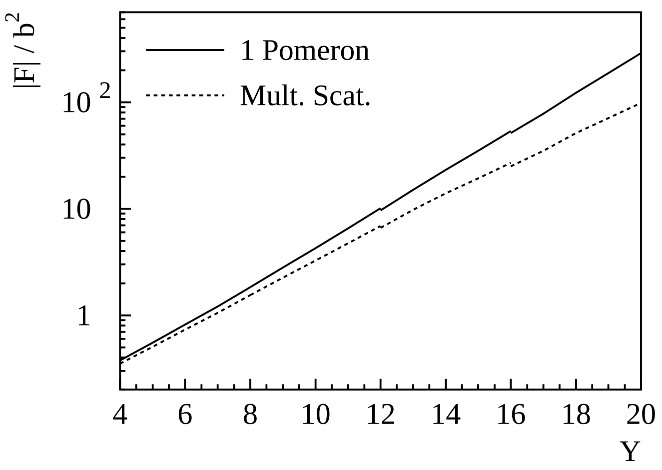

Figure 7.6: Total onium-onium amplitude, with and without multiple-scattering corrections, as obtained from the Monte Carlo simulation.

So at high rapidities, to understand multiple-pomeron corrections it is necessary to resum multiple scattering before summing over configurations of the two onia. The results of this are shown in figure 7.6. The effects of multiple-scattering corrections set in gradually: even when the amplitude for two pomeron exchange is many times larger than the one-pomeron amplitude, the amplitude with multiple-scattering corrections carries on growing relatively fast. At a rapidity of $Y \simeq 19$, the reduction in the effective power is only about 25% (see figure 7.12). The key to understanding why multiple-scattering corrections set in so gradually is in the profile of the amplitude in impact parameter.

7.3 The spatial distribution of the interaction

The first stage of investigating the spatial distribution of the amplitude, is to make sure that it corresponds to the analytical expectation:

$$F^{(1)}(b, b', r, Y) = \frac{8\pi\alpha_S^2 bb'}{r^2} \ln\left(\frac{16r^2}{bb'}\right) \frac{\exp[(\alpha_{I\!P} - 1)Y - \ln^2(16r^2/bb')/kY]}{(\pi k Y)^{3/2}}, \tag{7.2}$$

for $r \gg b, b'$ and $\ln r^2/bb' \ll kY$. This is compared with the Monte Carlo results in figure 7.7 and

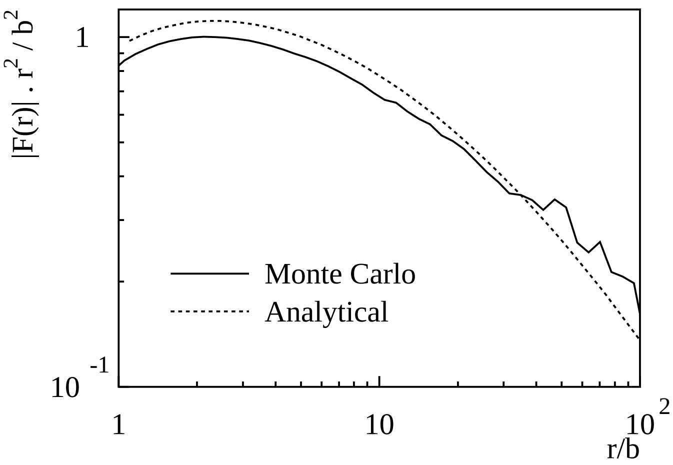

Figure 7.7: Comparison of analytical and Monte Carlo results for spatial distribution of interaction, for $Y = 14$. The analytical curve corresponds to eq. (7.2).

one sees a good general agreement, though there are discrepancies which are of the same order as those found when looking at the spatial distribution of dipoles in an onium wave function.

The importance of the profile in impact parameter of the amplitude, $F(r)$, is that it allows one to determine which region contributes most to the cross section, and also which region which has the largest multiple-scattering corrections. The top plot of figure 7.8 shows $F(r)$ against r. As one would expect, the amplitude is largest at small r and dies off quickly at larger r. However, to understand the contribution to the total amplitude, it is necessary to weight the amplitude with integration area:

$$F = \int \mathrm{d}\ln r \; 2\pi r^2 F(r). \tag{7.3}$$

The lower plot of figure 7.8 shows the amplitude weighted with r^2, so that the total amplitude is proportional to the area under the curve. The largest contribution to the total amplitude does not come from the region where $F(r)$ is largest: the r^2 enhancement means that radii of the order of 2 or 3 times the parent size are the most important for the total amplitude, even though the average amplitude is considerably smaller there than at $r = 0$. This is related to the logarithmic prefactor in eq. (7.2), which causes the maximum to be situated at $r = (b/4)\mathrm{e}^{\sqrt{kY/8}}$.

The two-pomeron amplitude is also shown in figure 7.8. With increasing r, it dies off faster than the one pomeron amplitude, which means that when weighted with r^2, it is more central. This is as suggested by Mueller in [16], and the consequence is that the one-pomeron and two-pomeron amplitudes are dominated by different regions of impact parameter: the two-pomeron amplitude can become large without much affecting the total amplitude, because

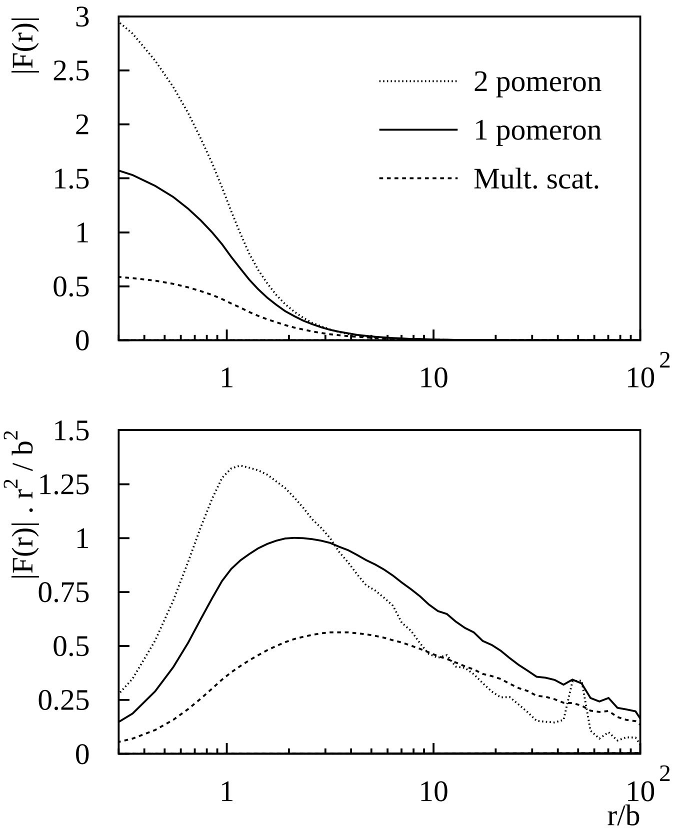

Figure 7.8: The top plot shows the average amplitude as a function of r. In the lower plot, the amplitude is weighted with r^2 so that the area under the curve is proportional to the cross section. $Y = 14$.

the two-pomeron contribution grows mostly near $r = 0$, while the total amplitude comes predominantly from larger radii. Note that while $|F^{(2)}(r)/F^{(1)}(r)|$ decreases with r, the ratio $|F^{(2)}(r)/[F^{(1)}(r)]^2|$ increases quite rapidly with r, as was predicted in [16] (in fact $|F^{(2)}(r)|$ decreases even more slowly with increasing r than was suggested there).

Looking again at figure 7.8, one sees that the largest multiple-scattering corrections are at also small r, so that the amplitude including multiple scattering, once weighted with r^2, has its maximum at larger r than the one-pomeron amplitude. However, there are significant corrections to the one-pomeron amplitude, even at radii where $F^{(1)}(r) \ll 1$. This is indicative of large fluctuations, or alternatively that eikonalisation is a poor approximation (and is also related to the strong rise in the ratio $|F^{(2)}(r)/[F^{(1)}(r)]^2|$ with increasing r). The eikonal approximation [1] (which appears for example in [148–150]) is valid in the limit of no fluctuations: if $F^{(1)}(\mathbf{r})$ is the same for each configuration-pair then the estimate for the amplitude including multiple-scattering corrections can be made after averaging over configurations:

$$F^{\mathrm{m.s.}}(r) \simeq F^{\mathrm{eik}}(r) = 1 - e^{-F^{(1)}(r)}. \tag{7.4}$$

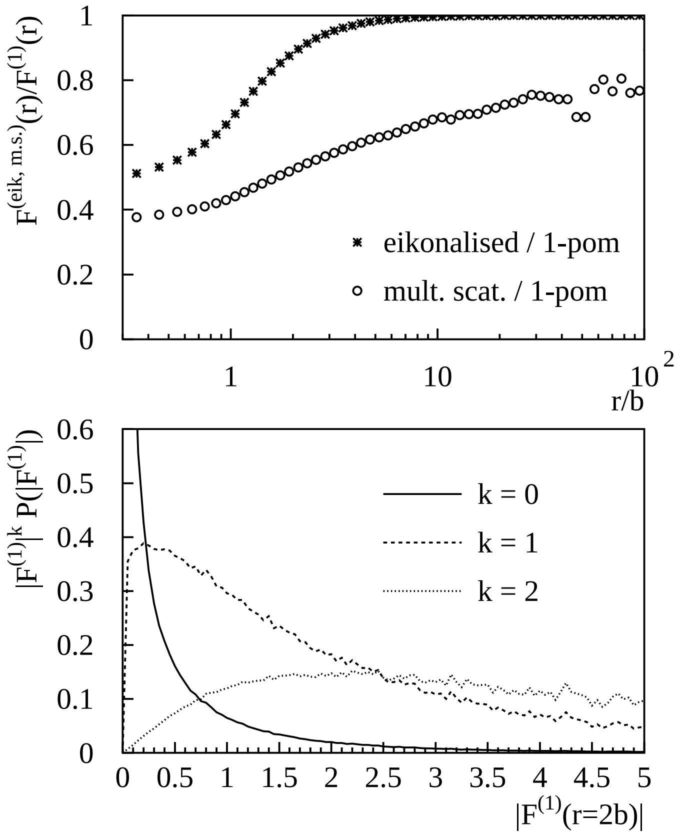

Figure 7.9: Top plot: the ratio of the amplitudes with multiple-scattering corrections and eikonalisation corrections to the one pomeron amplitude, as a function of r. Bottom plot: the probability distribution of $F^{(1)}$ for a fixed impact parameter, $|\mathbf{r}| = 2b$. Both plots are for $Y = 14$

Figure 7.9 shows the ratios $F^{\mathrm{m.s.}}/F^{(1)}$ and $F^{\mathrm{eik}}/F^{(1)}$. For small r where the amplitude is quite black, eikonal and multiple-scattering corrections both lead to similar, strong reductions of the amplitude. There are differences between them, and this is the form of failure of eikonalisation found in the toy model [16]. However if one examines the radii which contribute most to the total amplitude ($r \simeq 2b \to 3b$), eikonalisation would predict only very small corrections, whereas multiple scattering reduces the amplitude by roughly a factor of two. This means that the configurations contributing most to the one-pomeron cross section actually have relatively large amplitudes. Therefore for the average amplitude to still be low, the one-pomeron amplitude must be dominated by rare configurations.

The lower plot of figure 7.9 shows that this is in fact the case. The solid curve is the probability distribution of the amplitude $F^{(1)}(\mathbf{r})$ for $|\mathbf{r}| = 2b$. The dashed curve shows this probability distribution weighted by $F^{(1)}(\mathbf{r})$, normalised so that the total area under it is 1. The area under a particular region of the curve is indicative of how much that region contributes to the average amplitude at $\mathbf{r}$. The unweighted distribution is sharply peaked at $F^{(1)} = 0$. Yet the weighted distribution is spread over a wide range of $F^{(1)}$: 80% of the amplitude comes from from only 10% of the configurations. This is at the value of r which contributes most to the total amplitude. There is also a contrast between the curves for 1 pomeron and 2 pomeron (i.e. weighted with $[F^{(1)}]^2(r)$) exchange, however it is less marked: the region contributing 80% to the two pomeron amplitude contributes 40% to the one pomeron amplitude, though this region comes from only 2.5% of configurations, so that the two-pomeron amplitude here is dominated by somewhat rarer configurations than the one-pomeron amplitude. The same phenomenon, of rare configurations dominating one and multi-pomeron exchange is even more accentuated at larger r. It is also worth pointing out that since the total amplitude comes mostly from moderate values of r, it too is dominated by rare fluctuations: at $Y = 14$, two thirds of the total one-pomeron amplitude comes from only 10% of configuration-pairs.

The main reason why the amplitude at a given impact parameter is dominated by such a small fraction of configurations is that for an impact parameter somewhat away from the onium, dipoles are most likely to be first produced there later on in the evolution. But if they appear there only late then they won't have a sufficient rapidity range to build up in numbers. However if a dipole is produced there early on (an unlikely occurrence) then it will cascade into many dipoles and give a large interaction. These rare configurations dominate the amplitude, so that even though the amplitude will on average be small, it can still have significant multiple-scattering corrections. An example of such a rare pair of configurations is shown in figure 7.10. Superficially it looks very similar to the "event" shown in figure 7.2 (similar values for the one-pomeron amplitude) — except for the fact the interaction in figure 7.10 is spread over much larger range of impact parameters.

What allows the amplitude to continue growing at large rapidities, is that, for any given impact parameter, the probability of there being configurations with large interactions can carry on increasing until they become common. But there will always be larger radii at which big interactions are not yet common, so that the total amplitude can carry on increasing through an effective increase in the total area of interaction. This ignores of course the effect of saturation of the wave function, or confinement effects placing a maximum limit on the dipole size.

As a brief aside, it is to be noted that the characteristics of the large-r scattering amplitude for onia of similar sizes will apply to the central scattering of onia of very different sizes. This is a consequence of the conformal invariance of the scattering amplitude, which holds even when multiple-scattering corrections are included. For a more detailed of discussion of the conformal invariance properties of the scattering amplitude, the reader is referred to appendix B.

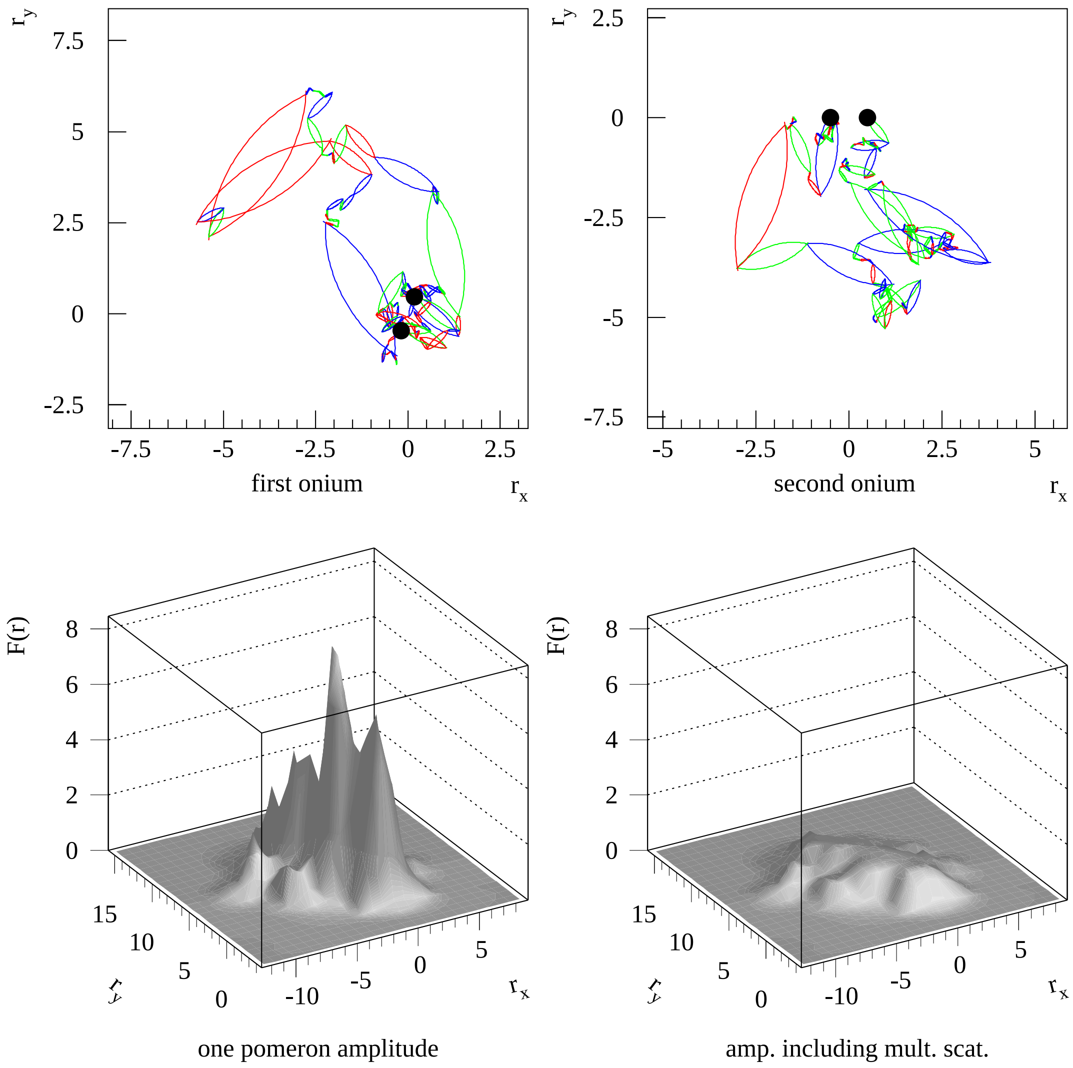

Figure 7.10: Example onium-onium interaction, extending over a large region of impact parameter. Each onium is evolved to a rapidity of $y = 10$.

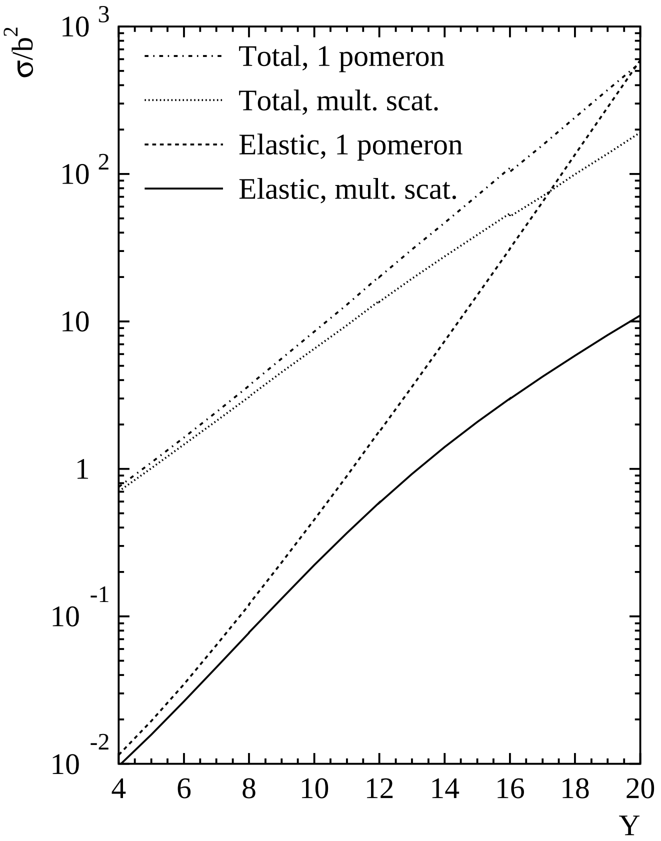

Figure 7.11: The elastic and total cross sections for onium-onium scattering, as a function of rapidity, showing both the one-pomeron approximation and the results including multiple-scattering corrections.

7.4 Elastic scattering

The effects of multiple-scattering corrections on the total amplitude (and correspondingly, total cross section) set in quite slowly, because the increase in the effective area of interaction allows the total cross section to carry on rising. However the amplitude is strongly modified at small impact parameters, and concentrating on this region should make it much easier to see the onset of multiple-scattering effects. A crude way of doing this is to look at the onium-onium elastic scattering cross section. An expression for the differential elastic cross section was given in eq. (4.67), but it is best to look initially at the integrated elastic cross section which can be written:

$$\sigma_{\mathrm{el}} = \int \mathrm{d}^2\mathbf{r} |A(\mathbf{r}, Y)|^2. \tag{7.5}$$

One should remember that $A(\mathbf{r}, Y)$ is obtained from $F(\mathbf{b}, \mathbf{b}', \mathbf{r}, Y)$ by integrating over $\mathbf{b}$ and

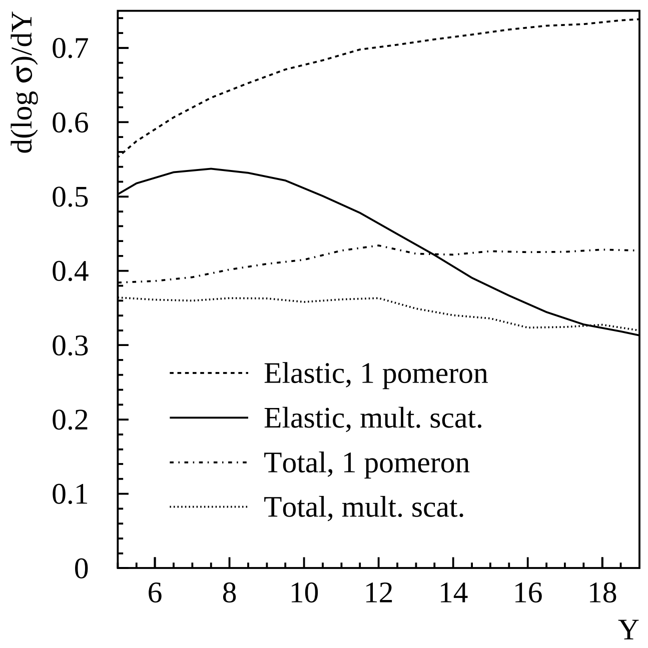

Figure 7.12: The power dependence in rapidity of the total and elastic cross sections, with and without multiple-scattering corrections, as a function of rapidity.

$\mathbf{b}'$ in the $q\bar{q}$ component of the wave functions of the two onia. However, for the purpose of understanding the essentials of the behaviour of the elastic cross section, this complication will be ignored: $|F|$ will be used instead of $|A|$. The leading power behaviour of F is $1/r^2$, which is why for the total cross section, large impact parameters can contribute. For the elastic cross section, though, one is integrating the square of the amplitude, which will fall off as $1/r^4$. So the integral is dominated by small r, where the multiple-scattering effects are strongest. Another aspect of the problem is that the elastic cross section can't exceed half the total cross section (the unitarity bound), but the asymptotic power growth with Y of the elastic cross section (in the one pomeron approximation) is twice that of the total cross section. Therefore there must be a reduction of the power growth of the elastic cross section by at least a factor of two.

Figure 7.11 shows the elastic cross section with and without multiple-scattering corrections, together with the analogous results for the total cross section, for reference. As suggested, the corrections to the elastic cross section are much larger than those to the total cross section, and one clearly sees the rate of increase of the elastic cross section tailing off to take the same value as that of the total cross section. At large rapidity, the fraction of the total cross section which comes from elastic scattering is still relatively small (about 0.06), certainly well below the unitarity bound of 1/2. The reason for this is, again, that the total cross section is coming from a large region in impact parameter where the amplitude is small, and so does not contribute much to the elastic cross section. It is also worth briefly noting, in view of the discussion on eikonalisation in the previous section, that the rapidity where the one-pomeron total and elastic cross sections cross over ($Y \simeq 20$), is the same as the point where the one and two pomeron contributions to the total cross section would cross if the eikonal approximation were valid, much larger than the rapidity ($Y \simeq 14$) where the one and two-pomeron amplitudes actually cross over — unitarity corrections set in at a rapidity six units lower than that suggested by the eikonal approximation.

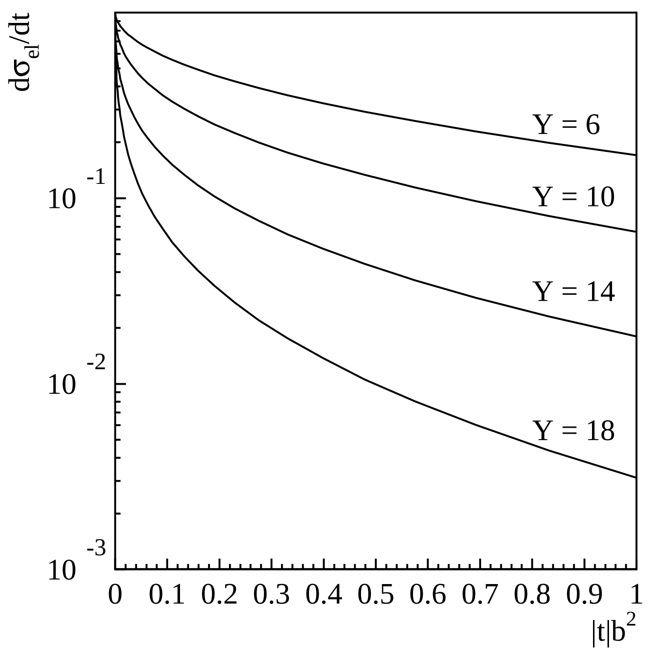

Figure 7.13: The differential elastic cross section (including multiple- scattering corrections) for different values of Y (normalised to be 1 at $t = 0$).

In figure 7.12, the effective power dependences of the total and elastic cross sections are plotted against Y. Looking first at the 1-pomeron cross sections, one sees that the powers vary with Y, tending only relatively slowly to their asymptotic values of 0.47 and 0.94 respectively. This is a result of the logarithmic corrections which are $1/\sqrt{Y}$ and $1/Y^3$ for the total and elastic cross sections. The power for the growth of the total cross section including multiple scattering deviates only slowly from the 1-pomeron power, and its variation with Y is also slow. On the other hand, the elastic cross section, including multiple scattering, grows with a power which differs quite noticeably from the 1-pomeron elastic cross section, and the variation of the power with Y is also very different, decreasing rather than increasing from $Y = 8$ onwards, tending towards the same power as the total cross section at large rapidity. This significant decrease in the elastic power, if not masked by other effects, might be a clear signal for the onset of unitarity corrections.

Finally, for completeness, it is worth looking at the differential elastic cross section, figure 7.13, as a function of the square of the exchanged momentum, t. It is strongly peaked at $t = 0$ (in fact there is a cusp there), because in impact parameter the amplitude dies off so slowly at large r. As Y increases, the mean region of interaction gets larger, which leads to a marked shrinkage of the elastic peak.

7.5 The AGK cutting rules and their implementation

As discussed in chapter 4, one cannot directly study particle production in the dipole formalism. Technically, this is because knowledge of the wave function is sufficient to describe forward elastic scattering, but not to describe an inelastic event where one must follow the time evolution of the wave function to a large positive time when particles (or jets) are produced. In terms of the diagrams which contribute to the scattering the cancellation of the final state interactions between real and virtual parts of the kernel no longer applies (in fact the cancellation probably doesn't occur even for the non-forward elastic scattering discussed in the last section [155]). However, using the Abramovskii, Gribov, Kancheli (AGK) cutting rules [156] one can relate particle production and forward elastic scattering involving one or more dipole scatterings. There has been no detailed proof of the AGK rules for QCD, so their validity will be extra assumption that is made here, though it is to be noted that in an explicit calculation of the triple-pomeron vertex and diffractive scattering by Bartels and Wüsthoff [8], the AGK rules have been found to be satisfied.

Schematically, the concept of cutting a BFKL pomeron is best understood in the ladder or t-channel representation, where the effect is to liberate the ladder gluons into the final state, as shown schematically in figure 7.14. The cutting is expected to yield a roughly uniform distribution of particles in rapidity. The details of the distribution of final state gluons which is liberated will not be discussed here. For information on that subject, the reader is referred

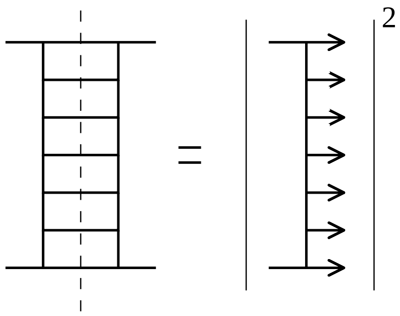

Figure 7.14: Schematic representation of a cut pomeron: the dashed line corresponds to the cut.

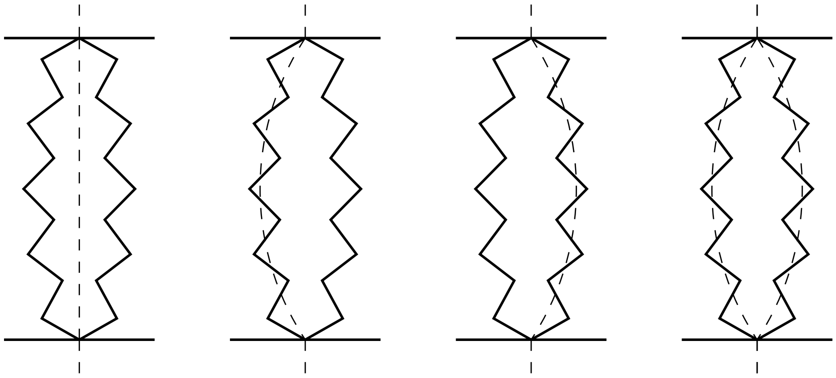

Figure 7.15: The different cuts which arise in two-pomeron exchange: the "springs" represent pomerons and the dashed lines are cuts.

to work by Marchesini and collaborators [128].

The matter which will be discussed here is the effect of multiple scatterings, or in the t-channel language, multiple pomeron exchange[1]. In this situation one or more of the pomerons can be cut and if each cut pomeron produces roughly the same number of final state particles, the multiplicity will be proportional roughly to the number of cut pomerons. So for a given number of exchanged pomerons one needs to know how many will be cut. This information is provided by the AGK cutting rules [156]. The types of cuttings for the two pomeron case are shown schematically in figure 7.15. In graph (a), the cut passes in between the two pomerons so that neither of them is cut. In (b) and (c), only one of them is cut: thinking in terms of the $2 \to n$ amplitudes represented on the right hand side of figure 7.14, an additional "complete" pomeron is present either in the amplitude or in the complex-conjugate amplitude. For this two pomeron case, the relative contributions from $a : (b + c) : d$ are $1 : -4 : 2$, which adds up to give -1, which is the overall weight of the 2-pomeron contribution to the total cross section.

The most convenient form for the AGK cutting rules is that which can be found in [157]. The cross section, σ_k involving the exchange of exactly k cut pomerons can be expressed as follows:

$$\sigma_k = \sum_{\nu=k}^{\infty} (-1)^{k+1} 2^{\nu} C_k^{\nu} F^{(\nu)}, \tag{7.6}$$

where $F^{(\nu)}$ is the amplitude for the exchange of ν pomerons. In this notation, the total cross section σ_{tot} is

$$\sigma_{\text{tot}} = 2 \sum_{\nu=1}^{\infty} F^{(\nu)}. \tag{7.7}$$

[1]This study, as well as the use of eqs. (7.6) and (7.9), were proposed by Mueller [155]

One knows from the work of sections 4.6, 6.5 and 7.2, that as a consequence of rare configurations of the onia, the terms of the sum in eq. (7.7) diverge as a factorial, and therefore so will the terms in eq. (7.6). The solution, as before, is to sum multiple-pomeron amplitudes before averaging over onium configurations. Applying this method here one obtains the differential cross section for obtaining k cut pomerons. As usual, the ν-pomeron amplitude for a fixed impact parameter $\mathbf{r}$ between the two onia (of sizes $\mathbf{b}$ and $\mathbf{b}'$, evolved to rapidities y and $Y-y$) is:

$$F^{(\nu)}(\mathbf{r},\mathbf{b},\mathbf{b}',Y,y) = \frac{(-1)^{\nu+1}}{\nu!}\sum_{\gamma,\gamma'} P_\gamma(\mathbf{r}_0,\mathbf{b},y)P_{\gamma'}(\mathbf{r}_0+\mathbf{r},\mathbf{b}',Y-y)(f_{\gamma,\gamma'})^\nu, \tag{7.8}$$

where $f_{\gamma,\gamma'}$ is the two gluon exchange interaction amplitude between a pair of configurations γ and γ' which occur with probabilities $P_\gamma(\mathbf{r}_0,\mathbf{b},y)$ and $P_{\gamma'}(\mathbf{r}_0+\mathbf{r},\mathbf{b}',Y-y)$ from onia situated at $\mathbf{r}_0$ and $\mathbf{r}_0+\mathbf{r}$. Substituting this into eq. (7.6) gives

$$\frac{\mathrm{d}^2\sigma_k}{\mathrm{d}^2\mathbf{r}} = \frac{1}{k!}\sum_{\gamma,\gamma'} P_\gamma(\mathbf{r}_0,\mathbf{b},y)P_{\gamma'}(\mathbf{r}_0+\mathbf{r},\mathbf{b}',Y-y)(2f_{\gamma,\gamma'})^k\exp(-2f_{\gamma,\gamma'}). \tag{7.9}$$

The cross section for obtaining no cuts is the difference between the total cross section (including all multiple-pomeron corrections) and $\sum_{k=1}^{\infty}\sigma_k$, which comes out as:

$$\frac{\mathrm{d}^2\sigma_0}{\mathrm{d}^2\mathbf{r}} = \sum_{\gamma,\gamma'} P_\gamma(\mathbf{r}_0,\mathbf{b},y)P_{\gamma'}(\mathbf{r}_0+\mathbf{r},\mathbf{b}',Y-y)\left(1-\mathrm{e}^{-f_{\gamma,\gamma'}}\right)^2. \tag{7.10}$$

In the work that follows, y will be set to $Y/2$, with the result that when one talks about the number of pomerons, this corresponds to the number at a central rapidity. Therefore the number of cuts should be proportional to the multiplicity at central rapidities.

7.5.1 Toy model calculation

As was the case for the multiple-pomeron corrections, the evaluation of eq. (7.9) is difficult to do analytically, because it requires a detailed understanding of the distribution of dipole configurations for an onium. However some of the features of multiple-cut cross sections can be extracted using the toy model, where the absence of transverse degrees of freedom greatly simplifies the problem.

In the toy model, the cross section for an interaction with k cut pomerons is

$$\sigma_k = \frac{1}{k!}\sum_{m,n}(2f\alpha_\mathrm{s}^2 nm)^k\exp(-2f\alpha_\mathrm{s}^2 nm)P_mP_n, \tag{7.11}$$

where the interaction amplitude between two dipoles is defined to be $f\alpha_\mathrm{s}^2$ (equivalent to $f_{\gamma,\gamma'}$ above). There are two limits which can be taken. Let $F^{(1)}$ be the amplitude for exchange of one pomeron. If $kF^{(1)} = kf\alpha_\mathrm{s}^2\mu^2 \ll 1$, then the exponential factor is not too important, and the evaluation of the cut cross sections is similar to the evaluation of the multiple-pomeron amplitudes (section 4.6):

$$\sigma_k \simeq k!(2F^{(1)})^k \mathrm{e}^{-2k^2 F^{(1)}}. \tag{7.12}$$

The opposite limit is when "unitarisation" effects are important, $kF^{(1)} = kf\alpha_{\mathrm{s}}^2\mu^2 \gg 1$ (and also $k/F^{(1)} \gg 1$). Approximating the sums by integrals, and changing variables to $n = \sqrt{u}\mathrm{e}^{\xi}$ and $m = \sqrt{u}\mathrm{e}^{-\xi}$ gives

$$\sigma_k \simeq \frac{1}{\mu^2 k!}(2f\alpha_{\mathrm{s}}^2)^k \int \mathrm{d}u\mathrm{d}\xi u^k \mathrm{e}^{-2f\alpha_{\mathrm{s}}^2 u}\mathrm{e}^{-2(\cosh\xi)\sqrt{u}/\mu}. \tag{7.13}$$

Performing the ξ integration using the saddle point approximation, it is clear that the integral is dominated by a region where m and n are similar. Performing the second integration gives

$$\sigma_k \simeq \frac{1}{2F^{(1)}}\left(\frac{2F^{(1)}\pi^2}{k}\right)^{1/4} \exp\left(-\sqrt{\frac{2k}{F^{(1)}}}\right). \tag{7.14}$$

The unusual feature of this result is the square root dependence on k in the exponential. Given that the number of cuts is related to the final state multiplicity, one might have expected the usual KNO type [147] exponential distribution. The origin of the $\sqrt{k}$ behaviour is that, in the region of configuration space contributing to the k-cut amplitude, the factor $(2f\alpha_{\mathrm{s}}^2 nm)^k \exp(-2f\alpha_{\mathrm{s}}^2 nm)$ is the most rapidly varying and fixes the dominant values of $n, m \propto \sqrt{k}$. The probabilities associated with the relevant configurations just fix the normalisation, with $P(\sqrt{k}) \sim \mathrm{e}^{-\sqrt{k}}$.

7.6 Results for multiple cut pomerons

7.6.1 Monte Carlo results for differential cut cross sections

One is most likely to find a similarity between the toy model results and the realistic situation, by examining the differential cut cross sections, which eliminates two of the transverse degrees of freedom. In section 7.2 the correspondence between the toy model and Monte Carlo results for zero impact parameter was established for the multiple pomeron exchange amplitudes. The main difference was that where the quantity ν occurred in an expression relating to ν-pomeron exchange, it had to be replaced with $(\nu + n)$ where n was a constant which originated from the details of the dynamics in the transverse dimensions. One might expect a similar effect when looking at cut cross sections, and one can examine the differential cross section at small impact parameters for behaviour of the form

$$\frac{\mathrm{d}^2\sigma_k}{\mathrm{d}^2\mathbf{r}}(r \simeq 0) \simeq \exp[-A(k+n)^\gamma + B], \tag{7.15}$$

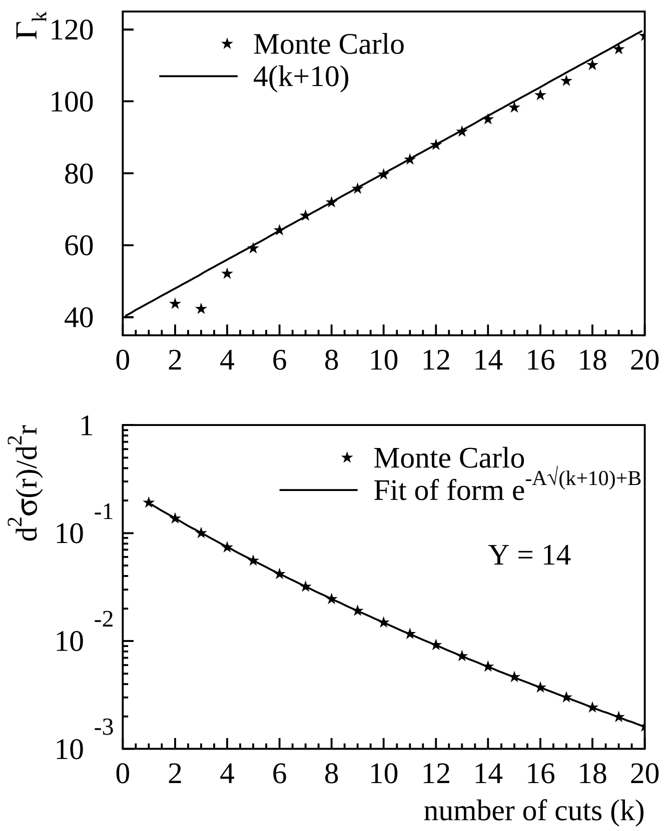

Figure 7.16: The upper plot shows Γ_k for fixed impact parameter: a test that the cut cross sections show the behaviour corresponding to eq. (7.15) (actually averaged over a range of $r = 0 \to 0.6b$); the lower plot shows the multiple-cut cross sections together with a fit of the form eq. (7.15) (for the range $r = 0.2b \to 0.3b$).

where A, B, n and γ are constants to be determined. The first stage is to ensure that one really does have $\gamma = 1/2$. By defining $l_k = -\ln \mathrm{d}^2\sigma_k/\mathrm{d}^2\mathbf{r}$ and plotting

$$\Gamma_k = \frac{l_{k+1} - l_{k-1}}{2l_k - l_{k-1} - l_{k+1}} = \frac{2(k+n)}{1-\gamma} + O(1/(k+n)), \tag{7.16}$$

(essentially the ratio of first and second derivatives) one can eliminate A and B. Figure 7.16 shows this quantity, determined using the Monte Carlo simulation, as a function of k. For k sufficiently large, the linear behaviour is clearly visible, and the slope corresponds to $\gamma = 1/2$. The value of the intercept with the k axis yields n, which has a value of 10. This is somewhat larger than the corresponding value found for multiple pomeron exchange ($\nu \to \nu + n$, with $n \sim 3$). The difference can be explained by arguing that the multiple-pomeron and multiple-cut cross sections are sensitive to the dipole distributions (and the manner in which they differ from an exponential) in different ways.

The other property to examine is the variation of A with Y. One clearly cannot expect A to be exactly $\sqrt{2/F^{(1)}(0)}$, however it might be reasonable for it to be proportional to $\sqrt{2/F^{(1)}(0)}$. Table 7.1 gives A for two values of Y, indicating that to within the accuracy of the Monte Carlo results, this proportionality does hold.

Y	n	A	$F^{(1)}(0)$	$A/\sqrt{2/F^{(1)}(0)}$
10	7	4.45	0.436	2.08
14	10	2.21	1.62	1.99

Table 7.1: Parameterisations of cut distributions at central impact parameters.

The dependence of the distributions on n is relatively weak which is why it is not determined more accurately.

7.6.2 Monte Carlo results for the integrated cut cross sections

In an experimental situation, one might be able to determine the cross sections for various ranges of central rapidity multiplicities, but this will correspond to cut cross sections integrated over impact parameter, for which there will not necessarily be any correspondence with the toy model. However figure 7.17 shows that a fit of the form eq. (7.15)

$$\sigma_k \simeq \exp[-A(k+n)^{1/2} + B] \tag{7.17}$$

works remarkably well. The value of n turns out to be considerably smaller than for eq. (7.15): this is associated with the fact that at larger impact parameters the value of n decreases.

It is not clear why the $\exp(-A\sqrt{k+n})$ behaviour also applies to the integrated cross section. One should note though that the results do suggest that the variation of the coefficient A with the rapidity is not as simple as in the toy model (or in the fixed impact parameter case). The numerical results for the variation with rapidity of the fraction of the cross section coming from different numbers of cuts are shown in figure 7.18. For small rapidities, the fractions of the cross section coming from 0 and 2 cuts are roughly in the ratio 1 : 2, as one expects from the AGK cutting rules in a region where one can ignore anything other than 1 and 2 pomeron exchange. As the rapidity increases, the 2-pomeron reaches a maximum, and then stays fairly constant (in fact it decreases a little). Increased average multiplicity then comes from the contributions of higher numbers of cuts, which increase rapidly and then become constant as well.

7.6.3 Spatial distribution of cut cross sections

One might ask to what extent a high-multiplicity event can be used as a trigger for a central collision: just as high numbers of pomeron exchange tend to be dominated by small impact

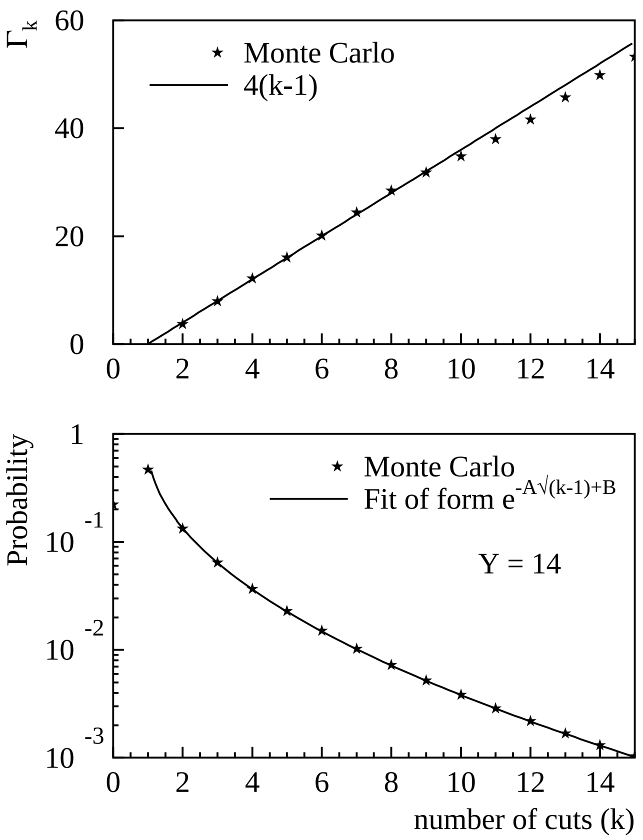

Figure 7.17: The upper plot shows Γ_k for the integrated cross sections; the lower plot shows the multiple-cut cross sections together with a fit of the form eq. (7.15).

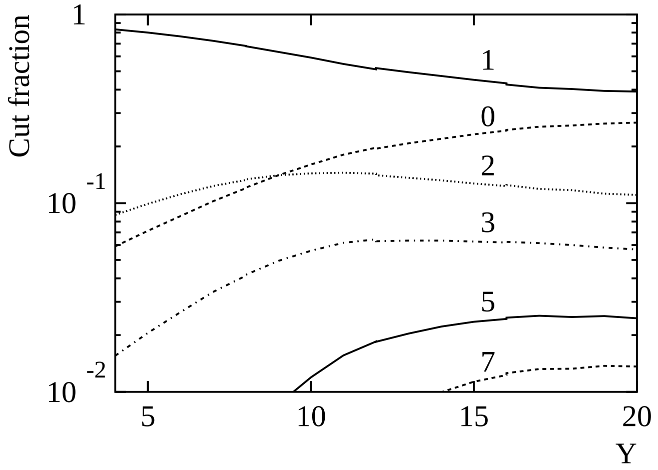

Figure 7.18: The fraction of the total cross section coming from different numbers of cuts (indicated by the labels next to the curves) as a function of rapidity.

parameters, one can expect events with large numbers of cuts also to be relatively central, because they are dominated by dense configurations, which arise most commonly at small impact parameters. This is illustrated in figure 7.19, which shows $\sigma_k(r > R)/\sigma_k$, the fraction of the k-cut cross section which comes from impact parameters larger than R, for various numbers of cuts, as a function of R.

One sees for example that about half the one-cut cross section is coming from a region $r < 3.2b$, whereas the first half of the 5-cut cross section comes from $r < 1.4b$. There is of course a limit to how central the many cut cross section can become, since any cross section is bound to be spread out over a region at least the size of the onia. The no cut cross section is also quite central: like the many cut cross sections, it is particularly sensitive to dense configurations. Note that all these cross sections have significant tails at large r. This is to be contrasted with the 5-pomeron curve, where the tail dies off quickly: the difference arises because of the "unitarity" corrections that are associated with multi-cut cross sections but not multi-pomeron contributions, and which limit the relative contributions from dense configurations.

7.7 Conclusions

This chapter has studied in detail the results of the Monte Carlo simulation for onium-onium interaction cross sections and the corresponding multiple-scattering corrections. The latter in particular are not amenable to analytical evaluation. The main conclusions are as follows:

- The multiple-scattering series diverges because of rare but dense configurations of the onia. To obtain a cross section which includes all numbers of multiple scatterings, it is

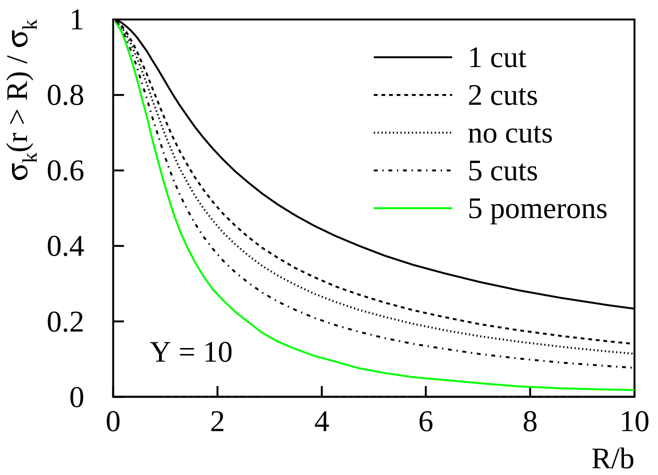

Figure 7.19: The fraction of the multiple-cut cross section which comes from impact parameters larger than R for a variety of numbers of cuts. At this rapidity, the mean number of cuts is ~ 1.3

necessary to resum multiple scattering before averaging over configurations of the onia.

- The effect of these corrections on the total cross section is to reduce by a small amount the power of its growth. This becomes noticeable only at rapidities $Y \gtrsim 14$. This is because the total cross section is dominated by moderate impact parameters, where the interaction amplitude is small, as are the multiple-scattering corrections.

- Nevertheless the corrections are much larger at moderate and large impact parameters than one would expect from an eikonal approximation, which gives corrections occurring six units higher in rapidity than when they are taken into account properly. The reason for the failure of the eikonal approximation is that it corresponds to neglecting the fluctuations in the onium configurations, and these fluctuations are important especially at large impact parameters, where rare configurations dominate the amplitude.

- The type of reaction where corrections are the most significant is elastic scattering, because it is dominated by central impact parameters, where the interaction amplitude is largest. Multiple-pomeron contributions affect the power for rapidities as low as $Y \simeq 8$, and at large rapidities the power of the growth of the elastic cross section, instead of being twice that of the total cross section, instead seems to reach the same value as that for the total cross section. In other words the elastic cross sections tends to a (roughly) constant fraction, about 5%, of the total cross section.

- As an additional signature for the presence of multiple-scattering corrections, results have been obtained on final state multiplicities, using the AGK cutting rules. They indicate that events with central multiplicities proportional to k should have a probability which is exponentially suppressed in $\sqrt{k}$. This is borne out both by analytical calculations for the toy model, and by the Monte Carlo simulation. It should be kept in mind though that no account is made of energy conservation, which would be expected to reduce the multiplicity associated with each cut pomeron when there are many which are cut.

CHAPTER 8

Saturation

The last chapter was devoted to the study of multiple-scattering corrections. If one looks back to chapter 4, one will remember that to the same order in $1/N_{\mathrm{C}}$ there were also corrections to the square of the onium wave function due to interactions between dipoles in the same onium. These interactions and their consequences for the evolution of the onium wave function will be referred to as saturation effects.

The justification for neglecting saturation was that in the centre-of-mass frame, where both wave functions are evolved to $Y/2$, multiple-scattering corrections will set in when $\alpha_{\mathrm{S}}^2 e^{(\alpha_{\mathbb{P}}-1)Y} \sim 1$, while saturation corrections for a particular dipole should be of the order $\alpha_{\mathrm{S}}^2 e^{(\alpha_{\mathbb{P}}-1)Y/2}$. Two problems can arise with this argument. The first relates to the question of whether α_{S} is small enough. In the calculations presented here, $\alpha_{\mathrm{S}} \sim 0.2$, so when multiple scattering is important one might expect $\alpha_{\mathrm{S}}^2 e^{(\alpha_{\mathbb{P}}-1)Y/2} \sim 0.2$. Since the conditions for saturation can only be guessed to within a factor of order 1, one is potentially close to the onset of saturation corrections as well. Secondly, the argument is based on the principle that the mean dipole density will be a good gauge of the saturation corrections, but it has already been shown in the previous chapter, for the case of multiple-scattering corrections, that the use of mean interactions can be misleading.

A second motivation for studying saturation corrections is to try and understand the behaviour of the wave function (and of scattering cross sections) at very high energies, i.e. at rapidities where even $\alpha_{\mathrm{S}}^2 e^{(\alpha_{\mathbb{P}}-1)Y/2}$ becomes of order 1.

Saturation effects show up as a modification of the simple branching picture of dipoles in constructing the square of the onium wave function. So a non-independence of the dipoles in an onium wave function is a measure of saturation. But it is not known how to estimate the interaction of dipoles in an onium wave function directly. One expects that the interaction of a slightly right-moving dipole with higher rapidity right-moving dipoles in a right-moving onium should be similar to that of a slightly left-moving dipole with the right-moving onium. This latter interaction is just the scattering amplitude for a simple dipole with an onium state and is straightforward to calculate. Thus one measure of saturation of an onium wave function is the

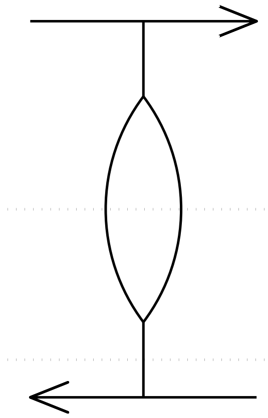

Figure 8.1: A t-channel representation of the correspondence between saturation and multiple-scattering corrections. The lines with arrows represent fast moving onia. The solid lines between them each represent pomerons. Rapidity increases vertically in the diagram. The dotted lines represent the division of rapidity between the two onia in centre-of-mass and lab frames.

interaction probability with an opposite moving elementary dipole. This measure of saturation is however time-consuming to evaluate. A more efficient measure is the *overlap* that a given dipole in the onium wave function has with all the other dipoles in the wave function. These two measures are strongly correlated so that the simpler overlap measure can be used. The first step in understanding the onset of saturation is to examine the distribution of the maximum saturation in the wave function for a given rapidity, and also to see how it correlates with the multiple-scattering corrections. It turns out that these results, on their own, are inconclusive, as they indicate that one might or might not be on the edge of the region where saturation matters — which, from the arguments above, we already know.

To go further, it will once again be useful to resort to the toy model, exploiting the simplicity which arises from the lack of transverse dimensions to illustrate techniques which can be useful. The principal idea that will be used is that cross sections must be frame invariant. As has already been shown in section 4.6, if one includes only the multiple-scattering corrections then the S-matrix is different depending on whether it is evaluated in the centre-of-mass (CM) or lab frames. But if one looks in the lab frame of the "left-moving" onium then the scattering looks exactly like the measure for saturation which has been discussed above since now the left-moving onium is simply a single dipole. Thus the multiple scatterings in the centre-of-mass system must show up as saturation effects in a system where one of the onia carries almost all the energy.

The connection between saturation and multiple scattering is in some way best understood by looking at the t-channel picture, figure 8.1, for two-pomeron exchange. In the t-channel, one has evolution of a single pomeron starting from the right-moving onium, which then branches to two pomerons. These evolve independently for a while, rejoin into one and then couple to left-moving onium. In the dipole picture (without saturation), all the $1 \to 2$ pomeron vertices are contained in the evolution of the wave function. In particular, there is no $2 \to 1$ type branching, so that the only way one can have a pomeron loop is if 2 onia evolving in opposite directions (in rapidity) join up together. Therefore in the centre-of-mass frame, where the two onia have equal rapidities, the graph of figure 8.1 is included. On the other hand, in the lab frame (left-moving onium nearly stationary) the only way the diagram shown can contribute is if the $2 \to 1$ vertex is also included in the evolution: this corresponds to two dipoles which come from separate evolution chains, interacting so that they then evolve as one object. This is what is being classified as saturation.

There are two ways of exploiting these ideas. The first, is to use the consistency condition of frame invariance to constrain the branching rate as a function of the number of other dipoles in the onium, such that if one collides two onia then the cross section should be independent of which one is more evolved. The branching rate which comes out depends on the interaction which is put in: if one has "one-pomeron" type interactions then one obtains the normal branching. But inclusion of multiple interactions gives a different branching rate when there are many dipoles, so that at high rapidities, the number of dipoles grows linearly rather than exponentially.

The second approach, suggested by Mueller [155] is to examine the results for the S-matrix in different frames, without saturation. In certain specific cases, one can deduce (roughly) the net effect of the saturation on the probability distribution of configurations which is needed to restore frame invariance. In the case of the toy model, it is necessary to look at onium-nucleus collisions, and one obtains a result which agrees with that found using the first method.

In QCD, such complete analytical calculations are not possible. But one can nevertheless make use of the same idea of frame invariance. On the one hand, the technique suggested by Mueller of examining the S-matrix in two different frames allows one to obtain information about the small-impact parameter properties of *typical* configurations of very high rapidity onia. The other approach will be to introduce a phenomenological modification of the dipole branching, choosing it so that it leads to frame invariance of the scattering amplitude. This is the only way of obtaining information about the effect of saturation at larger impact parameters, and of determining its overall effect on the total cross section.

8.1 Measures of saturation

It is first necessary to develop a measure of saturation. Two methods will be used here. Firstly one can probe a wave function with an (unevolved) onium[1]. The two gluon exchange amplitude between the wave function and the onium indicates the local density of dipoles of size similar to the onium and might be similar to the interaction that a dipole in the wave function would have with its neighbours. Since the dipole-dipole interaction has spikes wherever two sources

[1] This method was developed in conjunction with Mueller [155]

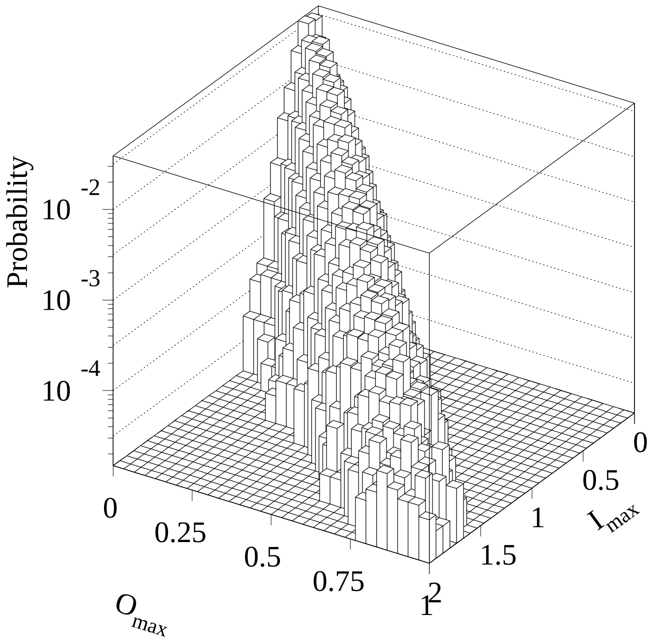

Figure 8.2: The probability of a given onium configuration lying in a certain $I_{\max}$, $O_{\max}$ bin, for $y = 10$.

overlap, one should average the interaction over a region of roughly the onium size. The choice of the size of the region over which to average is one of the main uncertainties with this method. It also has the disadvantage of being relatively slow, because one needs to determine dipole-dipole interactions at many points to determine the saturation over the whole extent of the wave function and if one wants the saturation associated with dipoles of different sizes, one must use probes of different sizes.

The second method is more arbitrary, but much faster to compute. Each dipole has an "overlap" associated with it. For each pair of dipoles within the onium wave function which are separated by less than a certain distance (proportional to the dipole sizes) the quantity $\alpha_s^2 c_<^2/c_>^2$ is added to the overlap for each of the two dipoles (where, as usual, the smaller dipole has size $c_<$ and the larger, size $c_>$). This function is loosely based on the fact that the total two-gluon interaction amplitude between a pair of dipoles (moving fast relative to each other) has the form $\alpha_s^2 c_<^2/c_>^2(1 + \ln c_>/c_<)/2$ and that it is dominated by a region where the two dipoles are close in impact parameter. This method has the advantage that one obtains a value of the saturation for each dipole.

Comparing the two methods one finds that there is a good (linear) correlation between them, as can be seen in figure 8.2 which shows the frequency distribution for configurations with various values of $I_{\max}$ (the maximum interaction with the probe) and $O_{\max}$ (the maximum

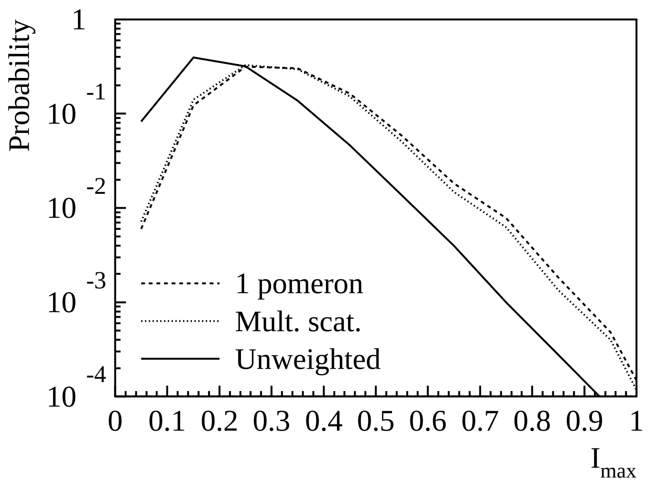

Figure 8.3: The probability distribution of the larger $I_{\max}$ from a pair of onia ('unweighted' curve), and the fractions of cross sections coming from configuration pairs with particular values of $I_{\max}$ ('1-pomeron' and 'mult. scat.' curves); $Y = 12$.

overlap). One can carry out other comparisons, in particular considering the location in impact parameter of the maximum saturation, and one again finds that the two methods give similar results. If one examines other values of rapidity, one finds that the factor relating $I_{\max}$ and $O_{\max}$ stays approximately the same.

8.1.1 Distribution of $I_{\max}$

The degree of saturation is obviously just related to the density of dipoles. Therefore the distribution of $I_{\max}$ should be related to the probability of obtaining large densities, which has been shown to be exponential in chapter 6, the slope of the exponential being proportional to the mean density of dipoles. Instead of searching the whole relevant region of impact parameter for the location of $I_{\max}$, one finds the location of the dipole corresponding to $O_{\max}$ and bases the search for $I_{\max}$ around that point. The probe size is always the same as the onium size.

One finds, as expected, that $I_{\max}$ also shows an exponential behaviour, with a slope varying in proportion to the local density of dipoles. One also finds that the maximum saturation is usually close to the original onium which is also unsurprising since that is where the evolution has the longest rapidity range to produce a large number of dipoles.

While these properties are of general interest, one of the main reason for studying saturation is to see whether it is likely to affect the onium-onium cross section. So one needs to know the typical values of $I_{\max}$ and also the correlation between $I_{\max}$ for a pair of onium configurations and the interaction cross section for that pair of configurations.

The most appropriate value of rapidity to examine is $Y = 12$, since this is the rapidity for which the mean 1-pomeron amplitude at $r = 0$, $F^{(1)}(r = 0)$, is equal to 1. Consider first the 'unweighted' curve of figure 8.3: this is the probability distribution of $I_{\max}$ in onium-onium collisions with a total rapidity $Y = 12$. The rapidity for each onium is $y = Y/2 = 6$. $I_{\max}$ is now defined to be the larger of the $I_{\max}$ values for the two onium configurations. One sees that typical values of saturation are $0.1 \to 0.3$. The exponential probability distribution for large saturation is relatively clear. More relevant though are the distributions weighted with the onium-onium cross section for each configuration pair: the weighted distributions correspond to the fraction of the cross section coming from configuration pairs with a certain $I_{\max}$, and one sees that the typical saturation has increased to be in the range $0.2 \to 0.45$. There are two main reasons why configuration pairs with larger cross sections are associated with larger saturation. Firstly if one of the onia has a high density of dipoles in some region, then the interaction of that region with a second onium will be enhanced. A second possibility, which will be considered in more detail later, is that configurations which lead to a large interaction (e.g. those with large dipoles) are most likely to be produced by branching sequences that pass through a high-density stage.

There remains the problem of assessing the effect that this degree of saturation would have. One can assume that saturation will start to become important when $I_{\max} \sim 1$, but this is an approximate condition, being uncertain to within at least a factor of two. This factor of two is critical: if the condition for saturation is $I_{\max} \sim 2$ then there will be no problem with saturation at $Y = 12$, on the other hand if it is $I_{\max} \sim 1/2$ then saturation could significantly alter the results at this rapidity. If saturation is important then one wants to know how it will affect the evolution: for example the saturation might be large in one region of impact parameter, but the bulk of the cross section might come from different regions, not affected by saturation. The next sections address these and other issues.

8.2 Saturation in the toy model

8.2.1 Evolution including saturation

One approach to the problem is from the toy model, using the condition that the scattering amplitude must be independent of the frame in which calculation is performed. Equivalently, it shouldn't matter which of the two onia one chooses to evolve. Starting with a state containing n dipoles, the rate of branching into a state containing $n+1$ dipoles is defined to be R_n, while the interaction between two states with n and m dipoles respectively is $F(n, m)$. If the evolution is partitioned such that for an increase δY in total rapidity, the onium with n dipoles evolves by $\xi \delta Y$ and the one with m dipoles evolves by $(1-\xi)\delta Y$, then the evolution of the amplitude F will be

$$\frac{\mathrm{d}F}{\mathrm{d}Y} = \xi R_n \left[F(n+1, m) - F(n, m)\right] + (1-\xi) R_m \left[F(n, m+1) - F(n, m)\right]. \tag{8.1}$$

In the case of one pomeron exchange, one has $R_n = (\alpha_{\mathrm{IP}} - 1)n$ and $F(n,m) = f\alpha_{\mathrm{S}}^2 nm$ (where f sets the strength of the interaction), giving

$$\frac{\mathrm{d}F^{(1)}}{\mathrm{d}Y} = [\xi + (1-\xi)](\alpha_{\mathrm{IP}} - 1)f\alpha_{\mathrm{S}}^2 nm, \tag{8.2}$$

which is clearly independent of ξ.

If for $F(n,m)$ one uses the form which includes multiple-scattering corrections, $F(n,m) = [1 - \exp(-f\alpha_{\mathrm{S}}^2 nm)]$, one obtains the following expression for the evolution of the interaction:

$$\frac{\mathrm{d}F^s}{\mathrm{d}Y} = \left[\xi R_n^s \left(1 - \mathrm{e}^{-f\alpha_{\mathrm{S}}^2 m}\right) + (1-\xi)R_m^s \left(1 - \mathrm{e}^{-f\alpha_{\mathrm{S}}^2 n}\right)\right] e^{-\alpha_{\mathrm{S}}^2 mn}, \tag{8.3}$$

where the superscript s indicates that saturation is being taken into account. The condition that the growth of the cross section be independent of ξ, as well as one's knowledge of the branching rate for small n (where saturation should be unimportant) leads to the following expression for the rate of branching:

$$R_n^s = \frac{(\alpha_{\mathrm{IP}} - 1)}{f\alpha_{\mathrm{S}}^2}\left(1 - \mathrm{e}^{-f\alpha_{\mathrm{S}}^2 n}\right). \tag{8.4}$$

Note that though the interaction with a second onium was used in the determination of this branching rate, the result is independent of the state of the second onium.

To see what effect saturation will have on the final probability distribution of dipoles, one can use the following arguments. First take the case without saturation, in the continuum limit for n. The probability distribution satisfies

$$\frac{\mathrm{d}P}{\mathrm{d}y} = -\frac{\mathrm{d}R_n P}{\mathrm{d}n} = -(\alpha_{\mathrm{IP}} - 1)\frac{\mathrm{d}nP}{\mathrm{d}n}. \tag{8.5}$$

Changing variables to $Q = nP$, $\zeta = (\alpha_{\mathrm{IP}} - 1)y$ and $\nu = \ln n$, one has

$$\frac{\mathrm{d}Q}{\mathrm{d}\zeta} = -\frac{\mathrm{d}Q}{\mathrm{d}\nu}, \tag{8.6}$$

whose solution (from our knowledge that $P = \exp[-(\alpha_{\mathrm{IP}} - 1)y - n\exp(-(\alpha_{\mathrm{IP}} - 1)y)]$) is

$$Q = \exp\left(\nu - \zeta - \mathrm{e}^{\nu - \zeta}\right). \tag{8.7}$$

In the case with saturation one has

$$\frac{\mathrm{d}P^s}{\mathrm{d}y} = -\frac{\mathrm{d}R_n^s P^s}{\mathrm{d}n} = -\frac{(\alpha_{\mathrm{IP}} - 1)}{f\alpha_{\mathrm{S}}^2}\frac{\mathrm{d}(1 - \mathrm{e}^{-f\alpha_{\mathrm{S}}^2 n})P^s}{\mathrm{d}n}. \tag{8.8}$$

By an appropriate change of variables, $Q^s = (1 - \mathrm{e}^{-f\alpha_\mathrm{S}^2 n})P^s/(f\alpha_\mathrm{S}^2)$, $\zeta = (\alpha_\mathrm{I\!P} - 1)y$ and $\nu^s = \ln[(\mathrm{e}^{f\alpha_\mathrm{S}^2 n} - 1)/(f\alpha_\mathrm{S}^2)]$, one can obtain an equation identical to eq. (8.6)

$$\frac{\mathrm{d}Q^s}{\mathrm{d}\zeta} = -\frac{\mathrm{d}Q^s}{\mathrm{d}\nu^s}. \tag{8.9}$$

Because, in the limit of small n and ζ, $Q^s \simeq Q$ and $\nu^s \simeq \nu$, the equation for Q^s will have the same initial conditions as that for Q and therefore their solutions will be the same. Translating this back to the variables P^s and n, one has

$$P^s(n,y) = \exp\left[f\alpha_\mathrm{S}^2 n - (\alpha_\mathrm{I\!P} - 1)y - \frac{1}{f\alpha_\mathrm{S}^2}\left(\mathrm{e}^{f\alpha_\mathrm{S}^2 n} - 1\right)\mathrm{e}^{-(\alpha_\mathrm{I\!P}-1)y}\right]. \tag{8.10}$$

For $\mathrm{e}^{(\alpha_\mathrm{I\!P}-1)y}, n \ll 1/(f\alpha_\mathrm{S}^2)$ this approximates to the solution without saturation. The main feature of this solution though is that at large y, instead of there being an exponential distribution in n with mean $\exp((\alpha_\mathrm{I\!P} - 1)y)$, one now has a solution which has a maximum at

$$n = \frac{1}{f\alpha_\mathrm{S}^2}\left[(\alpha_\mathrm{I\!P} - 1)y + \ln f\alpha_\mathrm{S}^2\right], \tag{8.11}$$

and which dies off quickly beyond that.[2]

One effect of this modified probability distribution is to increase the value of the S-matrix at very large rapidities. If one calculates the S-matrix in the centre-of-mass frame (rapidity Y divided equally between the two onia) neglecting saturation one obtains (eq. (4.103)):

$$S(Y) \sim \frac{-1}{f\alpha_\mathrm{S}^2\mathrm{e}^{(\alpha_\mathrm{I\!P}-1)Y}}\ln\left[f\alpha_\mathrm{S}^2\left(1 + \frac{1}{f\alpha_\mathrm{S}^2\mathrm{e}^{(\alpha_\mathrm{I\!P}-1)Y/2}}\right)^2\right]. \tag{8.12}$$

Note that this is much larger than the value of the S-matrix that one obtains from typical configurations (namely $\exp(-f\alpha_\mathrm{S}^2 e^{(\alpha_\mathrm{I\!P}-1)Y})$). This difference arises because the S-matrix is dominated by a small fraction of configurations which have few dipoles.

Calculating the S-matrix including saturation (done in the lab frame, to reduce sensitivity to the use of the continuum limit, though the result is of course independent of frame), one obtains

$$S(Y) \sim \frac{1}{f\alpha_\mathrm{S}^2\mathrm{e}^{(\alpha_\mathrm{I\!P}-1)Y}}\left[\ln f\alpha_\mathrm{S}^2\mathrm{e}^{(\alpha_\mathrm{I\!P}-1)Y}\right]. \tag{8.13}$$

When $f\alpha_\mathrm{S}^2\mathrm{e}^{(\alpha_\mathrm{I\!P}-1)Y/2} \ll 1$, eqs. (8.12) and (8.13) give the same result, consistent with the idea that saturation should not be important in the centre-of-mass frame for that energy range.

[2] Note that beyond $n = (\alpha_\mathrm{I\!P} - 1)y/f\alpha_\mathrm{S}^2$ the solution eq. (8.10) breaks down because the continuum limit used in its derivation is no longer valid (P^s varies too rapidly over a range $\delta n \sim 1$). Numerical solution shows though that there is still a rapid fall off beyond the maximum, having roughly a Poisson distribution, since the branching rate $n \to (n+1)$ becomes independent of n.

However for $f\alpha_S^2 e^{(\alpha_{\mathbb{P}}-1)Y/2} \gg 1$, eqs. (8.12) and (8.13) do differ (the saturated case has a logarithmic dependence on energy, absent from the calculation without saturation), because saturation then matters in the evolution of the onium wave functions, even in the centre-of-mass frame.

8.2.2 Saturation from the S-matrix in different frames

While the above approach works well for the toy model, in the real case, an analogous method will turn out to be too complex to be useful. Nevertheless, as pointed out by Mueller [155], one can also make use of the effect of a change of frame on the average amplitude (including multiple-scattering corrections). The simplest pair of frames to examine would be centre-of-mass and lab frames for onium-onium scattering. However one finds that, except for logarithmic factors, the S-matrix behaves in a similar way in the two. Consider instead collisions between a toy onium and a toy "nucleus" consisting of N onia. Two frames will be used: a lab frame L_O where the onium is at rest, and a lab frame L_N where the nucleus is at rest. At high energies (neglecting saturation), in frame L_N, with the onium being evolved, the S-matrix is approximately

$$S_N \simeq \frac{1}{N f \alpha_S^2 e^{(\alpha_{\mathbb{P}}-1)Y}}. \tag{8.14}$$

Except for logarithmic terms (and the factor N) this has the same leading energy behaviour as the centre-of-mass onium-onium S-matrix, and is similarly dominated by those rare configurations of the onium which have few dipoles (the common configurations have such a large number of dipoles that their contribution to the S-matrix can be neglected).

In the L_O frame, it is the nucleus which it is evolved. Assuming for the sake of the argument that the constituent onia evolve independently (consistent with our neglect of saturation), configurations with few dipoles will be much rarer, because they require that none of the N constituent onia should have evolved much. Accordingly, when one calculates the S-matrix, one finds

$$S_O \simeq \frac{1}{\left(f \alpha_S^2 e^{(\alpha_{\mathbb{P}}-1)Y}\right)^N}, \tag{8.15}$$

which is much smaller than the result in the L_N frame. One way of restoring the correspondence is by requiring that saturation alter the probability distribution of the number of dipoles so that the value of the S-matrix for a *typical* configuration of the nucleus is now

$$S_O^{\text{typical}} \sim \frac{1}{N f \alpha_S^2 e^{(\alpha_{\mathbb{P}}-1)Y}}. \tag{8.16}$$

Equivalently the typical number of dipoles must be of the order of $[(\alpha_{\mathbb{P}}-1)Y + \ln N f \alpha_S^2]/(f\alpha_S^2)$. Note that this is just the result of eq. (8.11) (except for the $\ln N$ term which is a result of the use of nuclei). The advantage of examining the effect of frame changes on the average S-matrix is that one can transfer the arguments fairly straightforwardly to the case of scattering with transverse dimensions.

8.3 Saturation and central collisions

The real case, including transverse dimensions, is much more complicated, to a large extent because the dipole picture breaks down at high dipole densities and one needs to take into account quadrupoles, hexapoles, and other more complicated colour structures [19, 158]. This section will deal with various approaches that one can nevertheless try in order to deduce more information about the effects of saturation in the real case, still using the requirement of frame independence.

It is simple to write down the equation which must be satisfied for frame independence to hold. This will be the equivalent (with transverse dimensions) of the independence of eqs. (8.1) and (8.3) on ξ. Let γ be a particular gluon configuration and $\{\gamma_{\mathbf{b}}\}$ be the set of all colour configurations with an extra gluon added at transverse position $\mathbf{b}$, with $\gamma_{\mathbf{b}}$ being any particular one of these. In the dipole approximation (large N_C), a particular $\gamma_{\mathbf{b}}$ corresponds to the gluon having originated from a particular dipole. Define also $F_{\gamma,\gamma'}(\mathbf{r})$ to be the interaction between configurations γ and γ' (moving in opposite directions) when they have a relative separation in impact parameter of $\mathbf{r}$. Then for the scattering to be frame independent (or equivalently for it not to matter which onium is evolved) the rate of evolution $R(\gamma \to \gamma_{\mathbf{b}})$ must satisfy

$$\sum_{\{\gamma_{\mathbf{b}}\}} \int \mathrm{d}^2\mathbf{b} R(\gamma \to \gamma_{\mathbf{b}}) \left(F_{\gamma_{\mathbf{b}},\gamma'} - F_{\gamma,\gamma'}\right) = \sum_{\{\gamma'_{\mathbf{b}}\}} \int \mathrm{d}^2\mathbf{b} R(\gamma' \to \gamma'_{\mathbf{b}}) \left(F_{\gamma,\gamma'_{\mathbf{b}}} - F_{\gamma,\gamma'}\right). \tag{8.17}$$

In the case of of the one-pomeron approximation for the scattering amplitude F, and the normal dipole evolution kernel for R, if one can show that eq. (8.17) holds for a single dipole in each onium, then because dipoles in each onium interact (and evolve) independently of one another eq. (8.17) automatically holds for any collection of dipoles in each onium. The fact that eq. (8.17) holds for the 1-pomeron case is a result of the conformal invariance of the dipole-dipole interaction and of the dipole evolution kernel. The details are given in appendix B.

The effect of including multi-pomeron interactions is to connect the interaction of different dipoles within the same onium, and as a result dipoles no longer necessarily evolve independently of one another: this is the breakdown of the dipole picture of evolution which necessitates that one take into account quadrupoles and more complicated terms. Unfortunately it has not so far been possible to solve eq. (8.17) to obtain detailed information on the effects of saturation.

One can nevertheless use frame independence to deduce some limited information. We will first examine the effect of saturation on central impact parameters. The argument will be along similar lines to the toy-model approach discussed at the end of the last section, except that now it will just be sufficient to consider simple onium-onium scattering in lab (L) and centre-of-mass (CM) frames. In chapter 6 it was shown that there is a close correspondence between toy model and real results for the probability distribution of the number of dipoles when this number is high compared to the mean. However the arguments used here depend on the probabilities of having unusually low dipole densities, where the toy model is a poor approximation to the real case. In a lab frame one finds that the S-matrix is approximately $S_L \propto \mathrm{e}^{-\beta(Y-Y_0)^2}$ instead of $S_L \propto \mathrm{e}^{-\beta(Y-Y_0)}$ in the toy model. Qualitatively, the difference can be understood as coming from the extra dynamics associated with the diffusion in dipole sizes. In the toy model, the probability of having no evolution is just the exponentially suppressed probability of a single dipole not branching over a rapidity Y. In the real case the probability ($P_\rho(Y)$) of a dipole of size b not directly producing any new dipoles larger than a small size ρ is

$$P_\rho(Y) = \exp\left(-\frac{2\alpha_{\mathrm{S}} N_{\mathrm{C}} Y}{\pi} \ln\frac{b}{\rho}\right). \tag{8.18}$$

The extra element which arises is in the choice of ρ, since in the rapidity interval Y one must also require that none of the dipoles produced below size ρ branch back up into ones of size b. Forcing the probability of producing an extra large dipole from the small dipoles to be small (approximately $e^{(\alpha_{\mathbb{P}}-1)Y}\rho^2/b^2 \ll 1$), one obtains the condition $\ln b/\rho \propto Y$ which leads to the observed dependence of the S-matrix on Y^2 (since the S-matrix is dominated by the configurations with small interactions and therefore few dipoles).

The behaviour in the centre-of-mass frame will be similar, except that the condition for a small interaction will be that both onia should be unevolved, so

$$S_{CM} \propto \left\{\exp\left[-\beta\left(\frac{Y-Y_0'}{2}\right)^2\right]\right\}^2 = \exp\left[-\beta\frac{(Y-Y_0')^2}{2}\right]. \tag{8.19}$$

The value of Y_0' is different from Y_0 because it depends on the interaction between the two onia, the details of which are different in the lab and centre-of-mass frames. Figure 8.4 shows results from the Monte Carlo simulation, plotting the derivative of $\ln S$. The clear straight line behaviour at the higher values of Y is the signal of the Y^2 term in the exponent. Fits to the slopes of the derivatives show exactly the predicted factor of two between the lab and centre-of-mass frames. For $\alpha_{\mathrm{S}} \simeq 0.18$, the value of β is $\beta \simeq 0.042$. If one performs similar calculations for onium-nucleus collisions, one expects (and sees) similar behaviour: in the L_N frame, the slope is identical to the onium-onium lab frame results, and the L_O slope is twice the L_N slope (where the nucleus consists of two onia).

Since, for onium-onium collisions, the asymptotic value of the S-matrix is much smaller in the lab frame than in the centre-of-mass frame, one concludes that saturation in the lab frame will increase the S-matrix, and so that the *typical* value of the S-matrix, including saturation will be

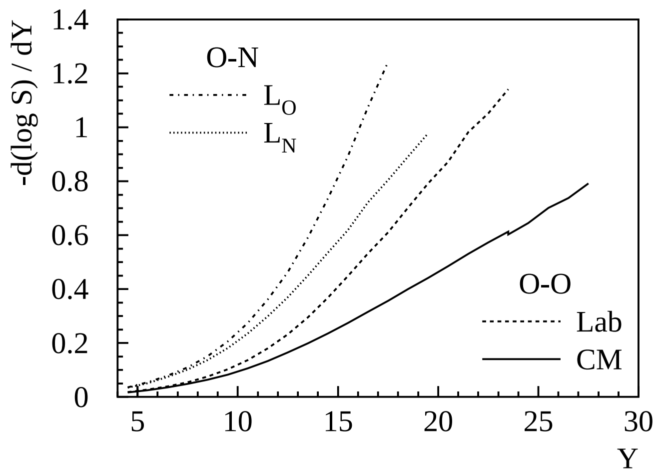

Figure 8.4: The logarithmic derivative of the zero impact parameter S-matrix for centre-of-mass and lab frames. Curves under the heading O-O are for onium-onium collisions, while the O-N curves are for onium-nucleus collisions, where the nucleus consists of two onia with a random relative transverse position of the order of the onium size.

$$S^{typical}(Y) \simeq \mathrm{e}^{-\beta\frac{(Y-Y_0')^2}{2}}, \tag{8.20}$$

very different from the typical value without saturation, $\sim \exp[-\alpha_S^2 \mathrm{e}^{(\alpha_{\mathbb{P}}-1)Y}]$. From the behaviour of the S-matrix it should be possible to determine the typical colour fields in an evolved onium or nucleus and this is being done in [158]. For a general discussion of small-x effects in terms of colour fields, the reader is referred to work on quark and gluon distributions for large nuclei by McLerran and Venugopalan [159–161], and for more recent results, to [162] and the references therein.

8.4 A phenomenological modification of the dipole branching

A second approach to saturation in the real case is primarily intended to give some information on what happens at non-zero impact parameters. First, one can compare the amplitude (including multiple scattering) for the lab and centre-of-mass frames as a function of r (the amplitudes have been multiplied by r^2 to indicate which regions contribute most to the total cross section). This is shown[3] in figure 8.5. The slight mismatch between the 1-pomeron curves at moderate r is due to statistical error (the amplitude at larger values of r comes from rare

[3]Note that the calculation of multiple-scattering corrections in the lab frame is potentially incorrect, because the formula, $F^{(m.s.)} = 1-\exp(-f)$, used to include the multiple-scattering corrections for a pair of configurations which give an interaction f with one pomeron exchange, breaks down when the number of interacting dipoles

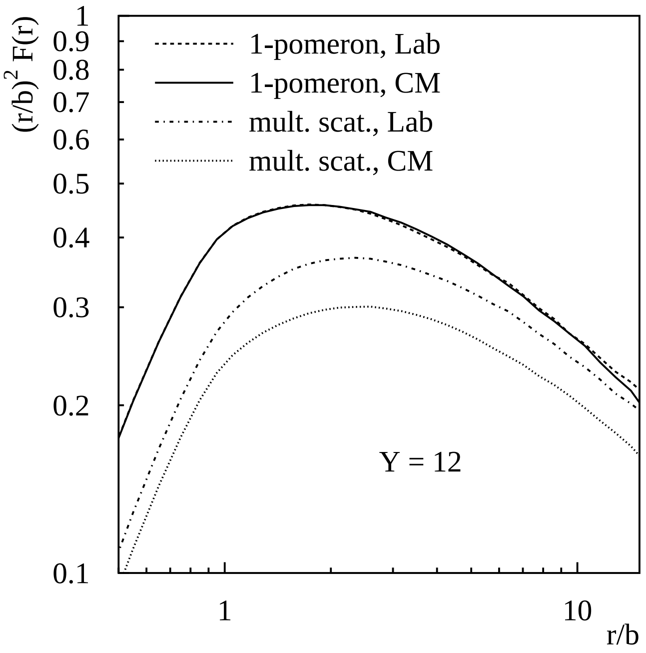

Figure 8.5: The onium-onium elastic amplitude, with and without multiple-scattering corrections, in centre-of-mass and laboratory frames.

configurations). As one expects, due to the neglect of saturation, the corrections in the lab frame are significantly smaller than in the centre-of-mass frame. Note in particular though that whereas at small impact parameters the difference between the two frames is only a small fraction of the multiple-scattering effects, at large impact parameters, most of the corrections present in the centre-of-mass frame are absent in the lab frame. This suggests that in the lab frame, saturation effects will in fact be considerably larger than the multiple-scattering corrections at large r. One way of investigating this further is to try to include some simulation of the effects of saturation.

The problem is that one doesn't know how to include saturation effects. The approach taken will be to use a simple model of saturation which retains the basic properties of normal dipole evolution and where saturation changes only the rate of dipole branching, not the spatial distribution. This is not expected to give accurate quantitative information on evolution with saturation, only to produce some understanding of the types of effects which are liable to be

in either of the onia is small (and also when the fields in either onium become so strong that the dipole picture fails completely). A solution to the problem is to examine a moderately asymmetric frame, for example where the rapidity is divided in the ratio 1:3, so that the balance between saturation and multiple-scattering is still different than in the CM frame, but where the slow moving onium has a sufficient number of dipoles that one can reliably estimate the multiple-scattering terms. If one does this, one finds answers very similar to those obtained by comparing the lab and CM frames.

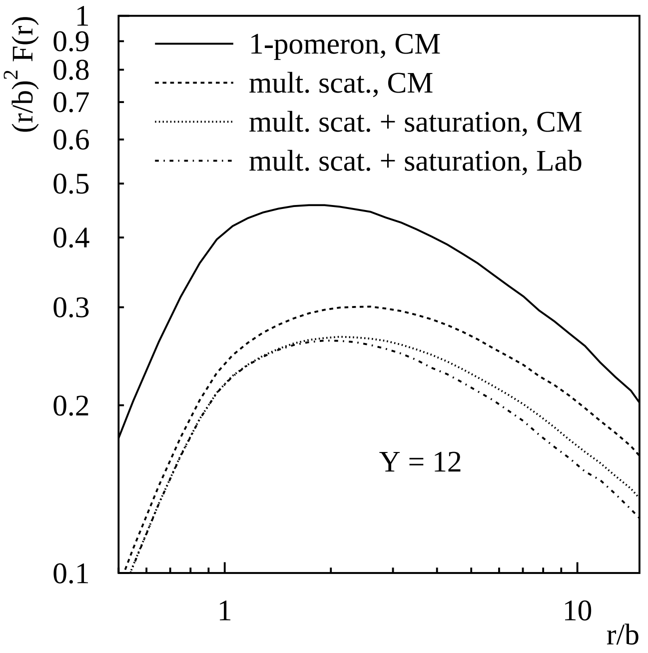

Figure 8.6: The onium-onium scattering amplitude, showing the frame invariance that results when both multiple-scattering and saturation corrections are included.

important if one does take saturation into account properly. In analogy with the toy model, we will use a rate of branching including saturation, R_i^s, of a dipole i of size b into two, of sizes $c_<$ (the smaller) and $c_>$ (the larger)

$$\frac{R_i^s(b \to c_<, c_>)}{R_i(b \to c_<, c_>)} = \left(1 - \mathrm{e}^{-O_i/\Omega}\right) . \frac{\Omega}{O_i}, \tag{8.21}$$

where R_i is the normal rate of branching (i.e. without saturation)[4]. The overlap measure of saturation, O_i, is used because it is much faster to calculate, and during the Monte Carlo evolution, it will be the calculation of the saturations for each dipole which will be the limiting factor. Since the functional form of this saturation is taken from the toy model, one doesn't know what normalisation Ω to use for the overlaps. The procedure used for choosing Ω will be to find a value which gives a frame independent result for $F(r = 0)$ (r is the relative impact

[4]Strictly, eq. (8.21) requires that one reevaluate the evolution environment for *all* the dipoles every time one of them evolves. Numerically this would be too CPU intensive to implement, and any tricks that one might consider to speed it up (such as using changes in saturation, rather than recalculating all the saturations) would require too much memory. Instead, one determines the saturation for each of the dipoles and allows them to evolve over a small interval in rapidity ($\Delta y = 1$ was chosen). If a dipole evolves, its children inherit its saturation value. At the next step in rapidity, all the saturations are reevaluated and the procedure is repeated. As a check on this technique, the size of the rapidity step was halved, and it was found that this made little difference.

parameter between the colliding onia) at a single value of rapidity (which is always possible), and then to see whether this also works at other values of r and rapidity. This has been done for $Y = 8$, where $\Omega \simeq 0.33$. Reexpressed in terms of a more natural quantity, the probe interaction I, this corresponds to a reduction of the branching rate by a factor $\simeq (1+I/1.3+O(I^2))$, which seems reasonable.

The procedure for determining Ω is non-trivial, because on the computers available, to determine whether a particular value gave agreement between different frames required nearly a day of CPU time. The method that was actually used relates to the way in which the Monte Carlo results are stored (see chapter 5 and appendix C): for each set of evolutions, information is kept on the probability distribution of the 1-pomeron amplitude, at a range of impact parameters. By rescaling both the rapidity and these interactions, one effectively varies α_s for the evolution and the interaction, while the ratio Ω/α_s^2 stays constant — which is equivalent to just varying Ω.

Figure 8.6 shows the scattering amplitudes for centre-of-mass and lab frames, including saturation for $Y = 12$. The centre-of-mass results with no saturation (with and without multiple scattering) are also plotted for reference. The procedure has worked insofar as the results in the two frames agree for small r for the second rapidity. At larger r there is still a small discrepancy between the two frames: the lab frame result is too low — there is a little bit too much saturation at large r — this discrepancy is however small compared to the overall effect of saturation at those values of r. The same is found at all other values of rapidity (including $Y = 8$). Other implementations of saturation (i.e. with different forms for eq. (8.21)), give similar results, as long as the effect of saturation on branching rates is linear for small overlaps.

As a second check on this form of saturation, one can examine onium-nucleus collisions. As well as the two lab frames discussed earlier we examine also a "centre-of-mass" frame (or more accurately, a frame in which the mean number of central dipoles is the same for the onium and the nucleus). Neglecting saturation, one expects the L_O frame to have the lowest multiple-scattering corrections (since with the nucleus containing all the rapidity, it will have the largest saturation corrections), followed by the L_N and CM frames. Figure 8.7 shows this ordering of the amplitudes. Once saturation is included (using exactly the same procedure as for onium-onium collisions), the three frames give very similar amplitudes, though again there is a small discrepancy at larger r.

One thing to examine is how this implementation of saturation affects the typical S-matrix for small impact parameters, and whether this is in accord with the arguments presented earlier. The asymptotic $e^{-\beta(Y-Y_0)^2/2}$ behaviour sets in only for relatively large rapidities (one needs $Y \gtrsim 14$), and determination of the saturation corrections at these rapidities is slow, because the computation time is proportional to the square of the number of dipoles: so it is difficult to obtain accurate results, which is why none are plotted here.

Nevertheless, one can calculate the effect of saturation on the S-matrix in the CM frame, and one finds that it has only a small effect on the slope of $-\mathrm{d}(\ln S)/\mathrm{d}Y$ (a slight reduction,

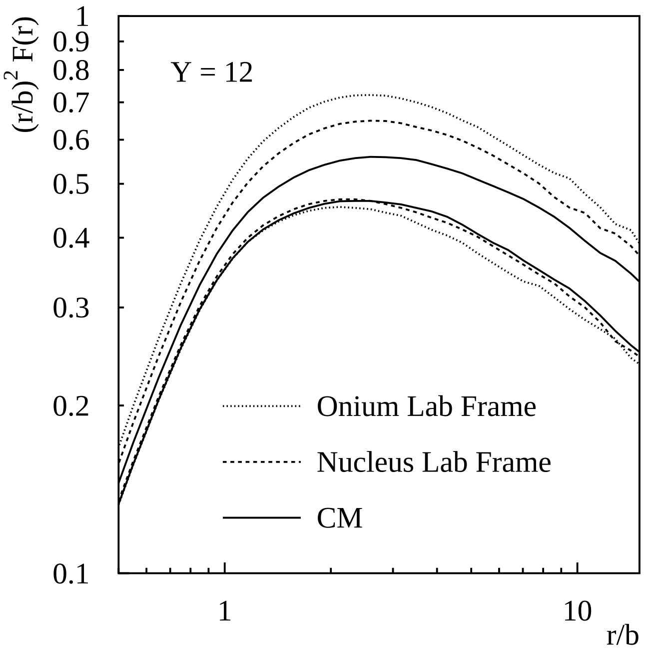

Figure 8.7: Onium-nucleus collisions (nucleus consists of two onia) in various frames: the upper set of three curves contains only multiple-scattering corrections, while the lower set also has saturation corrections.

the size of which goes down if one examines lower values of α_S). The only way of accessing the asymptotic behaviour in the *lab* frame is to use a large value of α_S, so that the saturation corrections set in much earlier. But the large value of α_S is hard to justify. One result is that the derivative of the"1-pomeron" interaction (a measure of the typical number of dipoles) is linear in y, i.e. that at high y the number of dipoles is proportional to y^2. This is the same as would be obtained, if one naively tried to deduce to deduce the typical number of dipoles from the typical lab frame S-matrix, eq. (8.20), but the two results have been obtained using significantly different approaches.

Considering again figure 8.6, one sees that at small r saturation seems to have a fairly small effect on the centre-of-mass amplitude. This is as expected from the basic argument that each onium has half the rapidity, and should be well away from saturation when multiple-scattering corrections start to set in. At large r, however, the effect of saturation is bigger, and in fact of the same order as the multiple-scattering effects (which relates to the observation for figure 8.5 that at larger r there is a big difference between the centre-of-mass and lab frame results, indicating that saturation must have a significant effect at large r).

The dynamics involved in producing the saturation effects at large r are complex: because the multiple-scattering corrections are small, the densities of dipoles must be small, and one might be misled into thinking that saturation corrections should unimportant. One reason why this argument fails is that there are a variety of ways in which large r interaction can occur. A large dipole can be produced early in the evolution, which can then evolve to produce many other dipoles of similar size and the final density of dipoles will be indicative of the relevant saturation corrections (these evolution paths tend to also have significant multiple-scattering corrections). Another evolution path involves only small dipoles for most of the rapidity and a branching to larger dipoles at a late stage. The evolution of the small dipoles may have been subjected to significant saturation; but once the branching occurs to large dipoles, multiple-scattering corrections and any further saturation corrections (at the large scale) are no longer affected by what is happening on the small scale. The history of saturation can therefore have an important effect on the evolution, even though the diluteness of the final configuration might make one think one could neglect saturation. This is illustrated in the upper part of figure 8.8: at two values of rapidity ($y = 6$ and $y = 8$), the maximum dipole size, $c_{\max}(y)$ is determined. The maximum overlap, $O_{\max}$ is then calculated for all dipoles with size c, where $c_{\max} > c > c_{\max}/3$, in effect giving the saturation on the scale of the largest dipole. The figure shows the ratio $O_{\max}(y = 8)/O_{\max}(y = 6)$, the increase in saturation (on the largest scale), as a function of $c_{\max}(y = 8)/c_{\max}(y = 6)$, the increase in the largest dipole size. The main point is that when there is a large increase in dipole size, the ratio of the saturations drops to below one, confirming that if one looks only at the final configuration, the history of the saturation can be hidden. A similar reduction of saturation with increasing rapidity can probably also take place for the small dipoles produced from large ones (since the small ones will be more dilutely spread out).

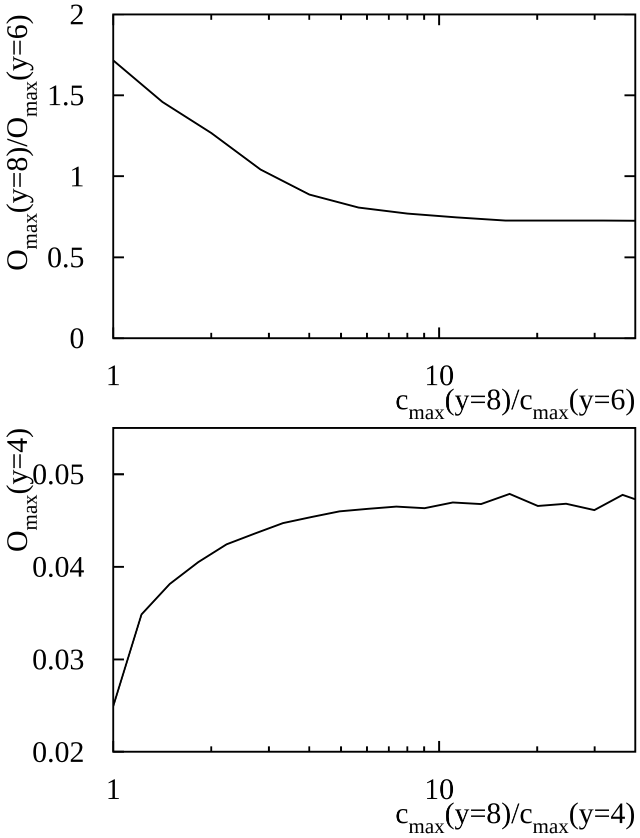

Figure 8.8: Saturation at different stages of evolution. The maximum dipole size at a given rapidity is $c_{\max}$, and $O_{\max}$ is the maximum overlap of any dipole between $c_{\max}$ and $c_{\max}/3$ (essentially a measure of the saturation on the scale of $c_{\max}$). Errors are large at large r because of a lack of statistics in that region.

A second effect is shown in the lower part of figure 8.8: the production of a large dipole tends to be a rare event. By a simple probabilistic argument, the larger the number of dipoles on a small scale, the greater the likelihood that at least one of them will branch to give a large dipole, which means that evolution paths that produce a large dipole are more likely to include an intermediate high-saturation stage. The lower plot of figure 8.8 demonstrates this by showing the maximum saturation (again on the largest scales) at $y = 4$ as a function of the ratio of the largest scales at $y = 8$ and $y = 4$. As the ratio of the scales increases so does the maximum intermediate saturation.

Finally in the centre-of-mass frame, one has the possibility of situations where one of the onia is small and moderately dense, while the other has a dilute distribution of small dipoles (the only ones which will interact with the small dense onium) at large r. The saturation corrections in the evolution of the small dense onium will then be of the same order as the multiple-scattering corrections between the two onia at large r; i.e. there is an asymmetry between the two onia and arguments for neglecting saturation when multiple-scattering effects set in rely on the symmetry between the two onia. This is distinct from the $r = 0$ case where moderate densities of dipoles in *each* onium led to strong multiple-scattering corrections.

8.5 Summary

In the toy model it is possible to use the requirement of frame invariance to obtain full information on saturation. At very large rapidities, the effect of saturation is convert a very broad distribution with a mean number of dipoles $\mathrm{e}^{(\alpha_{\mathbb{P}}-1)y}$, into one where there is a typical number of dipoles proportional to the rapidity.

But for the study of saturation effects in QCD, the toy model is a much poorer approximation than it is for multiple-scattering effects. The reason is that the latter are dominated by the high-density configurations of the onia, where there is a correspondence with the toy model, namely in the exponential tails for the probability of the high-density configurations (in particular, in both cases, the slope of the tail is inversely proportional to the mean number of dipoles). Saturation effects, as seen through the correspondence between lab and CM frames, are dependent on the probability of low density configurations, where the QCD case has a factor $\sim \mathrm{e}^{-\beta y^2}$ which is not present in the toy model. This leads to the conclusion that in the lab frame, the typical value of the S-matrix for central collisions is $\mathrm{e}^{-\beta(Y-Y_0)^2/2}$.

For the calculation of scattering amplitudes, small-r and large-r regions are affected differently by saturation. At small r, the argument that one can neglect saturation effects seems to work well. Even at rapidities where saturation does become significant, the S-matrix is dominated by those (rare) configurations where saturation doesn't play a role.

At large r, the arguments used to justify the neglect of saturation break down: (a) asymmetric configurations can play a role in the scattering amplitude; (b) the amplitude at large impact parameters is affected by saturation at small impact parameters (where densities are

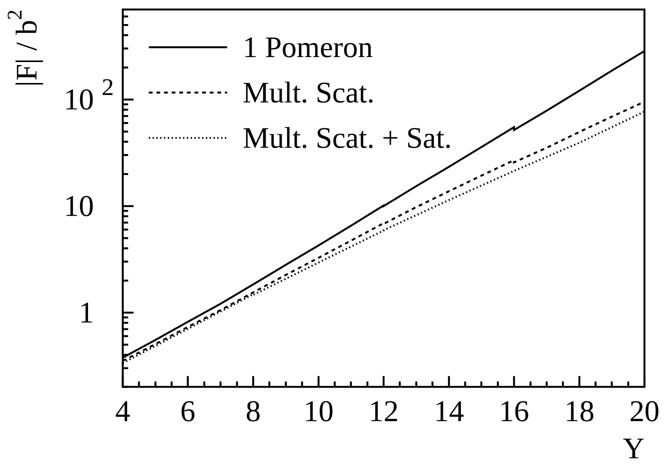

Figure 8.9: The effect of saturation on the total amplitude.

high), whereas multiple scattering is affected only by the large impact parameters (where the amplitudes are smaller); (c) in fact, of the configurations which are small at moderate rapidities, it is the denser ones which would normally be most likely to produce large configurations at high rapidities.

This might be of some concern when determining the corrections to the total cross section, which has a significant component coming from moderate to large r. However, to the extent that it is possible to gain any reliable quantitative information from this simple simulation of saturation, one finds that in the total cross section, saturation corrections (up to $Y \simeq 18$) are only a small fraction of the multiple-scattering corrections, as can be seen from figure 8.9.

CHAPTER 9

Conclusions

Each of the main results chapters has its own detailed summary. The purpose of this chapter is to give an overview of the conclusions to be drawn from work presented in this dissertation, as a whole.

The subject of discussion has been the determination of the high-energy behaviour of onium-onium scattering, including the corrections which contribute to the restoration of the unitarity of the scattering amplitude.

The cross sections have been evaluated using Mueller's dipole formulation of high-energy scattering, which can be divided into two parts: (a) a probabilistic evolution of the squared onium wave function and (b) the evaluation of the interaction between pairs of evolved onia, including multiple scatterings.

To study the properties of the onium wave functions and of onium scattering, a Monte Carlo program was written which simulates the evolution of the onium and calculates the interaction between pairs of evolved onium configurations. A variety of analytical techniques were used to complement the numerical work.

The main numerical results of this dissertation are contained in figure 7.11 (page 131) which shows the effect of multiple-scattering corrections on the total and elastic onium-onium cross sections. This is the first well defined quantitative determination of perturbative unitarity corrections to BFKL evolution.

In terms of obtaining a qualitative understanding of the dynamics behind unitarity corrections, there are two main themes which recur. The first is that mean properties of the wave function tend to be misleading when it comes to understanding the multiple-pomeron contributions.

At small impact parameters, the fact that there are exponential fluctuations in the density of dipoles in each onium leads to the divergence of the multiple-scattering series, and necessitates that one resum it before averaging over onium configuration.

At large impact parameters, the low mean interaction amplitudes are not indicative of small multiple-scattering corrections. In fact the low mean amplitude is a consequence of there only rarely being any interaction at all. But when there is an interaction, it tends to be significant.

When trying to work out final state properties, it is the large fluctuations in the densities of dipoles which are responsible for the unusually long tail of the probability distribution for the number of cut pomerons ($\sim \mathrm{e}^{-\sqrt{k}}$ for k cut pomerons).

Finally, making use of the properties of configurations with very few dipoles the typical value of the S-matrix for the central collision of a very fast-moving onium with a stationary one has been found to be of the form $\mathrm{e}^{-\beta(Y-Y_0)^2/2}$. This information can be used to establish the values of the typical fields in a very fast moving onium, in the asymptotic limit, far beyond the BFKL domain [158].

The second consideration which frequently plays a role, is the difference between large and small impact parameters: at small r the scattering amplitudes are much greater than at large r.

Thus, the elastic cross section, which is much more central, receives large multiple-scattering corrections, whereas the total cross section, dominated by moderate to large impact parameters receives considerably smaller corrections.

Events with unusually high or low multiplicity final states will also be more central, because they are dominated by regions where the 1-pomeron amplitude is large.

The contrast between different impact parameters is particularly visible when examining saturation, as determined from the requirement of frame invariance: at small r, naïve expectations work well and saturation is unimportant compared to multiple scattering. Yet for large r scattering, the dynamics of saturation are vastly more complex, depending on the asymmetries between configuration pairs, and on the evolution history of the configurations including a subtle interplay between small-r and large-r effects.

There are a variety of areas in which further understanding is needed. At the theoretical level, there are the next-to-leading modifications to the evolution kernel. These will lead to the running of α_{S}, and to the inclusion of recoil effects (of the parent from which the "soft" gluon is emitted). Given the interplay of different scales, and the importance of rare configurations with many dipoles, such corrections may be quite important.

Phenomenologically, one should try to extend the understanding of multiple-scattering and saturation corrections to realistically measurable processes, in particular deep inelastic scattering, where the presence of two scales (the virtuality of the photon and the mass or size of the hadron) will lead to considerably different dynamics. There will also be the modifications due to the infra-red region: the total cross section carries on growing rapidly at large energies, well beyond the point where unitarity corrections set in, because of an increase in the mean size of the onium configurations. Infra-red effects would probably limit the maximum configuration size, strongly reducing the high-energy growth of the cross section.

APPENDIX A

Analytical results for onium wave functions

A.1 Fluctuations in the localised dipole number

The approach used will be to study the equations for the moments of the dipole distribution within a region of radius ρ. The first step is to note that branching sequences that include dipoles of sizes larger than ρ will not contribute to high-density fluctuations: the number of dipoles of size ρ coming from a dipole of size $R \gg \rho$ will be at most enhanced by a factor proportional to R/ρ (just the usual factor in front of the BFKL saddle point solution). However dipoles will be spread out over a region of size R^2, so that the density of dipoles will be suppressed by a factor ρ/R. Therefore in calculations one can leave out all dipoles larger than ρ. One can also neglect the transverse positions of the dipoles, since, if a dipole starts inside a region of size ρ, and the branching involves no dipoles larger than ρ, most of the child dipoles will still be inside the region.

Define $n_\rho^{(q)}(c,b,y)$ to be the q^{th} moment of the number of dipoles of size c in a region of radius ρ originating from a parent of size b $(= b_{01})$ after an evolution through rapidity y. (The q^{th} moment being $\langle n(n-1)\dots(n-q+1)\rangle$). It will then approximately satisfy the following equation:

$$\frac{\mathrm{d}n_\rho^{(q)}(c,b,y)}{\mathrm{d}y} = I_\rho^{(q)} + \frac{\alpha_\mathrm{S} N_\mathrm{C}}{2\pi^2}\int^\rho \frac{b^2 \mathrm{d}^2\mathbf{b}_2}{b_{02}^2 b_{12}^2}\left[n_\rho^{(q)}(c,b_{02},y) + n_\rho^{(q)}(c,b_{12},y) - n_\rho^{(q)}(c,b_{01},y)\right]. \tag{A.1}$$

The inhomogeneous term, $I_\rho^{(q)}$, is

$$I_\rho^{(q)} = \frac{\alpha_\mathrm{S} N_\mathrm{C}}{2\pi^2}\int^\rho \frac{b^2 \mathrm{d}^2\mathbf{b}_2}{b_{02}^2 b_{12}^2}\sum_{i=1}^{q-1} C_i^q n_\rho^{(i)}(c,b_{02},y) n_\rho^{(q-i)}(c,b_{12},y). \tag{A.2}$$

This is obtained from the generating functional, eq. (4.24), with an upper cutoff placed on the dipole size in the $\mathbf{b}_2$ integration.

The first approximation to make relies on the large Y limit. At large Y, with c and b not too different, one has for the average number of dipoles:

$$n(c,b,Y) \sim \frac{b}{c}\mathrm{e}^{(\alpha_{\mathrm{I\!P}}-1)Y}. \tag{A.3}$$

The important point is that the b dependence (which shows a power behaviour) factors out from the c and Y dependences. This will apply to the moments of the localised dipole distribution as well. It will further be useful to make the assumption (reasonably justifiable) that the b dependences of the moments are also power behaviours. One can then parameterise each moment by two constants e_q and λ_q, which should depend only weakly on b:

$$n_\rho^{(q)}(c,b,Y) = e_q q! A^q(c/\rho)\left(\frac{b}{\rho}\right)^{\lambda_q}\mathrm{e}^{q(\alpha_{\mathrm{I\!P}}-1)Y}. \tag{A.4}$$

It is not necessary to know the exact c dependence, which is why it is left as $A(c/\rho)$. With this parameterisation, eq. (A.1) can be written as:

$$q(\alpha_{\mathrm{I\!P}}-1)\left(\frac{b}{\rho}\right)^{\lambda_q} e_q = \frac{\alpha_{\mathrm{S}}N_{\mathrm{C}}}{\pi}\left[k_{\lambda_q}\left(\frac{b}{\rho}\right)^{\lambda_q} e_q + \left(\frac{b}{\rho}\right)^2 \sum_{i=1}^{q-1} e_i e_{q-i} l_{\lambda_i\lambda_{q-i}}\right]. \tag{A.5}$$

The following integrals have been defined ($b = b_{01}$):

$$k_\lambda = \frac{1}{2\pi}\left(\frac{b}{\rho}\right)^{-\lambda}\int^\rho \frac{b^2\mathrm{d}^2 b_2}{b_{02}^2 b_{12}^2}\left[\left(\frac{b_{02}}{\rho}\right)^\lambda + \left(\frac{b_{12}}{\rho}\right)^\lambda - \left(\frac{b}{\rho}\right)^\lambda\right], \tag{A.6}$$

and

$$l_{\lambda\lambda'} = \frac{1}{2\pi}\left(\frac{b}{\rho}\right)^{-2}\int^\rho \frac{b^2\mathrm{d}^2 b_2}{b_{02}^2 b_{12}^2}\left[\left(\frac{b_{02}}{\rho}\right)^\lambda\left(\frac{b_{12}}{\rho}\right)^{\lambda'}\right]. \tag{A.7}$$

For $1 \le \lambda < 2$ (as should be the case for all q), k_λ and $l_{\lambda\lambda'}$ will depend only weakly on b/ρ (except for l_{11} which has a logarithmic dependence on b/r — this is discussed later).

The main difference between the two terms is that the $l_{\lambda\lambda'}$ integral is dominated by large $b_2 \sim \rho$, while the k_λ integral, because of the condition given above on λ, is dominated by small $b_2 \sim b$. This is the origin of the different power behaviours of the two integrals.

To solve eq. (A.5) one uses the fact that $\lambda_q < 2$, therefore for large ρ/b the inhomogeneous term drops out, leaving:

$$q(\alpha_{\mathrm{I\!P}}-1) \simeq \frac{\alpha_{\mathrm{S}}N_{\mathrm{C}}}{\pi}k_{\lambda_q}. \tag{A.8}$$

Through the λ dependence in k_λ, this fixes λ_q. For moderately large q, k_λ can be approximated as

$$k_\lambda \simeq \frac{2}{2-\lambda}, \tag{A.9}$$

giving

$$\lambda_q = 2 - \frac{1}{2q\ln 2}. \tag{A.10}$$

Note that this is just the solution to the equation $\chi(\lambda) = q\chi(1)$, in the limit $\lambda \to 2$, with the BFKL characteristic function χ defined as in eq. (4.36). The other region which can be studied to help solve eq. (A.5) is that of b close to ρ. For the case of λ close to 2, i.e. for large q, at large b, the integral for k_λ is much smaller than its asymptotic value (it only reaches its asymptotic value for $\rho/b \sim \exp[1/(2-\lambda)]$), while that for $l_{\lambda\lambda'}$ should be much closer to its asymptotic value (the integrand is approximately proportional to b_2). Therefore the k_λ term can be neglected, giving

$$e_q \simeq \frac{1}{4\ln 2}\frac{1}{q}\sum_{i=1}^{q-1} e_i e_{q-i} l_{\lambda_i\lambda_{q-i}}. \tag{A.11}$$

A reasonable approximation for $l_{\lambda_1\lambda_2}$ is:

$$l_{\lambda\lambda'} \simeq \frac{1}{\lambda+\lambda'-2}. \tag{A.12}$$

By iterating eq. (A.11), one can determine all the moments of the fluctuations. Its form is such that for large q, e_q should behave as follows:

$$e_q \simeq BC^q. \tag{A.13}$$

Because of the complicated behaviour of the coefficients of the iteration for low values of q, it is not possible to provide an analytical approximation for B and C, though they can be determined numerically. This then gives an exponential distribution for the fluctuations in dipole number in a restricted region, $\mathrm{e}^{-n/\mu}$ where

$$\mu(c/r) = A(c/r)Ce^{(\alpha_{\mathbb{P}}-1)Y}. \tag{A.14}$$

It is difficult to compare this directly with the results from the Monte Carlo simulation, because $A(c/r)$ contains various logarithmic factors which are difficult to estimate accurately. However the mean number of dipoles of a given size in a certain region is something that can be obtained from the Monte Carlo distribution and so $A(c/\rho)$ can be factored out:

$$\frac{\mu(c/\rho)}{n_\rho(c,\rho,Y)} \simeq C \simeq \lim_{q\to\infty} \frac{e_q}{e_{q-1}}. \tag{A.15}$$

In evaluating C from the recursion relations there are some complications because the first relation contains l_{11} which varies logarithmically with b/ρ (this is the reason why the expression given in eq. (A.12) diverges). Given that the values of e_q are determined by the region of b close to ρ, it is then natural to use a value of l_{11} corresponding also that region of b. For $b = 0.5\rho$, $l_{11} = 1.9$ (determined numerically), while for $b = 0.25\rho$, $l_{11} = 2.7$. This range will be used when calculating the e_q to gauge the uncertainty in the calculation.

Another uncertainty arises because at the rapidities available to the Monte Carlo simulation, the logarithmic prefactors affect the effective power growth of the distribution. To gauge this effect, one can replace $(\alpha_{\mathbb{P}} - 1)$ with a measured effective power and look at the difference that this makes to C. The final range of values obtained for C is from 0.34 to 0.75.

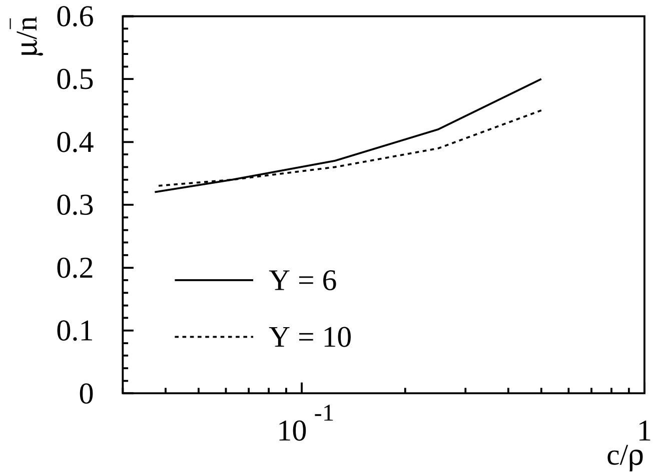

Figure A.1: The parameter C of eq. (A.15), as determined by Monte Carlo simulation for two values of y.

Figure A.1 shows the value of $C_{MC} = \mu(c/\rho)/[2n_\rho(c,\rho/2,Y)]$ determined from the Monte Carlo simulation for two values of Y and a range of c/ρ. Since $n_\rho(c,\rho,Y) \simeq 2n_\rho(c,\rho/2,Y)$, this is equivalent to plotting $\mu(c/\rho)/[n_\rho(c,\rho/,Y)]$, as used in eq. (A.15). The values for C from the iteration of eq. (A.11) are consistent with the Monte Carlo results. However the Monte Carlo results do depend slightly on Y and on c/ρ. For the variation with Y at $c \sim \rho$, C_{MC} decreases as Y increases. This could be because at larger Y, the effective power is larger. A larger effective power leads to a reduced value for e_q/e_{q-1} (this can be seen by making some simple analytic approximations, and is also obtained in the numerical iterations). A second effect is that at smaller c/ρ, the presence, non-asymptotically, of factors of the form $\exp[-\ln^2(c/\rho)/kY]$ leads to an increase in the effective power with decreasing c, giving a decreasing C. At larger Y this effect would be smaller, so, at larger Y, C should decrease more slowly with decreasing c. Both of these observations are qualitatively in accord with the Monte Carlo results.

A.2 The mean spatial distribution of dipoles.

The discrepancy, discussed in section 6.6, between the Monte Carlo results for the dipole distribution and the analytical prediction from Mueller [16] is related to the details of one of the integrals involved in its evaluation. In determining eq. (6.27) one goes through the following stage (eq. (4.59), taking only the $n=0$ term):

$$n(c,b,r,y) \simeq \int \frac{\mathrm{d}\nu}{2\pi} H_\nu(\mathbf{c},\mathbf{b},\mathbf{r}) \frac{b}{c} \exp\left[\frac{2\alpha_{\mathrm{S}} N_{\mathrm{C}}}{\pi}\chi(1+2i\nu)y\right] \tag{A.16}$$

where

$$H_\nu(\mathbf{c},\mathbf{b},\mathbf{r}) = \frac{4\nu^2}{\pi^2} b^{-2i\nu} c^{2i\nu} \int \frac{\mathrm{d}^2\mathbf{R}}{[|\mathbf{R}-\mathbf{b}/2||\mathbf{R}+\mathbf{b}/2|]^{1-2i\nu}[|\mathbf{R}+\mathbf{r}-\mathbf{c}/2||\mathbf{R}+\mathbf{r}+\mathbf{c}/2|]^{1+2i\nu}} \tag{A.17}$$

The BFKL characteristic function, $\chi(1+2i\nu)$, is

$$\chi(1+2i\nu) = \psi(1) - \frac{1}{2}\psi\left(\frac{1}{2}+i\nu\right) - \frac{1}{2}\psi\left(\frac{1}{2}-i\nu\right), \tag{A.18}$$

as in eq. (4.36). First, one cuts out the regions $R < Pb$ and $|\mathbf{R}+\mathbf{r}| < Pc$, where P is an arbitrary constant satisfying $P \gg 1$ and $4\nu \ln P \ll 1$. The integration without these regions gives:

$$\frac{2i\nu}{\pi r^2}\left[\left(\frac{r^2}{P^2bc}\right)^{-2i\nu} - \left(\frac{r^2}{P^2bc}\right)^{2i\nu}\right]. \tag{A.19}$$

One can see, by taking the limit $\nu \to 0$, that there should be no terms of order ν within the square bracket, because the integral is similar to the one evaluated in section 4.2, eq. (4.26), for the virtual corrections to the dipole kernel. The result obtained in [16] is equivalent to taking $P=1$ and neglecting other contributions. Now consider one of the regions that was cut out. It can be integrated as follows:

$$\begin{aligned}\frac{4\nu^2}{\pi^2}\frac{b^{-2i\nu}c^{2i\nu}}{r^{2+4i\nu}} \int^{R<Pb} & \frac{R\mathrm{d}R\mathrm{d}\theta}{(R\sqrt{b^2-2bR\cos\theta+R^2})^{1-2i\nu}} \\ & \simeq \frac{4\nu^2}{\pi^2}\frac{(P^2bc)^{2i\nu}}{r^{2+4i\nu}} \int^{R<Pb} \frac{\mathrm{d}R\mathrm{d}\theta}{\sqrt{b^2-2bR\cos\theta+R^2}}.\end{aligned} \tag{A.20}$$

The approximation giving the second line is valid because of the condition $\nu \ln P \ll 1$, so that in the range of R important for the integration, the power ν has little effect on the value of the integrand. The angular integration can be performed to give a complete elliptic integral of the first kind [163], $[4\mathbf{K}(R/b)/b]$ for $R < b$ and $[4\mathbf{K}(b/R)/R]$ for $R > b$. Evaluating the R integral then gives

$$\frac{8\nu^2}{\pi r^2}\left(\frac{r^2}{P^2bc}\right)^{-2i\nu}[\ln 4P + O(\nu)] \simeq \frac{2i\nu}{\pi r^2}\left(\frac{r^2}{P^2bc}\right)^{-2i\nu}\left[(16P^2)^{-2i\nu} - 1 + O(\nu^2)\right]. \tag{A.21}$$

Adding this, and a similar term for the dipole of size c, to eq. (A.19) gives

$$H_\nu(\mathbf{c},\mathbf{b},\mathbf{r}) \simeq \frac{2i\nu}{\pi r^2}\left[\left(\frac{16r^2}{bc}\right)^{-2i\nu} - \left(\frac{16r^2}{bc}\right)^{2i\nu}\right]. \tag{A.22}$$

Following through the calculation, gives for the dipole density:

$$n(c,b,r,y) \simeq \frac{2b}{cr^2}\ln\left(\frac{16r^2}{bc}\right)\frac{\exp[(\alpha_{\mathbb{P}}-1)y - \ln^2(16r^2/bc)/ky]}{(\pi k y)^{3/2}}. \tag{A.23}$$

This is much more central and agrees well with the Monte Carlo distributions.

A P P E N D I X B

Analytical results for onium scattering

B.1 Frame invariance of the one-pomeron amplitude

This section demonstrates the invariance of the one-pomeron scattering amplitude with respect to the choice of frame. It will be shown explicitly that it is invariant for the evolution of a single dipole in each onium. Because each dipole evolves independently, and because its interaction with the other onium is independent of the other dipoles in the onium to which it belongs, this will imply that the onium-onium scattering amplitude is invariant under changes of frames at the one-pomeron level.

Let the first dipole have sources at b_1 and b_2, and the second dipole have sources at b_3 and b_4 (with the b_n being complex variables). The condition for invariance of the scattering amplitude with respect to the transfer of a small amount of rapidity between them, eq. (8.17), can be written as

$$\begin{aligned}\int \mathrm{d}^2 b_5 \left|\frac{b_{12}}{b_{15}b_{25}}\right|^2 \left(\ln^2\left|\frac{b_{13}b_{54}}{b_{14}b_{53}}\right|^2 + \ln^2\left|\frac{b_{23}b_{54}}{b_{24}b_{53}}\right|^2 - \ln^2\left|\frac{b_{13}b_{24}}{b_{14}b_{23}}\right|^2\right) \\ = \int \mathrm{d}^2 b_5 \left|\frac{b_{34}}{b_{35}b_{45}}\right|^2 \left(\ln^2\left|\frac{b_{13}b_{25}}{b_{15}b_{23}}\right|^2 + \ln^2\left|\frac{b_{14}b_{25}}{b_{15}b_{24}}\right|^2 - \ln^2\left|\frac{b_{13}b_{24}}{b_{14}b_{23}}\right|^2\right). \quad \text{(B.1)}\end{aligned}$$

The first step will be to show that the integrands (including the integration measure) are conformally invariant, namely that they are not changed by any sequence of transformations consisting of translations, rotations and inversions. The invariance under translations and rotations is obvious. Inversions have the following action:

$$b_i \rightarrow \frac{1}{b_i}, \tag{B.2}$$

$$\mathrm{d}^2 b_i \rightarrow \frac{\mathrm{d}^2 b_i}{|b_i|^4}, \tag{B.3}$$

$$|b_{ij}|^2 \rightarrow \frac{|b_{ij}|^2}{|b_i|^2 |b_j|^2}, \tag{B.4}$$

so that the invariance under inversions of (a) the gluon emission kernel and (b) the arguments of each of the logarithms, follows straightforwardly.

To prove the equality in eq. (B.1), one considers the particular conformal transformation

$$b \rightarrow \frac{b+V}{Ub-1}, \tag{B.5}$$

with

$$U = \frac{b_1 - b_2 + b_3 - b_4}{b_1 b_3 - b_2 b_4} \tag{B.6}$$

$$V = \frac{b_1^{-1} - b_2^{-1} + b_3^{-1} - b_4^{-1}}{b_2^{-1} b_4^{-1} - b_1^{-1} b_3^{-1}}, \tag{B.7}$$

which has the property of mapping $b_1 \rightarrow b_3$, $b_2 \rightarrow b_4$, $b_3 \rightarrow b_1$ and $b_4 \rightarrow b_2$, thus converting the lower integral in eq. (B.1) to the upper integral (and vice-versa). Since the integrands are invariant under conformal transformations, the two integrals must be equal to each other and therefore the one-pomeron onium-onium scattering amplitude is independent of the frame in which the calculation is performed, if the evolution is carried out using the dipole kernel and the interaction is by two gluon exchange.

B.2 Conformal invariance and the large-r scattering amplitude

The conformal invariance properties discussed in the last section make it easy to understand why the large-r scattering amplitude depends only on the combination r^2/bc. The starting point is the consideration of one dipole of size b, centred at $r = 0$, and of a second very small dipole of size δ, at position ρ close to $r = 0$, such that $\delta \ll \rho \ll b$. The interaction amplitude between δ and b is dimensionless, and will not depend on ρ, so that one can write

$$F(b, \delta, \rho, Y) = F\left(\delta/b, Y\right), \tag{B.8}$$

One then introduces the conformal transformation

$$x \rightarrow \frac{b^2}{4x}, \tag{B.9}$$

which conserves the position of the dipole b. The effect on dipole δ is to take it to a position r

$$r = \frac{b^2}{4\rho}, \tag{B.10}$$

and its size becomes c

$$c = \frac{b^2\delta}{4\rho^2}. \tag{B.11}$$

Re-expressing δ/b in terms of b, c and r gives

$$\frac{\delta}{b} = \frac{bc}{r^2}. \tag{B.12}$$

Hence, the scattering amplitude has the property that

$$F(b, c, r, Y) = F\left(\frac{bc}{r^2}, Y\right), \tag{B.13}$$

which holds as long as $r^2 \gg b, c$. Since the property of conformal invariance holds for the $1 \to 2$ pomeron branching (see below), as well as the evolution and dipole-dipole interactions, the multi-pomeron amplitudes will also depend only on bc/r^2.

In fact the requirement, $c \ll r$, is only important for simplifying the evaluation of the conformally transformed positions. As long as no point is close (in some well-defined sense) to the invariant dipole (b), one can obtain information on the amplitudes for a much wider range of r using just the explicit evaluation from a single set of $r \gg b, c$ results. For example the $c \gg b$, $r < c/2$, amplitudes can be obtained by the inversion used above, a small shift and a repeat of the same inversion, to take one into the region $r \gg b, c$.

B.3 Conformal invariance of the triple-pomeron vertex

Bartels, Lipatov and Wüsthoff have shown [164] that the form of the $2 \to 4$ gluon vertex to be found in [8] (the triple pomeron vertex in the appropriate limits), is conformally invariant. This is quoted as being an important step in defining a conformally invariant effective field theory for QCD in the high-energy limit (see for example [12–15]).

No exact connection has been established between the $2 \to 4$ gluon vertex of Bartels and Wüsthoff and the triple-pomeron vertex in the dipole formulation. The former does not make use of the large $1/N_C$ approximation, and because it is based on the momentum space BFKL approach it will include the final state corrections (which cancel in the dipole approach). This section shows that the dipole triple-pomeron vertex also has the property of conformal invariance. The proof is given for the situation where there is no evolution beyond that necessary for the vertex. Since the dipole kernel is conformally invariant, it is straightforward to generalise to the case where there is evolution.

The simplest case where one has a $1 \to 2$ pomeron coupling is where one onium ($b_{1,2}$) has evolved into two dipoles ($b_{1,g}$, $b_{2,g}$) by the production of a gluon at b_g. The triple pomeron vertex can be extracted by considering the interaction of the two dipoles with two separate onia ($b_{3,4}$ and $b_{5,6}$) [18]. The possible interactions are

$$\begin{array}{rl} & b_{1,g} \text{ with } b_{3,4} \text{ and } b_{2,g} \text{ with } b_{5,6} \\ \text{or} & b_{1,g} \text{ with } b_{5,6} \text{ and } b_{2,g} \text{ with } b_{3,4} \end{array}$$

giving an overall interaction of

$$\frac{\alpha_{\mathrm{S}} N_{\mathrm{C}}}{2\pi^2} \left(\frac{\alpha_{\mathrm{S}}^2}{8}\right)^2 \int \frac{b_{12}^2 \mathrm{d}b_g}{b_{1g}^2 b_{2g}^2} \left(\ln^2 \left|\frac{b_{13} b_{g4}}{b_{14} b_{g3}}\right|^2 \ln^2 \left|\frac{b_{25} b_{g6}}{b_{26} b_{g5}}\right|^2 + \ln^2 \left|\frac{b_{15} b_{g6}}{b_{16} b_{g5}}\right|^2 \ln^2 \left|\frac{b_{23} b_{g4}}{b_{24} b_{g3}}\right|^2 \right), \tag{B.14}$$

(where integrations over rapidities have been left out). From the contents of the section B.1, it is easy to show (just by inspection) that the integrand is conformally invariant, and therefore that the triple-pomeron vertex is conformally invariant as well.

One phenomenological consequence of this is that all the results concerning multiple-scattering and saturation corrections for the large impact parameter scattering of two onia of similar sizes should apply to the more central scattering of onia of very different sizes: arguments that corrections will be unimportant, because the mean interaction is dilute everywhere, will fail — in the same way that the eikonal approximation fails at large r.

APPENDIX C

OEDIPUS

This appendix gives a description of the structure of the program OEDIPUS (Onium Evolution, Dipole Interaction and Perturbative Unitarisation Software), written in Fortran 90, which was used to generate most of the numerical results presented in this dissertation.

The program comes in many different files in various directories: `basic_src/` contains all the common subroutines which are involved with data input and output, initialisation and evolution of onia, as well as routines for determining onium-onium interaction amplitudes. It does not contain any code for analysing the results from the evolution or interaction: this must be provided as a "driver" program by the user. In the version of the software that has been made publicly available, a number of examples are to be found, including drivers to examine the spatial distribution of dipoles in the onium wave function and to determine the total and elastic scattering cross sections.

C.1 Storage of gluons and dipoles and evolution

Gluons and dipoles each have a specific data type:

```
type gluon
   complex(kind(1d0))    :: psn     ! stores the transverse position
   double precision      :: rapidity
end type gluon
```

Complex variables are used throughout the program to deal with transverse positions. The dipole type is

```
type dipole
   type(gluon), pointer  ::  lo_y_gluon, hi_y_gluon
   double precision      ::  size
```

```
   type(dipole), pointer ::  child_1, child_2
   integer               ::  index
end type dipole
```

It is useful to separate the gluon content of the dipole into high rapidity and low rapidity, mainly for ease of coding. In the case of the initial onium, the two quarks are represented by `gluon` types. The `child_1` and `child_2` pointers are needed to store the tree structure of the evolved onium. If they are not `associated` then the dipole has no descendents (for example, because any descendents would have a rapidity larger than the maximum of the evolution). Each dipole in an onium has a different `index` — this can be useful in analysing the branching structure.

The following sequence of routines is needed to produce an onium and evolve it, for each loop (or "event") of the program. First, various internal counters must be reset by calling

```
subroutine reset_counters
```

Then an onium is produced with

```
subroutine init_onium(onium, onm_size, phi)
```

This returns a *pointer* `onium` to a dipole of size `onm_size`, centred at $(0,0)$, with orientation `phi`. To produce a randomly oriented dipole, call

```
subroutine init_onium_rnd_phi(onium, onm_size)
```

The onium is evolved up to a rapidity `maxy` by calling

```
subroutine evolve_onium(onium, maxy, n_tree)
```

where, on return, `n_tree` is the total number of dipoles in the tree. To be able to analyse the results, one wants only the dipoles associated with a particular rapidity `y`, so one must extract them with:

```
subroutine extract_onium_dpls(onium, y, extrctd_dpls, n_extrctd)
```

The array `extrctd_dpls(:)` is of type `dpl_pntr` (arrays of pointers are not permitted in Fortran 90 — the solution to this is to define a type which contains nothing but a pointer), and on return contains pointers to the `n_extrctd` dipoles. The array must be sufficiently large: one can ensure that it is, by dynamically allocating it to be of size `(n_tree / 2 + 1)`. The array of dipole pointers can then be processed by the user.

This sequence allows one to first evolve the onium up to the maximum rapidity that one is interested in, and then examine the dipole structure over a range of rapidities.

Additional onia (for use simultaneously) can be produced, evolved, and the dipoles extracted, by repeating the same set of calls (omitting the call to `reset_counters`).

C.2 Onium-onium interaction

Two sets of routines are provided which calculate amplitudes for onium-onium scattering. The first returns a reasonable estimate for the elastic scattering amplitude between a pair of onium configurations, for all relevant impact parameters:

```
subroutine onm_onm_grid(ext_dpls1, n1, ext_dpls2, n2, grid, gh_lo, &
    & gh_int, gv_lo, gv_int)
```

It takes a pair of dipole sets (`n1` dipoles in `ext_dpls1` and `n2` dipoles in `ext_dpls2`) and determines the range of relative separations over which they interact. The onium-onium interaction is then determined for each point of a grid covering this area (`grid(:,:)` must be a two-dimensional square array; its size determines the resolution of the sampling) — the program returns information relating the array to the physical grid being used: the horizontal and vertical positions of the bottom left hand edge of the grid (`gh_lo` and `gv_lo`), as well as the horizontal and vertical spacing (or interval) of the grid (`gh_int` and `gv_int`). For each dipole pair, it only works out the contribution to those points on the grid where the dipole-dipole separation is not too large (as discussed in section 5.3.1). The amplitudes are always worked out at the centres of the grid rectangles.

The second approach works out a binned probability distribution for the amplitude in many sections along a radial line. The details of the binning are held in the `binning` module which provides a variable `bn` of type `bin_prms`:

```
type bin_prms
   ! binning vars for amplitude prob distributions
   integer            :: n_f_lo, n_f_hi, nf
   double precision   :: f_mid, f_lo_lgint , f_hi_lgint
   ! binning vars for r
   integer            :: n_r_lo,  n_r_hi, nr
   double precision   :: r_mid, r_hi_lgint
end type bin_prms
```

The binning of the amplitude probability distribution is divided into two regions: the lower region is for amplitudes below `f_mid` and the bins are indexed 0 to (`n_f_lo - 1`), logarithmically spaced with an interval `f_lo_lgint`. It is important to have a bin explicitly for the absence of interaction (otherwise when integrating the interaction over a large area the smallest bin amplitude could contribute significantly) — this is bin `-1`. The lowest non-zero bin must be sufficiently small to accurately reproduce the integral of the dipole-dipole interaction (bearing in mind that because the interaction dies off as $1/r^4$, there are regions where the amplitude can be quite small, but whose overall contribution to the amplitude is non-negligible). It is to allow adequate coverage of this wide range of small amplitudes that logarithmic binning (in the small amplitude region) is used. For amplitudes above `f_mid` the binning is performed logarithmically with an interval `f_hi_lgint`. The large amplitude region will contribute more significantly to the total amplitude and dividing the binning into two regions allows one to sample it more accurately in the regions which are more important. The reason to have logarithmic binning for large amplitudes is to be able to store the very large amplitudes which can occur at large rapidities. It is sometimes useful to have the index of the highest amplitude bin, which is `nf = n_f_lo + n_f_hi`. The variable `bn` is initialised with default values which reproduce total amplitudes to an accuracy of about one percent.

The binning in r, the distance along the radius, is also divided into two regions, but for different reasons: there are occasional events with very large transverse extents. To be able to include them with linearly spaced bins would require a prohibitively large number of bins. So for large r, logarithmic spacing of the bins is useful. But for small r, the most efficient sampling is one where each bin corresponds to a region of similar area — linear binning in r is more appropriate there. There are bins numbered `0` to (`n_r_lo - 1`) linearly spaced from $r = 0$ to `r_mid`. Above this, there are `n_r_hi` logarithmically spaced bins, with an interval `r_hi_lgint`.

To help bin and "unbin" the data, the following functions are provided:

```
function bin_of_f(f)
```

returns the bin number associated with an amplitude `f`. If the amplitude falls into a bin higher than `nf` then it is put into bin `nf` — this serves as a form of overflow procedure: if the highest bin contains any entries then the program should have been run with a larger number of amplitude bins. The inverse function

```
function f_of_bin(bin)
```

returns the value of the amplitude corresponding to the (logarithmic) centre of the bin (on average, the optimal value to use in reconstructing amplitudes).

For a given dipole-dipole pair, it is useful to know to which radial bins their interaction will contribute. The function

```
function irad(r)
```

aids this by returning the bin corresponding to a given radius (the interaction region for a pair of dipoles is defined by two radii, which are converted into the range of bins which must be sampled). For each radial bin, it is useful to sample at a random radius within the bin. The random value of r returned by

```
function rad_rnd(i)
```

has a probability distribution which increases linearly with r within the bin `i`, replicating the distribution of radii that would be obtained by choosing a random position in the corresponding ring. Finally it can be necessary to know the lower radius of a given bin (for example when analysing binned results), which is obtained by calling

```
rad_lo(i)
```

Given a pair of dipoles sets from evolved onia (`n1` dipoles in `ext_dpls1` and `n2` dipoles in `ext_dpls2`), the following routine

```
subroutine add_f_to_bins(ext_dpls1, n1, ext_dpls2, n2, fbins_single)
```

adds 1 to the appropriate amplitude bin of

```
fbins_single(-1:bn%nf, 0:bn%nr)
```

for a radius chosen randomly with `rad_rnd` in each radial bin.

C.3 Data input and output, and initialisation

A wide variety of information can be extracted from the evolved onium and the program needs to have the flexibility to input and output whatever information the user wants. In addition, it must be possible to restart a Monte Carlo run to add to previously determined data — this should be as automatic as possible. A number of routines are provided to make this simpler.

```
read_params_fdat(onm_size, maxy, n_prev_events, n_new_events)
```

This routine first parses the command line. Defining `argn` to be the n^{th} command line argument, it opens `arg1.dat` (a file containing formatted data from the evolution) and `arg1.prm` (a file containing the parameters of the evolution). The number of evolutions (or events) to be performed in this run of the program (`n_new_events`) is the value of `arg2`. It then looks to see if `arg3` is present: if not (or if it is a dash) then the evolution is a continuation of a previous one and the contents of `arg1.prm` are read in, in the following format:

```
jseed(1)  jseed(2)
r_cut_lo  r_cut_hi
onm_size  maxy
data_io
n_prev_events
```

with the following definitions:

`jseed(1:2)` the pair of integers used as a seed for the random number generator `HWRGEN`, which uses l'Ecuyer's method, described in [165], as implemented in the HERWIG [137] event generator;

`r_cut_lo` the lower cutoff on dipole sizes;

`r_cut_hi` the upper cutoff (if it is negative, then no upper cutoff is implemented);

`onm_size` the onium size;

`maxy` the maximum rapidity up to which onia are evolved;

`data_io` a variable provided by the user in the module `data_prms` holding any additional information needed by the user's program for treating the data (e.g. a range of dipole sizes being studied). It can be of any type (including user defined type);

`n_prev_events` the number of "events" (i.e. Monte Carlo evolutions) processed so far.

The routine also performs the initialisation which is necessary before evolution can be carried out: a call to `init_lives` which sets up an array tabulating dipole lifetimes as a function of their size, and a call to `nullify_child_set` which nullifies pointers to child dipoles (since Fortran 90 has no mechanism for specifying the initial status of a pointer). It is the user's responsibility to read in the data from unit `idat` (since the format and nature of the data will vary from program to program).

If `arg3` is present then the file `starters/arg3` (path from top directory of the distribution) is read in. The format is the same as the first three lines of `arg1.prm`. If either value of `jseed(1:2)` is zero then the default seed is used; `n_prev_events` is set to zero. It is then the user's responsibility to initialise any data variables and provide default values for `data_io`. This mechanism makes it much easier to run the same program with different values of cutoffs and rapidity (the most commonly varied parameter) by having a single set of starter files in the `starters/` directory — effectively by a command line argument, rather than by having to edit a new parameter file each time. A number of starter files are provided with the distribution and are described in the file `starters/README`.

```
write_params_fdat(onm_size, maxy, n_events, param_arg, dat_arg)
```

This routine is called to output the updated parameters of the evolution (usually only the seed and the number of evolutions so far, `n_events`, will have changed). It `rewind`s both the parameter and data devices. Normally the parameter and data devices (`param_arg` and `dat_arg`) will be the same as those used for input (`iprm` and `idat`) but the arguments are available (though optional) because there is occasionally a need to use different output devices (e.g. if the user wants to retain the original data). It is the user's responsibility to output the data.

The advantage of using formatted data is that it is easy to examine or plot. But it is very inefficient for storing large amounts of data. Two routines are provided for dealing with unformatted data (the parameters file is still formatted):

```
read_params_ufdt(onm_size, maxy, n_prev_events, n_new_events)
write_params_ufdt(onm_size, maxy, n_events, param_dev, ufdt_dev)
```

They are very similar to the previous routines. The main difference is that the data device is now `iufdt`, which is opened for unformatted output. Since the most common use of unformatted input and output is for the binned probability distribution of the amplitude (see section C.2) the parameter file contains the additional set of parameters: `bn` (a variable in the `binning` module, of type `bin_prms`) which defines the spacing of the bins. With the unformatted data files it will often be necessary to read them in again to analyse them. Because the various parameters may be needed to know how to read in and process the data a routine

```
read_params_old_ufdt(prnt_size, maxy, n_events)
```

is provided. It looks at `arg1` to determine the files to use and opens them (with the `OLD` specifier, to prevent them being accidentally altered). It does not perform any initialisation for the evolution.

For binned amplitude data, the format is fairly constant, so routines are also provided for reading and writing the data:

```
subroutine allc_read_fbins(n_y, n_prev_events)
```

This allocates an array

```
fbins(-1:bn%nf, 0:bn%nr, n_y)
```

in accord with the format for binned data discussed in section C.2 reads it in from device `iufdt`. The extra dimension comes in because one might want to store results for several (`n_y`) values of rapidity from a single run. The reason for the argument `n_prev_events` is to produce the correct normalisation for the data: on disk, it is stored so that each bin contains the probability associated with it. When adding extra data, it is convenient to use a normalisation where each bin contains the number of events contributing to it. If `n_prev_events` is 0 then the bins are not read in, but instead initialised to zero. If the argument is not present then the normalisation of the bins is not changed.

To write the data, one uses the routine

```
subroutine write_fbins(n_events, iufdt_arg)
```

It is sometimes useful to be able to specify a different device, `iufdt_arg` (optional), for output than for input, for example when writing out only a portion of the data. The number of events needs to be provided so that the stored normalisation on output is consistent with each bin containing a probability.

The data is stored as `real` rather than `double precision` to reduce the use of disk space.

C.4 Some internal details

The gluons and dipoles which are generated by evolution have to be stored, for example so that one can then work out onium-onium interactions. One of the main problems is that one doesn't know beforehand how many dipoles will be produced — the mean number of dipoles can be estimated, however the fluctuations above this are very large (see section 6.4). A solution is to dynamically allocate memory for gluons and dipoles as the evolution proceeds. This slows down the evolution (by nearly a factor of two on some systems) because of the time needed for allocation and deallocation.

The alternative is to provide fixed size arrays for the dipoles and gluons, where the size is chosen beforehand — essentially by trial and error. For cases where the largest configurations will be using a significant fraction of a machine's resources, this has the disadvantage that by having previously allocated the memory, it is taken up for the whole duration of the job (even if there is nothing stored there), whereas with dynamic allocation, the memory is used up only when it is needed.

Limits have been coded into the `gluon` module for the maximum number of gluons: the variable `max_gluons`. For the situation with dynamic allocation, this is the maximum number of gluons in each onium. It is present simply to allow the program to handle cases which might otherwise cause it to crash because they used all the available data store for that process. In the case of the fixed arrays, the quantity represents the maximum number of gluons in total (i.e. from all evolved onia). Apart from that, when using the subroutines described above for initialising onia, evolving them, etc., the functionality should not depend at all on the method of gluon storage.

There are ways round the limitations on the maximum number of dipoles. One could store very large configurations on disk (the computer would normally be doing this anyway with the swap space — but if the program is responsible then the swap space is still left for other processes). Alternatively, there are situations where the dipole structure need not be stored at all. The occasions when a stored dipole structure is needed is when looking at some kind of correlation between dipole pairs (such as onium-onium interaction), because for each dipole, one needs access to all the other dipoles. But in these situations, the time per configuration is normally the limiting factor, since this is proportional to the square of the number of dipoles. In cases where the time taken for some analysis is linear in the number of dipoles, often, it is not necessary to have knowledge of the whole configuration. So an evolution routine can be written which calls an analysis routine each time it reaches the "tip" of a "branch" of the dipole "tree", and it never has to store more than a single path from the base of the tree to the furthest "tip". Such an evolution routine was used to generate the lab-frame results of figure 8.4.

C.5 Compilation

The program is provided in the form of a number of separate files, the contents of which are documented in `README` files. To aid in the compilation process, two shell scripts are provided which select the correct set of source files. Detailed information on their functioning is provided as part of the distribution, however a summary is given here:

```
mkf driver [ dyn | sml | lrg ]
```

This is for compiling a driver routine which uses formatted data i/o. The name of the driver should be provided without the `.f90` extension. The second command line argument indicates the kind of gluon and dipole storage used — the default is to use dynamic allocation (corresponding to the option `dyn`). Two fixed size array storage options are also provided: `sml` (up to 5000 gluons) and `lrg` (up to 400000 gluons, which with a lower cutoff of $0.01b$, should be adequate for evolution up to rapidities of $y \simeq 15$). The executable is named `driver_dyn` (or `sml` or `lrg` as appropriate) to allow multiple copies of the executable, with different gluon storage, to coexist.

```
mku driver [ dyn | sml | lrg | noev ]
```

This is for compilation of drivers which use unformatted data i/o. It also compiles in the routines and modules associated with binning of the amplitude. The command line arguments are the same as for `mkf`, except for the extra option available as the second argument: `noev`. This is to be used for drivers which analyse data from a previous evolution — no evolution routines are compiled, and the data and parameter files are opened with the `'OLD'` specifier, meaning that they cannot be modified. Naming of the executable follows the same convention as for `mkf` except when the `noev` option is used, in which case the executable is named `driver` (since there should be no need to have multiple copies compiled with different gluon storage methods).

C.6 Test run

The run described here, and shown in figure C.1, tests the evolution of the onia, determination and binning of the interaction amplitude, and subsequent analysis of data for onium-onium interactions. It is for moderate rapidities and small statistics to ensure that it runs quickly (a few seconds) on most systems. It is necessary to first compile the evolution routine (to be found in the `sample/` directory of the distribution) with

```
> mku onm-onm-bnd dyn
```

which includes the dynamic allocation of memory for gluons and dipoles. The first command shown in figure C.1 starts an evolution (with 10 events), where the maximum rapidity for each onium is 4, giving a total rapidity for the collisions of 8. The lower cutoff used is 0.1 times the onium size. The binned, unformatted data are stored in `test_y8.ufdt` (beware: this file is over 1MB in size) and the parameters in `test_y8.prm`. The format of the variable `data_io` (together with the defaults used here) is

```
data_io%y_wvfn = 0d0
data_io%y_int  = 0.5d0
data_io%n_y    = 5
```

which specifies that the onium-onium interaction is determined for 5 values of rapidity, each separated by 0.5 (note that this is for each onium — so the intervals in total rapidity are 1.0). The maximum rapidity at which dipoles are extracted from each onium is `maxy`, but each onium is evolved to `data_io%y_wvfn` (or `maxy`, if this is larger) allowing different runs to effectively use the same dipole configurations but to examine the interactions at different values of rapidity. Various messages are output at the start of the program, as different parts of the startup procedure are accomplished. The line dealing with backups may be preceded by other messages on some systems (e.g. those using the NAG compiler — see section C.8), because the compiler does not offer the facility of running a system command.

The next command causes the evolution to be continued for a further 5 "events" (simply to allow a test of the continuation function). One then wants to analyse the results of the evolution. In this test we will look at the total amplitudes (the onium-onium amplitude integrated over all impact parameters, which is equal to half the onium-onium total cross-section). The program to do this is compiled with

```
mku ftot noev
```

The option `noev` ensures that unnecessary routines (such as those required for evolution) are not compiled in. The output includes various messages at the beginning indicating the initialisation procedure (these messages are sent to standard error, while the numerical output is sent to standard output, to allow it to be redirected to a file). The format of the numerical output from `noev` is one line for each value of rapidity, where each line has:

```
(total rapidity)  (unitarised amplitude) (1 pomeron amplitude) ...
      (n_pom pomeron amplitude)
```

(all on one line), and `n_pom = 4` is a parameter in the program. It is the absolute values of the amplitudes which are output.

A second test run, which tests the formatted data output is provided and documented within the distribution. In addition, some other driver and analysis routines are provided. These can all be found in the `samples/` directory.

Typical rapidities for which adequate statistics are accessible with a day's running are $Y \leq 20$, using a lower cutoff of $0.01b$.

TEST RUN

```
> onm-onm-bnd_dyn test_y8 10 y4
 Starting a new evolution
 HWRGEN will use its default seed
 Lifetimes have been initialised
 Have allocated bins
If there are no error messages then the backups have been done
 Am about to evolve
> onm-onm-bnd_dyn test_y8 5
 Continuing a previous evolution....
 HWRGEN has been initialised
 Lifetimes have been initialised
 Have allocated bins
If there are no error messages then the backups have been done
 Am about to evolve
> ftot test_y8
 Reading from a previous evolution....
 HWRGEN has been initialised
 Have allocated bins
 4.0000E+00 1.3183E-01 1.3466E-01 2.9205E-03 9.6577E-05 3.3521E-06
 5.0000E+00 1.8955E-01 2.0176E-01 1.4294E-02 2.4481E-03 4.1440E-04
 6.0000E+00 2.0235E-01 2.1490E-01 1.4465E-02 2.2114E-03 3.4580E-04
 7.0000E+00 4.2093E-01 4.7515E-01 6.3966E-02 1.1441E-02 1.9750E-03
 8.0000E+00 4.4738E-01 5.0385E-01 6.5855E-02 1.0901E-02 1.7452E-03
>
```

STARTER FILE: y4

```
 0      0
 0.1    -2.0
 1.0    4.0
```

Figure C.1: The output from the test run and the starter file `y4` (default seed, lower cutoff of 0.1, no upper cutoff (-2.0), onium size of 1.0, and maximum rapidity for each onium of 4.0).

C.7 Distribution

The distribution consists of a number of directories. Details of their contents are documented in extensive `README` files. Installation is performed with a shell script which is provided. Instructions are also included for installation by hand.

C.8 Portability

The main issues of portability relate to accessing command line arguments and causing a shell script (which performs backups of data and parameter files) to be executed. Interfaces to the system routines to perform these functions are provided as routines whose names start with the `lcl_` prefix, held in a file

```
basic_src/common/lcl_???.f90
```

where `???` may be `dec`, `nag` or `std` (or the user can generate a new file for his/her operating system). The file to be used must be specified as part of the installation procedure. With the NAG compiler (version 2.1), there does not seem to be any way of causing a shell script to be executed (the usual unix `system` subroutine seems to be absent). The routines for accessing command line arguments while available, do not seem to be documented. If the Fortran 90 compiler offers no mechanism for accessing the command line arguments then one can use `lcl_std.f90`, which prompts the user for the information held in each of the arguments. It conforms to the standard.

Local implementations are also necessary for writing large, unformatted arrays to disk (on some systems, the i/o buffer is not sufficiently large and the array must be written in small sections). Details are provided in the `lcl_???.f90` files.

To port to a non unix system (such as VMS), it would in addition be necessary to rewrite the compilation scripts.

C.9 Global data

All global data is stored in the form of modules. These are summarised in table C.1 (numbers in brackets refer to default values). In addition there are modules associated with the binning routines. These are summarised in table C.2.

Module name	Variables	Description
constants	alpha_s	α_S, the strong coupling constant (0.17777...)
	nc	N_C, the number of colours in QCD (3)
	alpha_no_nc	the value of α_S to be used when it appears without a factor of N_C (=alpha_s).
cuts	r_cut_lo	the lower cutoff
	r_cut_hi	the upper cutoff
	hi_cut_implem	true if an upper cutoff is being used
iomodule	iprm	i/o device for parameters (10)
	idat	i/o device for formatted output (12)
	iufdt	i/o device for unformatted data (14)
gluons	type gluon	the type definition for gluons
	type dipole	the type definition for dipoles
	type dpl_pntr	type definition for a pointer to a dipole
	max_gluons	the maximum number of gluons to be generated
data_defs	data_io	variable of user chosen type, with details of data i/o. This module must be provided by the user.
sub_defs		interface blocks for all the main subroutines

Table C.1: A list of the modules (and their main contents) needed by user's programs. Numbers in brackets are default values.

Module name	Variables	Description
binning	type bin_prms	type definition to store all the parameters for binning of amplitudes
	bn	variable actually containing the information
fbins_mdl	fbins	array containing amplitude bins
bin_interface		interface blocks for the binning routines

Table C.2: Modules associated with routines for binning the amplitude probability distribution.

References

[1] P. D. B. Collins; *Introduction to Regge Theory*; Cambridge University Press; 1977.

[2] I. Y. Pomeranchuk; Equality of the nucleon and antinucleon total interaction cross section at high energies.; Sov. Phys. JETP **7**, 499 (1958).

[3] Y. Y. Balitskiĭ and L. N. Lipatov; The pomeranchuk singularity in quantum chromodynamics; Sov. J. Nucl. Phys **28**, 822 (1978).

[4] E. A. Kuraev, L. N. Lipatov, and V. S. Fadin; The pomeranchuk singularity in non-abelian gauge theories; Sov. Phys. JETP **45**, 199 (1977).

[5] L. N. Lipatov; The bare pomeron in quantum chromodynamics; Sov. Phys. JETP **63**, 904 (1986).

[6] A. De Rújula et al.; Possible non-Regge behavior of electroproduction structure functions; Phys. Rev. **D10**, 1649 (1974).

[7] L. V. Gribov, E. M. Levin, and M. G. Ryskin; Semihard processes in QCD; Phys. Rep. **100**, 1 (1983).

[8] J. Bartels and M. Wüsthoff; The triple Regge limit of diffractive dissociation in DIS; Zeit. f. Phys. **C66**, 157 (1995).

[9] J. Bartels; High-energy behavior in a non-abelian gauge theory (II). First corrections to $T_{n\to m}$ beyond the leading logarithms approximation; Nucl. Phys. **B175**, 365 (1980).

[10] T. Jaroszewicz; Infrared divergences and Regge behavior in QCD; Acta Phys. Polonica **B11**, 965 (1980).

[11] J. Kwieciński and M. Praszalowicz; Three gluon integral equation and odd C singlet Regge singularities in QCD; Phys. Lett. **B94**, 413 (1980).

[12] L. N. Lipatov; High-energy asymptotics of multicolor QCD and two-dimensional conformal field theories; Phys. Lett. **B309**, 394 (1993).

[13] L. N. Lipatov; High-energy asymptotics of multicolor QCD and exactly solvable lattice models; JETP Lett. **59**, 596 (1994).

[14] L. N. Lipatov; Gauge invariant effective action for high-energy processes in QCD; Nucl. Phys. **B452**, 369 (1995).

[15] L. D. Faddeev and G. Korchemsky; High-energy QCD as a completely integrable model; Phys. Lett. **B342**, 311 (1995).

[16] A. H. Mueller; Unitarity and the BFKL pomeron; Nucl. Phys. **B437**, 107 (1995).

[17] A. H. Mueller; Soft gluons in the infinite momentum wavefunction and the BFKL pomeron; Nucl. Phys. **B415**, 373 (1994).

[18] A. H. Mueller and B. Patel; Single and double BFKL pomeron exchange and a dipole picture of high energy hard processes; Nucl. Phys. **B425**, 471 (1994).

[19] Z. Chen and A. H. Mueller; The dipole picture of high energy scattering, the BFKL equation and many gluon compound states; Nucl. Phys. **B451**, 579 (1995).

[20] N. N. Nikolaev and B. G. Zakharov; The triple-pomeron regime and the structure function of the pomeron in the diffractive deep inelastic scattering at very small x; Zeit. f. Phys. **C64**, 631 (1994).

[21] N. N. Nikolaev, B. G. Zakharov, and V. R. Zoller; The s-channel approach to Lipatov's pomeron and hadronic cross-sections; JETP Lett. **59**, 6 (1994).

[22] P. A. M. Dirac; Forms of relativistic dynamincs; Rev. Mod. Phys. **21**, 392 (1949).

[23] S. Weinberg; Dynamics at infinite momentum; Phys. Rev. **150**, 1313 (1966).

[24] J. B. Kogut and D. E. Soper; Quantum electrodynamics in the infinite-momentum frame; Phys. Rev. **D1**, 2901 (1970).

[25] J. D. Bjorken, J. B. Kogut, and D. E. Soper; Quantum electrodynamics at infinite momentum: Scattering from an external field; Phys. Rev. **3**, 1382 (1971).

[26] M. Froissart; Asymptotic behavior and subtractions in the Mandelstam representation; Phys. Rev. **123**, 1053 (1961).

[27] A. Martin; Unitarity and high-energy behavior of scattering amplitudes; Phys. Rev. **129**, 1432 (1963).

[28] J. D. Bjorken and S. D. Drell; *Relativistic Quantum Fields*; McGraw-Hill; 1865.

[29] C. Itzykson and J.-B. Zuber; *Quantum Field Theory*; McGraw-Hill; 1980.

[30] R. K. Ellis, W. J. Stirling, and B. R. Webber; *QCD and Collider Physics*; Cambridge University Press; 1996.

[31] Y. L. Dokshitzer, V. A. Khoze, A. H. Mueller, and S. I. Troyan; *Basics of Perturbative QCD*; Editions Frontières; 1991.

[32] L. D. Faddeev and V. N. Popov; Feynman diagrams for the Yang-Mills field; Phys. Lett. **25B**, 29 (1967).

[33] E. Abers and B. W. Lee; Gauge theories; Phys. Rep. **9**, 1 (1973).

[34] O. Nachtmann; *Elementary Particle Physics: Concepts and Phenomena*; Springer-Verlag; 1990.

[35] G. P. Lepage and S. J. Brodsky; Exclusive processes in quantum chromodynamics; Phys. Rev. **D22**, 2157 (1980).

[36] S. J. Brodsky and H.-C. Pauli; Light-cone quantisation of QCD; in *Proceedings of Schladming Winter School: Recent Aspects of Quantum Fields*; pages 51–121; 1991.

[37] D. J. Gross and F. Wilczek; Ultraviolet behaviour of non-abelian gauge theories; Phys. Rev. Lett. **26**, 1343 (1973).

[38] D. J. Gross and F. Wilczek; Asymptotically free gauge theories; Phys. Rev. **D8**, 3633 (1974).

[39] H. D. Politzer; Reliable perturbative results for strong interactions; Phys. Rev. Lett. **30**, 1346 (1973).

[40] H. D. Politzer; Asymptotic freedom: An approach to strong interactions; Phys. Rep. **C14**, 129 (1974).

[41] W. E. Caswell; Asymptotic behavior of non-abelian gauge theories to two-loop order; Phys. Rev. Lett. **33**, 244 (1974).

[42] O. V. Tarasov, A. A. Vladimirov, and A. Y. Zharkov; The Gell-Mann-Low function of QCD in the three-loop approximation; Phys. Lett. **93B**, 429 (1980).

[43] S. A. Larin and J. A. M. Vermaseren; The three-loop QCD β-function and anamolous dimensions; Phys. Lett. **B303**, 334 (1993).

[44] G. 't Hooft; A planar diagram theory for strong interactions; Nucl. Phys. **B72**, 461 (1974).

[45] E. Witten; Baryons in the $1/N$ expansion; Nucl. Phys. **B160**, 57 (1979).

[46] N. P. Chang; Impact parameters: A geometrical picture of inelastic scattering; Nucl. Phys. **B66**, 381 (1973).

[47] F. S. Henyey; Impact parameter description of multiparticle and elastic scattering; Phys. Lett. **45B**, 363 (1973).

[48] B. R. Webber; The impact parameter structure of multiparticle production; Nucl. Phys. **B87**, 269 (1975).

[49] V. N. Gribov and L. N. Lipatov; Deep inelastic ep scattering in perturbation theory; Sov. J. Nucl. Phys **15**, 438 (1972).

[50] Y. L. Dokshitser; Calculation of the structure functions for deep inelastic scattering and e^+e^- annihilation by perturbation theory in quantum chromodynamics; Sov. Phys. JETP **46**, 641 (1977).

[51] G. Altarelli and G. Parisi; Asymptotic freedom in parton language; Nucl. Phys. **B126**, 298 (1977).

[52] P. V. Landshoff; The soft pomeron; Preprint DAMTP 96/48, hep-ph/9605383, to appear in the proceedings of the *International Workshop on Deep Inelastic Scattering and Related Phenomena*, Rome, 1996.

[53] G. F. Chew and S. C. Frautschi; Principle of equivalence for all strongly interaction particles within the S-matrix framework; Phys. Rev. Lett. **7**, 394 (1961).

[54] A. Donnachie and P. V. Landshoff; Total cross sections; Phys. Lett. **B296**, 227 (1992).

[55] A. Donnachie and P. V. Landshoff; Dynamics of elastic scattering; Nucl. Phys. **B267**, 690 (1986).

[56] P. V. Landshoff and O. Nachtmann; Vacuum structure and diffraction scattering; Zeit. f. Phys. **C35**, 405 (1987).

[57] E. M. Levin, G. Marchesini, M. G. Ryskin, and B. R. Webber; Evolution paths for small-x structure functions; Nucl. Phys. **B357**, 167 (1991).

[58] A. Askew, J. Kwieciński, A. Martin, and P. Sutton; QCD predictions for deep inelastic structure functions at HERA; Phys. Rev. **D47**, 3775 (1993).

[59] A. Askew, J. Kwieciński, A. Martin, and P. Sutton; Properties of the BFKL equation and structure function predictions for HERA; Phys. Rev. **D49**, 4402 (1994).

[60] R. K. Ellis, F. Hautmann, and B. R. Webber; QCD scaling violation at small x; Phys. Lett. **B348**, 582 (1995).

[61] J. C. Collins and P. V. Landshoff; Exploring the Lipatov equation; Phys. Lett. **B276**, 196 (1992).

[62] B. Andersson, G. Gustafson, and J. Samuelsson; The linked dipole chain model for DIS; Nucl. Phys. **B467**, 443 (1996).

[63] J. Kwiecinski, A. D. Martin, and P. J. Sutton; Constraints on gluon evolution at small x; Preprint DTP/96/02, hep-ph/9602320.

[64] S. Catani and F. Hautmann; Quark anomalous dimensions at small x; Phys. Lett. **B315**, 157 (1993).

[65] S. Catani and F. Hautmann; High-energy factorization and small-x deep inelastic scattering beyond leading order; Nucl. Phys. **B427**, 475 (1994).

[66] L.N.Lipatov and V.S.Fadin; Gluon production in a quasi-multi-Regge kinematics; JETP Lett. **49**, 352 (1989).

[67] V.S.Fadin and L.N.Lipatov; High-energy production of gluons in a quasi-multi-Regge kinematics; Sov. J. Nucl. Phys **50**, 712 (1989).

[68] V. S. Fadin and R. Fiore; Quark contribution to the gluon-gluon-reggeon vertex in QCD; Phys. Lett. **B294**, 286 (1992).

[69] V. S. Fadin, R. Fiore, and M. I. Kotskiĭ; Gluon reggeization in QCD in the next-to-leading order; Phys. Lett. **B359**, 181 (1995).

[70] V. S. Fadin, R. Fiore, and M. I. Kotskiĭ; Gluon Regge trajectory in the two loop approximation; Preprint BUDKERINP-96-35, hep-ph/9605357.

[71] V. S. Fadin, R. Fiore, and A. Quartorolo; Reggeization of quark-quark scattering amplitude in QCD; Phys. Rev. **D53**, 2729 (1996).

[72] V.S.Fadin and L.N.Lipatov; Next-to-leading corrections to the BFKL equation from the gluon and quark production; Preprint DESY-96-020, hep-ph/9602287.

[73] V. Del Duca; Real next-to-leading corrections to the multigluon amplitudes in the helicity formalism; Preprint DESY-95-249, hep-ph/9601211.

[74] V. Del Duca; Quark-antiquark contribution to the multi-gluon amplitudes in the helicity formalism; Preprint EDINBURGH-96-3, hep-ph/9604250.

[75] R. K. Ellis, Z. Kunszt, and E. M. Levin; The evolution of parton distributions at small x; Nucl. Phys. **B420**, 517 (1994).

[76] R. D. Ball and S. Forte; Summation of leading logarithms at small x; Phys. Lett. **B351**, 513 (1995).

[77] J. R. Forshaw, R. G. Roberts, and R. S. Thorne; Analytic approach to small-x structure functions; Phys. Lett. **B356**, 79 (1995).

[78] M. Ciafaloni; Coherence effects in initial jets at small Q^2/s; Nucl. Phys. **B296**, 49 (1988).

[79] S. Catani, F. Fiorani, and G. Marchesini; Small-x behavior of initial state radiation in perturbative QCD; Nucl. Phys. **B336**, 18 (1990).

[80] J. Kwieciński, A. D. Martin, and P. J. Sutton; The gluon distribution at small x obtained from a unified evolution equation; Phys. Rev. **D52**, 1445 (1995).

[81] A. H. Mueller and J. Qiu; Gluon recombination and shadowing at small values of x; Nucl. Phys. **B268**, 427 (1986).

[82] A. H. Mueller; Small-x behaviour and parton saturation: a QCD model; Nucl. Phys. **B335**, 517 (1990).

[83] A. Askew, J. Kwieciński, A. Martin, and P. Sutton; A structure function test of the QCD Lipatov behaviour at HERA; Mod. Phys. Lett. **A8**, 3813 (1993).

[84] E. Gotsman, E. M. Levin, and U. Maor; A screened BFKL interpretation of F_2 in the exceedingly small-x limit; Preprint TAUP-2307-95, hep-ph/9512316.

[85] H1 Collaboration, S. Aid et al.; A measurement and QCD analysis of the proton structure function; Preprint DESY-96-039, hep-ex/9603004.

[86] ZEUS Collaboration, M. Derrick et al.; Measurement of the proton structure function F_2 at low x and low Q^2 at HERA; Zeit. f. Phys. **C69**, 607 (1996).

[87] ZEUS Collaboration, M. Derrick et al.; Measurement of the F_2 structure function in deep inelastic e^+p scattering using 1994 data from the ZEUS detector at HERA; Preprint DESY-96-076, hep-ex/9607002.

[88] NMC Collaboration, M. Arneodo et al.; Measurement of the proton and deuteron structure functions, F_2^p and F_2^d; Phys. Lett. **B364**, 107 (1995).

[89] E665 Collaboration, M. R. Adams et al.; Proton and deuteron structure functions in muon scattering at 470GeV; Preprint FERMILAB-PUB-95-396-E.

[90] A. Donnachie and P. V. Landshoff; Proton structure function at small Q^2; Zeit. f. Phys. **C61**, 139 (1994).

[91] A. Capella, A. Kaidalov, C. Merino, and J. Tran Thanh Van; Structure functions and low-x physics; Phys. Lett. **B337**, 358 (1994).

[92] A. D. Martin, R. G. Roberts, and W. J. Stirling; Pinning down the glue in the proton; Phys. Lett. **B354**, 155 (1995).

[93] CTEQ Collaboration, J. Botts et al.; CTEQ parton distributions and flavor dependence of sea quarks; Phys. Lett. **B304**, 159 (1993).

[94] H. Lai et al.; Global QCD analysis and the CTEQ parton distributions; Phys. Rev. **D51**, 4763 (1995).

[95] A. D. Martin, R. G. Roberts, and W. J. Stirling; Parton distributions: a study of the new HERA data, α_s, the gluon and $p\bar{p}$ jet production; Preprint DTP/96/44, hep-ph/9606345.

[96] H. Lai et al.; Improved parton distributions from global analysis of recent deep inelastic scattering and inclusive jet data; Preprint MSUHEP-60426, hep-ph/9606399.

[97] M. Glück, E. Reya, and A. Vogt; Dynamical parton distributions of the proton and small-x physics; Zeit. f. Phys. **C67**, 433 (1995).

[98] R. D. Ball and S. Forte; Double asymptotic scaling at HERA; Phys. Lett. **B335**, 77 (1994).

[99] H. Navelet, R. Peschanski, and C. Royon; Deep inelastic onium scattering; Phys. Lett. **B366** (1996).

[100] H. Navelet, R. Peschanski, C. Royon, and S. Wallon; Proton structure functions in the dipole picture of BFKL dynamics; Preprint SPhT-96-043, hep-ph/9605389.

[101] J. R. Cudell, A. Donnachie, and P. V. Landshoff; The BFKL pomeron: can it be detected; Preprint ULG-PNT-96-1-JRC, hep-ph/9602284.

[102] B. Andersson; Running coupling and small transverse momenta; To appear in the proceedings of the *International Workshop on Deep Inelastic Scattering and Related Phenomena*, Rome, 1996.

[103] S. Forte and R. D. Ball; Double scaling violations; Preprint DFTT 35/96, hep-ph/9607291, to appear in the proceedings of the *International Workshop on Deep Inelastic Scattering and Related Phenomena*, Rome, 1996.

[104] E. Witten; Heavy quark contributions to deep inelastic scattering; Nucl. Phys. **B104**, 445 (1976).

[105] M. Glück and E. Reya; Deep inelastic quantum chromodynamic charm leptoproduction; Phys. Lett. **83B**, 98 (1979).

[106] Y. L. Dokshitser, D. I. Dyakonov, and S. I. Troyan; Hard processes in quantum chromodynamics; Phys. Rep. **58**, 269 (1980).

[107] E. Laenen, S. Riemersma, J. Smith, and W. van Neerven; Complete $O(\alpha_{\mathrm{S}})$ corrections to heavy flavor structure functions in electroproduction; Nucl. Phys. **B392**, 162 (1993).

[108] S. Riemersma, J. Smith, and W. L. van Neerven; Rates for inclusive deep-inelastic electroproduction of charm quarks at HERA; Phys. Lett. **B347**, 143 (1995).

[109] B. Badełek et al.; Working group report on the structure of the proton; J. Phys. **G22**, 815 (1996).

[110] M. Lancaster; Proton structure at HERA: F_2, QCD fits and beyond; J. Phys. **G22**, 747 (1996).

[111] F. Sefkow; Heavy flavour production at HERA; To appear in proceedings of *Results and Perspectives in Particle Physics*, La Thuile, Italy (hep-ex/9606009).

[112] A. M. Cooper-Sarkar, R. C. E. Devenish, and M. Lancaster; Measurement of $F_L(x, Q^2)$ at low-x and extraction of the gluon distribution; in *Physics at HERA*, edited by W. Buchmüller and G. Ingelman; page 155; 1991.

[113] L. Favart, M. Gruwé, P. Marage, and Z. Zhang; On the possibility of measuring $F_L(x, Q^2)$ at HERA using radiative events; Preprint LAL-96-32, hep-ph/9606465.

[114] M. G. Ryskin; Diffractive J/ψ electroproduction in LLA QCD; Zeit. f. Phys. **C57**, 89 (1993).

[115] S. J. Brodsky, L. Frankfurt, J. F. Gunion, A. H. Mueller, and M. Strikman; Diffractive leptoproduction of vector mesons in QCD; Phys. Rev. **D50**, 3134 (1994).

[116] M. Ryskin, R. Roberts, and A. Martin; Diffractive J/ψ photoproduction as a probe of the gluon density; Preprint DTP/95/96, hep-ph/9511228.

[117] L. L. Frankfurt, W. Koepf, and M. Strikman; Hard diffractive electroproduction of vector mesons in QCD; Preprint TAUP-2290-95, hep-ph/9509311.

[118] J. Nemchik, N. N. Nikolaev, E. Predazzi, and B. G. Zakharov; Color dipole phenomenology of diffractive electroproduction of light vector mesons at HERA; Preprint DFTT-71-95, hep-ph/9605231.

[119] ZEUS Collaboration, M. Derrick et al.; Measuremnt of the cross section for the reaction $\gamma p \to J/\psi\, p$ with the ZEUS detector at HERA; Phys. Lett. **B350**, 120 (1995).

[120] H1 Collaboration, S. Aid et al.; Elastic electroproduction of ρ_0 and J/ψ mesons at large Q^2 at HERA; Nucl. Phys. **B468**, 3 (1996).

[121] H1 Collaboration, S. Aid et al.; Elastic and inelastic photoproduction of J/ψ mesons at HERA; Preprint DESY-96-037, hep-ex/9603005.

[122] H1 Collaboration, T. Ahmed et al.; First measurement of the deep inelastic structure of proton diffraction; Phys. Lett. **B348**, 681 (1995).

[123] ZEUS Collaboration, M. Derrick et al.; Measurement of the diffractive cross-section in deep inelastic scattering; Zeit. f. Phys. **C70**, 391 (1996).

[124] K. Golec-Biernat, J. Kwieciński, A. D. Martin, and P. J. Sutton; Transverse energy flow at HERA; Phys. Lett. **B337**, 367 (1994).

[125] ZEUS Collaboration, M. Derrick et al.; Comparison of energy flows in deep inelastic scattering events with and without a large rapidity gap; Phys. Lett. **B338**, 483 (1994).

[126] H1 Collaboration, S. Aid et al.; Transverse energy and forward jet production in the low-x regime at HERA; Phys. Lett. **B356**, 118 (1995).

[127] J. Kwieciński, C. A. M. Lewis, and A. D. Martin; Observable jets from the BFKL chain; Preprint DTP/96/48, hep-ph/9606375.

[128] G. Marchesini; Coherence and final states in DIS at small x; to appear in the proceedings of the *International Workshop on Deep Inelastic Scattering and Related Phenomena*, Rome, 1996.

[129] B. Andersson, G. Gustafson, H. Kharraziha, and J. Samuelsson; Structure functions and general final state properties in the linked dipole chain model; Preprint LU-TP-95-34.

[130] A. H. Mueller and H. Navelet; An inclusive minijet cross section and the bare pomeron in QCD; Nucl. Phys. **B282**, 727 (1987).

[131] V. Del Duca and C. R. Schmidt; Dijet production at large rapidity intervals; Phys. Rev. **D49**, 4510 (1994).

[132] W. J. Stirling; Production of jet pairs at large relative rapidity in hadron-hadron collisions as a probe of the perturbative pomeron; Nucl. Phys. **B423**, 56 (1994).

[133] D0 Collaboration; The azimuthal decorrelation of jets widely separated in rapidity; Preprint Fermilab-PUB-96/038-E, hep-ex/9603010.

[134] W. Giele, E. Glover, and D. Kosower; Higher order corrections to jet cross sections in hadron colliders; Nucl. Phys. **B403**, 633 (1993).

[135] W. Giele, E. Glover, and D. Kosower; The two-jet differential cross section at $O(\alpha_s^3)$ in hadron collisions; Phys. Rev. Lett. **73**, 2019 (1994).

[136] V. Del Duca and C. R. Schmidt; BFKL versus $O(\alpha_s^3)$ corrections to large-rapidity dijet production; Phys. Rev. **D51**, 2150 (1995).

[137] G. Marchesini, B. R. Webber, G. Abbiendi, I. G. Knowles, M. H. Seymour, and L. Stanco; HERWIG a Monte Carlo event generator for simulating Hadron Emission Reactions With Interfering Gluons; Comp. Phys. Commun. **67**, 465 (1992).

[138] B. R. Webber; Private communication.

[139] A. De Roeck, on behalf of the H1 and ZEUS Collaborations; Forward jets in deep inelastic scattering at HERA; in *Proceedings of the Workshop on Deep Inelastic Scattering and QCD*; Paris; 1995.

[140] E. Mirkes and D. Zeppenfeld; Dijet production at HERA in next-to-leading order; Preprint TTP95-42, hep-ph/9511448.

[141] E. Mirkes and D. Zeppenfeld; Jet production and deep inelastic scattering at HERA; Preprint TTP-96-10, hep-ph/9604281.

[142] A. Askew, D. Graudenz, J. Kwieciński, and A. D. Martin; Dijet production at HERA as a probe of BFKL dynamics; Phys. Lett. **B338**, 92 (1994).

[143] A. Białas and R. Peschanski; Initial state color dipole emission associated with QCD pomeron exchange; Phys. Lett. **B355**, 301 (1995).

[144] A. Białas and R. Peschanski; Hard diffraction in the QCD dipole picture; Preprint TPJU-19-95, hep-ph/9512427.

[145] A. Białas and R. Peschanski; Hard diffraction from quasielastic dipole scattering; Preprint TPJU-8-96, hep-ph/9605298.

[146] R. Peschanski; Private communication.

[147] Z. Koba, H. B. Nielsen, and P. Olesen; Scaling of multiplicity distributions in high energy collisions; Nucl. Phys. **40**, 317 (1972).

[148] E. Gotsman, E. M. Levin, and U. Maor; A quantitative investigation of the pomeron; Zeit. f. Phys. **C57**, 677 (1993).

[149] E. Gotsman, E. M. Levin, and U. Maor; Effects of shadowing in double pomeron exchange processes; Phys. Lett. **B353**, 526 (1995).

[150] M. Braun; The bootstrap condition for many reggeized gluons and the photon structure function at low x and $N_{\rm C} \to \infty$; Preprint SPbU-IP-1995/3, hep-ph/9502403.

[151] K. D. Anderson, D. A. Ross, and M. G. Sotiropoulos; How to run the coupling in the dipole approach to the BFKL equation; Preprint SHEP-96-06, hep-ph/9602275.

[152] J. R. Forshaw, P. N. Harriman, and P. J. Sutton; On the relevance of the BFKL equation to deep-inelastic scattering at HERA; Nucl. Phys. **B416**, 739 (1994).

[153] M. F. McDermott, J. R. Forshaw, and G. G. Ross; An analytic solution of the BFKL equation with momentum cutoffs; Phys. Lett. **B349**, 189 (1995).

[154] Y. L. Dokshitzer, V. A. Khoze, A. H. Mueller, and S. I. Troyan; *Basics of Perturbative QCD*; chapter 5, pages 132–138; Editions Frontières; 1991.

[155] A. H. Mueller; Private communication.

[156] V. Abramovskiĭ, V. Gribov, and O. Kancheli; Character of inclusive spectra and fluctuations produced in inelastic processes by multipomeron exchange; Sov. J. Nucl. Phys **18**, 308 (1974).

[157] J. Koplik and A. H. Mueller; Hadron-nucleus collisions at high energies; Phys. Rev. **12**, 3638 (1975).

[158] Y. Kovchegov, A. H. Mueller, and S. Wallon; In preparation.

[159] L. McLerran and R. Venugopalan; Computing quark and gluon distribution functions for very large nuclei; Phys. Rev. **D49**, 2233 (1994).

[160] L. McLerran and R. Venugopalan; Gluon distribution functions for very large nuclei at small transverse momentum; Phys. Rev. **D49**, 3352 (1994).

[161] L. McLerran and R. Venugopalan; Green's functions in the color field of a large nucleus; Phys. Rev. **D50**, 2225 (1994).

[162] J. Jalilian-Marian, A. Kovner, L. McLerran, and H. Weigert; The intrinsic glue distribution at very small x; Preprint TPI-MINN-96-1429, hep-ph/9606337.

[163] I. S. Gradshteyn and I. M. Ryzhik; *Table of Integrals, Series and Products*; Academic Press; 1965.

[164] J. Bartels, L. N. Lipatov, and M. Wüsthoff; Conformal invariance of the transition vertex $2 \rightarrow 4$ gluons; Nucl. Phys. **B464**, 298 (1996).

[165] F. James; A review of pseudorandom number generators; Comp. Phys. Commun. **60**, 329 (1990).